OTTO VON GUERICKE
UNIVERSITÄT
MAGDEBURG

ENHANCED REACTOR PERFORMANCE BY DYNAMIC OPERATION: APPLICATION OF INHERENT AND FORCED PERIODIC BEHAVIOR

DISSERTATION

zur Erlangung des akademischen Grades

Doktoringenieur
(Dr.-Ing.)

von M.Sc. Matthias Felischak
geboren am 16. Juni 1989 in Magdeburg

genehmigt durch die Fakultät für Verfahrens- und Systemtechnik
der Otto-von-Guericke Universität Magdeburg

Promotionskommission:	Prof. Dr.-Ing. Kai Sundmacher	(Vorsitz)
	Prof. Dr.-Ing. Andreas Seidel-Morgenstern	(Gutachter)
	Prof. Dr.-Ing. Christof Hamel	(Gutachter)
	Prof. Dr.-Ing. Robert Güttel	(Gutachter)

eingereicht am	29.09.2020
Promotionskolloquium am	21.12.2020

Abstract

There is usually an interest in realizing continuous steady-state processes, for the production of large product amounts by chemical synthesis. Specific process characteristics, for example catalyst deactivation, often require deviations from this simple standard regime and periodic changes of operating parameters are necessary to maintain production. Inherently dynamic unsteady operation modes offer the potential to increase desired target values when the ongoing process steps are well understood and mathematically described. In contrast to unavoidable process dynamics, there is the possibility of deviating from stationary operation by imposing periodic fluctuations. Compared to stationary modes, both mentioned types of periodic process operation have rarely been investigated comprehensively and are often evaluated and designed empirically. Especially, the forced dynamic mode of operation has hardly been applied in the industry.

The present thesis aims to investigate the potential for enhancements by investigating two dynamic heterogeneous and homogeneous process operations. For the precise validation and description of dynamic systems, accurate mathematical models and suitable parameters are necessary. Corresponding methodological approaches are developed, described and applied in this thesis.

The inherent dynamic mode of operation is not imposed onto the system. Instead, the reaction system forces the operator to accept varying objectives over time, such as conversion, productivity, catalyst activity or others. This mode is particularly noticeable in heterogeneously catalyzed reactions. The desired reaction is superimposed by deactivation effects and a periodic coupling with a regeneration step is necessary. This process operation results in inherently dynamic behavior. As a challenging example, the direct conversion of ethene to propene on an aluminized and nickel-impregnated MCM-41 catalyst is considered. The individual steps of the reaction, deactivation and regeneration are analyzed. Based on the obtained data a reaction network consisting of dimerization, isomerization and catalytic cracking could be postulated. This conclusion contrasts to an established network with metathesis instead of cracking. Both reaction networks are evaluated and the occurring mechanisms are verified by deriving and validating kinetic models. Based on longtime experiments, the deactivation could be correlated to the reaction temperature as the main cause. With the help of a suitable regeneration strategy, the operating time of a single catalyst bed could be extended to more than 2000 h. Quantifying the overall process sequence, a program was developed in which the time constants of the individual steps were implemented and optimal termination criteria for the individual steps can be determined.

The concept of a forced dynamic period reactor operation was studied for the homogeneous hydrolysis of acetic anhydride to acetic acid. An experimental setup was developed and realized for implementing perturbations of selected input parameters. The necessary flexibility concerning the type of periodic input functions and the variation of the excited input parameters was of particular interest. Based on an established simple kinetic model for the reaction, promising forcing parameters and dynamic operating conditions could be determined using the nonlinear frequency response (NFR) method. These parameters included both the modulation of a single input and the simultaneous modulation of a combination of two quantities with a corresponding phase shift. It was possible to effectively assess and impose distinct fluctuations of two input parameters for the first time experimentally. The resulting changes in the time-average of the product yield are in good agreement with the predicted output changes.

The results presented in this thesis provide a basis for the development of methodological approaches for the systematic application of transient operation in reaction engineering. Dynamic reactor operation offers numerous promising options for process improvement.

Kurzfassung

Bei der Herstellung großer Produktmengen durch chemische Synthesen besteht in der Regel ein Interesse daran, eine kontinuierliche und unter stationären Bedingungen ablaufende Prozessführung zu realisieren. Häufig erfordern Prozessmerkmale, wie die Katalysatordeaktivierung, Abweichungen von diesem gewünschten Regime und periodische Veränderungen von Betriebsparametern sind zur Aufrechterhaltung des Betriebs erforderlich. Solche unvermeidlich dynamisch instationären Betriebsweisen erfordern es, die ablaufenden Einzelschritte exakt zu beschreiben. Im Gegensatz zu diesen unvermeidlich dynamischen Prozessregimen besteht die Möglichkeit, an sich stationär realisierbare Prozesse durch Aufprägen periodischer Störungen erzwungen instationär zu betreiben. Durch die exakte Wahl der fluktuierenden Parameter kann der Prozess intensiviert werden. Verglichen mit stationären Betriebsweisen sind beide genannten Arten der periodischen Prozessführung bisher in ihrer Gesamtheit wenig untersucht und werden häufig empirisch bewertet und ausgelegt. Insbesondere die erzwungen dynamische Betriebsweise findet bisher kaum industrielle Anwendung.

Ziel der vorliegenden Arbeit ist es, unvermeidlich und erzwungen dynamische Prozesse für heterogene und homogene Reaktionen zu untersuchen. Für die exakte Validierung und Beschreibung dynamischer Systeme sind genaue mathematische Modelle und die entsprechenden Parameter notwendig. Zur exakten Vorhersage des Austrittverhaltens in Abhängigkeit der dynamischen Parameter wurden methodische Herangehensweisen abgeleitet, beschrieben und angewendet.

Der unvermeidbar dynamische Betrieb ist gekennzeichnet durch einen Effekt, der dem System nicht zusätzlich aufgeprägt wird. Stattdessen zwingt das Reaktionssystem dem Betreiber zeitlich variierende Zielgrößen auf, wie Umsatz, Produktivität, Katalysatoraktivität oder ähnliche. Besonders bei heterogen katalysierten Reaktionen ist dieser Effekt festzustellen. Durch die Überlagerung der Reaktion durch die Deaktivierung und einem anschließend notwendigen Regenerationsschritt ist ein dynamisches Regime die Folge. Als Beispielreaktion wurde die direkte heterogen katalysierte Umsetzung von Ethen zu Propen an einem aluminierten und mit Nickel imprägnierten MCM-41 Katalysator betrachtet. Zur Untersuchung dieses Problems wurden die einzelnen Schritte der Reaktion, Deaktivierung und Regeneration analysiert. Anhand der Daten konnte ein Reaktionsnetzwerk bestehend aus Dimerisierung, Isomerisierung und katalytischem Cracking postuliert werden. Dieses weicht ab vom etablierten Netzwerk unter Berücksichtigung einer Metathesereaktion anstelle des Crackings. Unter Verwendung kinetischer Modelle wurde die Gültigkeit des Reaktionsnetzwerkes und der dabei ablaufenden Mechanismen validiert. Die beobachtete Deaktivierung konnte anhand von Langzeitexperimenten auf die Reaktionstemperatur als Hauptursache zurückgeführt werden. Mithilfe einer geeigneten Regenerationsstrategie konnte die Betriebsdauer eines einzelnen Katalysatorbettes auf mehr als 2000 h verlängert werden. Auf Basis der erwähnten Prozessschritte wurde ein Simulationsprogramm entwickelt, mit dem Zeitkonstanten der Einzelschritte in unterschiedlichen Verhältnissen zueinander implementiert werden können und optimale Abbruchkriterien anhand der Katalysatoraktivität bestimmt werden.

Um das zweite Konzept einer erzwungen dynamisch periodischen Reaktionsführung zu realisieren, wurde die homogene Hydrolyse von Essigsäureanhydrid zu Essigsäure betrachtet. Hierfür wurde ein experimenteller Aufbau entwickelt und umgesetzt, um die Eingangsparameter periodisch zu stören. Bei der Konzeptionierung war die notwendige Flexibilität, hinsichtlich der periodischen Eingangsfunktionen und der Variation der angeregten Eingangsparameter, von besonderem Interesse. Anhand einer abgeschätzten Kinetik für die Reaktion, konnten vielversprechende Betriebsfenster unter Verwendung der nonlinear frequency response (NFR) Methode bestimmt werden. Diese umfassten sowohl die Modulation eines einzelnen Eingangsparameters, als auch die gleichzeitige Modulation einer Kombination von zwei Größen mit einer entsprechenden Phasenverschiebung. So war es erstmalig möglich, valide und effektiv ein oder gleichzeitig zwei angeregte Eingangsparameterfluktuationen aufzuprägen. Die resultierenden Veränderungen des zeitlichen Mittelwertes der Ausbeute waren in guter Übereinstimmung mit den von der NFR Methode vorhergesagten Änderungen.
Die präsentierten Ergebnisse tragen zum gezielten Einsatz transienter Betriebszustände in der Reaktionstechnik bei. Ein optimierter dynamischer Reaktorbetrieb bietet die Möglichkeit von signifikanten Prozessverbesserungen zu erzielen.

Table of contents

I Introduction - Dynamic Reactor Operation 1

1 Types of Dynamic Reactor Operation 5
- 1.1 Inherent Dynamic Reactor Operation 6
- 1.2 Forced Dynamic Reactor Operation 8

2 Mathematical Modeling of Chemical Reactors 11
- 2.1 Reactor Balance Equation 11
  - 2.1.1 Batch-Reactor 13
  - 2.1.2 Plug Flow Tubular Reactor 13
  - 2.1.3 Continuously Stirred Tank Reactor 14
- 2.2 Thermodynamic Equilibrium 15
- 2.3 Kinetics 16
  - 2.3.1 Reaction Kinetics 17
  - 2.3.2 Kinetics of Deactivating Catalysts 22
  - 2.3.3 Kinetics of Regenerating Catalysts 24
  - 2.3.4 Parameter Estimation 25

3 Model Reactions for Two Different Case Studies 27
- 3.1 Ethene to Propene Reaction 27
- 3.2 Hydrolysis of Acetic Anhydride 35
- 3.3 Conclusion 37

II Inherent Dynamic Reactor Operation 41

4 Preliminary Theoretical Study of Inherent Periodic 45
- 4.1 Fundamental Assumptions 45
- 4.2 Continuously Stirred Tank Reactor 48
  - 4.2.1 Influence of Residence Time 48
  - 4.2.2 Influence of Switching Time 49
  - 4.2.3 Influence of Rates for the three Individual Process Steps 51
- 4.3 Plug Flow Tubular Reactor 52
- 4.4 Conclusion 54

5 Experimental Study: Ethene to Propene Reaction 56
- 5.1 Experimental Setup and Procedure 56
  - 5.1.1 Laboratory Reactor for Kinetic Screening 56

5.1.2 TGA/DSC 58
5.2 Catalyst Preparation 58
5.3 Results 59
5.3.1 Characterization 59
5.3.2 Experimental Investigation of Catalytic Activity (Step 1) 62
5.3.3 Experimental Investigation of Deactivation (Step 2) 67
5.3.4 Experimental Investigation of Regeneration (Step 3) 73
5.4 Conclusion 75

6 Modeling of the ETP Process Steps 78
6.1 Kinetics of Reaction (step 1) 78
6.1.1 Evaluation of Kinetic Mechanisms of Catalytic Cycles 78
6.1.2 Data Analysis 81
6.1.3 Model Derivation 81
6.1.4 Evaluation of Kinetic Reaction Models 84
6.2 Kinetics of Deactivation (step 2) 91
6.3 Kinetics of Regeneration (step 3) 94
6.4 Conclusion 95

III Forced Dynamic Reactor Operation 99

7 Kinetics of the Hydrolysis of Acetic Anhydride 102
7.1 Experimental Setup and Procedure 102
7.2 Experimentally Obtained Kinetic Data 105
7.3 Kinetic Model Derivation 107
7.4 Parameter Estimation 109
7.5 Conclusion 112

8 Analysis and Demonstration of Forced Periodic Operation 113
8.1 Nonlinear Frequency Response 113
8.1.1 Single Input Modulation using NFR 115
8.1.2 Simultaneous Modulation of Multiple Input Parameters using NFR 116
8.1.3 Reactor model evaluated by the NFR 118
8.2 Simulative Results 120
8.3 Single Input Modulation 125
8.4 Simultaneous Input Modulation of Inlet Concentration and Total Flow Rate 129
8.4.1 Variation of Inlet Concentration Amplitude 132
8.4.2 Variation of Total Flow Rate Amplitude 134
8.4.3 Variation of Phase Difference 136
8.5 Conclusion 138

IV Concluding Remarks **141**

9 Concluding Remarks and Outlook **143**
9.1 Conclusions 143
9.2 Outlook 145

Bibliography . . . . . **i**

Nomenclature . . . . . **xxv**

Glossary . . . . . **xxviii**

List of Figures . . . . . **xxxii**

List of Tables . . . . . **xxxix**

V Appendix **A1**

A Inherent Dynamic Operation **A3**
A.1 Theoretical Study of Inherent Dynamic Optimization A3
A.2 Analysis of the Process steps for the ETP reaction A4
A.2.1 Experimental Configurations A4
A.2.2 Catalyst Characterization A6
A.2.3 ETP Activity Evaluation A6
A.2.4 Deactivation A7
A.3 Reaction Kinetics A11
A.4 Two-Stage Reactor Concept A19
A.4.1 Pilot Plant Setup A19
A.4.2 Single-Stage Setup Results A21
A.4.3 Metathesis Catalysts - Literature Survey A22
A.4.4 Catalyst Preparation A22
A.4.5 Metathesis Catalyst Evaluation A25
A.4.6 Two-Stage Setup A31

B Forced Dynamic Operation **B1**
B.1 Theoretical Evaluation B1
B.2 Sinusoidal Wave B2
B.3 Square Wave B5
B.3.1 Definition of General Input Function Modulation using NFR B5
B.3.2 Experimental Implementation B7

Part I

Introduction - Dynamic Reactor Operation

> *Nothing in life is to be feared, it is only to be understood. Now is the time to understand more, so that we may fear less.*
>
> —Marie Curie

The chemical industry is currently at a crossroads. On the one hand, it is of utmost interest to increase efficiency; on the other hand, the compatibility of production with the environment is to be improved at the same time. A central aspect of the design is the use of reaction engineering approaches to improve chemical systems with the application of innovative concepts and enhancement of existing setups. Accordingly, dynamic operating behavior can improve process control and increase efficiency.

Hereby, two concepts with inherent and forced dynamic operation can be depicted for application. Concerning the first aspect, the inherent dynamics are particularly noticeable in catalytic reactions. Catalyzed processes make up the majority of all chemically relevant reactions, mainly heterogeneous catalysis. The observable deactivation of the applied catalyst is one of the main reasons for the dynamic reactor operation, since catalysts must be periodically regenerated or exchanged. This disturbance in the operation must be considered when designing the process to keep the effectiveness accordingly high.

Of particular interest are forced dynamically operated reactive systems that present great potential. The idea to improve reactor performance, by applying a forced perturbation altering certain parameters periodically at the reactor inlet, was studied for the first time systematically by Horn [Horn and Lin, 1967; Horn and Bailey, 1968; Horn, 1970] and Bailey [Bailey and Horn, 1969; Bailey and Horn, 1971a; Bailey and Horn, 1971b; Bailey and Horn, 1972a; Bailey and Horn, 1972b]. Substantial early contributions to this field were made by Douglas [Douglas and Rippin, 1966; Douglas, 1972a; Douglas, 1972b] and by Renken [Renken, 1972; Renken, 1974; Renken, 1982; Renken, 1983].

Between 1975 - 1990 numerous theoretical investigations have been carried out to explain and to quantify possible performance improvements due to forced dynamic operation, to optimize such regimes and to control them [Farhad Pour, 1976; Farhadpour and Gibilaro, 1981; Schädlich et al., 1983; Grabmüller et al., 1985; Hoffmann and Schädlich, 1986]. Nevertheless, although it was mathematically proven that the implementation of forced dynamic regimes is capable to outperform optimized steady-state operation, such advanced concepts were not implemented on an industrial scale. In a review paper published in 1995 major drawbacks of forced periodic operation were identified: (a) increased process complexity and (b) insufficient quantitative predictability of the process outcome [Silveston et al., 1995]. It was shown recently using the nonlinear frequency response (NFR) [Nikolić et al., 2014a; Nikolić et al., 2014b; Nikolić et al., 2015; Nikolić et al., 2016a; Nikolić et al., 2016b] as a new predictive method that the forced dynamic operation of a reactor can lead to targeted improvements as well as to detrimental outputs during the implementation. Therefore, the predictability of a reactor's response to a dynamic change is essential.

With these possibilities in mind, the present thesis deals with the increase of selected process parameters through the targeted, dynamic operation of chemical systems. For the first time, a test setup shall be realized, which dynamically fluctuates single as well as several input parameters simultaneously. Furthermore, the individual process steps of the reaction, deactivation and regeneration of a heterogeneous catalyzed system for the direct conversion of ethene to propene shall be kinetically described.

The present thesis is divided into three parts. In an introductory **first part**, the two applied concepts of dynamic reactor operation are introduced. Afterward, the necessary mathematical formulations of the reactor level, the thermodynamics of chemical systems and the kinetics of the occurring effects of reaction, deactivation and regeneration are presented. Within, the implied concepts for kinetic modeling are explained and the chosen reaction models are derived in detail. In the following, the reactive chemical systems employed for the evaluation of dynamic reactor operation for forced (hydrolysis of acetic anhydride) and inherent (ethene to propene reaction) are introduced. The focus of this chapter is to give a thorough overview of the current state-of-the-art research.

Within the **second part**, the inherent dynamic operation is investigated for a heterogeneously catalyzed reaction. Initially, a theoretical study is conducted to illustrate the potential of precise process control of the sub-processes. For this, for a fictitious reaction network and kinetic parameters, a simulative program is developed and applied. Thereby, the influence of periodic operation is evaluated for varying termination criteria of the lower and upper boundary of activity. Therefore, these values are optimized for a continuously stirred tank reactor (CSTR) and a plug flow tubular reactor (PFTR). The heterogeneously catalyzed ethene to propene reaction is evaluated. Therefore, the analysis of the resulting products for varying reaction conditions is performed. In the following, the obtained results are adopted for the reaction network (step 1) evaluation. Further, the deactivation (step 2) is investigated and consequently its activity a. To obtain reproducible catalytic results, regeneration (step 3) strategies and conditions are validated. Subsequently, the separate process steps of the reaction, deactivation and regeneration are kinetically modeled.

The **third part** focuses on forced periodic reactor operation, where first the kinetic models are exploited for applicability to the performed adiabatic steady-state experiments. Next, the newly build experimental setup for the implementation of single and multiple simultaneous input parameter modulation for a homogeneous reaction is presented. Here, the ideas behind the nonlinear frequency response (NFR) concept are elucidated to allow for reliable evaluation of the steady-state and dynamic operation. With suitable kinetic parameters, for the hydrolysis of acetic anhydride, a forced dynamic operation based on predictions by the nonlinear frequency response (NFR) method is applied. The analytical solution for the prediction of single and multiple input parameter variations is obtained. The derived predictions are experimentally evaluated for sinusoidal input modulations.

1 Types of Dynamic Reactor Operation

Dynamic phenomena occur frequently in chemical processes. Well-known is the possibility of instabilities during the start-up or shut-down of continuous reactors, in which oscillation may occur that can lead to safety issues [Baerns, 2013]. The dynamic operation can distinctly be separated into two operational modes. First, the inherent dynamic operation, and second, the forced dynamic operation. Inherent dynamic operation is typical for deactivating catalytic systems. For this operational mode, the chemical system enforces a periodic behavior onto the operator. A time for production, consisting of reaction (step 1) and concurrent deactivation (step 2), with decreasing activity over time, is followed by a period of regeneration (step 3) when no product can be obtained. Both time arrays, for reaction/deactivation and regeneration, give the overall process cycle time. This period is necessary for calculating the time-average of the desired performance parameters, used for optimization. Accordingly, thorough knowledge regarding the reaction kinetics, the deactivation kinetics and the regeneration kinetics of the catalyst is essential for precise predictions of the outcome of the cyclic operation.

As mentioned it is also possible to force the reactive system to operate dynamically. For this second type, the operator imposes a periodic or transient behavior onto the system. The perturbation of the input parameters results in explicit variations of the reactor output, following the transfer functions of the system and as illustrated in Figure 1.2. The imposed variation can occur periodically, by a corresponding function such as a sinusoidal variation, or by transient behavior, as a step profile of e.g. the temperature in adsorptive processes. For the evaluation, the time-averaged value of a selected target quantity must be considered.

Global players in the chemical industry, such as BASF, Bayer or Dow Chemicals, have developed processes for the production of basic or specialty chemicals that generate desired products. Over the course of the production cycle, it is necessary to make the process more efficient to keep it competitive and reduce possible costs. The tuning can be done based on the operating mode, on the catalyst or reactor level.

Pioneering work by Horn [Horn, 1970], Bailey [Bailey and Horn, 1971a] and Renken [Renken, 1972; Renken, 1974] beginning in the 1960's and 70's focused on exceeding steady-state operation. Their approach was based on dynamic reactor operation, either by transient [Truffer and Renken, 1986], forced [Lange et al., 1999; Nikolić et al., 2016a] or inherent [Silveston et al., 1995] operation. Fields of application range from chemical engineering [Horn, 1970; Bailey and Horn, 1972a; Schädlich et al., 1983; Grabmüller et al., 1985; Hoffmann and Schädlich, 1986] and bio-processes [William A. Cupples and Rodger D. Loutzenhiser, 1998; Silveston et al., 2008] to vibrational operation [Liao and Shiang, 1991] and turbines [Xu and Wang, 2007]. It could be proven mathematically, that the implementation of dynamics can exceed the optimal steady-state (ss) output. However, dynamic operation modes were rarely implemented to industrially relevant applications.

The reasons are assumed to be complexity, the necessary investments in control and predictability of the outcome. Industrially speaking, no sufficient incentive exists to change from the constant output to continuously modulated ones. The possible beneficial economic feasibility did not convince personnel to pursue the necessary investment in this technology [Stankiewicz and Kuczynski, 1995]. Knowledge regarding the occurring effects is needed to overcome the existing doubts [Silveston, 2013]. Nevertheless, investigation of forced periodic operation has been ongoing [Güttel, 2013; Meyer et al., 2017] and there are examples of applied dynamic process operations, like pressure-swing-adsorption [Aaron and Tsouris, 2005; Grande and Rodrigues, 2005] and the Matros reactor [Matros, 1985].

1.1 Inherent Dynamic Reactor Operation

As mentioned, inherent dynamics, are usually caused by the reactive system itself [Murzin, 2010; Murzin, 2013]. Information about instabilities is essential to avoid spontaneous, dynamic changes [Elnashaie and ElShishini, 1996]. In the case of tempered systems, it is possible to obtain oscillatory behavior for specific conditions. Another form of inherent dynamic reaction control is the use of a batch reactor (BR). With this discontinuous procedure, so-called dead times [Hertwig et al., 2018; Baerns, 2013] occur besides the actual reaction time, reducing the productivity of the process. A typical example is the polymerization of styrene-butadiene [Osakada, 2014].

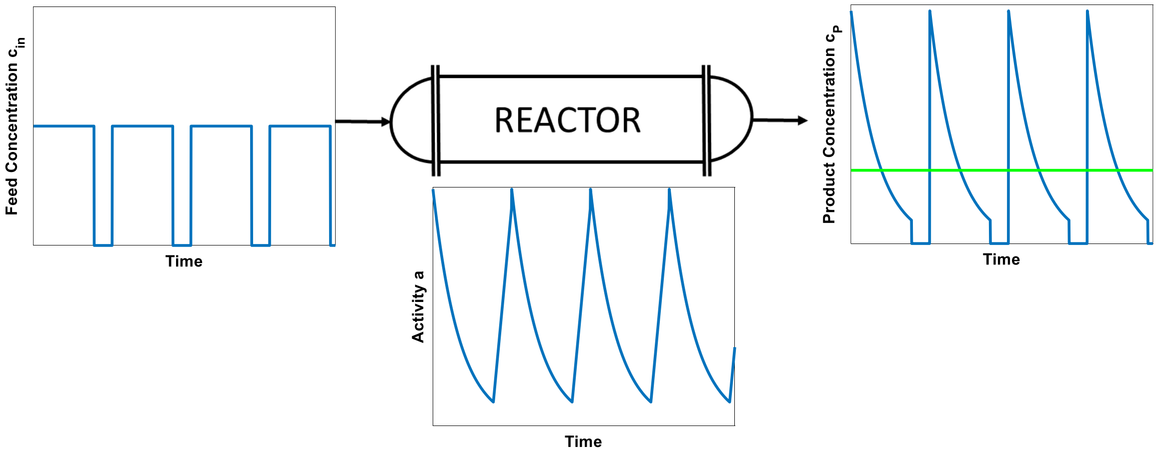

Figure 1.1: Schematic display of an inherent cyclic reactor operation carrying out a catalyzed reaction facing deactivation effects.

In the present work, no reference is made to the behavior of the reactor. As it is necessary for example in the case of the Matros reactor, which is based on forced flow reversal, or the adsorptive reactor, in which a product is adsorbed from the stream and must subsequently be desorbed [Bunimovich et al., 2008]. The focus will be on catalytic processes consisting of a reaction phase (step 1) with a superposition of deactivation (step 2) and a regeneration phase (step 3), as shown in Figure 1.1. Based on these two phases, the total process time is composed, as in the batch reactor, which must necessarily be used for optimization. For homogeneous processes [Gerlach et al., 2017], but especially in heterogeneously catalyzed processes [Argyle et al., 2014], deactivation effects are a considerable factor when designing and operating the reactor, as well as the overall process, respectively [van Santen, 2017].
A typical dynamic process is observed in the case of propane dehydrogenation, in the form of de-

activation. Industrially relevant and implemented examples are e.g. the Honeywell/UOP OLEFLEX process and the STAR by Uhde [Zimmermann, 2013]. In the case of the OLEFLEX process, propane is converted with heated steam and a mixture of residue propane and hydrogen in a series of several tubular reactors. The process is continuous by circulation of the catalyst through the reaction chamber and subsequent removal of coke in a separate regeneration apparatus. The STAR process, on the other hand, uses deactivation to shift the equilibrium and thus reduce the conversion X. However, to generate higher conversions, dehydrogenation is combined with an oxidative step. This combination increases the conversion but also enhances the formation of CO_2. Therefore, several tubular reactors are used in parallel. A switch between the reactive and regenerative process steps by decoupling the respective reactor is necessary [Zimmermann, 2013]. The aim of the cyclic operation is the maximization of the reaction/deactivation time to the regeneration time frame.

The effects leading to deactivation are generally poisoning of the catalyst and rotting, thermal decomposition and sintering, discharge into the gas phase and mechanical attrition of the catalyst. The typical service life of the catalysts and the reason for their deactivation are given in the following for examples of important industrial processes [Argyle and Bartholomew, 2015]. For the ammonia synthesis on an iron catalyst with promoters (K_2O) and a stabilizer (Al_2O_3), a typical period for the catalyst is 10 - 15 years. Under reaction conditions of 450 - 470 °C and 200 - 300 bar, the activity decreases only slowly due to the sintering of the catalyst system. Copper-zinc catalysts on alumina support for methanol synthesis exhibit similar behavior. Due to sintering processes and poisoning by sulfur, chlorine and carbonyls, the activity decreases substantially in 2 - 5 years. Further, the oxidative and reductive sites of the methanol catalyst are of interest, leading to varying catalyst activity with time-on-stream (TOS) [Ovesen et al., 1997; Fichtl et al., 2015; Frei et al., 2019].

For butane oxidation to maleic anhydride, the loss of phosphor from the vanadium phosphorus oxide catalyst, mixed with transient metal additives, and the attrition of the catalyst pellets are the reason for the loss of activity and selectivity over 1 - 2 years. The deactivation for the ammonia oxidation is much faster at 800 - 900 °C and 1 - 10 bar. The Pt-Rh alloy gauze loses its selectivity to the target product within 0.1 - 0.5 years due to platinum loss and surface roughening. An even faster deactivation process occurs in the case of catalytic cracking. Under reaction conditions of 500 - 560 °C with 2 - 3 bar, the synthetic zeolites are deprived of their activity within minutes by very rapid coking. Therefore, continuous regeneration is necessary, which often leads to mass losses in the applied fluidized beds' [Argyle and Bartholomew, 2015].

An inherently dynamic process used in industry for the purification of material and mainly exhaust gas streams is the pressure swing adsorption (PSA). Typically, the polluted exhaust air stream is brought in a column to adsorb CO_2. In parallel, a second apparatus is regenerated with a desorbent or vacuum dissolving CO_2 that is passed through a separate outlet [Aaron and Tsouris, 2005; Bunimovich et al., 2008]. The process can be operated efficiently and continuously by controlled switching between the two columns. The PSA can also be used to separate unwanted by-products. For example, with a suitable metal organic framework (MOF), the complex separation of ethine and ethene can be carried out effectively [Baerns, 2013].

As a modification of such classical purification processes, the simulated moving bed (SMB) has been used for the separation of complex mixtures. Lamia [Lamia et al., 2007] showed the high quality of the process for the separation of propene and propane when a suitable desorbent is selected and the switching times are appropriate. The SMB is a multi-column arrangement in which the columns are not moved. Instead, the feed position of the reactants is switched. Accordingly, a counter-current flow can be simulated [Kim et al., 2017], leading to transient behavior. In most cases, this is only possible for low concentrated systems due to smearing and overlapping. If a concentrated feed is desired, a certain trade-off has to be made with a reduction in the process robustness [Mazzotti et al., 1997]. Nevertheless, the process has proven to be effective in separating even enantiomeric separation [Shen and Okamoto, 2016]. An analogy to a distillation column can be created with separation stages and a corresponding purity. Here, the use of a dividing wall is to be investigated in a project by Lee [Lee, 2020]. With the help of this simple modification, the number of separation zones will be increased, which improves the continuous operation mode and at the same time leads to increased separation of overlapping mixture components.

Another effect that causes changes in process control is the attrition of reactor components. Thus, the abrasion or destruction of packing's can lead to a changed separation efficiency, which must be counteracted with control variables accordingly [Afandizadeh and Foumeny, 2001]. The example of the Fischer-Tropsch synthesis showed that the catalyst particles are abraded and smaller particles result. As a consequence the pressure drop increases, transport processes on the catalyst change and the transport passing sieves can cause filter blockages [Tsakoumis et al., 2010]. In a study by Wu [Wu et al., 2015] it could be shown that the abrasion leads to a change of the surface and the resulting smoothing is variable in time. Further, the change in particle size can lead to fragmentation, which can strongly influence the operation of the entire system.

1.2 Forced Dynamic Reactor Operation

For forced dynamically operated reactive systems the transient behavior is enforced on the system by the operator, as illustrated in Figure 1.2.

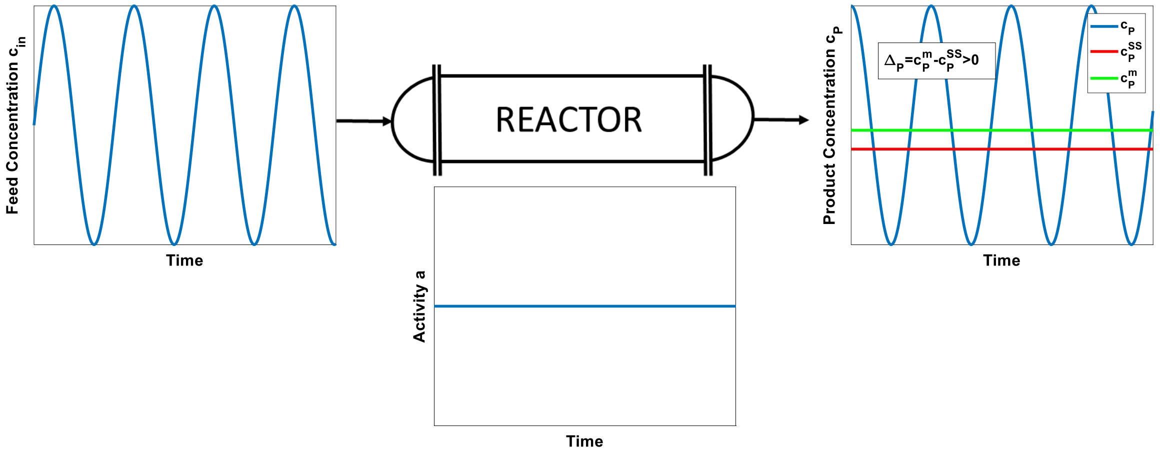
Feed Concentration c_{in}
Time
REACTOR
Activity a
Time
Product Concentration c_P
$\Delta_P = c_P^m - c_P^{SS} > 0$
c_P
c_P^{SS}
c_P^m
Time

Figure 1.2: Exemplified display of the forced periodic reactor operation concept with imposed fluctuation of an input parameter.

In previous studies, well to handle reactions were investigated, like ethanol dehydration to diethyl ether [Golay et al., 1998] or ethane dehydrogenation [Liwu et al., 1990]. The chosen hydrolysis of acetic anhydride in an adiabatic CSTR excludes transient behavior, e.g. ad- or desorption equilibrium, or self-induced effects, e.g. catalyst deactivation. Although this reaction has no industrial relevance, it provides the chance to gain insight into the effects of dynamic reactor operation and their predictability.

Regarding the industrial application of dynamic process control, it must be ensured that the generated profit exceeds the investment made. However, this leads to further process limitations. Concerning forced dynamic operation, it must, therefore, be considered how long the analysis of individual samples takes and how accurate the determined kinetic parameters are. When considering the first point, the measurement time should be sufficiently short to validate the quality of the imposed dynamics. Otherwise, no effects will be detected, which could lead to safety risks [Stankiewicz and Kuczynski, 1995].

Furthermore, the prediction of the output for the imposed modulations should indicate the influence of the kinetics. For the operation of industrial plants, there are often no exact mathematical descriptions available, in particular for a wide window of operation [Baerns, 2013]. Therefore, the areas of dynamic operation for variable, kinetic parameters have to be evaluated in advance to exclude risks. Here, the nonlinear frequency response (NFR) analysis can support the evaluation process. Due to the fast solution of the derived analytical functions, a multitude of possible forcing parameters can be validated [Petkovska and Do, 1998; Marković et al., 2008; Petkovska and Seidel-Morgenstern, 2013; Nikolić et al., 2014b]. The NFR method does not merely evaluate chosen dynamic forcing parameters (amplitude, frequency) for a single input parameter variation, but also multiple input variations. Consequently, the phase difference as another parameter opens up more degrees of freedom for the optimization process. The NFR method, based on control theory and higher-order harmonic functions, is capable of determining optimal parameters for the objective function [Petkovska and Seidel-Morgenstern, 2013].

It is conceivable that industrially fluctuating inlet conditions must be expected. A change in the observable reactor behavior can be caused by a change of the supplier or by the interconnection within a network of reactors. Accordingly, the predictions of the NFR can be used to determine to what extent the simultaneous modulation of operating parameters can intensify a process, with corresponding frequency, amplitude and phase shift. Therefore, the nonlinear frequency response method is experimentally realized and validated in this thesis for a homogeneous reaction.

The currently well-known case for the use of fluctuating input variables is the ENERGY TRANSITION (German: ENERGIEWENDE). The aim is to turn away from fossil raw materials to renewable sources. Accordingly, energy generated by wind and solar power is to be used to create chemical intermediate storage compounds. The central aspect here is the coupling of energy and chemistry [Eichel et al., 2020]. In these power-to-gas or power-to-liquid processes, electrochemistry and catalysis play a central role.

As is well known, renewable energy sources are subject to "natural intermittency". During the day, the sun can generate a lot of electricity which cannot be fully demanded by consumers and therefore has to be stored in energetically favorable raw materials for its use when needed. Especially the production of hydrogen in sufficient quantities seems promising to convert it with CO or CO_2 to methanol or dimethyl ether [Güttel et al., 2020]. These can be converted to fuel in subsequent steps. Thus, the "methanol economy", suggested by Olah [Olah, 2005; Olah et al., 2009], can be efficiently realized.

In the context of the examples presented here it is necessary to adapt the processes to the local value chains [Güttel et al., 2020]. This includes not only the existing plants but also the integration of existing raw materials and the production possibilities of electricity. This reorientation places new demands on the processes. Such criteria include robustness to variable inputs, the tolerance of the process to such variations, constant safety and, above all, consistent product quality. Mathematical models are necessary to maintain such processes and simultaneously increase target values by fluctuation. Based on these models, optimizations must be carried out and uncertainties must be evaluated. Ultimately, "the bottleneck is now in the understanding of the [dynamic] process" [Güttel et al., 2020]. At this point, the following chapters will try to contribute to a better understanding and predictability of inherent and forced dynamic reactor operation.

For the prediction and evaluation of dynamic reactor operation, it is necessary to have suitable methods available. These approaches are derived and applied to the mentioned case studies in the following chapters. The results of the present work should increase the applicability of dynamic plant operation to assess the occurring effects and thus to intensify the process.

2 Mathematical Modeling of Chemical Reactors

In this chapter, all the mathematical fundamentals, necessary for understanding the investigated concepts and reactors, will be presented. The applied reactor models will be derived and the formulas for chemical thermodynamics are presented. Further, kinetic approaches for the mentioned sub-processes are illustrated. Besides, methods for the evaluation of forced and inherent dynamic operation are presented by the nonlinear frequency response (NFR) and the cyclic reactor operation.

2.1 Reactor Balance Equation

The centerpiece in the design process and calculation of chemical reactors are the material and energy balance. These are presented and explained in generalized form in the following section.
Generally, the material change of a component i is determined by a material flow and a source therm, R_i.

$$\frac{\partial c_i}{\partial t} = -div\left(\vec{j}_i\right) + R_i \tag{2.1}$$

When a homogeneous reaction system is considered, no mass transport effects occur. Therefore, the material flow can be simplified utilizing only a convective $\vec{j}_{K,i}$ and diffusive material flow $\vec{j}_{D,i}$.

$$\vec{j} = \vec{j}_{K,i} + \vec{j}_{D,i} = c_i w - D_i grad c_i \tag{2.2}$$

The source term, which represents the involvement of component i in a variety of reactions, is the expression of the reaction rate r_j in conjunction with the respective stoichiometric coefficient ν_i of the component in this reaction to represent degradation and formation.

$$R_i = \sum_j \nu_{i,j} r_j \tag{2.3}$$

Insertion of the two terms (eqs. (2.2) and (2.3)) results in the following expression.

$$\frac{\partial c_i}{\partial t} = -div\left(c_i w - D_i grad c_i\right) + \sum_j \nu_{i,j} r_j \tag{2.4}$$

Similarly, the energy balance can be represented as follows, [Hertwig et al., 2018]:

$$\frac{\partial (V_R \rho c_P T)}{\partial t} = -div(\dot{q}_W) + \dot{Q}_{disp} + V_R \sum_j r_j \left(-\Delta_R H_j\right) \quad . \tag{2.5}$$

In the case of a generalized formulation of the heat balance, the heat flow consists of convective flow ($\dot{q}_{CW}$), a diffusive flow ($\dot{q}_{DW}$) and a heat transfer by heating or cooling along the reactor wall ($\dot{q}_{Wall}$).

$$\dot{q}_W = \dot{q}_{CW} + \dot{q}_{DW} + \dot{q}_{Wall} = \rho w c_P T - \lambda grad T + k_W A_W T \tag{2.6}$$

Analogous to the material balance, the source term is dependent on the reaction rate, which couples both balances. By substitution of eq. (2.5) and neglecting the heat of dissipation $\dot{Q}_{disp}$, the following form eq. (2.7) is obtained.

$$\frac{\partial(V_R \rho c_P T)}{\partial t} = -div(\rho w c_P T - \lambda grad T + k_W A_W T) + V_R \sum_j r_j \left(-\Delta_R H_j\right) \tag{2.7}$$

Due to the complexity, diffusive terms are not considered in the present work. For the precise description of the diffusive effects, it is necessary to vary the size and amount of catalysts involved. Though, the preparation of catalysts was not the main focus of the present work. Thus the mass (eq. (2.8)) and energy balances (eq. (2.9)) for the investigated reactive systems are simplified.

$$\frac{\partial c_i}{\partial t} = -div(c_i w) + \sum_j \nu_{i,j} r_j \tag{2.8}$$

$$\frac{d(V_R \rho c_P T)}{dt} = -div(\rho w c_P T + k_W A_W T) + V_R \sum_j r_j \left(-\Delta_R H_j\right) \tag{2.9}$$

The balance equations consist of an accumulation term, convective terms and a contribution by reaction. Also, a cooling or heating term along the reactor wall is included for the energy balance.
For heterogeneous catalytic reactions employing a fixed-bed, the flow velocity w can be expressed as the weight-to-flow ratio (W/F), eq. (2.10).

$$W/F = \frac{m_{cat}}{F_{tot}^{in}} \tag{2.10}$$

This definition allows both the catalyst mass m_{cat} and the total flow rate F_{tot}^{in} to be considered. That way different input ratios are correlated to one another. In the case of stirred tanks, this coefficient is not used. Instead the residence time τ (eq. (2.11)) is used for homogeneous reactions, which is the ratio of reactor volume V_R to total volumetric flow F.

$$\tau = \frac{V_R}{F} \tag{2.11}$$

It is necessary to quantify the quality of the respective system using evaluation variables, so-called performance parameters. In the present work conversion X (eq. (2.12)), selectivity S (eq. (2.13)) and yield Y (eq. (2.14)) are considered.

Conversion of component i: $$X_i = \frac{\dot{n}_i^0 - \dot{n}_i^{exp}}{\dot{n}_i^0} \tag{2.12}$$

Selectivity of product k: $$S_k = \frac{\dot{n}_k^{exp}}{\sum_l \dot{n}_l} \tag{2.13}$$

Yield of product k: $$Y_k = \frac{\dot{n}_k^{exp}}{\dot{n}_i^0} \cdot \frac{(-\nu_i)}{\nu_k} \tag{2.14}$$

The conversion is the difference between the reactant i fed $\dot{n}_i^0$ and the number of moles in the reactor at a given time $\dot{n}_i^{ex}$ in ratio to the quantity of reactant initially fed into the system. For the selectivity of a product component k, the experimentally determined molar quantity is normalized to the sum of all products l analyzed in the reaction system, where $k \in l$ is one component. This normalization guarantees that the selectivity will result in values between zero and one. In contrast, the yield of product k is linked to the reactant i. The specific amount of moles of product k in the reactor at a given time is related to the number of moles of limiting reactant i. The stoichiometric ratios within the reaction are considered by the reciprocal ratio of the respective stoichiometric coefficients of the participating components.

In the following subsections, the applied reactor types are presented in detail.

2.1.1 Batch-Reactor

With the batch reactor (BR), the only discontinuous system is presented. No in- or outlet streams occurr, while the system is assumed ideally mixed. Therefore, the mass balance eq. (2.1) is simplified, where the concentration change is only dependent on the occurring chemical reaction, in which component i is involved.

$$\frac{dc_i}{dt} = \sum_j \nu_{i,j} r_j \tag{2.15}$$

In case of the discontinuous reactor, there are also no in- or outflows in the energy balance. Accordingly, the temperature change is determined by the heat exchange along the wall and by the reaction in the reactor.

$$\frac{d(V_R \rho c_P T)}{dt} = -k_W A_W (T - T_{cool}) + V_R \sum_j r_j \left(-\Delta_R H_j\right) \tag{2.16}$$

With these expressions for the mass (eq. (2.15)) and energy balance (eq. (2.16)) the BR can be mathematically formulated.

2.1.2 Plug Flow Tubular Reactor

As a counterpart to discontinuous operation, which is flexible but faces unwanted dead times for filling, emptying and cleaning, continuous reactors such as the plug flow tubular reactor (PFTR) can generate high product flows with consistent product quality.

The application of continuous systems is of great interest. In comparison to the above mentioned discontinuous BR, the mass balance as a whole, including convection, is considered for a general flow of $\vec{j}_i$.

$$\frac{\partial c_i}{\partial t} = -div\left(\vec{j}_i\right) + \sum_j \nu_{i,j} r_j \tag{2.17}$$

In the case of the PFTR, the reactor is assumed to have no back-mixing and is considered to be one dimensional in the z-direction. As a result, the divergence term can be represented by change of molar flow $\dot{n}$ along the reactor in z-dimension over a cross-section area A (eq. (2.18)).

$$div\left(\vec{j}_i\right) = \frac{1}{A}\frac{\partial \dot{n}_i}{\partial z} = \frac{1}{A}\frac{\partial (c_i \cdot F)}{\partial z} \tag{2.18}$$

When investigating concentration profiles, the molar flow is substituted by the product of concentration c and volumetric flow F. The total differential in eq. (2.18) can be simplified with the assumption of constant total flow. Thus, another valid and generally applied simplification is the assumption of steady-state behavior. In the case of unsteady operation a partial differential equation results [Hertwig et al., 2018], as shown in eq. (2.19).

$$\frac{\partial c_i}{\partial t} = -\frac{F}{A}\frac{\partial c_i}{\partial z} + \sum_j \nu_{i,j} r_j \tag{2.19}$$

For the stationary tubular reactor, the mass balance has not temporal dependency resulting in a comparable formula to the BR. A distinction is made between a change caused by reaction over a time scale, in the case of the discontinuous system, and the local coordinate for the continuous plug flow system. Nevertheless, both equations result in the same trends from a mathematical point of view. The energy balance is analogous to the mass balance. Here, the complete balance must be considered. In addition to accumulation, convection and reaction must be included.

$$\frac{\partial T}{\partial t} = -u\frac{\partial T}{\partial z} + \frac{1}{\rho c_P}\sum_j \left(-\Delta_R H_j\right) \cdot r_j \tag{2.20}$$

2.1.3 Continuously Stirred Tank Reactor

In contrast to the PFTR, the continuously stirred tank reactor (CSTR) is a perfectly mixed, continuous reaction system. Thus the divergence can be expressed by the difference between the concentrations at the inlet and outlet. Due to the ideal mixing of the system, no gradients occur within the reactor, analogous to BR. The concentration at the outlet is equivalent to the concentration in the reaction chamber and therefore no longer locally dependent.

$$div\left(\vec{j}_i\right) = \frac{F}{A}\frac{dc_i}{dz} = \frac{F}{A}\frac{\Delta c_i}{\Delta z} = \frac{F}{A \cdot z} \cdot (c_i - c_i^0) \tag{2.21}$$

Subsequently, this expression can be used for the convective term in the general form (eq. (2.17)), resulting in the following equation eq. (2.22) with a difference of the inlet concentration c_i^0 and the outlet concentration, the concentration in the reactor, c_i.

$$\frac{dc_i}{dt} = -\frac{F}{V_R}\left(c_i - c_i^0\right) + \sum_j \nu_{i,j} r_j \tag{2.22}$$

Similarly, the polytropic energy balance with accumulation, convection, heating/cooling and the reaction is established (eq. (2.23)).

$$V_R \overline{\rho c_P}\frac{dT}{dt} = F\overline{\rho c_P}(T_{in} - T) + k_W A_W (T_K - T) + V_R \sum_j (-\Delta_R H_j) r_j \tag{2.23}$$

For an adiabatic CSTR, no cooling or heating is available. Therefore, the term for energy exchange along the walls of the reactor and the temperature dependence of the average system properties $\overline{\rho c_P}$ is neglected for the ideal case (eq. (2.24)).

$$V_R \overline{\rho c_P}\frac{dT}{dt} = F \cdot \overline{\rho c_P} \cdot (T_{in} - T) + V_R \sum_j \left(-\Delta_R H_j\right) \cdot r_j \tag{2.24}$$

In case of an adiabatic system a relevant chemical engineering parameter is the adiabatic temperature raise (ΔT_{ad}). This value calculates the maximum increase in temperature, when no heat exchange is available and the vessel temperature is influenced by the heat generated or consumed by the reaction. The coefficient is defined as follows:

$$\Delta T_{ad} = \frac{(-\Delta_R H) \cdot c^0}{\rho c_P} \quad . \tag{2.25}$$

With the information regarding the maximum change in temperature, the stability of the reactive system can be evaluated.

Based on the immediate dispersion of the concentration in the CSTR, an increase in feed concentration will have a lesser effect on the reaction system, compared to the other mentioned reactors. Therefore, the CSTR will present less conversion in the same period, compared to the previously mentioned BR and PFTR. Meaning, the reactor itself is significant to achieve the desired product in a time-span.

2.2 Thermodynamic Equilibrium

Various factors are required for the calculation and design of chemical reactors. One essential part is chemical thermodynamics. Chemical thermodynamics is determined solely by the initial and final states of the present molecules [Wedler and Freund, 2012; Onken et al., 1996; Gmehling and Kolbe, 1992]. Accordingly, these calculations are independent of the pathway of the reaction. Thus, the compositions at thermodynamic equilibrium can be calculated in advance, when the enthalpy of reaction $\Delta_R H$, the entropy of reaction $\Delta_R S$ and the free enthalpy of Gibbs $\Delta_R G$ are known from data collections [Yaws, 1999].

The reaction enthalpy $\Delta_R H$ indicates whether heat is released (exothermic) or energy is drawn from the system (endothermic) during the reaction (eq. (2.9)). It is dependent on the enthalpy of formation H_F of the components involved in the reaction. These values are generally defined for standard conditions and must be adjusted, according to the reaction conditions (T,p). Pressure has a negligible influence on the thermodynamic equilibrium constant, though the composition is dependent. The temperature dependence is significant and is included via the specific heat capacity $c_P(T)$ of the component in eq. (2.9). The temperature correlated value of enthalpy is calculated according to the following relationship (eq. (2.26)), the *Law of Kirchhoff* [Baerns, 2013].

$$\Delta_R H = \sum_i \nu_i \Delta_F H_i^{\oslash} + \sum_i \int_{T^0}^{T} \nu_i \cdot c_{P,i}(T) dT \tag{2.26}$$

Similarly, the reaction entropy $\Delta_R S$ can be calculated, where the temperature-dependent function is related to the reaction temperature, see eq. (2.27).

$$\Delta_R S = \sum_i \nu_i \Delta_F S_i^{\oslash} + \sum_i \int_{T^0}^{T} \nu_i \cdot \frac{c_{P,i}(T)}{T} dT \tag{2.27}$$

Using the variables of enthalpy $\Delta_R H$ and entropy $\Delta_R S$, the free enthalpy (Gibbs enthalpy) $\Delta_R G$ can be calculated (eq. (2.28)).

$$\Delta_R G = \Delta_R H - T \cdot \Delta_R S \tag{2.28}$$

This equation is the *Gibbs-Helmholtz equation* and provides answers regarding the spontaneity of the reaction [Hertwig et al., 2018]. A reaction can be exergonic, spontaneous reaction converting reactants to products, or endergonic.

The multitude of chemical reactions is characterized by reversible behavior, with a forward and backward reaction. If a system is settled at the chemical equilibrium, both reaction steps take place at equal speed and thus, no changes of the chemical composition can be determined [Baerns, 2013]. At this point, the change in Gibbs enthalpy has a minimum and the equilibrium constant K_P^{TD} can be calculated accordingly (eq. (2.29)).

$$K_P^{TD} = exp\left(-\frac{\Delta_R G}{R \cdot T}\right) \tag{2.29}$$

Depending on the value of K_P, the position of the equilibrium can be evaluated. At a value of one, equivalent quantities of reactants and products are present. With a value higher than one, the equilibrium is on the product side. This relationship is concluded by the ratio of the reaction rate constants of the forward reaction to the backward reaction (eq. (2.30)).

$$K_P = \frac{k_{forward}}{k_{backward}} \tag{2.30}$$

Accordingly, the equilibrium constant cannot only be formulated as a function of the thermodynamic quantities, as in eq. (2.29), but also on the mass action law, eq. (2.31). It is evident that the material composition of the system can express the value of K_P^{mass} in equilibrium. At the same time, the influence of reaction pressure on the equilibrium is illustrated. Since the thermodynamic quantities define the value of the equilibrium constant K_P, an adjustment of the individual mole fractions would compensate for a pressure variation in the case of ideal gases to a reference pressure $p^{\oslash}$.

$$K_P^{mass} = \prod_i \left(\frac{p_i}{p^{\oslash}}\right)^{\nu_i} = \left(\frac{p_{tot}}{p^{\oslash}}\right)^{\sum_i \nu_i} \cdot \prod_i {x_i}^{\nu_i} \tag{2.31}$$

At equilibrium, both, K_P^{TD} and K_P^{mass}, are of equal value.

2.3 Kinetics

In comparison to the thermodynamic description of a chemical system, kinetics does not deal with compositions in a state of equilibrium. Instead, the temporal sequence of a reaction is considered. The kinetic calculation is a necessity for solving chemical and reaction engineering aspects, as well as predicting their dynamics. For thermodynamically feasible reactions, qualitative aspects, e.g. the reactor type, and quantitative targets, like yield, reactor volume or reaction control [Baerns, 2013], can be determined with reliable kinetic approaches.

It is essential to describe both product and intermediate formation properly. This results in a functional relationship of the reaction rate r and the corresponding variables, such as concentration c, pressure p, temperature T or the applied catalyst.

Micro- and macro-kinetic calculations can be considered for modeling reactive systems. In the case

of micro-kinetics, the individual reaction steps are considered, which can be validated by spectroscopic investigations and have a corresponding reaction rate for each step.
Macro-kinetics further consider transport processes, diffusive effects and adsorption or desorption onto active sites. These effects especially concern heterogeneous systems, which can be classified into gas-liquid reactions, fluid-solid and enzyme reactions. First, reactants have to be transported by a mass flow to the active sites on the catalyst surface. The energy has to proceed accordingly by heat transfer. As a result, gradients of concentration and temperature occur [Baerns, 2013].
In the following, different modeling approaches for chemical systems will be discussed.

2.3.1 Reaction Kinetics

The kinetics of a chemical reaction considers the initial time range in which relevant concentration changes occur. Here, local and temporal concentration profiles are represented reaction-specific utilizing kinetic approaches. The models used contain parameters that must be determined with data from performed experiments. For homogeneous reactions, the reaction kinetics are equivalent to the chemical kinetics. In the case of heterogeneous reaction systems, the model considers additional information on heat and mass transport effects [Levenspiel, 1999; Hertwig et al., 2018].
For the general formulation of the reaction rate r, a temporal change in moles or concentration is assumed (eq. (2.32)).

$$r = \frac{1}{\nu_i}\frac{1}{V_R}\frac{dn_i}{dt} \overset{V=const.}{=} \frac{1}{\nu_i}\frac{dc_i}{dt} \tag{2.32}$$

Depending on the considered system, the change must be independent of the size or residence time in this reactive area for comparability. In the case of homogeneous systems (eq. (2.32)), the reference is usually made to the reactor volume V_R or the volumetric flow F. For heterogeneous reactions, the catalyst mass m_{Cat} or the volume of the catalyst are used as reference values (eq. (2.33)).

$$r \cdot V = r_{Cat} \cdot m_{Cat} = r_V \cdot V_{Cat} \tag{2.33}$$

For specific characteristics of individual reactions, the reaction rate r is considered as a combination of functions dependent on temperature, concentration and the employed catalyst (eq. (2.34)) [Baerns, 2013].

$$r(c,T) \cong f_1(T) \cdot f_2(c) \cdot f_3(Catalyst) \cdot \,... \tag{2.34}$$

The first part connected to temperature dependency (eq. (2.35)) can be attributed to the reaction rate constant k(T). Further, the second function (eq. (2.36)) is based on the kinetic rate laws, such as Power-Law (PL) or Langmuir-Hinshelwood-Hougen-Watson (LHHW). The third functional expression relates to the active catalytic sites that can be included in the kinetic rate law.

$$f_1(T) = k(T) \tag{2.35}$$

$$f_2(c) = \text{ kinetic rate laws} \tag{2.36}$$

$$f_3(Catalyst) = \text{ active catalyst center} \tag{2.37}$$

The first functional correlation (eq. (2.35)) can be expressed by the commonly used Arrhenius equation (eq. (2.38)) [Beller, 2012].

$$k(T) = k_\infty \cdot exp\left(-\frac{E_A}{R \cdot T}\right) \tag{2.38}$$

The structure illustrates that both the activation energy E_A and the collision factor k_∞ are directly connected. Accordingly, the simultaneous change of the two values causes a combined response leading to issues in the parameter estimation. Schwaab and Pinto [Schwaab and Pinto, 2007] proposed the following modification to verify the influence of the respective parameter, by introducing a reference temperature T_{Ref}.

$$k(T) = exp\left[ln(k_\infty) - \frac{E_A}{R \cdot T_{Ref}} + \frac{E_A}{R \cdot T_{Ref}}\left(\frac{T - T_{Ref}}{T}\right)\right] \tag{2.39}$$

When subsequently canceling T_{Ref}, this results in the general Arrhenius equation. Alternatively, the following form with a reduced parameter correlation is proposed and was adequately tested [Kiedorf et al., 2014; Kiedorf et al., 2016a; Jörke et al., 2015].

$$k(T) = k_\infty^{ref} \cdot exp\left[-\frac{E_A}{R}\left(\frac{1}{T} - \frac{1}{T_{Ref}}\right)\right] \tag{2.40}$$

For the second functional of the reaction rate (eq. (2.36)), several possibilities for the derivation of kinetic rate laws are available [Sundmacher et al., 2005; Hamel, 2015]. Namely power-law [Levenspiel, 1999; Hertwig et al., 2018], Langmuir-Hinshelwood-Hougen-Watson [Langmuir, 1916; Baerns et al., 1992; Baerns, 2013] and mechanistic modeling [Helfferich, 2004; Murzin and Salmi, 2005; Murzin, 2013]. Each will be explained and derived individually in the following subsections, as these are exploited in the further presented work.

Power-Law Kinetics

The power-law approach is used for a wide range of reactions due to its simplicity. Especially for simple elementary reactions, it is shown that this approach provides good agreement and can, therefore, be applied. It is based on the product sum of the involved concentrations with a reaction order as the exponent for an irreversible reaction step (eq. (2.41)).

$$r = k(T) \cdot \prod_i c_i^{\iota_i} \tag{2.41}$$

For elementary reactions, the exponent corresponds to the stoichiometric coefficient. Generally, this value is acts as an optimization parameter.

In the case of reversible reactions, the backward reaction has to be included. This is realized by combination with the thermodynamically calculated equilibrium constant K_P. The reason is the difficulty to measure the reaction rate constant for the backward reaction separately. This kinetic rate law is assumed for a variety of reactions, e.g. Argyle [Argyle et al., 2014] for the Fischer-Tropsch-Reaction. Extrapolation of the kinetic parameters beyond the experimental range is not reliable, limiting the applicability. Still, within it is useful and trustworthy.

Langmuir-Hinshelwood-Hougen-Watson Kinetics

In contrast to the power-law assumption, the Langmuir-Hinshelwood-Hougen-Watson (LHHW) kinetic rate law recognizes resistances by preexisting adsorption on the catalyst surface [Langmuir, 1916].

Assuming a reaction of $A_{ads} + B_{ads} \leftrightarrow C_{ads} + D_{ads}$ the overall reaction rate is

$$r = k \cdot \left(\theta_A \theta_B - \frac{1}{K_P} \cdot \theta_C \theta_D \right) \quad . \tag{2.42}$$

Here, all involved components can adsorb onto the surface [Baerns, 2013]. The expression for the reaction rate follows the form of a reversible power-law approach. Both forms can be distinguished by the considered information of each component. For the power-law, the concentrations are used and in the case of LHHW, the individual loadings of all components i θ_i on the catalyst are included. The loading is generally expressed by *Langmuir adsorption isotherms* (eq. (2.44)). In contrast to homogeneous reactions, heterogeneous system reactions are preceded by mass transport, adsorption and desorption processes, these are assumed to be in equilibrium, see eq. (2.43) [Hertwig et al., 2018].

$$r_i = r_{adsorption,i} - r_{desorption,i} = k_{ads,i} \cdot p_i \cdot \theta_{free} - k_{des,i} \cdot \theta_i = 0 \tag{2.43}$$

The equation for the adsorption isotherm θ_i can be derived by transformation as a function of the partial pressure of the component p_i, the adsorption equilibrium constants K_i, as a ratio of ad- and desorption of component i, and the free adsorption sites Θ_{free} (eq. (2.44)).

$$\theta_i = K_i \cdot p_i \cdot \theta_{free} \tag{2.44}$$

The complex analysis of heterogeneous catalysts limits the exact determination of the available adsorption sites on the catalyst surface in reasonable time intervals. Thus, the assumption that the totality of all the adsorption sites, the free and the individually loaded with components, can always be summed up to 100 % (eq. (2.45)). By rearrangement, an expression for Θ_{free} can be obtained (eq. (2.46)).

$$1 = \theta_{free} + \sum_i \theta_i \tag{2.45}$$

$$\theta_{free} = \left(1 + \sum_i K_i \cdot p_i \right)^{-1} \tag{2.46}$$

This form can be inserted into the individual adsorption isotherms (eq. (2.44)) and, subsequently, be used for the adsorption isotherms θ_i in eq. (2.42). Thus, the following expression for the reaction rate of an equation described by LHHW is obtained (eq. (2.47)).

$$r = k \frac{K_A p_A K_B p_B - \frac{1}{K_P} K_C p_C K_D p_D}{\left(1 + K_A p_A + K_B p_B + K_C p_C + K_D p_D\right)^2} \tag{2.47}$$

The numerator contains a modified form of the homogeneous, power-law form and the denominator consists of the adsorptive species, as an inhibition. An increase in the respective partial pressures of the reactants does not cause a steady linear increase in the rate of the reactive system. But would lead to a limitation, because the denominator contains correspondingly high values. This fact is a logical consequence of the necessary adsorption of both reactants onto the catalyst surface for carrying out the reaction. If a component is introduced into the system at a significantly higher partial pressure, the competing interaction results in a preferred loading of the catalyst with this component. As a result, the reaction rate would decrease, since the other input substance can no longer adsorb on the surface and is therefore not available for the reaction.

Mechanistic Kinetics

A powerful and more generalized alternative to LHHW models is the application of mechanistic kinetic models (MM). The approach is based on the investigation of reaction networks on a mechanistic level as reviewed by Helfferich [Helfferich, 2004; Marin and Yablonsky, 2011]. It is necessary to have suitable knowledge of the ongoing elementary steps for each occurring reaction. This approach has been applied successfully both for homogeneously [Kiedorf et al., 2014; Jörke et al., 2015] and heterogeneously catalyzed systems [Murzin and Salmi, 2005; Kiedorf et al., 2016a; Mueller et al., 2018].
For illustration, the derivation of the mechanistic model for the catalytic network is given in eq. (2.48). The general structure for a rate expression of a reversible reaction is

$$r = \frac{r_{forward} - r_{backward}}{D} \tag{2.48}$$

Applying the methodology explained by Helfferich [Helfferich, 2004], the Christiansen Matrix (D) must be derived. Within this matrix, all intermediate steps in the specific catalytic cycle postulated are assumed as reversible. The reaction rates are expressed by frequencies λ_j. With $\lambda_j = k_j \cdot \prod_i c_{i,j}$, where each frequency is the product of the corresponding elementary reaction rate constant k_j and the product sum of the concentrations $c_{i,j}$ of the molecules involved in each step of the catalytic cycle.

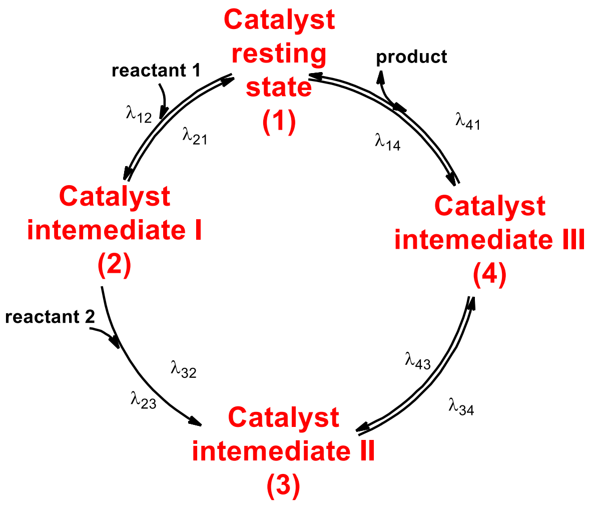
Catalyst resting state (1)
reactant 1
product
λ12
λ21
λ14
λ41
Catalyst intemediate I (2)
Catalyst intemediate III (4)
reactant 2
λ32
λ23
λ43
λ34
Catalyst intemediate II (3)

Figure 2.1: Exemplified catalytic cycle for the generation of a product from two reactants.

For the present catalytic cycle (Figure 2.1) a four-membered reaction pathway is assumed. Therefore all possible series of reactions, resulting in each of the involved catalytic intermediates have to be considered. The resulting *Christiansen Matrix* consists of rows, each representing the individual intermediate concentration. The reaction rate expression using frequencies is given in eq. (2.49).

$$
\begin{aligned}
r^{MM} = \frac{\lambda_{12}\lambda_{23}\lambda_{34}\lambda_{41} - \lambda_{14}\lambda_{43}\lambda_{32}\lambda_{21}}{\begin{aligned}&\lambda_{23}\lambda_{34}\lambda_{41} + \lambda_{34}\lambda_{41}\lambda_{21} + \lambda_{41}\lambda_{32}\lambda_{21} + \lambda_{43}\lambda_{32}\lambda_{21}+\\ &\lambda_{34}\lambda_{41}\lambda_{12} + \lambda_{41}\lambda_{12}\lambda_{32} + \lambda_{12}\lambda_{43}\lambda_{32} + \lambda_{14}\lambda_{43}\lambda_{32}+\\ &\lambda_{41}\lambda_{12}\lambda_{23} + \lambda_{12}\lambda_{23}\lambda_{43} + \lambda_{23}\lambda_{14}\lambda_{43} + \lambda_{21}\lambda_{14}\lambda_{43}+\\ &\lambda_{12}\lambda_{23}\lambda_{34} + \lambda_{23}\lambda_{34}\lambda_{14} + \lambda_{34}\lambda_{21}\lambda_{14} + \lambda_{32}\lambda_{21}\lambda_{14}\end{aligned}}
\end{aligned}
\tag{2.49}
$$

Introducing reaction rate constants, concentrations and considering generalized forms, without specific components eq. (2.50).

$$
r^{MM} = \frac{k_{12}k_{23}k_{34}k_{41}c_{Reac1}c_{Reac2} - k_{14}k_{43}k_{32}k_{21}c_{Prod}}{\begin{array}{llll} k_{23}k_{34}k_{41} & +k_{34}k_{41}k_{21} & +k_{41}k_{32}k_{21} & +k_{43}k_{32}k_{21}+ \\ k_{34}k_{41}k_{12}c_{Reac1}c_{Reac2} & +k_{41}k_{12}k_{32}c_{Reac1}c_{Reac2} & +k_{12}k_{43}k_{32}c_{Reac1}c_{Reac2} & +k_{14}k_{43}k_{32}c_{Prod}+ \\ k_{41}k_{12}k_{23}c_{Reac1}c_{Reac2} & +k_{12}k_{23}k_{43}c_{Reac1}c_{Reac2} & +k_{23}k_{14}k_{43}c_{Prod} & +k_{21}k_{14}k_{43}c_{Prod}+ \\ k_{12}k_{23}k_{34}c_{Reac1}c_{Reac2} & +k_{23}k_{34}k_{14}c_{Prod} & +k_{34}k_{21}k_{14}c_{Prod} & +k_{32}k_{21}k_{14}c_{Prod} \end{array}}
\tag{2.50}
$$

In a next step the numerous reaction rate constants k_{ij} can be grouped individually by combination of the respective concentrations. Further, k_{12} is designated as an overall reaction rate constant $k = k_{12}$, while $k_{23}k_{34}k_{41}$ are factored out. The ratio of $\frac{k_{41}k_{43}k_{32}k_{21}}{k_{12}k_{23}k_{34}k_{41}}$ correlates to the backward reaction divided by the forward reaction, this is equivalent to the reciprocal of the equilibrium constant K_P (eq. (2.30)).

$$
r^{MM} = \frac{k^{MM}c_{Reac1}c_{Reac2} - \frac{1}{K_P}c_{Prod}}{D}
\tag{2.51}
$$

$$
\begin{aligned}
D &= 1 + \left(\frac{k_{21}}{k_{23}} + \frac{k_{32}k_{21}}{k_{23}k_{34}} + \frac{k_{43}k_{32}k_{21}}{k_{23}k_{34}k_{41}}\right) \\
&+ \left(\frac{k_{12}}{k_{23}} + \frac{k_{32}k_{12}}{k_{23}k_{34}} + \frac{k_{43}k_{32}k_{12}}{k_{23}k_{34}k_{41}} + \frac{k_{12}}{k_{34}} + \frac{k_{43}k_{12}}{k_{34}k_{41}} + \frac{k_{12}}{k_{41}}\right) \cdot p_{Reac1}p_{Reac2} \\
&+ \left(\frac{k_{12}k_{32}k_{43}}{k_{23}k_{34}k_{41}} + \frac{k_{21}k_{14}k_{43}}{k_{23}k_{34}k_{41}} + \frac{k_{21}k_{14}}{k_{23}k_{41}} + \frac{k_{32}k_{21}k_{14}}{k_{23}k_{34}k_{41}} + \frac{k_{14}k_{43}}{k_{34}k_{41}} + \frac{k_{14}}{k_{41}}\right) \cdot p_{Prod}
\end{aligned}
$$

Assuming rate-determining steps and the knowledge of the irreversibility of elementary reactions, this complex equation (eq. (2.51)) can be simplified. These simplifications can be achieved by sensitivity analysis or by knowledge of physical and chemical phenomena. In the present case, Figure 2.1, the coupling of two reactants to the product is assumed to be irreversible ($\lambda_{32} = 0$). Finally, the equation can be further simplified by associating the rate constants for individual steps, into lumped inhibition constants K_x(x= α,...,γ).

$$
r^{MM} = \frac{k^{MM}p_{Reac1}p_{Reac2} - \frac{1}{K_P}p_{Prod}}{1 + K_{\alpha}^{MM} + K_{\beta}^{MM} \cdot p_{Reac1}p_{Reac2} + K_{\gamma}^{MM} \cdot p_{Prod}}
\tag{2.52}
$$

Eq. 2.52 is the final form, containing more assessable parameters than a LHHW or a power-law.

Though, with specific assumptions, the mechanistic form can be simplified to LHHW and PL kinetic approaches [Helfferich, 2004].
As mentioned in the introduction a deactivating system consists not just of the reaction step, but further faces deactivation (step 2) and regeneration (step 3) that must be modeled accordingly. The last two steps will be explained for kinetic modeling in the following sections.

2.3.2 Kinetics of Deactivating Catalysts

Deactivation is an effect that occurs in many catalyzed reactions and is increasingly gaining importance for the design and operation of chemical systems [Baerns, 2013]. Many industrial processes deal with this undesired effect, as illustrated in Figure 1.1. Nevertheless, deactivation occurs in a wide variety. The main effects [Argyle and Bartholomew, 2015] limiting the catalyst life or operational time are coking [Dumez and Froment, 1976; Lin et al., 1983; Bellare and Dadyburjor, 1993; Guisnet and Magnoux, 1997; Guisnet et al., 2009], poisoning [Butt, 1980; van Grieken et al., 2008], sintering [P. Desai and J.T. Richardson, 1980; Kuczynski, 1975], fracturing/crushing [Gwyn, 1969; Werther and Reppenhagen, 1999] and vapor formation producing volatile compounds [Hegedus, 1978; Summers and Hegedus, 1979; Busca et al., 1998].
A relevant parameter for the representation of deactivation is the activity a. The activity is a ratio of the reaction rate at a specific point in time for a catalytic process r(t) to the highest possible reaction rate, the initial speed r_0 [Hertwig et al., 2018].

$$a(t) = \frac{r(t)}{r(t=0)} \tag{2.53}$$

The temporal change in activity is correlated to a reaction rate for the deactivation rate r_D (eq. (2.54)) [Baerns, 2013].

$$\frac{da}{dt} = r_d \tag{2.54}$$

Similar to the reaction kinetics with the power-law approach (eq. (2.41)), a mathematical formulation for the deactivation is postulated. Here, the activity a and the deactivating component c_{Deac} form a source term for the decreased activity of the catalyst. Depending on the deactivation mechanism, the individual variables have a corresponding order σ and μ [Moulijn et al., 2001].

$$-r_d = -\frac{da}{dt} = k_d \cdot a^{\sigma} \cdot c_{Deac}^{\mu} \tag{2.55}$$

The deactivation rate constant can be validated by applying an Arrhenius approach (eq. (2.56)), with a deactivation collision factor $k_{d,\infty}$ and activation energy for deactivation E_D, similar to the reaction step [Fogler, 2006].

$$k_d(T) = k_{d,\infty} \cdot exp\left(-\frac{E_D}{R \cdot T}\right) \tag{2.56}$$

With the reaction orders μ=0 and σ=1, a special case can be assumed with no poisoning. This first-order deactivation reaction, results in the following integral expression (eq. 2.57).

$$a(t) = a_0 \cdot exp(-k_d \cdot t) \tag{2.57}$$

The process of coking is generally assumed to be of first-order, though the growth of the coke species must be addressed with more complex models, e.g. combining mono- and multilayer coke species [Gascon et al., 2003].

This simple approach is sufficient for many applications. Nevertheless, an interesting alternative combines the reduction of effective catalyst amount with time-on-stream (TOS) [Janssens, 2009]. The activity is hereby directly correlated with the conversion of the feed. Therefore, the temporal change of the conversion is expressed by chain rule with the contact time on the catalyst.

$$\frac{dX}{dt} = \frac{dX}{d\tau} \cdot \frac{d\tau}{dt} \tag{2.58}$$

For a suitable mathematical expression the individual derivatives have to be substituted. First, the catalyst amount m is correlated with the activity a (eq. (2.57)) and the conversion X (eq. (2.12)).

$$\frac{dm}{dt} = -a \cdot X^p \tag{2.59}$$

The exponent p relates to the deactivation order of the reaction system. When this formula is expanded with $\frac{1}{V}$ on both sides of the equation, the residence time τ can be introduced and a "new" activity a' is obtained.

$$\frac{d\tau}{dt} = -a' \cdot X^p \tag{2.60}$$

For the second derivative of eq. (2.58), the stationary mass balance of the PFTR with one reaction r is used.

$$\frac{F}{A}\frac{dc_i}{dz} = \nu_i \cdot r \tag{2.61}$$

In this expression, the reaction rate is correlated to the volume. Though, it must be the amount of catalyst, as previously shown in eq. (2.33).

$$r = \frac{m}{V} r_m = \rho_m \cdot r_m \tag{2.62}$$

Further, the contact time τ can be expressed as follows, accounting for the volume V_m and density ρ_m of the catalyst, as well as the reactive area A_m and the length of the reaction zone z:

$$\tau = \frac{m}{\dot{V}} = \frac{V_m \cdot \rho_m}{\dot{V}} = \frac{A_m \cdot z \cdot \rho_m}{\dot{V}} \quad . \tag{2.63}$$

Eq. 2.63 can be rearranged, resulting in a term for the length z of the reactive zone in the reactor.

$$z = \frac{\tau \cdot \dot{V}}{A_m \rho_m} \tag{2.64}$$

Hence, the equations eq. (2.62) and eq. (2.64) can be implemented into eq. (2.61).

$$\frac{dc_i}{d\tau} = \nu_i \cdot r_m \tag{2.65}$$

Finally, the expressions for the separate terms of the chain rule (eq. (2.58)) can be substituted by eqs. (2.60) and (2.65) , resulting in the final expression (eq. (2.66))

$$\frac{dc_i}{dt} = (-\nu_i)a'\left(1-\frac{c_i}{c_i^0}\right)^p \cdot r_m \quad . \tag{2.66}$$

With this balance, the catalyst deactivation, based on the conversion of component i, can be calculated accordingly.

2.3.3 Kinetics of Regenerating Catalysts

As mentioned, the majority of catalyzed processes face differently fast and severe effects of deactivation. For an efficient process operation, not only chemical factors but also economical and ecological criteria have to be considered. Factors are whether and how a catalyst is regenerated [Trimm, 2001]. In this thesis, the removal of coke deposits will be considered requiring regeneration.

There are two approaches to implement the regeneration. On the one hand, the reactor level and on the other hand, the catalyst level can be dealt with. A distinction must be made between intraparticular and intraprocess regeneration [Butt, 1984]. On the particulate level, the diffusion effects have to be considered. In the beginning, deposits on the outer surface are removed and only then the regeneration is continued in the interior of the catalyst particle. At the process level, the fluid and solid phases have to be considered. Different zones can form in the reactor, e.g. for heating and burning of the deposits. For the reactor level, concepts can be developed in which continuous regeneration takes place or reactors are connected in parallel to reduce dead times owing to deactivation. One possibility was presented by Fogler [Fogler, 2006] with a fluidized bed by continuously discharging the catalyst with the gas stream. After separation of solid and fluid, the catalyst undergoes regeneration and is then fed back into the reaction chamber. Kelling [Kelling et al., 2012] investigated a conceptual control strategy for a cyclic system with recirculation strategies. In this concept, a recycle flow has to be dynamically adapted depending on the degree of deactivation.

A large number of approaches are available for the catalyst level. In the case of naphtha reforming, Kern [Kern and Jess, 2005] determined for $Pt/Re-Al_2O_3$, that no external mass flow limitation occurs in the catalyst. At the same time, it was shown that two different coke forms occur. One on the metal sites and one on the carrier material, which is less reactive and assumed to be the result of acidic sites. Besides, the positive influence of hydrogen on deactivation was found.

The modeling of the regeneration of a catalytic process is carried out analogously to the process steps described above, according to eq. (2.67) [Butt, 1984].

$$r_{reg} = \frac{1}{\nu_i}\frac{1}{m_{cat}}\frac{d\dot{n}_i}{dt} \tag{2.67}$$

In comparison, the concentration of the carbon present and the local concentration of the oxidizing agent, usually oxygen, are included for this mathematical description. The individual terms are scaled with a corresponding reaction order [Dumez and Froment, 1976; Kern and Jess, 2005; Soerensen, 2017].

$$r_{Reg} = k_{reg} \cdot m_c^{\xi} \cdot \psi_{O_2}^{\psi} = \frac{dm_c}{dt} \tag{2.68}$$

With χ_{O_2} as the volumetric fraction of oxygen O_2 in the gas-phase and m_C the mass of coke. Following the previous descriptions of the reaction rate constant, the general form of the Arrhenius like equation (eq. (2.38)) is applied here as well [Kern and Jess, 2006].

$$k_{Reg}(T) = k_{Reg,\infty} \cdot exp\left(-\frac{E_{Reg}}{R \cdot T}\right) \tag{2.69}$$

Another possibility of mathematically modeling regeneration is a hyperbolic approach [Baerns, 2013]. The structure is similar to the LHHW and is based on the local concentration of the coking agent. Since the regeneration is the reversible deactivation reaction, the approach was modified to the following formulation eq. (2.70).

$$r = \frac{dm_i}{dt} = \frac{k_{Reg} \cdot m_c^{\xi} \cdot \chi_{O_2}^{\psi}}{\left(1 + K_C m_C + K_{O_2} \phi_{O_2}\right)^{\nu}} \tag{2.70}$$

2.3.4 Parameter Estimation

To evaluate the quality of estimated variables, the simulated results are compared with experimentally determined values, e.g. using the sum of squares of residues (SSR). A minimum of SSR can always be achieved by using well-chosen input parameters, a reliable optimization technique and a suitable target function. However, this is strongly dependent on the conditions mentioned above.

Different types of least square evaluation functions are available. The commonly chosen type ordinary least square (OLS) is given in eq. (2.71). This expression is applicable if no information of errors within the measurement is available and a uniform and independent error distribution is considered [Bates and Watts, 2007].

$$SSR\left(\Theta_{opt}\right)^{OLS} = \sum_{j=1}^{N} \left(y^{exp}(y_{in}) - y^{sim}(y_{in}, \Theta_{opt})\right)^2 \tag{2.71}$$

An extension of this methodology is the weighted least square (WLS). Here, the individual differences are normalized to the respective experimental value (eq. (2.72)). Thus, it is possible to compensate for significant differences in the considered values. Accordingly, all parameters are included more equally in the optimization. Though, for zero values this method is inapplicable.

$$SSR\left(\Theta_{opt}\right)^{WLS} = \sum_{j=1}^{N} \frac{\left(y^{exp}(y_{in}) - y^{sim}(y_{in}, \Theta_{opt})\right)^2}{y^{exp}\left(y_{in}\right)} \tag{2.72}$$

These objective functions (OF) can be evaluated for different optimization algorithms. There are several available simulation tools like Matlab capable of implementing specific algorithms, namely *Pattern Search*, *Levenberg-Marquardt* and *Trust region reflective* [Joshi, 2007; Kiedorf et al., 2016b; Bates and Watts, 2007].

For the pattern search algorithm, initially, a mesh for the optimization parameters is constructed, based on the chosen initial values. At each iterative step, the optimizer varies the parameters and checks the SSR. When an improvement is achieved, the new parameters are used for the generation of a renewed mesh. With each iteration, the mesh tightens itself closer to the optima [Mathworks, 2004].

The Levenberg-Marquardt algorithm is based on the Gauss-Newton method and the steepest gradients method. The Newton method solves linear equations approximated by Taylor-series. Unfortunately, the method may result in a singular matrix, if the initial values are close to the optima. This singularity can result in an oscillation of the system further away from the optima, based on the stepwise variation of the parameters. As a result, it is possible to obtain a local minimum that the solver is not capable of overcoming. Therefore, this approach is combined with sequential quadratic programming. Thus, convergence is achieved with high probability at the optima [Joshi, 2007; Levenberg, 1944; Marquardt, 1963].

Based on the Levenberg-Marquardt algorithm, the trust-region reflective was developed. For this algorithm, the objective function is approximated by a simpler function, reflecting the SSR reasonably to the initial point. Its standard approximation is performed using the first two terms of the Taylor series [More and Sorensen, 1983]. The final computation is performed in the sub-problem of the trust region. The parameter variation is performed with a deterministically limited step size. Resulting in qualitative changes of the approximated function and finally improving the objective function [Papageorgiou et al., 2012].

In the previous sections, the necessary mathematical formulas for chemical systems were explained and derived. For the exact design and analysis, models for the calculation of classical chemical reactors (batch reactor (BR), plug flow tubular reactor (PFTR) and continuously stirred tank reactor (CSTR)), equations for the calculation of thermodynamic behavior and kinetic approaches for the representation of occurring effects (reaction, deactivation and regeneration) were presented.

Each of these is essential for the analysis of chemically reactive systems. After the selection of a relevant and suitable reaction system, an adequate reactor is required. The maximum potential of the system can then be determined by thermodynamic calculations.

Furthermore, the already mentioned effects can be validated. For the description of the reaction rate, there are many possible approaches available (power-law approach, Langmuir-Hinshelwood-Hougen-Watson (LHHW), and mechanistic modeling (MM) approach). With suitable kinetic parameters, it is possible to evaluate the productivity and selectivity of a process accurately. However, many chemical processes are confronted with the effect of deactivation, with activity as the essential parameter. At the same time, it is necessary to return the system to its original state, if possible. To optimize the process accordingly, it is necessary to model the deactivation and the described regeneration accurately.

The content of the current chapter was the presentation of necessary equations for the mathematical description of chemical systems and the derivation of suitable methods to validate dependencies of these systems and the applied parameters. In the following, the two case studies considered in the present thesis will be discussed in detail.

3 Model Reactions for Two Different Case Studies

The derived kinetic models and optimization approaches, maximizing the temporal mean value of an objective function, are applied for model systems exploited in the present work. In the case of a heterogeneously catalyzed reaction, the direct conversion of ethene to propene is investigated. The hydrolysis of acetic anhydride is used as a homogeneous reaction system with simpler chemical properties.

The two cases are described in detail and findings from previous investigations are explained below.

3.1 Ethene to Propene Reaction

Over the course of the last decades, propene has become an increasingly important petrochemical feedstock [Lavrenov et al., 2015]. This development is based on the increasing use of propene in the production of polypropylene and propene oxide, among others. The constantly growing demand cannot be met with the current production technologies, mainly steam cracking [Lavrenov et al., 2015]. Therefore, new, more flexible and innovative processes have to be developed to close the widening gap between demand and supply. Due to the current production basis, paradigmatic changes must take place. Accordingly, today's concepts based on oil are inadequate and must be adapted. In the context of the "energy revolution", possibilities are evaluated to close the gap with appropriate sustainable processes.

Many approaches are intensively pursued in current research projects [Amghizar et al., 2017]. These include the dehydrogenation of propane [Kogan and Herskowitz, 2001] and the catalytic cracking of long-chain olefins [Mol, 2004; Zhu et al., 2005b; Zhu et al., 2009], the cross-metathesis of olefins [Mol, 2004; Huang et al., 2005] and the direct conversion of ethene to propene (ETP) [Iwamoto, 2008; Alvarado Perea et al., 2013]. In the following, these processes will be presented in detail.

In industry, These processes are designed as heterogeneous catalyzed processes to meet the industrial requirements. A problem that occurs is a cyclic deactivation-reactivation process. For a suitable description of an overall process, the three individual steps of reaction (step 1), deactivation (step 2) and regeneration (step 3) must be modeled accurately. The modeling of the intrinsic reaction kinetics plays a crucial role.

Dehydrogenation of Propane

Dehydrogenation processes are unique chemical processes that involve the elimination of hydrogen during the formation of propene from propane. A disadvantage of this reaction type is the necessary high reaction temperature (>600 °C) and the effect of catalyst deactivation. However, these operating condition are required to overcome chemical obstacles, even though side reactions are enhanced [Cavani et al., 2007]. Furthermore, at temperatures greater than 700 °C the cracking of the desired product propene to ethene and methane is pronounced [Wittcoff et al., 2013].

Various process technologies are available, which vary in terms of reactor design, reaction conditions and catalyst [Zhu et al., 2009]. In principle, dehydrogenation can be divided into oxidative and thermal process control. Contrary to the thermal dehydrogenation (TDH) process, the oxidative dehydrogenation (ODH) adds small amounts of oxygen to the feed, to overcome limitations by chemical equilibrium. This addition decreases the reaction temperature, but enhances the further oxidation of the obtained products. [Hamel, 2015]

Regarding sustainable chemical operation, Atanga [Atanga et al., 2018] presented an alternative to oxidative dehydrogenation. Propane is dehydrogenated to propene in the presence of CO_2, as a mild oxidant can overcome the problem of over-oxidation and low propene selectivity. In the review, the ratio of Si/Al for different catalyst systems influencing the process performance was shown. With decreasing aluminum content, the conversion of the catalyst decreases with a simultaneous increase in selectivity S to the desired target product propene. With the addition of CO_2, the yield Y could be further increased, because of intensified reverse water-gas-shift-reaction.

In the case of ZnO-HZSM-5, carbon dioxide helped suppress side reactions and thus shifted the chemical equilibrium to the desirable propene. Further, CO_2 enhances the oxidation of the catalyst surface [Mueller et al., 2018]. For Cr/SBA-15 (Santa Barbara Amorphous material (SBA)), a maximum of 80 % in selectivity is determined, which corresponds to a reduced conversion. An increase in the chromium content, increases the conversion, whereas the selectivity decreases analogously. Gomez [Gomez et al., 2018] used a bimetallic $NiPt/CeO_2$ catalyst. This modification presented 11.6 % conversion, with a selectivity of 2.8 % for propene and 96.2 % to CO, which is reasonable with the use of platinum as a catalytic converter.

Grabowski [Grabowski and Słoczyński, 2005] applied vanadium oxide on silica. The material showed an increase in conversion from 1.3 to 10.7 % with increasing contact time of the reactants on the catalyst. Simultaneously, selectivity to propene decreases from 18.6 to 3.4 % at 653 K. If the catalyst is doped with potassium, the conversion is enhanced from 1.7 to 16% at 753 K and higher residence time. In parallel, the selectivity drops from 76 to 16.2 %. The same metal oxide was used by Rostom and de Lasa [Rostom and de Lasa, 2018] on a zirconium oxide and gamma-alumina mixed carrier. For multiple injections, propene with 94 % selectivity could be obtained at 550 °C at a conversion of 25 %.

Using a Cr_2O_3/Al_2O_3 catalyst, Gascon [Gascon et al., 2003] performed kinetic studies. Deactivation is, in the case of TDH, a significant secondary reaction. This effect causes the catalyst to require regular regeneration. In the given example, an activity loss from 35 to 17.5 % conversion was observed within 100 minutes. In contrast, Li et al. [Li et al., 2011] found for $Pt-Sn-Al_2O_3$ that a constant activity was achieved with a maximum of 50 % conversion for high residence times.

An interesting possibility to overcome the occurring deactivation process is the application of membrane reactors. Coronas et al. [Coronas et al., 1995] applied ceramic membranes in combination with a Li/MgO catalyst for the dehydrogenation of ethane. Positively, the process could be intensified in comparison to a conventional fixed-bed reactor. A contrary result was observed by Ziaka et al. [Ziaka et al., 1993]. The group implemented $Pt-\gamma-Al_2O_3$ for the production of propene from propane and observed less conversion compared to the fixed-bed.

Hamel et al. [Hamel et al., 2010] went one step further for the dehydrogenation of ethane on $VO_X - \gamma - Al_2O_3$ and investigated distributed oxygen dosing profiles using a three-stage reactor cascade. The experimental setup showed that the process can be intensified with a membrane reactor, in contrast to the fixed-bed, generating 55.4 % conversion with a selectivity of 46.3%. In comparison to 50.1 % of conversion and 52.3 % of selectivity for the single packed-bed membrane reactor.

Cracking Reaction

Another interesting and widely applied process for the effective production of propene is the cracking reaction. Generally speaking, three types of cracking exist: thermal, catalytic and hydrocracking [Olah and Molnár, 2003]. Thermal cracking is the oldest process of the three, with pyrolysis as the typical application. The first commercially applied thermal cracking was the BURTON PROCESS. It operates at 450 - 550 °C and 5 - 6 bar of pressure. This process was later replaced by the DUBBS PROCESS, which is more efficient. However, the operation conditions with temperatures of 450 - 725 °C and pressures above 70 bar are more severe. [Olah and Molnár, 2003]

Hydrocracking operates at high pressures, with hydrogen added to the reactive system. Small fractions of Pt, Pd or Ni are added to zeolite structures, acting as promoters for increased initial activity for addition or dehydrogenation of the used reactants [Alvarez et al., 1996]. Further, Co-Mo and Ni-Mo on alumina are used at 270 - 450 °C and 80 - 200 bar [Olah and Molnár, 2003]. The primary reactions are isomerization, skeletal rearrangement and cracking on the acidic sites. The cracking generates olefins, however, these are immediately saturated on the hydrogenating sites. The absence of olefinic compounds prevents the system from deactivation. In a review by Rahimi [Rahimi and Karimzadeh, 2011] insight on the naphtha cracking concerning ethene and propene yield was presented.

The catalytic cracking gained interest during the world wars when oil could not be sufficiently provided [Olah and Molnár, 2003]. Initially, reactions were performed in liquid phase, with reaction temperatures at around 225 °C. The non-aromatic crude oil was distilled in the liquid phase, with high octane numbers and considerably less sulfur. Emerging from this, the HOUDRY PROCESS was established, working at 450 °C and using acid-treated montmorillonite, which generated significantly higher octane numbers [Olah and Molnár, 2003]. In the 1960's amorphous silica-alumina compositions, like X faujasites, increased the yield by margins of 10 - 50 %. Later ultra stable (US) zeolites, rare earth (RE) zeolites and zeolite socony mobil (ZSM)-5 became the commercially applied systems with conversions of 50 - 60 % and a high selectivity towards the respective products.

Catalytic cracking of longer chain olefins is an alternative route to provide propene. The cracking reactions proceed via complex networks of reactions [Buchanan et al., 1996]. Besides cracking multiple undesired side reactions occur, such as aromatization, oligomerization and hydrogen transfer. As a result, a wide spectrum of products [Corma et al., 2005] and a subsequent separation problem must be considered. Zeolites like ZSM-5, ZSM-23, and mobil composition of matter (MCM)-22 are highly active for classical catalytic cracking of butenes at temperatures between 600 and 650 °C [Wang et al., 2004; Zhu et al., 2005a; Zhu et al., 2005c; Lu et al., 2006; Zhu et al., 2009].

Von Aretin combined an unhydrogenated ZSM-5 for the cracking of pentene in a two-zone reactor [von Aretin et al., 2017a] and a subsequent recycle [von Aretin et al., 2017b]. It was observed that the mole fraction of propene increased from 10 to 50 % for the two-zone setup in comparison to a single catalyst bed. In parallel, the butenes mole-fraction increased only from 35 to 47 %. Lu [Lu et al., 2006] incorporated chromium into HZSM-5 for the cracking of isobutane at 625 °C. Yielding in a maximum of 56.1 % for both ethene and propene. Pure HZSM-5 presented less yield with 25 % for propene and 20 % for ethene. The conversion is above 99 % in both cases, while deactivation is significant at elevated temperatures.

Liu [Liu et al., 2016] compared the thermal cracking to catalytic cracking using ZSM-5 for ethene and propene as feed. It is apparent that the catalytic process converts the feed more intensively and suppresses the saturation via hydrogen transfer.

Another interesting possibility is Small-pore molecular sieves (SAPO)-34, implemented by Nawaz [Nawaz et al., 2009; Nawaz et al., 2010], in the range of 450 - 600 °C for the cracking of 1-hexene. It was shown that the small pores of the catalyst prohibited bimolecular reactions with conversion as high as 60 % and propene selectivity of 86.5 %. Nonetheless, strong deactivation is occurring with time-on-stream. Within 5 min the activity was reduced to 12.5 % of conversion through coking of the pore network. Reduced activity results in propane as the main reaction product.

The availability of butene motivated Zhu to investigate the 1-butene cracking [Zhu et al., 2005a] on MCM-22 at 530 - 650 °C. Conversion dropped from 95 to 65 % within 14 h on stream, though constant selectivities of 20 % for ethene and 45 - 50 % for propene were observed. A decrease in reaction pressure was detrimental for conversion, but an increased ratio of C_3/C_2 is achieved. Contrary, an increase in temperature and weight hourly space velocity (WHSV) resulted in higher conversion and a lower ratio of propene to ethene. When using potassium doped ZSM-5 [Zhu et al., 2005b] in the range of 540 - 650 °C the conversion slightly increased and propene selectivity was enhanced. Though, an optimal potassium content exists, with decreasing conversion above a limiting amount. When steam is added to the reactor, the conversion decreases slower with time-on-stream, due to less aromatics formed that are believed to cause the deactivation of the system. Further, the Si/Al_2 ratio was investigated [Zhu et al., 2009]. A higher ratio significantly increased the selectivity towards propene and ethene, because of decreased acidity.

For the mechanistic description of the cracking reaction, many suggestions were postulated [Kissin, 2001]. Cortright [Cortright et al., 1997] proposed that initially, a carbenium ion is formed. It adsorbs onto the catalyst surface, with a subsequent isomerization believed to occur. Next, a β -scission occurs, with two separate molecules resulting. Nevertheless, this step is not necessarily the only possibility. Further, oligomerization to long-chain olefins and hydride transfer for saturation of hydrocarbons can be observed. Kissin [Kissin, 1996], concluded that a tertiary carbon atom is used instead. With the predominant fission at the weakest C-C bond in α position. Here, the primary product is an olefin with less byproduct. Tiong Sie [Tiong Sie, 1992] further elaborated on a cyclopropyl intermediate that explains the observed effects and explains these observations.

A major side effect that is always observed, is the fast deactivation of the applied catalysts. Mance [Mance et al., 2017] studied a commercial fluid catalytic cracking (FCC) catalyst for high coke formation. For the analysis, a combined setup of nuclear magnetic resonance (NMR) with electron paramagnetic resonance (EPR), scanning electron microscope (SEM) and energy dispersive X-ray spectroscopy (EDX) was implemented. The investigation revealed that aromatics are formed at the outer shell of the catalyst on the active metal sites. In the inner pores of the mainly zeolitic catalyst supports, coke is predominantly formed in form of long-chain hydrocarbons.

With the cracking being a widely applied industrial process, kinetic data and parameters are necessary to optimize the respective processes. Feng [Feng et al., 1993] used single event kinetics for n-decane cracking employing RE-Y (rare earth zeolite Y) as the catalyst. Moustafa [Moustafa and Froment, 2003] generated a reaction network using computational studies, including the coke formation and subsequent deactivation. Within the network, deactivation was implemented as a function of the coke amount. Von Arentin [von Aretin and Hinrichsen, 2014] performed another kinetic study. In this case single event kinetics for the cracking of 1-hexene on a ZSM-5 at 350 °C were derived. The model comprises a wide spectrum of products, with the major product being branched isomers of pentene.

Metathesis Reaction Towards Propene

The metathesis is one of the novel organic reactions. Its significance has steadily grown over the past couple of decades. In 2005 the research was rewarded with the noble prize for chemistry for Chauvin [Herisson and Chauvin, 1971; Chauvin and Commereuc, 1992; Amigues et al., 1991], Grubbs [Grubbs and Stanley, 1991; Grubbs and Chang, 1998; Blackwell et al., 2000; Trnka and Grubbs, 2001; Grubbs, 2003; Grubbs, 2004; Vougioukalakis and Grubbs, 2010] and Schrock [Schrock, 1986; Schrock et al., 1990; Schrock, 2004], who pursuit significant milestones in the field of enhanced metathesis reactions. Relevant and interesting research work in the field of metathesis is presented below.

Metathesis can be performed both homogeneously and heterogeneously. Particular reference should be made to the work of Grubbs and Schrock. Based on their work, outstanding progress was achieved in this field. Grubbs developed catalysts based on ruthenium for specialized ring opening metathesis polymerization (ROMP) and ring closing metathesis (RCM). The obtained catalyst of the first generation could be produced by simple single pot synthesis [Grubbs and Chang, 1998; Grubbs, 2004]. Based on this effective and stable catalyst type, a second-generation was developed. Therefore, ligands were substituted accordingly, which resulted in higher activities of the reactive system in a homogeneous phase [Grubbs, 2006].

Schrock [Schrock, 1999; Schrock and Hoveyda, 2003] applied molybdenum and tungsten as classical representatives of heterogeneously catalyzed metathesis for homogeneous reaction systems. The metals and metal complexes were incorporated into imido alkylidene complexes. These active and significantly cheaper metals had the disadvantage of incompatibility with functional groups. Therefore, the research achieved types of catalyst with corresponding ligands to be more stable for the used complex reactants [Schrock, 2006].

The transferability of homogeneous and heterogeneous systems with polyfunctional organic groups to increase tolerance for ROMP and RCM was investigated and successfully implemented by Pariya [Pariya et al., 1998]. Thus, Bakala [Bakala et al., 2008] succeeded in applying a homogeneous complex to $\gamma - Al_2O_3$ and a mesoporous material. Conversions of 50 - 99 % and selectivity to the desired C_{14}-olefin of 20 - 100 % could be achieved depending on the reaction conditions.

With gaining knowledge and promising results, the industrial interest in large-scale implementation increased. Among others, the Meta-4 process is a prominent industrial application, which takes place at 35 °C and 60 bar on Re_2O_7/Al_2O_3 in the liquid phase. Another frequently used type is the Shell higher olefin process (SHOP) process. Homogeneous nickel-phosphine in 1,4-butanediol is used. The reaction temperature is set to 90 - 100 °C and significantly higher pressures of 100 - 110 bar. The Olefin Conversion Process (OCT) from Lummus is a commonly applied process. Here, WO_3/SiO_2 is used as a catalyst. MgO is introduced as a promoter of isomerization and inhibitor of side reactions. The temperature is even higher, with over 250 °C, whereas the pressure is moderate with 30 -

35 bar [Mol, 1999; Mol, 2004].

In experimental investigations by Kustov [Kustov et al., 2016], Re_2O_7/Al_2O_3 was used for the metathesis of C_5-C_8-olefin. Balcar implied the same metal oxide on mesoporous alumina for feeds of 1-octene and 1-decene [Balcar et al., 2004; Balcar et al., 2007; Balcar et al., 2009], and Kapteijn [Kapteijn et al., 1981] with propene as the reactant. Balcar achieved a conversion of over 90 % for higher temperatures in the range of 25 - 60 °C and increased rhenium concentrations. At the same time, the main components in the product stream with over 95 % are the desired alkenes. Kapteijn always observed insufficient conversions under 5 % for conditions at 1 - 2.5 bar and 40 - 130 °C.

Other typical metals and metal oxide systems are namely molybdenum and tungsten. Li [Li et al., 2007; Li et al., 2009a; Li et al., 2009b] utilized MoH$\beta-Al_2O_3$ for the metathesis of butenes with varying amounts of aluminum. For 30 % of aluminum at 393 K, a conversion of 80 % for butene is achieved, while the propene selectivity is greater than 95 %. Unfortunately, the catalyst is subjected to deactivation effects. The analysis of the distributed residue showed three coke species. These form at the beginning of the reaction. Coke is deposited on the active sites and results in a dynamic operation of the process. Subsequently, oligomerization is observed and is considered to be the main reason for the loss in catalytic activity [Li et al., 2009a], with the blockage of active sites and available pore structure.

The last-mentioned and generally applied metathesis catalyst is tungsten. In comparison to rhenium and molybdenum, this metal is less active at lower temperatures, however, tungsten is more resistant to impurities and more stable [Mol and can Leeuwen, 2008]. Therefore, tungsten and tungsten-oxide in various forms have been submitted to various research. Liu [Liu et al., 2009a] employed WO_3/Al_2O_3-xHY for 1-butene self-metathesis. The beneficial influence of a moist atmosphere was studied and found to improve the stability of the catalyst [Liu et al., 2009b]. As a typical candidate, WO_3/SiO_2 for the cross-metathesis of 1-butene with ethene towards propene was used in combination with MgO for isomerization of intermediate products. A conversion for butene greater than 80 %, with propene selectivity greater than 95 % at 280 °C with 30 bar was achieved when pretreated under nitrogen and hydrogen [Liu et al., 2015].

Bhuiyan impregnated tungsten on MCM-41 for a 2-butene feed at 500 °C [Bhuiyan et al., 2013]. As a result, the selectivity of propene was at 39 %. When SBA-15 was used, the value changed slightly to 37 %, with conversion kept at 80 %. For the metathesis, several olefinic feed compositions can be used. Therefore, Chen [Chen et al., 2013] exploited WO_3/SiO_2 for high $C_2:C_{10}$ ratios. It must be mentioned that the decene feed had 10 % of impurities, mainly octene and heptane. This ratio is beneficial for a conversion of decene with 80 %, while ethene conversion decreases from 50 % to 0 % under excess ethene. A maximum in propene selectivity with 75 % could be achieved for a ratio of 15:1, which falls to 65 % over 70 h on stream.

Ethene to propene reaction

The on-demand processes described at this point face significant disadvantages limiting the applicability, such as the reaction conditions, chemical equilibrium, undesired side reactions, catalyst deactivation or the use of valuable feedstock. Ethene, on the other hand, is easily available and relatively cheap as it is the main product of steam cracking. Therefore, the direct conversion of ethene to propene (ETP) is an attractive alternative to meet the growing demand for propene [Lavrenov et al., 2015]. In the recent past, much effort has been dedicated to achieve significant progress in this field of research. An overview of current investigations is given in Table 3.1. Taoufik et al., reported the direct transformation of ethene to propene over a tungsten hydride supported on alumina [Taoufik et al., 2007]. Though, the conversion decreased from 40 to 10 % within 10 h on stream. In parallel, the propene selectivity was always above 85 % respectively. Oikawa et al. [Oikawa et al., 2006] and Lin et al. [Lin et al., 2009] presented silicaaluminophosphate microporous molecular sieves, like SAPO-34 and H-ZSM-5 zeolite, as highly active catalysts for the ETP-reaction. The two catalytic systems resulted in more than 50 % of conversion, with 73 and 42 % of selectivity, respectively. Nevertheless, both faced severe deactivation with time-on-stream.

Iwamoto et al. [Iwamoto, 2008; Iwamoto, 2011] investigated nickel doped MCM-41 and found it to be active for the ETP reaction with conversion greater than 40 %. Lehmann et al. [Lehmann et al., 2011; Lehmann et al., 2012] and Alvarado Perea et al. [Alvarado Perea et al., 2013] studied the characteristics of Ni/MCM-41 and Ni/AlMCM-41. Alvarado-Perea showed that it is possible to regenerate the deactivating Ni/AlMCM-41 with Si/Al = 60. The conversion decreased over 30 h on stream from 43 to 35 % for 250 °C, from 78 to 65 % for 350 °C and from 80 to 40 % for 450 °C, while selectivity remained constant. Though, the highest reaction temperature resulted in irreversible deactivation of the reaction system. Filamentous carbon on the surface and reduction of the active nickel centers were identified as the main causes [Alvarado Perea et al., 2017]. Lehmann [Lehmann et al., 2011] applied different nickel precursors for the synthesis of Ni-MCM-41 and found that aluminum was unintentionally incorporated as an impurity of the used materials, analogous to the method by Iwamoto [Iwamoto, 2008].

Andrei coupled dimerization and isomerization with a metathesis step, in a one-pot catalytic concept, applying two catalysts in a setup with Ni/AlSBA-15 and $Mo_3-SiO_2-Al_2O_3$. Exploiting this approach, the selectivity of propene changed over 300 min of reaction from 70 to 50 %, while the butene selectivity increased from 20 to 50 % and conversion was constant [Andrei et al., 2015]. Lin [Lin et al., 2009] presented a loss in activity of 10 % in conversion over 4 h of time-on-stream for H-ZSM-5 and 60 % over 80 h. It is necessary to have high acidity H^+ for the reaction to be initiated and to increase activity for H-Na-ZSM-5. Additionally, for H-ZSM-5 more aluminum results in higher conversions, with a maximum for the Si/Al ratio of 38, corresponding to the highest aluminum content.

Epelde [Epelde et al., 2014a] investigated the different deactivation pathways of relatively constant activity for HZSM-5 and resulted in a complete lost of activity for SAPO-34. Observations reasoned the prohibited diffusion of the formed aromatic molecules through the catalyst channels and their blockage as the main reason for the deactivation. Mazoyer [Mazoyer et al., 2014] presented for WH/Al_2O_3 a deactivation from 36 to 10 % of conversion within the first 24 h of experiments, following mild decreases to 6 % up to 100 h on-stream. The specific results for conversion of ethene and selectivity towards propene are finally listed in Table 3.1 for their specific catalytic systems and reaction conditions.

In Figure 3.1, the selectivity towards propene as a function of ethene conversion is summarized for the following researches: Alvarado-Perea [Alvarado Perea et al., 2013], Amin [Amin and Anggoro, 2003], Andrei [Andrei et al., 2016], Dai [Dai et al., 2014], Ding [Ding et al., 2009], Frey [Frey and Hinrichsen, 2012], Henkel [Henkel, 2013], Iwamoto [Iwamoto, 2008; Iwamoto, 2011], Lavrenov [Lavrenov et al., 2015; Lavrenov et al., 2016], Lehmann [Lehmann et al., 2011], Li [Li et al., 2013], Lin [Lin et al., 2009], Liu [Liu et al., 2004], Oikawa [Oikawa et al., 2006] and Taoufik [Taoufik et al., 2007]. The graph shows

Table 3.1: Catalytic Systems for the direct conversion of ethene to propene, conversion of the reactant ethene, selectivity of propene and reaction conditions, catalytic system.

Reference	$X_{C_2H_4}$ %	$S_{C_3H_6}$ %	**Reaction conditions**	**Catalyst**
[Alvarado Perea et al., 2013]	75	35	400 °C	Ni/AlMCM-41, Si/Al = 60
[Andrei et al., 2015]	55	70	80 °C and 30 bar	NiAlSBA-15 with $MoO_3 - SiO_2 - Al_2O_3$
[Dai et al., 2014]	82.9	59.5	400 °C	H-SSZ-13
[Epelde et al., 2014a]	90	20	400 - 600 °C	HZSM-5
[Epelde et al., 2014a]	40	80	xxx	SAPO-34
[Frey and Hinrichsen, 2012]	40	56	350 °C	Ni(Al)MCM-48
[Iwamoto, 2008]	42	48	400 °C	Ni-MCM-41
[Lehmann et al., 2011]	36	45	400 °C	Ni-MCM-41
[Li et al., 2013]	60	80	50 °C	$NiSO_4/Re_2O_7$ $\gamma - Al_2O_3$
[Lin et al., 2009]	58	42	450 °C	H-ZSM-5
[Lunsford et al., 1998]	9.2	53	650 °C	LiCl+NaCl/MgO
[Mazoyer et al., 2014]	36	70	150 °C	WH/Al_2O_3
[Oikawa et al., 2006]	71.2	52.2	450 °C	SAPO-34
[Taoufik et al., 2007]	40	>90	150 °C	WH/Al_2O_3

that depending on the catalyst and the reaction conditions, a wide range of possible results emerges. The obtained results vary heavily concerning conversion. However, the majority of observable selectivity for propene from ethene feedstock range between 40 to 60%. In the Appendix Figure A.1, the correlation for other feedstock is shown. Depending on the desired reaction pathways, the conversion and the selectivity can be further optimized.

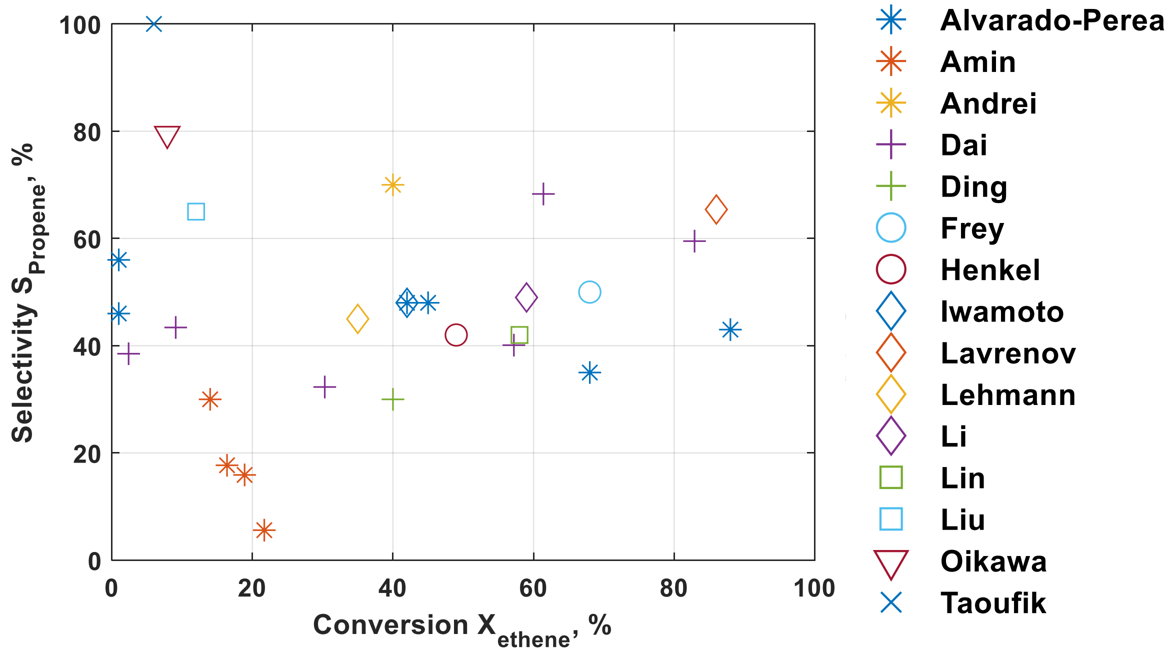

Figure 3.1: Propene selectivity of catalytic systems over the conversion of ethene.

Reaction Network

To carry out a reaction engineering investigation of the considered reaction and to enable a mathematical description, it is necessary to identify the exact reaction steps. Based on the application of nickel loaded mesoporous MCM-41 structures for the direct conversion of ethene to propene, a reaction network was postulated. The widely accepted mechanism for the ETP-reaction was proposed by Iwamoto et al. [Iwamoto, 2008] and will be extended in this present work.

It is believed to consist of three reaction steps. First, a dimerization reaction of ethene to 1-butene (eq. (3.1)) on the nickel ion of the catalyst. Afterward, isomerization of 1-butene to cis-/trans-butene (eq. (3.2)) catalyzed by the acidic sites occurs. Finally, a metathesis step of the generated 2-butene and unconverted ethene to provide two moles of propene (eq. (3.3)).

$$2C_2H_4 \rightarrow 1-C_4H_8 \tag{3.1}$$

$$1-C_4H_8 \leftrightarrow 2-C_4H_8 \tag{3.2}$$

$$C_2H_4 + 2-C_4H_8 \rightarrow 2C_3H_6 \tag{3.3}$$

It is supposedly assumed that Nickel initiates the metathesis step [Iwamoto, 2008; Lehmann et al., 2012; Alvarado Perea et al., 2013]. The postulated network does not consider the formation of relevant byproducts and their influence on the course of the reactions. Therefore, a more detailed reaction network is desirable.

To design and optimize the reaction system, a quantitative description of the underlying reaction mechanisms and kinetics is of considerable interest. Besides, deactivation is a highly relevant factor in this reaction network. For applicability in industry, an exact description of all kinetic steps (reaction, deactivation and regeneration) for the catalyst must be provided.

3.2 Hydrolysis of Acetic Anhydride

The hydrolysis of acetic anhydride to acetic acid is a frequently used example reaction in many studies. It is applied for the evaluation of measuring equipment [Zogg et al., 2003; Shatynski and Hanesian, 1993] and the testing of mathematical methods [Haji and Erkey, 2005; Takashima et al., 1971] for the determination of kinetic parameters. At first, the question arises: why this reaction generates so much interest, although it has no industrial relevance? Based on the reaction equation (eq. (3.4)), the relatively simple chemistry in a homogeneous phase is apparent. Only one micro-kinetic reaction takes place, while no side reactions occur.

Furthermore, both water and acetic anhydride are present in liquid phase and are therefore easy to handle. One limitation is the solubility of acetic anhydride in water. Above the solubility limit, a multi-phase system is formed which has different properties due to mass transport limitations. Below the limit, the reaction is sufficiently fast. Another advantage is that only one product must be analyzed. The limited product spectrum is advantageous, especially concerning the dissociation of the weak organic acid (acetic acid) in excess water.

$$(CH_3CO)_2O\ \mathbf{(AA)}\ + H_2O\ \mathbf{(W)}\ \rightarrow 2CH_3COOH\ \mathbf{(P)} \tag{3.4}$$

For the analysis of the hydrolysis of acetic anhydride, a variety of methods have already been used. Among others, conductivity measurements [Rivett and Sidgwick, 1910; Asprey et al., 1996; Kralj, 2007], titration [Orton and Jones, 1912; Cleland and Wilhelm, 1956] and colorimetry [Oakenfull, 1974] were used, as well as calorimetry [Gold, 1948; Glasser and Williams, 1971; Regenass, 1985] and spectroscopy [Bell et al., 1998; Zogg et al., 2004; Haji and Erkey, 2005]. To determine thermodynamic and kinetic parameters Bell [Bell et al., 1998] used in-situ Raman spectroscopy for the reaction of 5.17 mol/l acetic anhydride in super-critical water. Haji and Erkey [Haji and Erkey, 2005] used a batch reactor setup coupled with a Fourier Transformed Infrared Spectroscopy (FTIR) probe to investigate 0.66 mol/l anhydride solutions sufficiently. In another experiment, Antic [Antic, 2014] used NMR to analyze the ongoing reaction mechanisms by feeding deuterated water. Wiseman [Wiseman, 2012] applied pH probes for the recording of the reactions progress and concluded a two-step mechanistic implication. For this purpose, temperatures of 0 - 65 °C were adjusted and low concentrated solutions with up to 0.025 mol/l were used. However, sodium chloride must be added to adjust the ionic strength.

Besides, a combination of spectroscopic methods with calorimetric measurements was elaborated. Zogg implemented an infrared-attenuated total reflection (IR-ATR) at temperatures of 25, 40 and 55 °C [Zogg et al., 2003; Zogg et al., 2004] in a small scale calorimeter for fast and precise tracking of the reactive system. Visentin [Visentin et al., 2004] used the same setup and an external GC analysis to characterize the resulting solutions. In contrast, Ampelli [Ampelli et al., 2003; Ampelli et al., 2005] used a combination of a calorimeter and ultraviolet spectroscopy to study the reaction, confirming the reaction order from other studies.

The most frequently used analytic method is the calorimetric analysis of the reactions heat or the resulting steady-state temperature. Already in 1942 Conn et al. [Conn et al., 1942] studied anhydrides, mainly cyclic structures, to determine the heat of reactions. Also in the 1940s, Gold [Gold, 1948] analyzed the hydrolysis of acetic anhydride for isothermal batch reactors in aqueous and diluted acetone-water mixtures to successfully estimate kinetics. Dyne [Dyne et al., 1967] extended this study to 0.17 mol/l solutions in an adiabatic batch calorimeter. By recording the temporal temperature curves within the adiabatic reactor, Glasser [Glasser and Williams, 1971] solved the differential material and energy balance to calculate the changes in the extent of reaction. In contrast to these diluted systems, Janssen [Janssen et al., 1957] investigated the conversion of acetic anhydride in concentrated solutions. For these batch experiments, different molar ratios of anhydride to water between 1:1 and with anhydride excess of 7:1 were adjusted for different temperatures. A decreasing heat generation with increasing anhydride concentration could be determined. Similar results were postulated by Regenass [Regenass, 1985]. With decreasing mass-related water content in the reaction mixture, the value of the reaction rate constant decreases as well.

In the recent past, calorimetry of acetic anhydride has been continuously used and developed to generate more accurate results. Shatynski [Shatynski and Hanesian, 1993] measured adiabatic temperature rises for the hydrolysis of acetic anhydride to quantify the measurement setup. HPLC probing controlled the temperature measurement and the reaction progress was documented. Another more complex case was investigated by Hirota [Hirota et al., 2010]. A non-adiabatic CSTR was used for concentrated 4 mol/l acetic anhydride conversion. The obtained kinetic parameters significantly showed deviation from previous values, because of significantly higher anhydride to water ratio. The comparison of experimental and simulated results was the focus of the studies by Jayakumar [Jayakumar et al., 2010; Jayakumar et al., 2014]. Therefore, acid-catalyzed hydrolysis of acetic anhydride was considered for a non-isothermal CSTR. At temperatures between 20 and 40 °C concentrations of 5 - 8 M were implied. As a result, at low temperatures and concentrations the assumed power-law model represented the experimental data well. With increasing values of concentration and temperature, the deviation increased, whereby the transition behavior partly did not agree. Other effects were assumed to be ongoing, which necessarily require a different kinetic approach

Fritzler [Fritzler et al., 2014] could determine for the acid-catalyzed hydrolysis, for a wide spread input concentration between 0.02 - 10.1 M of anhydride, that with acid increase the reaction rate constant is increased. In experiments with 366 K reactor temperature, Asiedu [Asiedu et al., 2013] determined that the activation energy for systems with excess water is almost unchanged from the reactions at 25 °C. In contrast, the activation energy is significantly greater when anhydride is in excess. It was suspected that the reaction mechanism is changed and possibly limitations based on transport resistances occur.

Although calorimetry is the most commonly used analytical method for the hydrolysis of acetic anhydride (AA) to acetic acid (P), it is not the oldest and simplest method. Exact knowledge of the heat released must be available, therefore conductivity measurement is a more suitable alternative. Already in 1910, Rivett [Rivett and Sidgwick, 1910] published an article on the determination of kinetic parameters for the mentioned reaction based on stationary isothermal experiments. Kralj [Kralj, 2007] used a BR with a molar ratio of water to anhydride of 131:1 at room temperature. Due to the limited miscibility of acetic anhydride in water, the application ratio for conductivity measurements must always be below the limit of 1.4 $\frac{mol}{l}$. Thus it can be guaranteed that consistent and valid results are obtained without the risk of two-phase behavior. This limit is accounted for by Amenaghawon [Amenaghawon et al., 2013], who used a 0.73 M solution. An extension of the measurements performed was presented by Asprey [Asprey et al., 1996] with the temperature scanning method. Temperature ramps are used to obtain more reliable kinetic values. With a constant molar inlet ratio of 10:1 (water:anhydride), experiments could be carried out in heated water baths for PFTR, CSTR and BR.

For the hydrolysis of acetic anhydride, a variety of analytical methods for the description of concentration-time curves were presented in the previous section. These vary with the concentrations used and possible additives. In the case considered here, the simple methodology of conductivity measurement is used. Thereby, a direct analogy to the present product concentration can be established based on the signal to track the dynamic operating mode.

Due to the methodology used, however, it is necessary to limit the concentration range investigated with an upper limit to avoid miscibility gaps that would interfere with the measurement signal. Furthermore, the temperature is regulated to avoid evaporation and thus two-phase operation. However, relevant concentration and temperature ranges can be implemented and analyzed to validate the desired dynamic effects.

3.3 Conclusion

The focus of this chapter was a description and introduction of two case studies considered in this thesis.

First, the heterogeneously catalyzed production of propene was considered. To this point, dehydrogenation, catalytic cracking and metathesis were evaluated as possible on-demand applications for the widening propene gap between demand and production. Due to the availability of ethene and the deactivation of the catalyst used in these processes, the direct conversion of ethene to propene is highly interesting and promising. However, the performance of the respective catalytic system is influenced by the carrier materials and metals immobilized on them, along with the reaction conditions and the preparative method.

In a second case study, the homogeneous liquid phase hydrolysis of acetic anhydride was investigated. As analytical techniques conductivity, calorimetric and spectroscopic methods were used. The reaction conditions were analyzed and operational boundaries were identified.

The selected case studies will be thoroughly investigated for inherent dynamic operation (Part II) and forced dynamic operation (Part III) in the following chapters. For the inherent dynamic mode, the ethene to propene (ETP) reaction is exploited. The necessary process steps of reaction (step 1), deactivation (step 2) and regeneration (step 3) are analyzed individually and mathematically evaluated. In the case of forced dynamic operation, the hydrolysis of acetic anhydride is studied in an adiabatic CSTR. With a developed simple kinetic model the nonlinear frequency response (NFR) method is applied to predict mean outlet values of the periodically perturbed reaction system. Using a developed experimental setup, designed for dynamic operation, experiments are conducted in which one and multiple input parameters are periodically fluctuated.

The necessary equipment and procedures applied will be presented for both case studies in the following.

Part II

Inherent Dynamic Reactor Operation

Preface to Part II

The good thing about science is that it's true whether or not you believe in it.

—Neil deGrasse Tyson

The following part of the present thesis deals with the inherent periodic operation of a chemical reaction system. Such systems show a complex interconnection of the involved molecules in series, parallel and equilibrium limited reactions. For this purpose, the heterogeneously catalyzed direct conversion of ethene to propene on mesoporous MCM-41 support incorporated with nickel is considered. The catalyst was optimized in the work of Alvarado Perea [Alvarado Perea, 2014] for the selective formation of propene. Due to the effect of catalyst deactivation, a reaction analysis and optimization of the regeneration are necessary for optimal operation of the overall process.
Parts of the here presented chapters have been published in the following publications, to which the author contributed.

1. L. Alvarado Perea, M. Felischak, T. Wolff, C. Hamel, A. Seidel-Morgenstern, *Experimental reaction network investigation of the ethene to propene reaction on Ni/AlMCM-41 catalysts*, Chemie Ingenieur Technik, 89 (2017) 903-914, DOI: 10.1002/cite.201600166. [Alvarado Perea et al., 2017]

2. M. Felischak, T. Wolff, L. Alvarado Perea, A. Seidel-Morgenstern, C. Hamel, *Influence of process parameters on single bed Ni/AlMCM-41 for the ethene to propene reaction*, Chemical Engineering Science, 210 (2019) 115246, DOI: 10.1016/j.ces.2019.115246. [Felischak et al., 2019]

3. M. Felischak, T. Wolff, L. Alvarado Perea, A. Seidel-Morgenstern, C. Hamel, *Detailed kinetic model for the reaction of ethene to propene on Ni/AlMCM-41*, Chemie Ingenieur Technik, 92 (2020) 564-574, DOI: 10.10002/cite.201900139. [Felischak et al., 2020]

4. L. Alvarado Perea, M. Felischak, T. Wolff, C. Hamel, A. Seidel-Morgenstern, *Propene production at low temperature by bimetallic Ni-Mo and Ni-Re catalysts on mesoporous MCM-41 prepared using template ion exchange*, Fuel, 284 (2021) 119031, DOI: 10.1016/j.fuel.2020.119031. [Alvarado Perea et al., 2021]

The author of this thesis contributed substantially to the results presented in the contributions given above. In paper 1 the author supported the analysis of the obtained data for the evaluation of the reaction network. For the second publication, the contribution was to perform the experiments and the analysis of the obtained data. Based on the product spectra an alternative reaction network (step 1) was derived, postulated and verified. Additionally, the longtime application of a single catalyst bed to the cyclic operation was carried out, with the investigation of suitable regeneration (step 3) strategies. In the third publication, kinetic models were derived and evaluated for two reaction networks of different complexity. Lastly, the author supported the evaluation of the collected data to validate the ongoing mechanisms.

The long-term stability of the catalyst system is investigated in particular. Again, the reaction conditions will be varied to validate the effects of deactivation (step 2). Based on deactivated catalysts, the regeneration (step 3) is studied. In the following chapter, the effects described above are modeled mathematically. For the reaction, a large data set is used to evaluate two postulated reaction (step 1) mechanisms. The typical approach is LHHW for heterogeneously catalyzed systems [Langmuir, 1916], as well as mechanistic modeling based on the elementary steps according to the methodology of Helfferich [Helfferich, 2004; Kiedorf et al., 2014; Kiedorf et al., 2016a; Mueller et al., 2018; Jörke et al., 2015] are evaluated. These are compared with each other concerning applicability. Similarly, the experimental data for deactivation (step 2) and regeneration (step 3) are used to adapt parameters using established models favorably.

4 Preliminary Theoretical Study of Inherent Periodic

The inherent dynamic operation is characterized by two distinct phases, as shown in Figure 1.1. First, the phase of reaction (step 1) to the desired product, which is coupled with a loss in activity - the deactivation (step 2). Second, a phase in which production cannot take place because the system has to be regenerated (step 3). The individual steps must be mathematically approximated to define exact termination criteria. With the help of these termination criteria, as optimization parameters, it is possible to achieve an increase in the time-average of a desired target quantity, compared to rough estimates or empirical values. This approach is an alternative to the accurate and more complex NFR method.

Likewise, long production with low activity and long regeneration phases are detrimental, reducing the time-average yield. Therefore in the following sections, first a CSTR and then a PFTR is optimized for an exemplary reaction system concerning the times for the individual phases. These reactors are considered because they present the boundary cases of perfectly mixed and ideally unmixed flow systems.

4.1 Fundamental Assumptions

For the demonstration of this termination approach, an exemplary series reaction will be considered, in which first the reactant A is irreversibly converted to an intermediate B. Subsequently, the equilibrium-limited conversion of B to the desired product P takes place (eq. (4.1)).

$$A \xrightarrow{r_1} B \underset{k_{2,back}}{\overset{k_{2,for}}{\longleftrightarrow}} P \tag{4.1}$$

It is necessary to define parameters, for the individual process steps in advance, to carry out an instructive simulation study. The parameters are defined in the following Table 4.1. An isothermally operated reactor is assumed, which significantly reduces the complexity. Furthermore, the assumed catalyst used is regarded as equivalent for all reaction steps, with only one deactivation constant k_d considered. Further, it is assumed that the catalyst has an unchanged constitution over the entire time, thus no part is irreversibly deactivated or destroyed. Accordingly, the following three process steps of the reaction (step 1), deactivation (step 2) and regeneration (step 3) occur, which are described below.

Step 1 - Reaction

The ongoing reactions are assumed as elementary, resulting in the following kinetics eqs. (4.2) to (4.4).

Table 4.1: Kinetic Parameters for an exemplified reactive system for the cyclic process for inherent dynamic operation.

k_1	1	[1/s]
$k_{2,for}$	$1 \cdot 10^{-2}$	[1/s]
$k_{2,back}$	$1 \cdot 10^{-3}$	[1/s]
K_P	10	[-]
k_d	$2 \cdot 10^{-3}$	[-]
k_{Reg_1}	$2 \cdot 10^{-3}$	[-]
k_{Reg_2}	$1 \cdot 10^{-2}$	[-]
τ	100	[s]
a^0	1	[-]
c_A^{in}	0.74	[mol/l]

$$r_1 = k_1 \cdot c_A \cdot a_{d,1}(t) \tag{4.2}$$

$$r_{2,for} = k_{2,for} \cdot c_B \cdot a_{d,2,for}(t) \tag{4.3}$$

$$r_{2,back} = k_{2,back} \cdot c_P \cdot a_{d,2,back}(t) \tag{4.4}$$

It was explained initially (eq. (2.30)), that the equilibrium constant K_P is evidence for the progress of the reaction. Here, a value of 10 constitutes that the equilibrium of reaction is on the product side, but not by far.

Step 2 - Deactivation

As mentioned, the deactivation is considered to be equal for all reactions. Therefore, the following assumption (eq. (4.5)) is considered, for the catalyst capable of supporting all the occurring reactions.

$$a_d(t) = a_{d,1}(t) = a_{d,2,for}(t) = a_{d,2,back}(t) \qquad \forall t \tag{4.5}$$

The simulation study carried out can be divided into two distinct phases, as illustrated in Figure 4.1. In the first phase, the deactivation of the catalyzed system is considered, with the activity decreasing from a maximum to a minimum. The time span between the maximum (eq. (4.6)) and the minimum activity (eq. (4.7)) is calculated. Here the maximum possible activity a_0 is regarded as an initial offset and is set to a value of one for simplification of the equations.

$$t_{d,max} = -\frac{1}{k_d} \cdot ln\left(a_{d,max}\right) \tag{4.6}$$

$$t_{d,min} = -\frac{1}{k_d} \cdot ln\left(a_{d,min}\right) \tag{4.7}$$

The exact course of the deactivation can be mathematically described (eq. (4.8)), following a first-order deactivation, similar to eq. 2.57.

$$a_d\left(t_d\right) = a_0 \cdot exp\left(-k_d \cdot t_d\right) \qquad \forall t_d = [t_{d,max}, t_{d,min}] \tag{4.8}$$

Step 3 - Regeneration

In the second phase, the catalyst is reactivated, where the difference of the time points from the minimum $a_{Reg,min}$ (eq. (4.9)) to the maximum activity $a_{Reg,max}$ (eq. (4.10)) is determined.

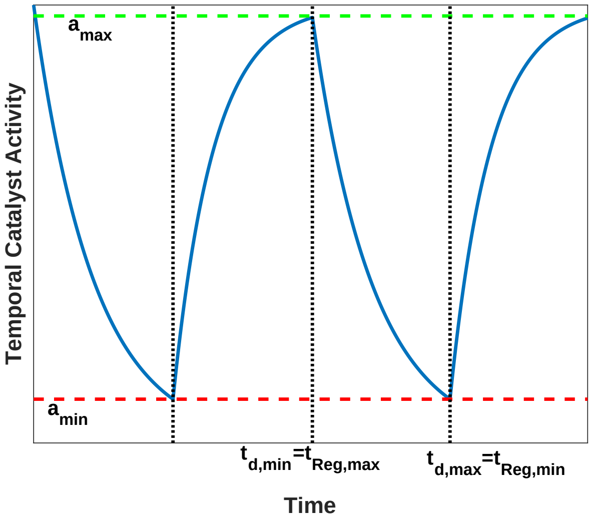

Figure 4.1: Illustration of the inherent dynamic operation with maximum and minimum activity, as well as their corresponding time arrays.

During the regeneration phase, the activity of the reaction system is restored. The times are calculated as an inverse exponential function in a simplified form (eqs. (4.9) and (4.10)).

$$t_{Reg,min} = -\frac{1}{k_{Reg}} \cdot ln\left(1 - a_{Reg,min}\right) \tag{4.9}$$

$$t_{Reg,max} = -\frac{1}{k_{Reg}} \cdot ln\left(1 - a_{Reg,max}\right) \tag{4.10}$$

The course of the regeneration can thus be represented analogously to the deactivation (eq. (4.11)).

$$a_{Reg}(t_{Reg}) = 1 - exp\left(-k_{Reg} \cdot t_{Reg}\right) \qquad \forall\, t_{Reg} = \left[t_{Reg,min}, t_{Reg,max}\right] \tag{4.11}$$

The maximum and minimum activities for deactivation and regeneration are equated utilizing closing conditions, to avoid discontinuity within the functions.

$$a_{max} = a_{d,max} = a_{Reg,max} \tag{4.12}$$

$$a_{min} = a_{d,min} = a_{Reg,min} \tag{4.13}$$

$$\vec{a} = [a_{max}, a_{min}] \tag{4.14}$$

Process Evaluation

To determine the cycle time Δt_{cycle}, both time arrays are summed (eq. (4.15)).

$$\Delta t_{cycle} = \underbrace{(t_{d,min} - t_{d,max})}_{\Delta t_d} + \underbrace{(t_{Reg,max} - t_{Reg,min})}_{\Delta t_{Reg}} \tag{4.15}$$

In the present simulative study, the yield is used as the objective function. This value represents the ratio between the product flow at the outlet and the input material flow of the limiting reactant, as defined in eq. (2.14). At this point, no volumetric changes occur and accordingly, the residence time is assumed constant. The time-dependent yield is related to the total cycle time, eq. (4.16) for the inherent dynamic operation. This fact penalizes long regeneration times, which lead to high activities but cause increased regeneration periods.

$$\underset{\vec{a}}{max}\left(\overline{Y}_{P/A}(\vec{a})\right) = \frac{1}{\Delta t_{cycle}} \int_{0}^{\Delta t_{cycle}} Y_{P/A}(t)dt \tag{4.16}$$

Optimization aims to maximize the time-averaged yield for the overall cyclic time by varying the minimum and maximum activities achieved.

4.2 Continuously Stirred Tank Reactor

First, the CSTR is considered. The continuously stirred vessel is ideally mixed, as to which no gradients occur within the reactor, thus reducing complexity.

4.2.1 Influence of Residence Time

For optimal evaluation of the output of a dynamic reactor, the influence of the residence time is analyzed at first in the range from 10 to 1000 s. The yield of the desired target product P (eq. (4.1)) and the efficiency specified in eq. (4.17) are evaluated. The efficiency η is defined as the temporal mean of the yield $\overline{Y}$ to the stationary yield Y_{ideal}, which occurs without deactivation.

$$\eta = \frac{\overline{Y}}{Y_{ideal}} \tag{4.17}$$

Due to the assumed high reaction rate of the first reaction, the conversion of the reactant A is relatively independent of the residence time, see Figure 4.2. For the assumed parameters, the value will always tend to 100 %, except for the shortest residence times. It becomes evident that with increasing residence time the yield of the desired target product increases. The reason for this lies in the Damköhler number (eq. (4.18)). This parameter is the ratio of the time given for reaction to the time required for the reaction [Baerns, 2013].

$$Da = k \cdot \tau \cdot c_0^{n-1} = k \cdot \frac{L}{w} \cdot c_0^{n-1} \tag{4.18}$$

This correlation is presented in Figure 4.2a for the previously mentioned reactive system in a CSTR. With less time given, the steady-state conversion is achieved within the first few seconds. Nevertheless, the system tends further toward full conversion of A.

In contrast to the continually increasing conversion with increasing residence time, a trend with a clear maximum is emerging for efficiency (Figure 4.2b). For each point, an optimized case for de-

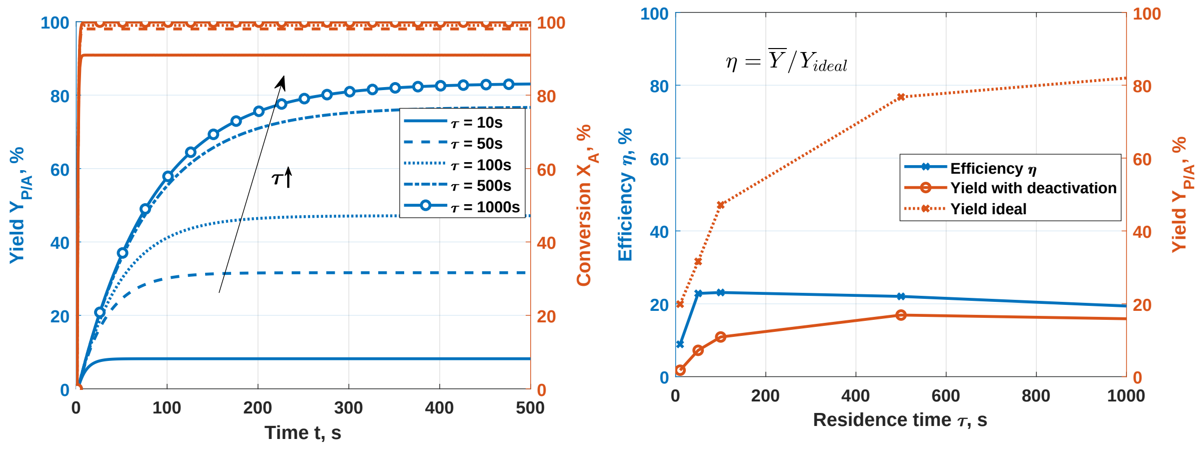

(a) (b)

Figure 4.2: Simulative results for a continuously stirred tank reactor (CSTR) of (a) the yield (blue) and conversion (orange) of the reaction network imposed for different residence times and (b) the efficiency (blue) of the process compared to the ideal system and the yield of product (orange) as functions of the residence time.

activation and subsequently, the mean value of yield was considered. The corresponding adjusted values for the termination criteria of the minimum and maximum activity are listed in the appendix (Section A.1). This trend with an extrema related to efficiency is based upon the fact that the mean yield of the fluctuating system does not increase to the same extent as the ideal system. It is apparent, however, that the maximum achievable yield reduces the potential for further improvement for optimized stoppage criteria. Meaning, it is more difficult for the system to effectively be enhanced, since the response behavior of the system with the very long residence times is washed out. The optimum is found at lower residence times because the ratio is ideal. As a result, a multitude of influencing variables limits the efficiency of the system. Accordingly, a specific residence time with 100 s is selected that optimizes the productivity of the assumed example.

4.2.2 Influence of Switching Time

With the selection of suitable operating parameters, the influence of the termination criteria of lower and upper activity is dealt with below. As described above, the operator needs to know how long the existing catalyst system has to be deactivated and regenerated accordingly. Or whether an oscillation of the activity with a small amplitude and a consequently higher frequency is optimal for the present case. For this purpose, calculations using the values given in Table 4.1 were performed for different minima and maxima of the activity, resulting in individual cyclic times.

These results are illustrated in Figure 4.3. First, in Figure 4.3a for the range between 5 and 15 %, Figure 4.3b for the range around 85 - 95 % and Figure 4.3c for a level of 45 - 55 % activity small amplitudes of cyclic operation are shown. In all cases, the deactivation rate constant k_d is equal to that of regeneration k_{Reg}. The trend of yield looks atypical but can be logically justified. Due to the necessary residence time in the system, the yield initially increases as a result of ideal mixing. Subsequently, a maximum is reached and the curve drops as a result of the decreasing activity and the associated accumulation in the system. At some point, the deactivation is more dominant than the reaction.

The time-average yield is below 5 % for all cases with small amplitudes. The oscillation at the lower

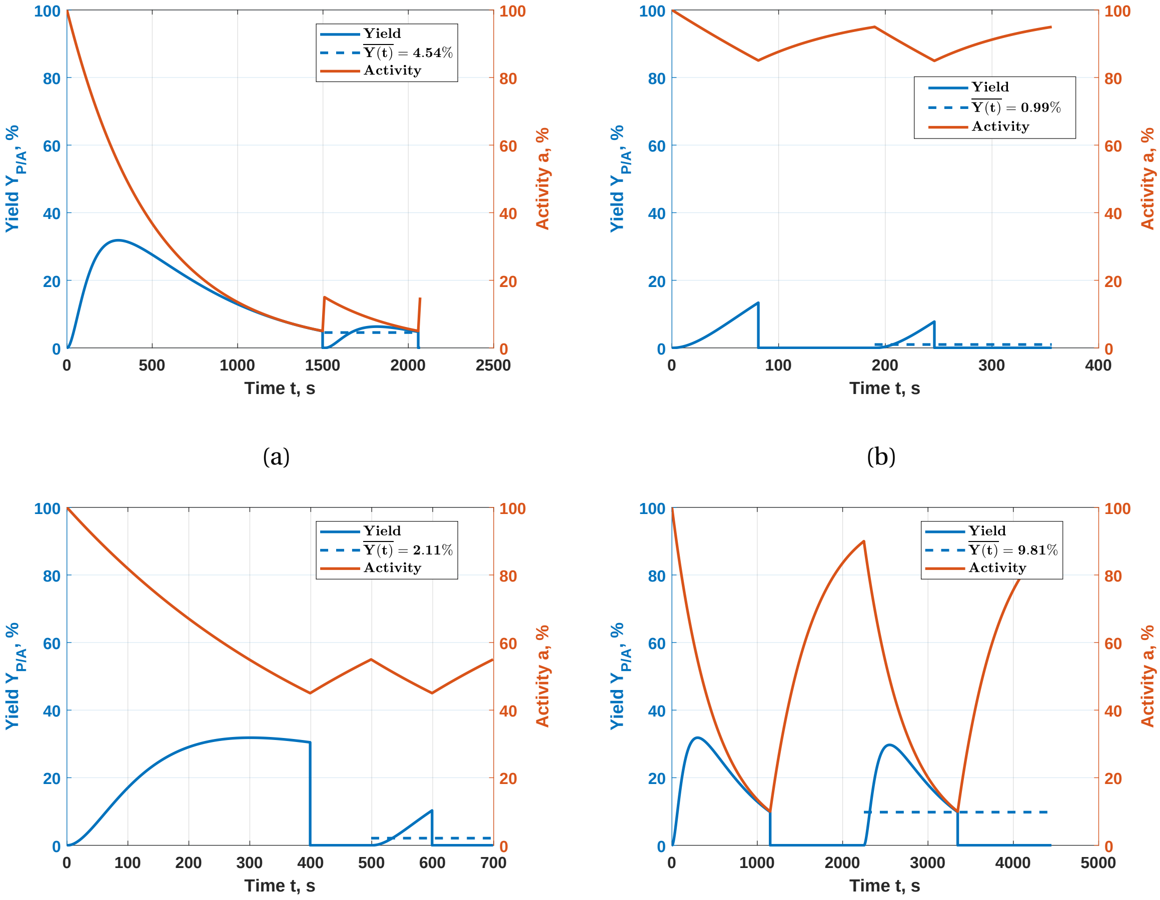

(a) (b)

(c) (d)

Figure 4.3: Simulative results of product yield and activity with time for the inherent dynamic operation of a continuously stirred tank reactor (CSTR) with a $k_D/k_{Reg} = 1$ for (a) a lower boundary of 5 % activity and an upper boundary of 15 % activity, (b) a lower boundary of 85 % activity and an upper boundary of 95 % activity, (c) a lower boundary of 45 % activity and an upper boundary of 55 % activity, (d) a lower boundary of 10 % activity and an upper boundary of 90 % activity.

activity level (5 - 15 %), as shown in Figure 4.3a, presents the highest yield due to the applied definition for deactivation and regeneration. The reaction phase with parallel deactivation is relatively long (549 s) and the dead time due to regeneration is low with 11 s. Only small amounts of the catalyst have to be reactivated for the restoration of the desired active state. This theoretical constrain assumes that the activity of an active center is immediately regained with the removal of the deactivating species. However, productivity is long, but not high due to the low activity of the catalyst. Thus the cycle time of 560 s is longer than for e.g. the fluctuation between 85 and 95 % with 166 s. In this case (Figure 4.3b), for only 56 s the desired product is obtained and 110 s are necessary to obtain the desired high activity level. For this purpose, the deactivated catalyst sites must be identified and specifically regenerated. When operating at a medium activity range (Figure 4.3c), a mixed form with process phases of approximately equal length is determined, which provides only a minimal yield value.

Another picture can be seen for the case study with large amplitudes between 10 and 90 % of activity (Figure 4.3d). An average yield of almost 10 % can be achieved, with the cyclic time of about 1000 s.

At first, a lot of desired product can be formed, while the system is severly deactivated. Afterward, it requires much effort to bring the system back to the desired activity level. Therefore, it is necessary to determine the exact solution of the termination criteria for the individual process steps to obtain an optimized average yield.

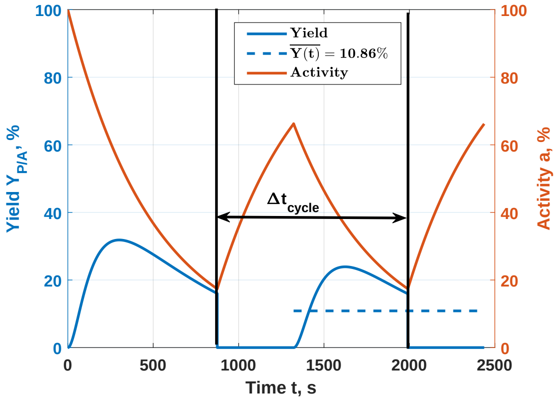

Figure 4.4: Simulative results of product yield and for optimized activity determination values with time for the inherent dynamic operation of a continuously stirred tank reactor (CSTR) for a $k_D / k_{Reg} = 1$.

This optimized operating case is shown in Figure 4.4. The optimal parameters are 17.38 % as the lower boundary and 66.26 % as the upper limit. An average yield of 10.86 % can thereby be achieved. The cycle time consisted of 669 s production and 448 s regeneration. Compared to the randomly selected values, the desired target can be doubled (Figure 4.3a), tenfold (Figure 4.3b), fivefold (Figure 4.3c) and increased by roughly 1 % (Figure 4.3d). In the last case, for the largest amplitudes, the obtained value was close to the optimized case. Therefore the consideration has to be made whether a rough choice of the parameter can lead to a simple operation, as it would be more difficult to operate with the optimized values.

The determination of the termination activities is influenced by the time constants of the respective individual steps, the applied reactive system and the chosen optimization parameter.

4.2.3 Influence of Rates for the three Individual Process Steps

In the previous section, it could be shown how appropriate termination criteria for inherent dynamic operation can lead to a significant increase in the time-averaged yield. An essential parameter is the cyclic time, which is the total time of a periodic process consisting of reaction coupled with deactivation and regeneration. In the case that the deactivation and the regeneration take place with the same speed, a comparison of the cases was conducted. However, it is of utmost importance for a process to be brought back to a practicable operating state as quickly as possible. For this purpose, it was assumed (Figure 4.5) that regeneration is faster by a factor of 5 than deactivation.

In this case (Figure 4.5), the determined optimal termination criteria were 21.14 % as the lower limit and 88.17 % as the upper limit of activity. Accordingly, a total cycle time of 903 s ($t_d = 714$ s and $t_{Reg} = 190$ s) is obtained, with an increase in time-average yield to 17.57 %. Adequate adjustment of the conditions for regeneration is thus helpful to reduce the period for a regeneration step and thus improve the periodic process by 7 %. The process is stopped at higher activity, but higher activity is achieved

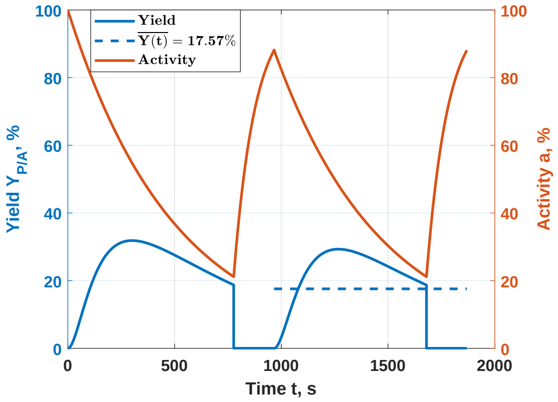

Figure 4.5: Simulative results of product yield and for optimized activity determination values with time for the inherent dynamic operation of a continuously stirred tank reactor (CSTR) for a $k_D / k_{Reg} = 0.2$.

faster, leading to increased productivity, due to less dead times without production.

Based on the results obtained, two findings become evident: first, larger amplitudes and the resulting longer period durations are advantageous, resulting in higher frequencies; second, it is necessary to have faster regeneration compared to deactivation, reducing dead times. The application of these two points significantly increases the time-averaged yield of the system. It is necessary to give the process sufficient time for the reaction to generate product, even if this results in extended regeneration phases. However, the most significant influence seems to be the regeneration phase. Rapid regeneration reduces the "downtime" without production, thus improves the yield.

In the following, the influence of the reactor type on the time-averaged yield is regarded as a further influencing variable in which the plug flow tubular reactor (PFTR) is applied.

4.3 Plug Flow Tubular Reactor

The PFTR is of particular interest concerning further intensification and simplification of processes. The tubular reactor offers simpler handling of fluid-solid reactions because no stirrer is required. This leads to a minimization of shear forces on the catalyst, which could lead to destruction. One simplification of the performed simulations is the uniform reduction of the activity along the catalyst bed. In a real catalyst bed, a deactivation front would emerge along the axial orientation. For the present case this was neglected.

It has been mentioned that the tubular reactor generates higher conversion for the same residence time than the CSTR. Accordingly, the PFTR can be smaller in dimension for constant productivity. When evaluating the dependency on the residence time, the tubular reactor always achieves a yield that is more than 10 % higher for the ideal reaction system without deactivation at a residence time of 100 s, compared to the ideally mixed stirred tank reactor.

When considering the system with deactivation, the achievable yield for the stirred tank reactor (Figure 4.2b) is always lower than for the PFTR (Figure 4.6). With the intensification of the process, the decrease in yield is also enhanced if the residence time is too long. As a result, the ratio of the ideal and deactivating yield, the efficiency η, is increased for the tubular reactor. This observation confirms the attractiveness of the tubular reactor. For the entire residence time range, the efficiency is around 40 %, in contrast to 20 % for the CSTR. But for the case discussed here, a steady decrease in efficiency can be observed. Analogous to the CSTR, the steadily increasing ideal yield cannot be adequately compensated by the deactivating system and the time-average yield. The deactivating system presents a weaker increasing and even a decreasing trend when the residence time is too high. Accordingly, less intensification can be achieved through cyclic operation, which reduces efficiency.

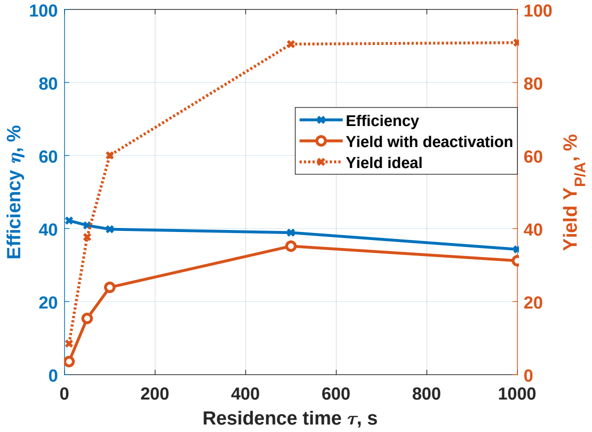

Figure 4.6: Simulative results for a plug flow tubular reactor (PFTR) of the efficiency (blue) of the process compared to the ideal system and the yield of product (orange) as functions of the residence time.

Due to the significantly improved result and the more realistic ratio of the time constants, only the operation with 5 times faster regeneration to deactivation is considered for the PFTR.

In Figure 4.7a for small amplitudes and in Figure 4.7b for large amplitudes, the influence of the defined oscillation range of the activity is considered more closely. Analogous to the CSTR, after one cyclic operation, an invariable mean yield of the desired target product can be determined. The yield trajectories follow the typically assumed trends, which decrease over time due to the decreasing activity. If activity is varied in the range between 5 and 15 % (Figure 4.7a), an average yield of 6.09 % can be achieved. The time for reaction and deactivation is 549 s and 11 s for regeneration. It turns out that the production phase is significantly longer than the regeneration phase without product formation. However, the reaction rates are significantly reduced due to the low activity and, therefore, no significant amounts of product are generated. For an activity modulation between 10 and 90 % (Figure 4.7b) a significantly higher value of 20.38 % is achieved. In this case, the time for deactivation is 1099 s and for regeneration 219 s. This increased productivity can be traced back to a long time for product formation. At the same time, the activity is higher, meaning the system does not inhibit the reaction itself. More product can be generated while a steeper activity loss is ongoing. Further, the reactor operatesfor a shorter time under lower catalyst activity.

Of great interest for the tubular reactor are the optimal parameters for the time-average yield by selecting lower and upper activity limits. As a result (Figure 4.7c), 20.92 % yield can be achieved for a lower limit of 18.71 % and an upper activity of 63.49 %. In parallel with this, the time for reaction and deactivation is 611 s, with a regeneration time of 80 s. Analogous to the CSTR, it must be noted that the previously considered periodic variation of the activity with the higher amplitude was in a similar range as the optimized case. Compared to the CSTR, the necessary cycle time of 691 s is significantly

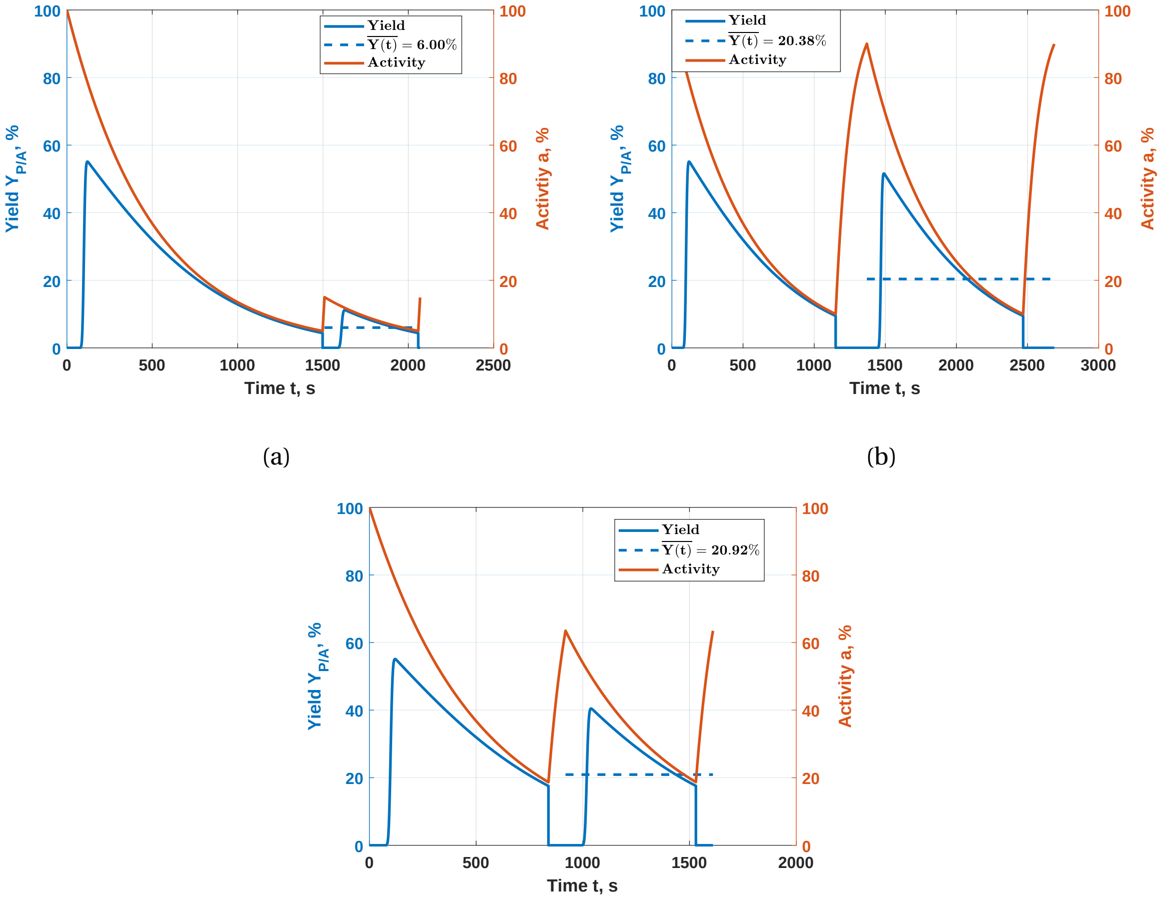

(a)

(b)

(c)

Figure 4.7: Simulative results of product yield and activity with time for the inherent dynamic operation of a plug flow tubular reactor (PFTR) with a k_D/k_{Reg} = 0.2 for (a) a lower boundary of 5 % activity and an upper boundary of 15 % activity, (b) a lower boundary of 10 % activity and an upper boundary of 90 % activity, (c) optimized determination values for activity.

shorter than 904 s. Furthermore, the narrower range is advantageous for operation due to the less flattening activity curves at lower values during deactivation and higher for regeneration.

4.4 Conclusion

With the presented preliminary theoretical study of the inherent dynamic reactor operation, it could be shown that for a continuously stirred tank reactor (CSTR) and a plug flow tubular reactor (PFTR) optimal amplitudes and specific frequencies can be determined by optimizing a desired output value. The analysis for the cyclic operation is based on the kinetic parameters of the individual process steps. The following results were achieved:

(a) A mathematical program and method was developed for the prediction of the mean value of an objective function for inherently dynamic reactor operation.

(b) Criteria to switch between production and regeneration were derived for the CSTR and PFTR.

(c) The ratio of characteristic time constants for the deactivation (step 2) and the regeneration (step 3) is essential. Slow deactivation and fast regeneration are beneficial, enhancing production time and reducing the "downtime" with no product generation.

(d) With the kinetic parameters of the reaction (step 1), deactivation (step 2) and regeneration (step 3), a reaction system can be optimized with respect to time intervals for the mentioned steps.

5 Experimental Study: Ethene to Propene Reaction

In the introductory part of this thesis (section 3.1) the economic importance of propene was presented. On-demand applications were evaluated, capable of overcoming the widening gap between supply and demand. Due to the attractiveness and availability of ethene it can be directly converted into propene. Alvarado-Perea [Alvarado Perea, 2014] developed a catalyst that effectively performs the necessary synthesis steps. For this purpose, an optimized carrier material based on a MCM-41 with a specific aluminum content (Si/Al = 60) was synthesized and nickel immobilized as an active catalyst species. Initial assumptions were made about the possible reaction pathways and the effect of deactivation was examined more closely [Alvarado Perea et al., 2017], which significantly limits catalyst life, efficiency and productivity.

In this chapter, the equipment used for the analysis of the individual sub-processes of reaction (step 1), deactivation (step 2) and regeneration (Step 3) is presented first. Then the catalyst system used is characterized and its significance for the observed activity is presented. Utilizing activity measurements, depending on the reaction conditions (input concentration, residence time, temperature and time-on-stream), detailed analysis and evaluation of the possible reactions taking place are carried out. Furthermore, the deactivation and the influences on this effect are analyzed. For this purpose, long-term experiments are carried out under varying reaction conditions. Based on the results, suitable reaction pathways to the deactivating species will be identified.

Finally, suitable regeneration strategies for extending the catalyst's operating time will be evaluated. The cyclic operation is carried out in this way concerning the highest possible and constant selectivity to propene, while at the same time, high ethene conversion rates are achieved.

5.1 Experimental Setup and Procedure

In the following, the experimental setups used for investigating the catalytic system are described in detail and the primary sequence for evaluation of the observed process steps is described.

5.1.1 Laboratory Reactor for Kinetic Screening

The evaluation of the catalytic activity was carried out in a fixed-bed laboratory reactor realized as an inert quartz glass tube and equipped with a ceramic oven (high temperature kinetic reactor (HTKR), see Figure 5.1), controlled using a thermocouple in the center of the catalyst bed, a catalytic afterburner and a gas chromatography. This configuration enabled the user to perform gas analysis of the reactants and the products of the reactive system with the application of a multi-positional valve .

The quartz tube had an inner diameter of 0.6 cm and an overall length of 40 cm. All experiments were performed at atmospheric pressure, with a sample mass of 0.5 g of catalyst. The feed consisted of ethene (Linde 99.9 %) and nitrogen (Linde 99.9993 %). For further evaluation, propene (Westfalen Gas 2.5) was introduced as an auxiliary and for regenerative process steps air (technical grade) was fed into the reactor. The catalyst bed was encased with inert particulate material (ZrO_2/SiO_2, d_p = 1 - 1.25 mm, *Mühlmeier*), to ensure an ideally mixed gaseous flow and for preheating of the fed gases. Different sets of experiments were performed. The reactor was embedded in an electrical oven (*HTM Reetz*). Following the safety regulation, the temperature could be set in the range of 25 - 1000 °C.

The quantitative analysis of the gaseous components was realized by GC/MSD (*Agilent GC 6890*), implying a thermal conductivity detector (TCD) sensor. For effective separation, the gas chromatography (GC) consisted of a two-column configuration, which in the first column (*HP Plot Q*) separated the hydrocarbons and in the second column (*HP Molsieve 5A*) separated the permanent gases. The analysis was based on thermal conductivity detection [Hamel et al., 2010].

The conditions were varied during the experiment to study the space velocity (weight of catalyst/flow rate, W/F) in the range of 250 - 2600 $\frac{kg_{cat} \cdot s}{m^3}$ and the molar fraction of ethene in the feed between 2.5 and 25 %. The temperature was varied between 50 and 350 °C in increments of 25 °C, to quantify the corresponding dependence.

To investigate the catalyst bed over an extended period under deactivation conditions, it was operated for 24 hours under constant reaction conditions. With varying the temperature at constant W/F and feed ratio for evalution of the influences. To set the initial temperature, the catalyst was heated under nitrogen to the desired reaction temperature. When the reaction temperature was reached, the inlet flow was adjusted according to the desired reaction conditions by mass flow controllers (MFCs) (*Bronckhorst*).

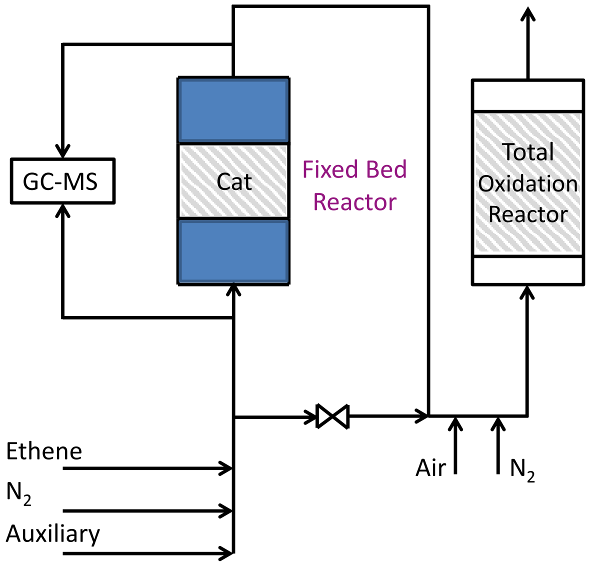

Figure 5.1: Experimental setup HTKR for testing catalytic activity.

After each experimental run, the catalyst bed was regenerated to retrieve the catalyst's initial activity. For this, the fixed-bed was heated to 500 $°C$ under nitrogen flow. When the desired temperature was reached, compressed air was added to the nitrogen feed stream. Both flows were adjusted to the desired conditions and kept constant for three hours. After the catalyst regeneration, the reactor was cooled down under nitrogen to 50 $°C$. The catalyst revealed a consistent activity and properties in subsequently carried reference runs with good reproducibility. However, not all experimental runs are presented, instead of a representative series of reaction conditions.

Each experimental point was measured at least twice, to obtain reliable and reproducible experimental results, and further, the carbon balance was analyzed for each of these points. The error was found to be within a ±5 % margin, which is within the accuracy of the analytic equipment. Therefore, applicability was ensured.

5.1.2 TGA/DSC

The Netzsch STA 445 F5 Jupiter was used for the controlled oxidative activation/regeneration of catalysts. Simultaneous thermal analysis (STA) allows the application of thermogravimetry (TG), differential thermal analysis (DTA) or differential scanning calorimetry (DSC) in one apparatus. Proteus software was used to evaluate and control the measuring system. Depending on the measuring method, it is possible to switch between a combined DSC/TG sample carrier and a TG sample carrier. The sample carrier is connected to a precision balance that registers the mass change of the sample. As a protective gas, nitrogen prevents other gases from entering the weighing system. Flow controllers adjust the oxygen concentration during activation via an air connection and another nitrogen connection. The entire measuring apparatus is vacuum-tight. A vacuum rotary vane pump evacuates the system several times with software protection to create an inert starting atmosphere for the experiments.

The furnace is operated with a silicon carbide heating element controlled by a thermocouple. The sample temperature was displayed by another thermocouple located directly below the crucible. A protection tube made of metal and a radiation shield made of aluminum oxide on the sample carrier minimize measurement errors due to heat radiation [Netzsch Thermal Analysis, 2018]. Figure A.3 shows a cross-section of the STA with the elements described.

Table 5.1: Specifications of Netzsch's thermogravimetric analysis (TGA).

Temperature range (SiC Element)	20 - 1200 °C
Temperature resolution (max)	0.001 K
Heating rate	0.001 - 50 K/min
Max. sample mass	35 g
Resolution Scale	0,1 μg
Max. sample volume	5 cm^3
Max. vacuum	0.01 mbar
Scale drift	<5 μg/h
Precision enthalpy	1 %

The process parameters and specifications of the TGA are summarized in Table 5.1.

5.2 Catalyst Preparation

The AlMCM-41 support was prepared by the method recently described by Alvarado-Perea et al. [Noreña-Franco et al., 2002; Alvarado Perea et al., 2013]. The precursor mixture had a molar composition of $1SiO_2$: 0.35 CTABr : 0.31 TBAOH : $0.000 - 0.2$ $NaAlO_2$: 55 H_2O and was manually stirred for 15 min. Sodium aluminate ($NaAlO_2$:Al_2O_3 50 - 56 % and Na_2O 40 - 45 %) was used as the aluminum source, with its amount being adjusted for generating a Si/Al ratio of 60. Subsequently, the mixture was filled into a Teflon bottle and aged 48 h at 100 $^\circ C$ in an oven. The resulting white solid was recovered by vacuum filtration and washed with deionized water. The produced powder was dried and calcinated to carry out the corresponding characterization. The Ni/AlMCM-41 catalyst was prepared using the template ion exchange method [Alvarado Perea et al., 2013]. Nickel nitrate (Merck, $Ni_2(NO_3)_2 \cdot 6H_2O \geq 99.0$ %) was used as Ni precursor. The resulting mixture was thermally treated in a Teflon bottle in a muffle furnace. The light green solid was subsequently recovered through vacuum filtration, washing and drying. The final product was calcinated at 600 $^\circ C$ for 6 h in air.

5.3 Results

In the following, the results of the experimental and model-based investigations for the Ni/AlMCM-41 catalyst are summarized and explained. Initially, the catalyst is characterized to ensure the expected behavior based on the preparation method. Afterward, the reaction, the deactivation and the regeneration are separately analyzed and described mathematically.

5.3.1 Characterization

A condensed summary is given below for powder x-ray diffraction (XRD), Brunauer-Emmett-Teller analysis (BET), Temperature Programmed Reduction (TPR) and Fourier Transformed Infrared Spectroscopy (FTIR). Further, detailed information is available in the thesis of Leo Alvarado Perea [Alvarado Perea, 2014]. Figure 5.2a reveals the structural characterization of the Ni/AlMCM-41 catalysts with a Si/Al ratio of 60. A broad band characterizes the crystalline structure of Ni/AlMCM-41 at low angles in the XRD spectrum.

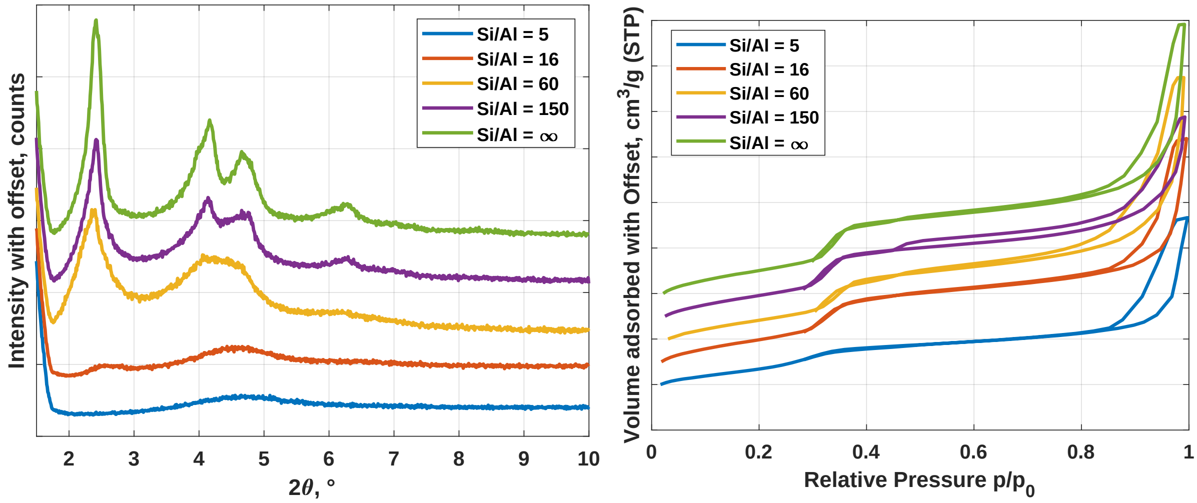

(a) (b)

Figure 5.2: Characterization of Ni/AlMCM-41 with (a) XRD patterns for different Si/Al ratios and (b) N_2-physiosoprtion isotherms for Ni/AlMCM-41 for different Si/Al ratios.

The catalyst without Al has a highly hexagonal ordered structure with the classic diffraction's (100), (110), (200) and (210) in the XRD spectra. For Ni/AlMCM-41, the intensity of all diffraction's is reduced, which indicates that the hexagonal phase is less ordered compared to the catalyst without Al. Therefore, it is concluded that the hexagonal ordering degree of the MCM-41 is sensitive to the presence of Al in the synthesis.

A type-IV isotherm in the N_2-adsorption measurements characterizes the type of catalyst, which is presented in Figure 5.2b. The MCM-41 materials show this adsorptive behavior and have capillary condensation at a relative pressure between 0.30 and 0.35 occurs. The N_2-adsorption data and Ni content of the Ni/MCM-41 and Ni/AlMCM-41 are summarized in Table 5.2. The BET specific surface was around 1000 $\frac{m^2}{g}$, which is typical for MCM-41 materials. From the XRD and N_2-physisorption results, Ni/AlMCM-41 with a Si/Al ratio of 60 occurs to reflects the typical structure of MCM-41 materials.

Table 5.2: Nitrogen adsorption data of Ni/AlMCM-41 with different aluminum content.

Catalyst Si/Al ratio	S_{BET}, $\frac{m^2}{g}$	V_P[I], $\frac{cm^3}{g}$	$d_{P;BJH,des.}$[II] **nm**	$d_{P;NLDFT,des.}$[III] **nm**
∞	937.9	0.91	3.5	3.7
150	961.1	0.99	3.7	3.8
60	983.0	1.05	3.4	3.8
16	806.9	0.88	3.0	3.8
5	533.2	0.55	3.0	3.6

[I] Pore volume

[II] Pore diameter determined by Barret-Joyner-Halenda method (BJH) from adsorption

[III] Nonlocal density functional theory (NLDFT) from desorption

It is commonly accepted that the incorporation of Al into the MCM-41 framework provides Brønsted acid sites catalyzing specific reactions. Therefore, it is important to distinguish between Brønsted and Lewis acid sites on the surface of the catalysts. Pyridine diffuse-reflectance FTIR of Ni/AlMCM-41 was carried out. The illustrated spectra before and after saturation with pyridine at 50, and 150 °C are depicted in Figure 5.3. Two characteristic bands at 3745 cm^{-1} designated to Si-OH groups and at 3550 - 3700 cm^{-1} corresponding to Al-OH and Si-OH-Al groups can be observed. The catalyst with a Si/Al ratio of 60 offered the highest intensity of both bands in comparison to other materials with varying Si/Al ratios.

New bands at 1400 and 1650 cm^{-1} were observed after the pyridine treatment, while the bands in the interval 3800 and 3550 cm^{-1} almost disappeared. A peak at 1448 cm^{-1} is attributed to the binding to Lewis acid sites, and the peak at 1596 cm^{-1} is characteristic for the adsorption to hydroxy groups with weak acidity. The band at 1489 cm^{-1} is due to a covalent binding with both Lewis and Brønsted acid sites. Finally, the band at 1580 cm^{-1} is consistent with the presence of a liquid layer of pyridine, which contributes to the band around 1448 cm^{-1} as well.

At 50 °C, all the bands associated with Lewis acid sites showed high intensity because the sample was saturated with pyridine at this temperature. The band associated with the Brønsted acid sites, 1489 cm^{-1}, increases for a lower Si/Al ratio because more Al is incorporated into the MCM-41 framework. At 150 °C, almost all bands disappeared, indicating the weak acidity of the catalyst. At this temperature, the band at 1489 cm^{-1} (associated with the Brønsted acid sites) became more intense. The acidity of the catalysts was found to be essential for an optimal activity concerning the conversion of ethene to propene.

To study the reducibility of Ni on Ni/AlMCM-41, H_2-TPR was carried out and is displayed in the pub-

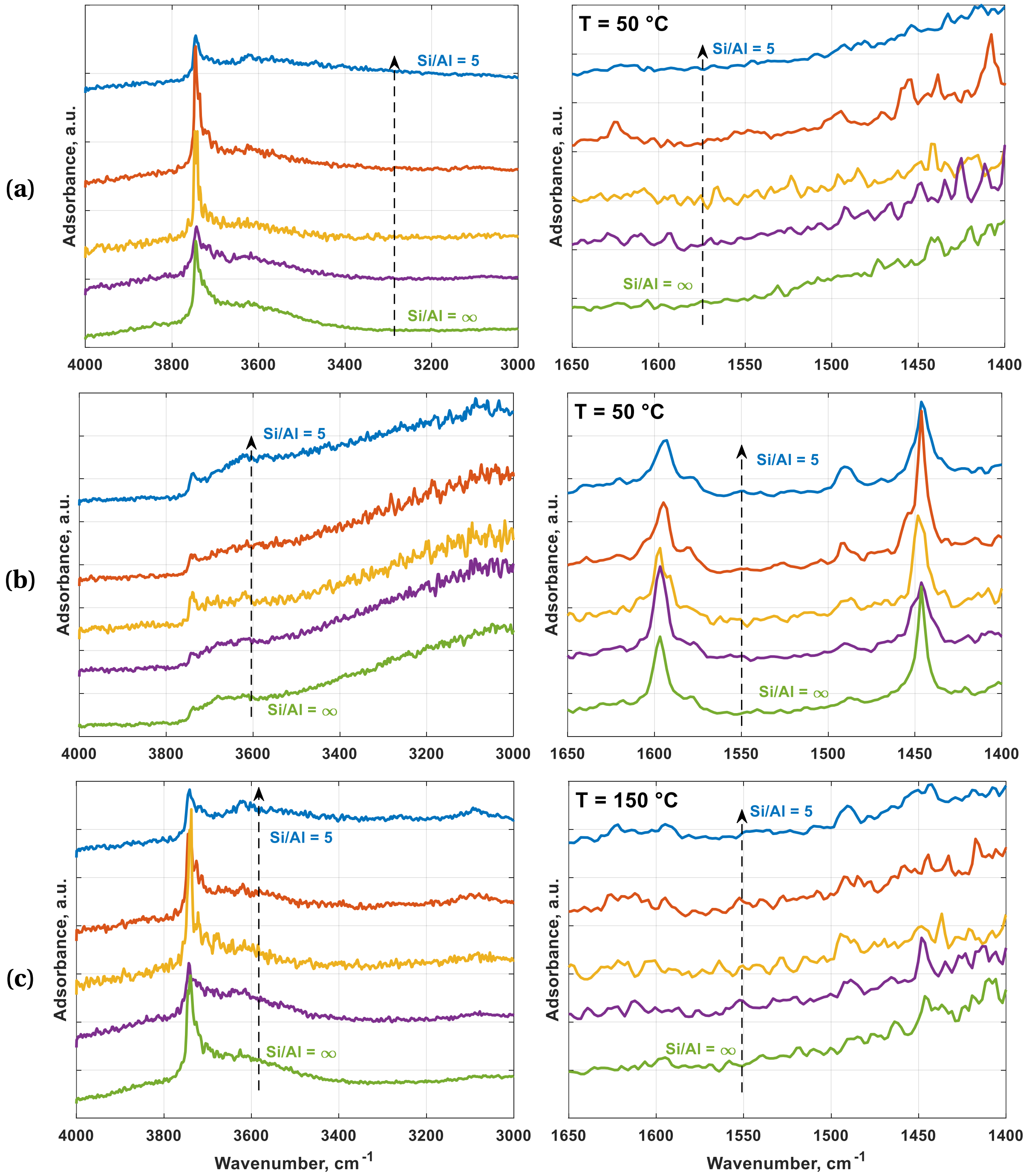

Figure 5.3: Pyridine diffuse-reflectance FTIR spectra of the Ni/MCM-41 and Ni/AlMCM-41 with different Si/Al ratio; a = 5, b = 16, c = 60, d = 150, e = ∞, before (a) and after pyridine adsorption at 50 °C (b) and 150 °C (c).

lication by Alvarado-Perea [Alvarado Perea et al., 2013]. Based upon the observation from the TPR experiments, the following statements can be summarized; nickel oxide is reduced in the range of 327 and 527 °C, the cationic form of Ni on the silica surface is reduced between 527 and 627 °C and the Ni ion forming composites can be reduced within 627 and 727 °C. A small peak in the temperature interval between 300 and 500 °C has been observed. In the interval of 500 and 750 °C, a broad peak with high intensity is observed, which can be attributed to bulky mixed nickel-silicates and nickelaluminosilicate. The catalyst with a Si/Al ratio of 60 Ni is mainly present in its cationic form and appears to be homogeneously distributed along the AlMCM-41. This indicates that under the applied reaction conditions the active nickel centers are spread out and not bulky. This observation helps to narrow down the temperature range, in which the catalyst can operate as desired.

5.3.2 Experimental Investigation of Catalytic Activity (Step 1)

With the knowledge of the nature and characteristic properties of the catalytic system, a detailed consideration of the activity for the catalyst selected (Ni/AlMCM-41 with Si/Al = 60) can be carried out. For this purpose, first an exemplary experiment for an ethene feed of 10 % and a W/F of 2600 $\frac{kg_{cat} \cdot s}{m^3}$ in a temperature range of 50 - 475 °C is shown in Figure 5.4.

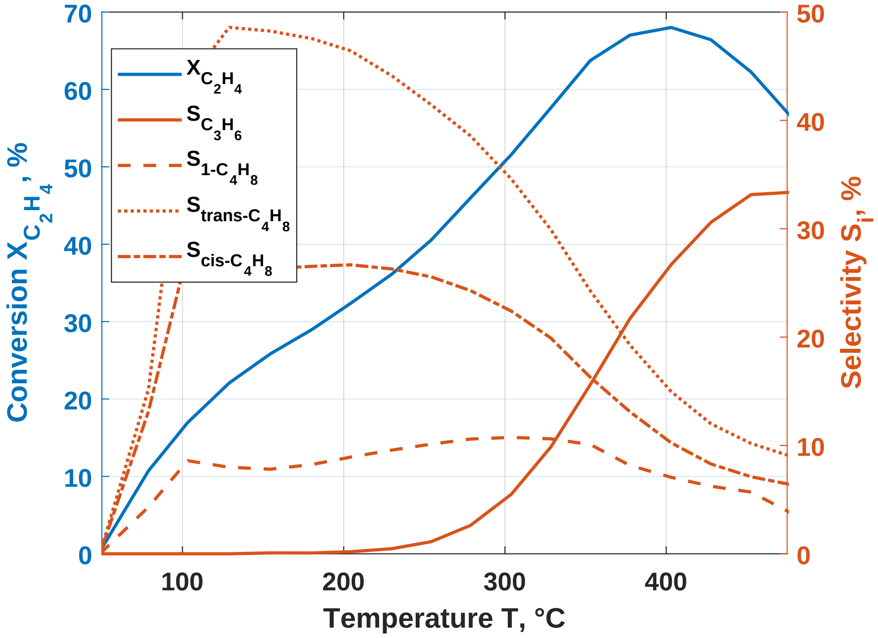

Figure 5.4: Temperature dependent conversion of ethene and selectivity of the main reaction products (propene, 1-butene, trans-butene and cis-butene) with 10 % ethene feed implying a Ni/AlMCM-41 catalyst with a Si/Al = 60 at a W/F ratio of 2600 $\frac{kg_{cat} \cdot s}{m^3}$.

The graph shows that the conversion of the catalyst increases steadily with increasing temperature and has a maximum of 68 % in the 400 °C range. Beyond, the conversion and correspondingly the activity of the system decreases. Furthermore, the experiment can be divided into the ranges lower (up to 250 °C) and high temperature (above 250 °C). In the low-temperature range, only butene isomers are formed, with trans-butene accounting for the largest share with just under 50 %, followed by cis-butene with a maximum of 30 % and 1-butene with 10 %. Accordingly, isomerization is much faster than dimerization. At the same time, no production of propene is observable in this temperature range. Interestingly, the selectivity for cis- and 1-butene is at a constant level, whereas trans-butene decreases slightly.

Starting at the high-temperature range, cis-butene begins to experience a slight drop in selectivity, as well. At the same time, the amount of 1-butene increases and, corresponding to the assumption of a metathesis reaction, the propene selectivity increases significantly. This value increases to a maximum of 33 % at a temperature of 450 °C. At this point, the maximum ethene conversion has already been exceeded. Though, propene is believed to be produced from the self- and cross-metathesis of butenes as well. This is supported by the fact that in parallel, the selectivity of butene isomers decreases significantly, especially for 2-butene. Thus, Iwamoto postulated the already mentioned reaction network based on these conclusions.

However, it could be determined that for the experiments under the optimal reaction condition for propene formation a strong and irreversible deactivation occurs [Alvarado Perea et al., 2013; Alvarado Perea et al., 2017]. Accordingly, the temperature for the reaction study is limited to 350 °C to achieve reproducible results with regenerated catalyst beds.

As the next step, a detailed analysis of the reaction network is presented. The considered and detected components are as follows ethene, propene, ethane, the three butene isomers (n-, cis- and trans-butene), pentene and hexene. Iso-butene was not considered, because it was not detected with sufficient confidence in the carried out experiments. Additionally, the isomers of pentene and hexene were lumped into C_5H_{10} and C_6H_{12} components. The identification of the individual isomers was not possible with the available analytics. Thus, the outputs, defined by eqs. (2.12) to (2.14), were evaluated.

Figure 5.5 illustrates the experimental results of varying reaction conditions for ethene feed concentration of 2.5, 5 and 10 %, and weight to flow ratio (W/F), of 250, 500 and 750 $\frac{kg_{cat} \cdot s}{m^3}$. Several trends can be identified from the graphs. With increasing reactant concentration and decreasing flow rate, the conversion of ethene increases (Figure 5.5a). For the highest feed concentration (10 mole-% ethene) and the highest residence time (W/F = 750 $\frac{kg_{cat} \cdot s}{m^3}$) the highest conversion was obtained at 350 $°C$ (roughly 20 %). Below 150 °C all experiments show less than 3 % of conversion. In the temperature range of 150 - 250 $°C$, the ethene conversion slightly increases at a rather constant and low rate. At 275 °C the ethene conversion is steeply increased (except for the case of the 2.5 % ethene feed), with the maximum possibly not reached at 350 °C.

The isomers 1- and 2-butene are generated at temperatures of 100 $°C$. Therefore, the initiation of the dimerization and the faster proceeding isomerization are pronounced over the entire temperature range. The catalyst is highly selective towards 2-butenes, consisting of the cis- and trans-isomer, as the main reaction product with > 60 % (Figure 5.5). The decreasing 2-butene selectivity at 250 $°C$ corresponds to the steep increase in ethene conversion and the presumable generation of propene. Based on similar observations, Iwamoto [Iwamoto, 2008] proposed metathesis to be the key reaction at higher reaction temperatures (see Figure 5.5). However, no typical metathesis metals, such as rhenium, tungsten and molybdenum, were incorporated and therefore the assumption of ongoing metathesis is to be validated. 1-butene stayed at a constant level and its selectivity started to decrease above 350 °C [Felischak et al., 2019].

A different trend can be seen for the selectivity concerning the desired product propene Figure 5.5b. The highest propene selectivity (44.9 %) was observed for the lowest feed concentration. The propene selectivity decreases with an increasing mole fraction of ethene, indicating the occurrence of side reactions, e.g. enhanced di- and oligomerization. No dependence on the selectivity by the W/F ratio was observed for the conditions considered. It was essentially influenced only by the reactant fraction in the feed stream and the reaction temperature.

The results indicate a kinetic inhibition of the C_3-olefin production route up to 250 $°C$. At higher temperatures, the energetic barrier seems to be overcome, leading to the desired product. The maxima

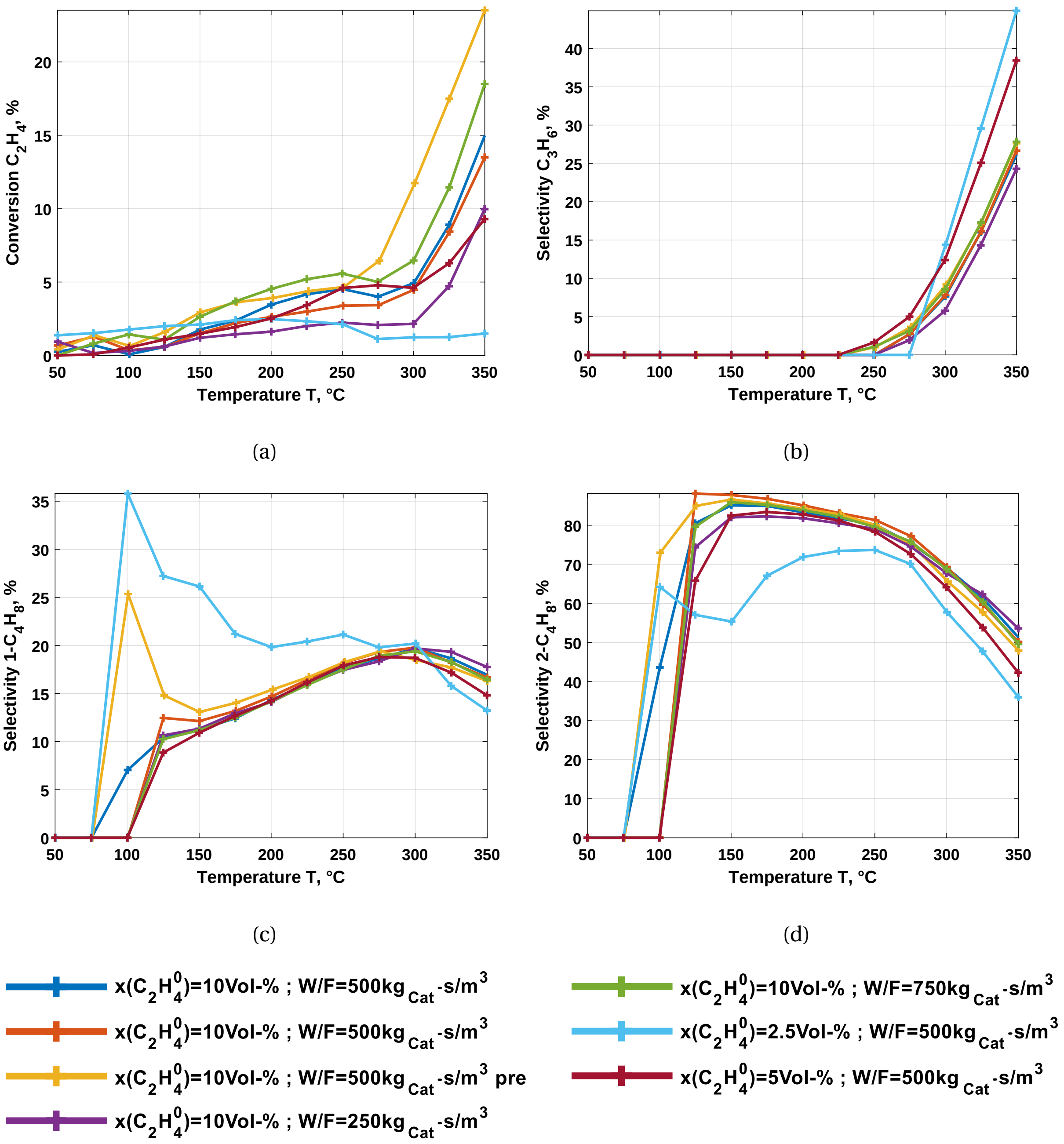

(a) (b)

(c) (d)

Figure 5.5: Comparative evaluation of the Ni/AlMCM-41 catalyst with a Si/Al ratio of 60, under varying reaction conditions of (a) conversion of ethene, (b) selectivity of propene, (c) selectivity of 1-butene and (d) selectivity of 2-butene as a function of temperature.

in selectivity and yield of the analyzed reaction products, observed in the entire range of the reaction conditions covered in this study, are visualized in Figure 5.5 and summarized in Table 5.3. Additional information regarding the observed yields of the main reaction products is available in the appendix Figure A.4.

In Table 5.3 the ethene feed with 10 % resulted in the highest conversion values, consequently leading to the highest yields. Though, the propene selectivity presented its maximum of 44.9 % at the lowest feed concentration of ethene. The undesired products result in a maximum total selectivity of 10 %, obtained under the desired reaction conditions.

Table 5.3: Highest selectivity and yield data detected of the investigated temperature, feed concentration and W/F ranges covered.

	Desired Product	intermediates		Undesired side products		
	Propene	1-Butene	2-Butene	Pentene	Hexene	Ethane
Selectivity S_k eq. (2.13)	44.9 %	35.8 %	88.1 %	4.1 %	3.4 %	3.7 %
Temp x_{in}	350 ° C 2.5 %	100 ° C 2.5 %	125 ° C 10 %	350 ° C 10 %	350 ° C 10 %	300 ° C 10 %
Yield Y_k eq. (2.14)	4.6 %	3.6 %	10.7 %	1.0 %	1.0 %	0.2 %
Temp x_{in}	350 ° C 10 %	350 ° C 10 %	350 ° C 10 %	350 ° C 10 %	350 ° C 10 %	350 ° C 10 %

A clear maximum of propene selectivity has not been reached for the operating temperature considered. Preliminary investigations revealed the occurrence of severe deactivation, at temperatures required for highest propene yields, specifically 450 °C as concluded by Alvarado Perea [Alvarado Perea et al., 2017]. After performing experiments at these temperatures, irreversible blocking of active sites by coke and possibly sintering of the active phase did not allow the catalyst to be regenerated. The blocking of active catalyst sites is a cause of the formed oligomers and aromatics of the compounds involved. Thus, to maintain sufficient catalyst activity, the reaction temperature has to be limited to approximately 350 ° C. This causes limited ethene conversions and propene yields as found here.

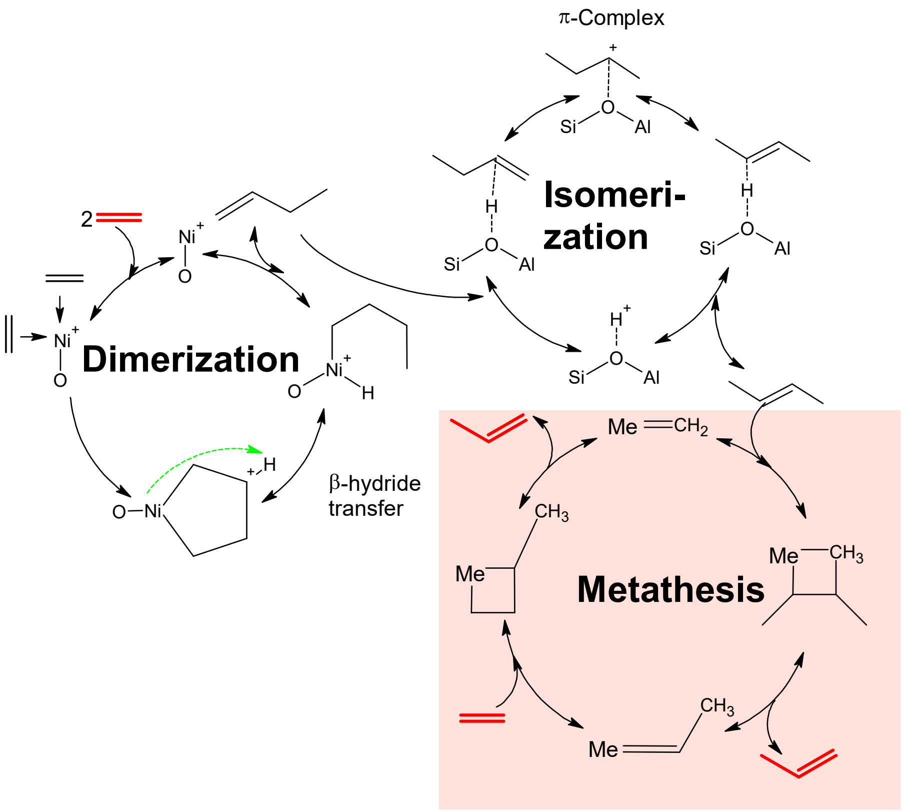

Figure 5.6: Catalytic cycle based on the reaction network proposed by Iwamoto [Felischak et al., 2019].

From the performed experimental product analysis and the obtained experimental perceptions, the mentioned reaction steps by Iwamoto, presented as an extended catalytic cycle in Figure 5.6, were found to be not sufficient to account for all phenomena observed. Formation of larger olefins, as pentenes and hexenes, can be explained by the metathesis of the intermediates and oligomerization of ethene, following a pseudo-Wittig mechanism [Amakawa et al., 2012]. However, the appearance of saturated hydrocarbons, like ethane, and the generation of coke species cannot be explained sufficiently [Argyle and Bartholomew, 2015]. Therefore, an alternative extended reaction mechanism was thought of. This sequential reaction network is illustrated in Figure 5.7. According to the literature [Bonneviot et al., 1983; Hartmann et al., 1996; Sohn and Park, 2000; Broene et al., 2005; Sohn et al., 2006], nickel active sites catalyze the oligomerization of ethene. The main product of this step are the butenes. This type of reaction proceeds via oxidative coupling of ethene [Andrei et al., 2015; Rabeah et al., 2016]. Also, the nickel sites further oligomerizes ethene to hexene at elevated temperatures. In parallel, the butenes may dimerize as well and the coupling of ethene with butenes can occur, respectively, resulting in longer chain olefins, e.g. hexene or octene. All of the present molecules can isomerize to the thermodynamically favored internal olefins, via π-allylic carbanion using acidic sites of the catalyst [Baird and Lunsford, 1972].

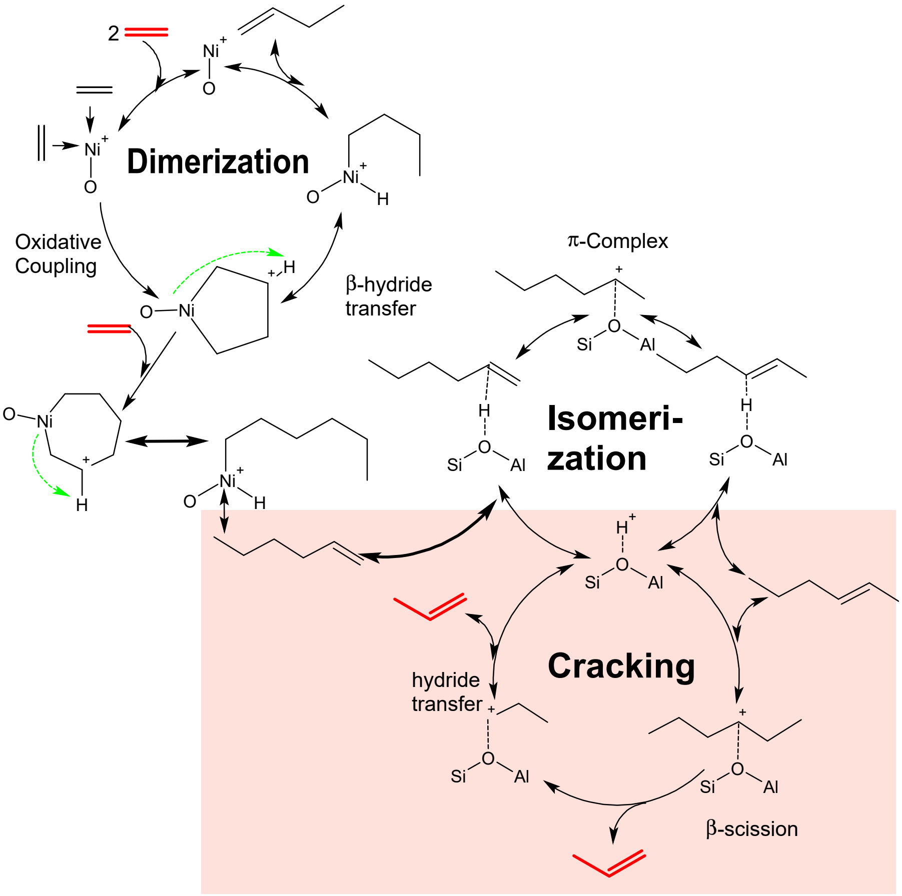

Figure 5.7: Catalytic Cycle of the reaction network implying catalytic cracking [Felischak et al., 2019].

The extended mechanism proposed in [Felischak et al., 2019], involves a conjunct polymerization up to hexene [Dejavifve, 1980; Alvarado Perea et al., 2017] and the subsequent cracking of the hexene. Materials, such as MCM-41 or ZSM-5, are well-known for their use in catalytic cracking [Buchanan et al., 1996; Corma and Orchillés, 2000; Bortnovsky et al., 2005; Chen et al., 2014]. A wide range of possible molecules can interact with the acidic sites, creating a complex network of cracking reactions. The cracking reaction does explain the product spectrum observed and the reaction to propene.

The cracking reaction proceeds via monomolecular protolytic cracking by β-scission of the longer chain olefins, as shown in Figure 5.7. Further oligomerization, aromatization and deprotonation may occur as side reactions. These undesired reactions explain the occurrence of alkanes, the severe deactivation by coking and the subsequent blocking of active sites. Thus, a reaction network, including catalytic cracking of formed 3-hexene, is suggested, which predominantly results in the desired product propene.

Based on the postulated reaction network including cracking, the resulting reaction products can be explained. Furthermore, it seems to be possible to integrate the effect of deactivation in a well-founded way. As shown in the literature [Argyle and Bartholomew, 2015] and explained in the introductory part, acidic zeolites, as they are used in catalytic cracking, are subject to a rapidly occurring deactivation and can be reversibly reactivated. To verify this effect more precisely, the deactivation of the Ni/AlMCM-41 used under ETP reaction conditions will be investigated below through long-term experiments.

5.3.3 Experimental Investigation of Deactivation (Step 2)

From the previous investigations, severe deactivation was observed with time-on-stream [Alvarado Perea et al., 2013; Alvarado Perea et al., 2017]. For the reference case of 10 % ethene feed and a weight-to-flow ratio of 500 $\frac{kg_{cat}\cdot s}{m^3}$, an experiment lasting 24 h was performed using the high temperature kinetic reactor (HTKR). The change in conversion and yield (Figure 5.8a), as well as selectivity of the main reaction products (Figure 5.8b) of propene and the butene isomers, are presented below, illustrating the occurring deactivation effect.

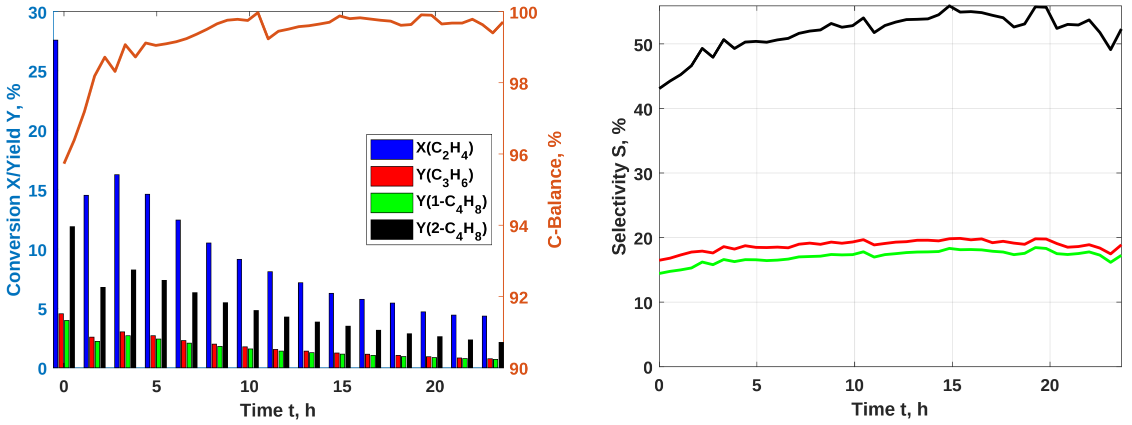

(a)

(b)

Figure 5.8: 24h Spectra of (a) conversion and yield of the main reaction products and carbon balance, (b) the product selectivity, for an ethene feed of 10 %, with a W/F = 500 $\frac{kg_{cat}\cdot s}{m^3}$ and 350 °C.

The graphs (Figure 5.8) show that with time-on-stream the conversion of ethene $X_{C_2H_4}$ decreases from 28 % to a value below 5 %. In accordance, the yield of the products decreases. However, the selectivity is kept constant for the entire reaction time. This observation indicates that the active catalytic sites are inhibited, mainly by coke. But nevertheless, the characteristics and properties of active sites are unchanged. Meaning, no selective deactivation or destruction of the catalytic structure occurs, at these non-optimal reaction conditions. Therefore, under the chosen reaction conditions a blocking of the catalyst by coke formation seems to be ongoing, without any poisoning, discharge or sintering. As shown in Figure 5.9 and explained later on, the darkened catalyst can be fully regenerated with appropriate oxygen concentration and regeneration time.

It is visible that the deactivated catalyst has carbon deposits on the surface compared to the fresh catalyst. The initially light gray catalyst bed changed into black color. With the other catalyst probes shown after a regeneration cycle, at a constant regeneration temperature of 500 °C, the significance of the oxygen concentration used is made clear. If oxygen is fed at 2.5 and 5 %, the catalyst shows clear residues of coke species after a regeneration time of 3 hours. It must be emphasized that at 5 % oxygen diluted in nitrogen, the regenerated zone is extended. However, a complete reactivation is not achieved because the oxygen is not surplus and therefore the deposits cannot be completely removed.

A different result is obtained at oxygen concentrations of 10 % and 20 %. The entire catalyst bed shows little to no color deviation from the fresh catalyst. At the same time, it is possible for these two higher oxygen feeds to reduce the length of the regeneration to 1 hour. Accordingly, it is possible to return the catalyst more effectively and quickly to an active state, while intensifying the process efficiency.

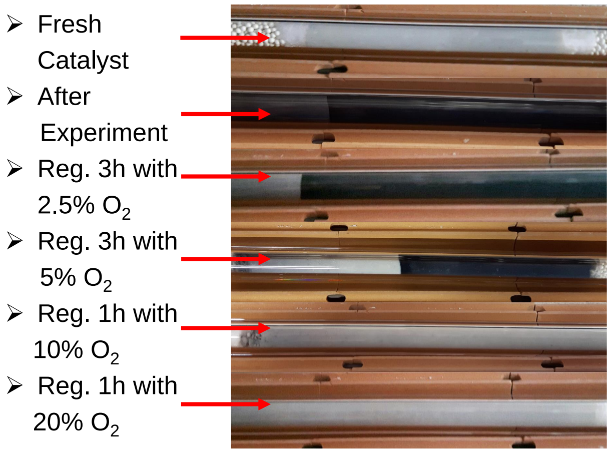

Figure 5.9: Change of catalyst color after regeneration at 500 °C and 500 $\frac{kg_{cat}\cdot s}{m^3}$.

The recovered activity is shown in Figure 5.10, illustrating the possibility of efficient catalyst regeneration. Nevertheless, the exothermal decomposition of the deposited coke should be addressed to exclude effects, such as destructive hot spots or changed catalyst stages.

The entity of all performed experimental runs for a single catalyst bed of Ni/AlMCM-41 (Si/Al = 60) with over 2000 h of time is summarized in Figure 5.10. After each experiment a regeneration took place. Similar initial activity was maintained. As for the experimental study, four regions can be divided. First, named "Feed+Temp", the experimental limits of the setup and the catalyst were evaluated. In this time frame, the regeneration strategy was optimized. Therefore, not all experiments are suitable for consideration. Even though for some experiments, not all of the preliminary activity could be regained, as shown in Figure 5.9, a prolonged regeneration allowed to regain the initial activity.

The second section, named "Temp", evaluated the longtime stability of the catalytic system while re-

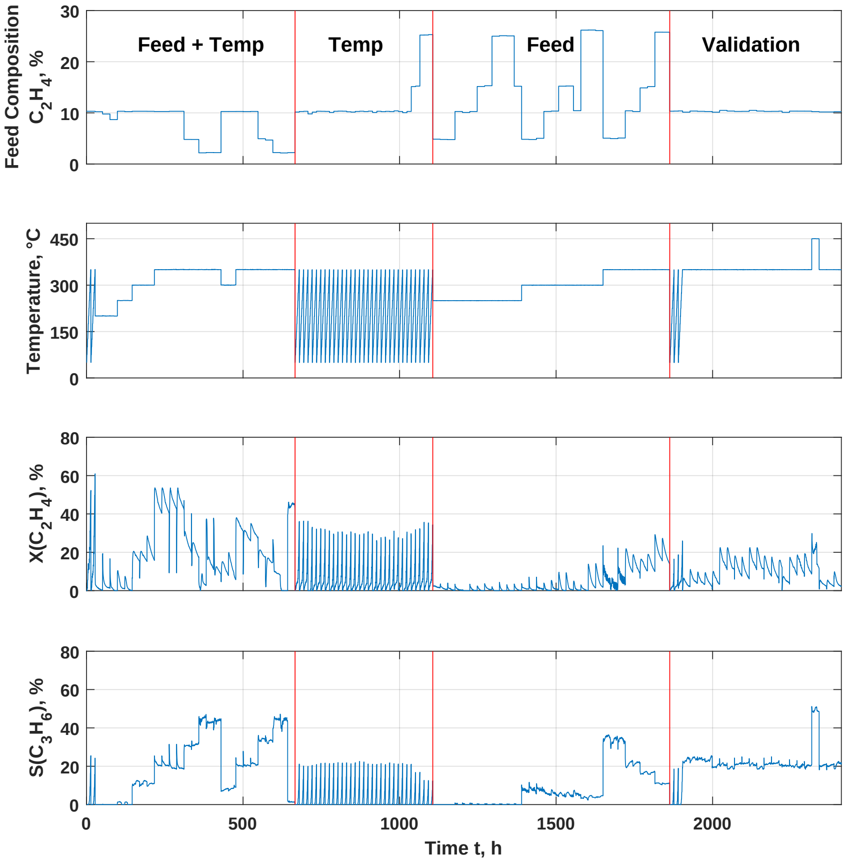

Figure 5.10: Varying feed composition (top), reaction temperature (2nd), conversion of ethene (3rd) and propene selectivity (bottom) over time for the verification of the longtime stability of a single catalyst bed.

peating temperature varying experiments. A steady profile for propene selectivity is observed. Even though the conversion offered a slight decrease, from 700 to 1000 h, thus, an active and productive catalytic system was observed. With the application of pretreatment and prolonged regeneration conditions, the catalytic activity could be restored after 1000 h. Additionally, Figure 5.10 displays that the reaction temperature is the major factor for the propene production in this complex reaction network. Nevertheless, this parameter is crucial for deactivation.

For the third section "Feed", inlet concentration was varied from 2.5 to 25 % of ethene for constant temperatures of 250, 300 and 350 °C. Here, the deactivation study presented below was performed. The temperature has a significant influence on the performance of the catalyst. For varying inlet concentration, two counter behaviors are monitored. A higher inlet concentration of ethene increases side reactions. Therefore, the selectivity of propene decreases. At the same time, the conversion of ethene increases, because of these side reactions. Further, the side reactions enhance the catalyst deactivation, as a result of more hydrocarbon material provided.

The fourth section of "Validation" presents a series of repetition experiments under constant conditions of 350 °C and 10 % of ethene feed. A reproducible saw tooth profile is obtained for conversion, while selectivity is constant. These results show that the catalyst is still active after 2000 h of time-on-stream. Its morphology and properties are unchanged, resulting in constant product distribution and quality. Though, the temperature of 450 °C resulted in significantly decreased conversion, thus, meaning the catalyst was not fully regenerated. Following, a detailed study of the deactivating catalyst is performed and the results are analyzed.

Study of Influence Parameters on Deactivation

For a thorough analysis of the deactivation, experiments with varying feed concentration, W/F ratio and reaction temperature were performed. These conducted experiments were characterized by operation under constant reaction conditions for 24 h and subsequent regeneration of the catalyst bed. Corresponding profiles could be obtained depending on the reaction temperature, the input concentration and the residence time. The results of this experimental set are presented in Figure 5.11. Within the graph, the conversion of the ethene is shown in Figure 5.11a, the selectivity of the main products propene (Figure 5.11b), 1-butene (Figure 5.11c) and 2-butene (Figure 5.11d). In accordance with the initial finding (Figure 5.8) only the conversion is affected by time-on-stream.

The consideration of the deactivation experiments confirms the preceding kinetic investigations (Figure 5.5) concerning the influence of the reaction conditions on the output of the reaction system. Thus, the desired target product propene (Figure 5.11b) increases when the reaction temperature is increased, the input concentration and the W/F ratio are lowered. In contrast, the selectivity of the butene (Figures 5.11c and 5.11d) shows an inversely proportional effect, in the order of the detected selectivity values. The effect of the reaction conditions on 2-butenes (Figure 5.11d) is further amplified. Nevertheless, the selectivity of the mentioned main products increases slightly with decreasing conversion, which indicates suppression of the undesired side reactions.

As mentioned above, the significantly influenced performance variable as a result of deactivation is the conversion of ethene (Figure 5.11a). The residence time has an extraordinary influence on the initial value of the conversion. With higher W/F ratios the initial conversion of the system enhances significantly, which is a logical consequence of the Damköhler number (eq. (4.18)). Though, the W/F ratio has a smaller influence on the temporal course. The slope for the conversion of ethene is especially influenced by the reaction temperature. With increasing operating temperature the decrease in time is significantly steeper. For temperatures above 400 °C the decrease is immense and as it seems irreversible [Alvarado Perea et al., 2013].

Parallel to this determination of the influence of the reaction temperature, it can be seen that the input concentration influences the slope, though to a minor extent. This effect becomes apparent when considering the experiment for 2.5 % and 10 % ethene concentration at the same temperature and residence time. The lower concentration has a flattened course, which indicates the minimization of undesired side reactions. As a result, ethene is not a driving force in the formation of coke. Unfortunately, the conversion is considerably less for lower feed concentrations.

In contrast to this, the main reaction products present a different picture. As explained, there is no selective deactivation of the catalyst. Accordingly, no significant temporal changes can be observed for propene (Figure 5.11b), 1-butene (Figure 5.11c) and 2-butene (Figure 5.11d) in their selectivity profiles. Only with the decreasing activity of the catalyst the selectivity, especially for the butene isomers, increases under all reaction conditions. This effect is due to the deposition of coke on the catalyst surface, which takes place preferentially at the acidic centers [Guisnet et al., 2009]. At the same time, these Lewis acid sites are responsible for the initiation of reactions towards secondary products, such as coke [Aguayo et al., 1999; Lin et al., 2014], is inhibited.

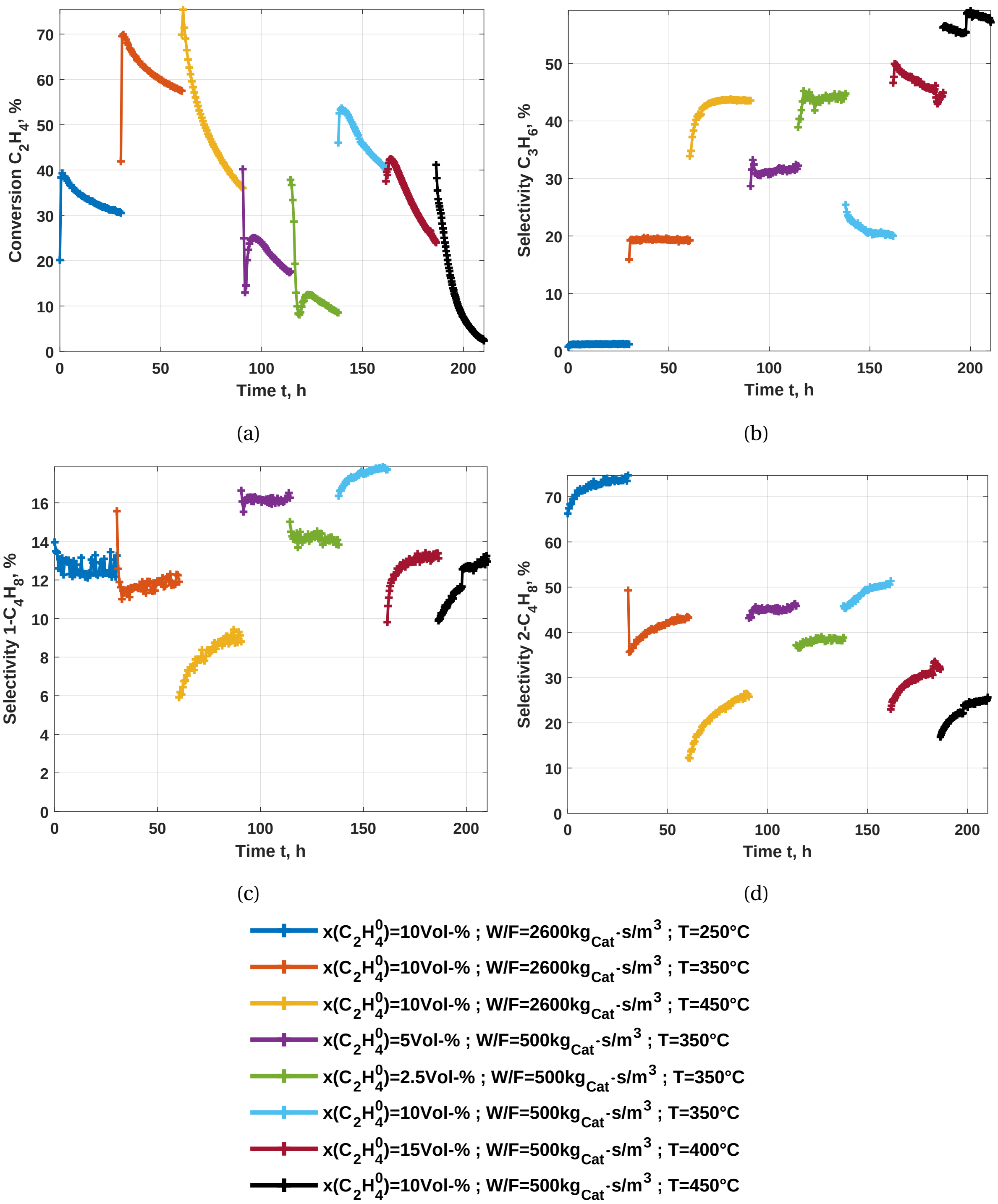

(a) (b)

(c) (d)

Figure 5.11: Comparative evaluation of the deactivation effect on the Ni/AlMCM-41 catalyst with a Si/Al ratio of 60, under varying reaction conditions of (a) conversion of ethene, (b) selectivity of propene, (c) selectivity of 1-butene and (d) 2-butene over time-on-stream.

However, ethene continues to be converted to butene on nickel active sites, responsible for dimerization. The assumed total reaction network, shown in Figure A.8, proposes the generation of dienes and cyclic components for the formation of coke species. A detailed spectroscopic analysis could validate whether the assumed cracking of long-chain hydrocarbons may take place at a different type of acidic sites in comparison to the reaction. The deactivation study presented here, under inherent dynamic operating modes, shows a complex interaction of the varied process parameters of temperature, concentration and residence time. It turns out that an increased reaction temperature significantly enhances the selectivity to propene (Figure 5.11b), as seen from the experiments at 10 % ethene concentration and 2600 $\frac{kg_{cat}\cdot s}{m^3}$. At the same time, it is possible to compensate for a reduction of the temperature by 100 °C by lowering the W/F ratio and the input concentration. In this respect, it must be mentioned that in the case of a lowered input concentration the side reactions are suppressed and the selectivity of the butene is increased, compared to the case with 450 °C and a W/F of 2600 $\frac{kg_{cat}\cdot s}{m^3}$. This again illustrates the complex interplay of the individual variables.

Increased reaction temperatures provide more energy for the reaction, which however supports all reactions, and the concentration provides more material for the reaction. This causes an intensification of all reaction steps, especially the network of cracking postulated here (Figure 5.7), with hexene as the essential intermediate product. Besides, a lower W/F ratio provides the system with more reactant over time and the components have less time to react. According to this, the reaction system's conversion will fall and the side reactions will be suppressed.

It must be emphasized that propene can be formed at 450 °C and 10 % feed concentration with over 50 % selectivity and at the same time, the proportion of butenes can be reduced below 40 %. However, this is associated with irreversible deactivation. A possible explanation for this may be the mechanism of coke species formation, established by Bartholomew [Bartholomew, 1982] and illustrated in Figure 5.12. At temperatures between 200 - 400 °C, hydrocarbons form the adsorbed and atomic form of coke, the so-called alpha configuration. Based on this adsorbed form, at 250 - 500 °C, the beta form is generated and the amorphous coke, where crystalline graphite originates from, is formed at 500 - 550 °C. It is possible to form a bulky metal carbide at low temperatures of 150 - 250 °C, the so-called gamma coke. Based on carbon on nickel metals, vermicular carbon structures can form in a vast range of 300 - 1000 °C.

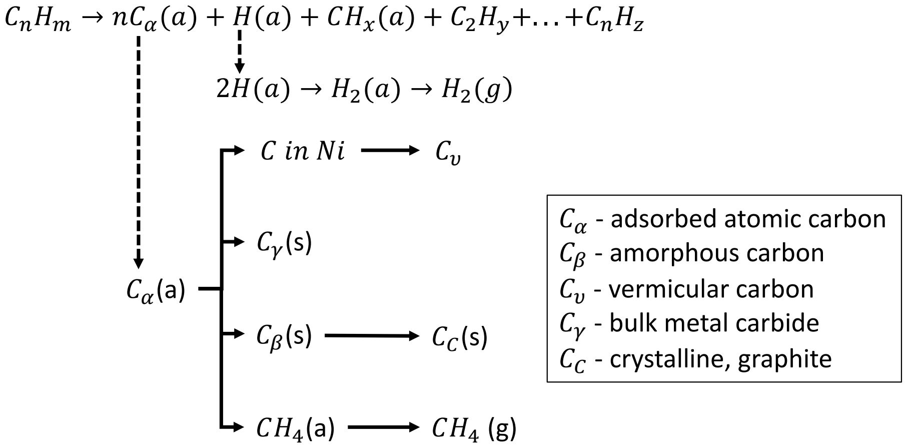
$C_nH_m \rightarrow nC_\alpha(a) + H(a) + CH_x(a) + C_2H_y + \ldots + C_nH_z$
$2H(a) \rightarrow H_2(a) \rightarrow H_2(g)$
C in Ni
C_v
C_γ(s)
C_α(a)
C_β(s)
C_C(s)
CH_4(a)
CH_4 (g)
C_α - adsorbed atomic carbon
C_β - amorphous carbon
C_v - vermicular carbon
C_γ - bulk metal carbide
C_C - crystalline, graphite

Figure 5.12: Types of carbonaceous residue and the inter-transformation [Bartholomew, 1982].

Based on these experimental results, it can be determined for the employed catalyst system that adsorbed atomic species are deposited on the catalyst but can be reversibly removed. Besides, it was possible to analyze in advance that vermicular carbon tubes are formed, which can be removed entirely [Alvarado Perea et al., 2013; Lehmann et al., 2012]. An indication for this is the transitional form of carbon on a metal center, such as nickel. The irreversible deactivation of the catalyst is supposedly caused by the formation of an amorphous beta-carbon, which converts to crystalline graphite with increasing temperature. This coke form, supposedly, causes the irreversible behavior of the system at 450 °C of reaction temperature by solid graphite.

5.3.4 Experimental Investigation of Regeneration (Step 3)

To overcome the detrimental effect of catalytic deactivation, the catalytic system must be regenerated. Accordingly, the effect of regeneration parameters, like regeneration time, regeneration temperature and oxygen concentration, are evaluated for reproducible and reliable results.

To specify the regeneration process, valid data on the course of regeneration to describe and optimize the process step is necessary. For this purpose, the catalysts deactivated in the previous section were first regenerated with the thermogravimetric analysis (TGA)/DSC under dynamic regeneration conditions to limit the area of investigation, and second, the influence of the parameters was studied under isothermal conditions.

An illustrative dynamic measurement for a deactivated Ni/AlMCM-41 is shown in Figure 5.13. Here the gravimetric mass decrease over a temperature function with a heating ramp of 10 K/min is shown in blue and the differential change of the mass in orange. After a large number of experiments, it could be determined that for porous media, the determination of a DSC signal is not effective. Due to the porosity, the heat tint within the material is significant. Therefore, this signal was not considered for further analysis.

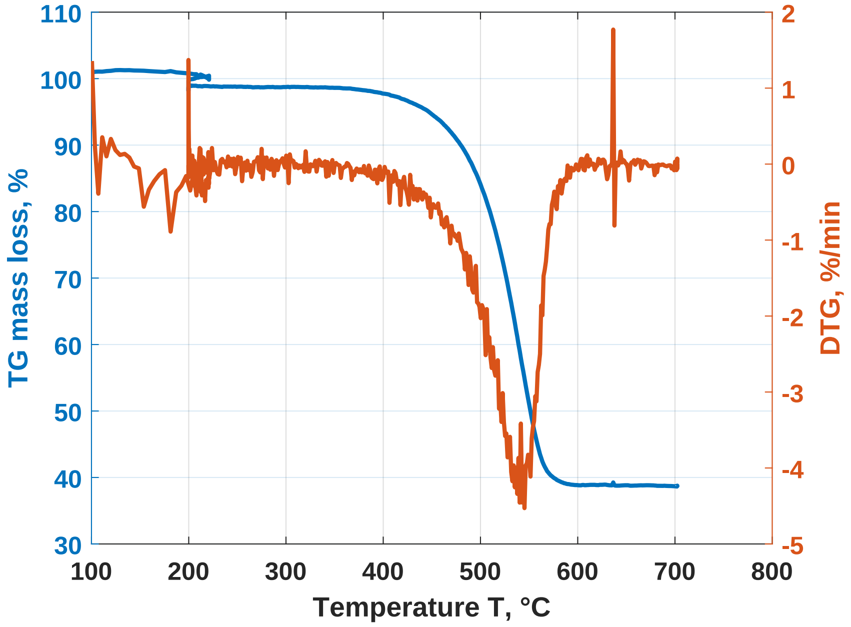

Figure 5.13: Exemplified dynamic regeneration experiment of gravimetric mass loss (blue) and differential mass loss (orange) with varying temperature.

In the present case (Figure 5.13), oxygen was present in the system at all times and it was constantly heated so that possible adsorption effects from the gas phase on the solid are not considered. The catalyst starts to lose mass from about 400 °C. With a further increase of the temperature, the mass decrease is enhanced and tends at 450 °C to a steep drop, with the inflection point, the point of largest change in mass, at approx. 550 °C. A mass decrease of 60 % indicates, to which extent the catalyst was loaded with carbonaceous residue. Subsequently, the curve flattens out, causing the differential mass change to tend towards zero. It is valid to assume an even higher DTG signal when operating at higher temperatures. However, this is not possible for the present catalytic system. The reason is the calcination temperature of the catalyst system at 600 °C, which would mean an unpredictable reaction behavior for a new measurement. Therefore, the range for efficient regeneration is set at 400 - 550 °C. The result is shown in the work of Bartholomew [Bartholomew, 1982] a scheme for the different coke species was established (Figure 5.12). To specify the deposits more precisely, peak fitting, using the differential rate of change of the mass was performed. In Figure 5.14 for two (left) and three (right) fitted peaks. A coefficient of determination with 98.1 % for two pseudo species and 99.2 % for three assumed carbonaceous components could be calculated.

Consequently, three different components are supposed to be found on the particles. The first component is burnt off over the range of 400 - 600 °C with a maximum of 500 °C. At this point, the second species begins to decompose and at 550 °C the third species, but both in a narrower temperature window. For an exact statement about the nature and composition of the individual coke species, it is necessary to use further analytical methods. However, likely the adsorbed alpha form, the amorphous and vermicular structure can be considered. These conclusions are based on the observations by Alvarado Perea [Alvarado Perea et al., 2013] and the temperature windows by Bartholomew [Bartholomew, 1982]. Another possibility is the crystalline type, which causes an irreversible deactivation and possibly blocks active centers.

By limiting the favorable temperature range for the regeneration of the used and deactivated catalyst for the ethene to propene (ETP) reaction, the influence of the oxygen concentration and the respective temperature in the isothermal regeneration process can be investigated. These are shown in Figure 5.15. In Figure 5.15a different regeneration temperatures at a constant oxygen concentration of 10 mole-% are presented, as to Figure 5.15b were temperature is varied at 20 % oxygen and in Figure 5.15c with a constant regeneration temperature at variable oxygen concentration.

Before the analysis of the illustrated results, an issue of the applied catalyst system must be discussed. The catalysts produced at the Max-Planck-Institute Magdeburg and deactivated in the HTKR revealed a significant inhomogeneity of the particle size distribution. The aluminized MCM structures have a high specific surface as a reason of the internal pore system. However, the loading of the individual particles depends on their respective size. Accordingly, different results of coke loading were determined depending on the particle size fraction used from the same catalyst bed. Therefore, the focus was preferably on fine grains, as these provided reproducible results. Besides, it must be mentioned that for heavily coke loaded catalysts, the color did not reverse to the original gray after regeneration. Instead, a white structure resulted, which is an indication of the discharge of the active nickel component from the catalyst into the gas phase. Though, these systems were deactivated at 450 °C, not considered for the reaction step.

Analyzing Figure 5.15, indications are apparent that with increasing regeneration temperature, the regeneration time can be significantly shortened. The same effect can be achieved with increasing oxygen concentration. At the same time, all regeneration experiments tend towards a residual mass of approximately 40 % of the initially loaded catalyst, except for regeneration with 5 % oxygen. Accordingly, it must be noted that there is, as shown in Figure 5.9, a necessary minimum concentration of oxygen to fully remove carbon deposits from the catalyst. This is based on the concentration profile along the catalyst radius and the fixed-bed length. Accordingly, certain areas of the catalyst particle

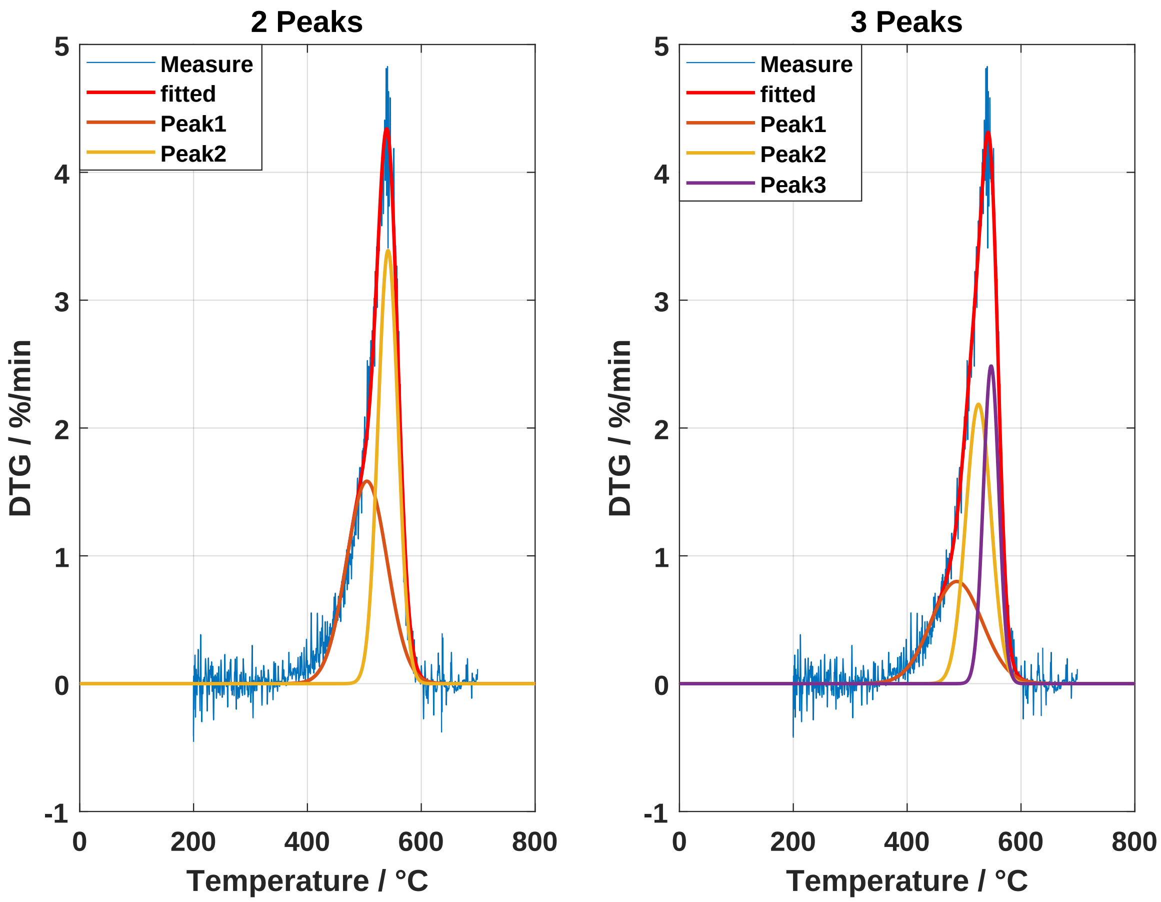

(a)

(b)

Figure 5.14: Gaussian peak fitting with (a) two and (b) three peaks of the differential mass loss signal.

would not be sufficiently supplied with oxygen and residues would remain.
Furthermore, it should be noted that an increase of oxygen content in the nitrogen stream from 10 to 20 % has a relatively marginal influence on regeneration, as illustrated in Figure 5.15c. It can be seen that the regeneration temperature determines the form of the temporal processes and that the oxygen concentration in combination determines the slope. This trend is illustrated by comparison with variable oxygen concentration and constant regeneration temperature (Figure 5.15c). In this case, the curves are very similar and closer together than at variable temperatures. Based on this knowledge, the significance of the set regeneration temperature becomes apparent. For regeneration, a minimal concentration must be used to achieve complete removal of coke and flow through the entire catalyst to reach all areas. However, this influence parameter is less significant as the overall time can be significantly reduced with an appropriate temperature.

5.4 Conclusion

Aluminized MCM-41 impregnated with nickel was used for the direct conversion of ethene to propene (ETP). In preliminary studies, this catalyst was identified as suitable for the mentioned synthesis. The catalyst is capable of supporting multiple reaction steps, namely oligomerization and isomerization,

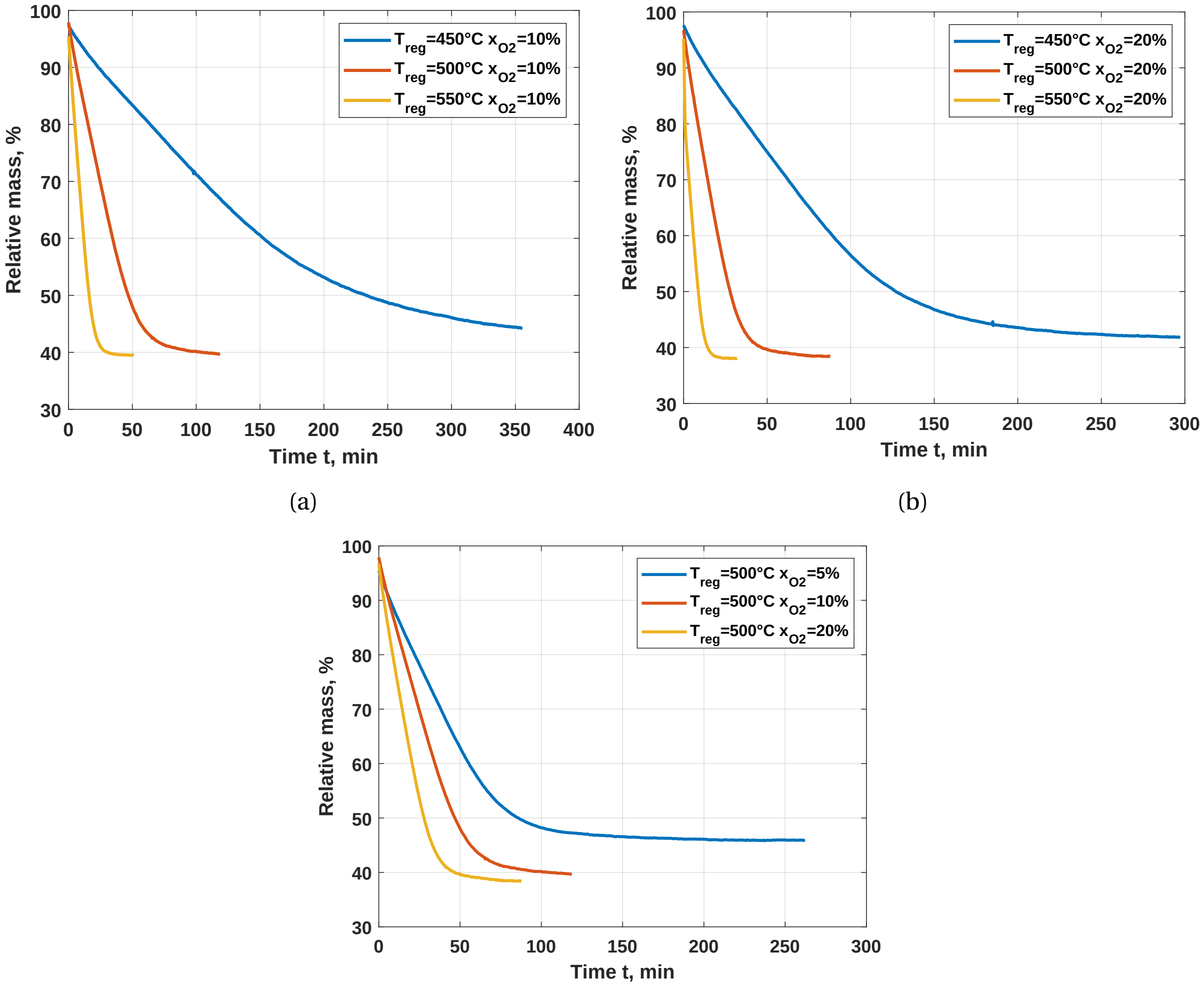

(a)

(b)

(c)

Figure 5.15: Isothermal regeneration experimental signals exploiting TGA measurement with (a) constant oxygen concentration of 10 % and varying temperature, (b) constant oxygen concentration of 20 % and varying temperature and (a) constant temperature of 500 °C and varying oxygen concentration.

catalytic cracking or metathesis. Studies of the reaction mechanism were carried out by varying feed concentrations and residence time. Butene in its isomeric forms (n, cis and trans) was analyzed as the main reaction product. The product spectra consisted further of propene (the target), pentene, hexene and ethane.

According to the investigations carried out using a fixed bed and thermogravimetric analysis (TGA), the following conclusions can be drawn regarding reaction, deactivation and regeneration.

(a) A reaction network for the direct conversion of ethene to propene is suggested, which includes catalytic cracking instead of metathesis.

(b) This reaction network explains the deactivation (step 2) under reaction (step 1) conditions and is capable to predict the occurring product spectrum quite well.

(c) Full regeneration (step 3) of the catalyst is possible when a minimum oxygen amount is introduced and the reaction (step 1) temperature was kept below 400 °C, thereby a single catalyst bed could be effectively operated for more than 2000 h.

The individual processes of reaction (step 1), deactivation (step 2) and regeneration (step 3) taking place on a Ni/AlMCM-41 catalyst for the direct conversion of ethene to propene will be modeled kinetically in more detail in the following chapter.

6 Modeling of the ETP Process Steps

The necessary data for the observed sub-processes of reaction (step 1), deactivation (step 2) and regeneration (step 3) has been presented and analyzed in the previous chapter 5. In the present chapter, mathematical models will be applied to the individual sub-processes. With the focus on the evaluation of the presented two reaction mechanisms (Figures 5.6 and 5.7).

6.1 Kinetics of Reaction (step 1)

The focus of the previously published studies was focused on the intensification of the catalysts activity or the increase of selectivity for a specific component. The kinetic modeling and the parameter derivation received less effort. Nevertheless, many groups and researchers derived models for the transformation of hydrocarbons to light olefins for various reaction types. Perez-Uriarte [Pérez-Uriarte et al., 2016] used HZSM-5 for the conversion of DME to olefins. The ZSM-5 was also applied by Beirnaert [Beirnaert et al., 2001] and von Aretin [von Aretin and Hinrichsen, 2014] for the cracking of hexene, Epelde [Epelde et al., 2014a] for the transformation of 1-butene and Gayubo [Gayubo et al., 2010] for ethanol conversion to olefins. Another interesting catalyst is SAPO-34 that was used by Mousavi [Mousavi et al., 2017] for the methanol to olefin process and by Zhou [Zhou et al., 2008] for the reaction of light alkenes. Van Speybroeck [Van Speybroeck et al., 2014] derived principle kinetics for applied zeolites. Pinto et al. [Pinto et al., 2004] applied alkanes, like hexane and heptane to obtain propene. Lwin [Lwin et al., 2016] and Kapteijn [Kapteijn et al., 1981] kinetically investigated the metathesis reaction as one of the most important organic reactions of the last century. Buluchevski [Buluchevskiy et al., 2014] applied $PdO-Re_2O_7-B_2O_3-Al_2O_3$ for the liquid phase reaction of ethene to propene.

The focus will be on the analysis of two different kinetic approaches for two reaction networks. Initially based on the reaction network suggested by Iwamoto, including metathesis, and second, the proposed network, including cracking reactions. Besides applying the Langmuir-Hinshelwood-Hougen-Watson (LHHW) rate expressions [Langmuir, 1916; Laidler and Meiser, 1982], more detailed mechanistic kinetic model (MM) equations will be applied.

The implementation of the latter, less frequently applied approach, considers the elementary steps of the two catalytic cycles (Figures 5.6 and 5.7) postulated, which can be instructive for the identification of rate-limiting steps [Helfferich, 2004; Murzin and Salmi, 2005; Kiedorf et al., 2014].

6.1.1 Evaluation of Kinetic Mechanisms of Catalytic Cycles

To estimate kinetic parameters, a set of reactions has to be postulated. The well-established network suggested by Iwamoto [Iwamoto, 2008] (Network I) and the proposed network, including cracking reactions (Network II), based on the experimental findings, are considered.

6.1.1.1 Iwamoto Mechanism

The set of reactions resulting from the mechanism of the ETP reaction proposed by Iwamoto [Iwamoto, 2008] is presented in eqs. (6.1) to (6.16) as Network I. The network consists of $L_I = 7$ species involved in $J_I = 16$ reactions, based on the assumed catalytic cycles in Figure 5.6. It includes oligomerization of ethene (eqs. (6.1) and (6.2)) and hexene formation (eq. (6.3)), isomerization reactions (eqs. (6.4) to (6.6)) and metathesis reactions (eqs. (6.7) to (6.16)).

Di-/Oligomerization

$$2C_2H_4 \longrightarrow 1-C_4H_8 \tag{6.1}$$

$$3C_2H_4 \longrightarrow C_6H_{12} \tag{6.2}$$

$$C_2H_4 + 1-C_4H_8 \longrightarrow C_6H_{12} \tag{6.3}$$

Isomerization

$$1-C_4H_8 \rightleftarrows cis-C_4H_8 \tag{6.4}$$

$$1-C_4H_8 \rightleftarrows trans-C_4H_8 \tag{6.5}$$

$$cis-C_4H_8 \rightleftarrows trans-C_4H_8 \tag{6.6}$$

Metathesis

$$C_2H_4 + cis-C_4H_8 \rightleftarrows 2C_3H_6 \tag{6.7}$$

$$C_2H_4 + trans-C_4H_8 \rightleftarrows 2C_3H_6 \tag{6.8}$$

$$2\ 1-C_4H_8 \rightleftarrows C_2H_4 + C_6H_{12} \tag{6.9}$$

$$1-C_4H_8 + cis-C_4H_8 \rightleftarrows C_3H_6 + C_5H_{10} \tag{6.10}$$

$$1-C_4H_8 + trans-C_4H_8 \rightleftarrows C_3H_6 + C_5H_{10} \tag{6.11}$$

$$1-C_4H_8 + C_3H_6 \rightleftarrows C_2H_4 + C_5H_{10} \tag{6.12}$$

$$C_6H_{12} + C_3H_6 \rightleftarrows 1-C_4H_8 + C_5H_{10} \tag{6.13}$$

$$C_6H_{12} + C_2H_4 \rightleftarrows C_3H_6 + C_5H_{10} \tag{6.14}$$

$$C_5H_{10} + cis-C_4H_8 \rightleftarrows C_3H_6 + C_6H_{12} \tag{6.15}$$

$$C_5H_{10} + trans-C_4H_8 \rightleftarrows C_3H_6 + C_6H_{12} \tag{6.16}$$

Such detailed reaction networks correlate with a high number of kinetic parameters. Nevertheless, they are necessary for accuracy, accounting for all occurring effects. Especially gas-phase reactions [Alwahabi and Froment, 2004; Norinaga and Deutschmann, 2007] and complex reactions, like pyrolysis [Norinaga et al., 2008; Norinaga et al., 2009], result in excessive numbers of parameters.

6.1.1.2 Extended Mechanism

With this extended and proposed reaction mechanism (Network II) [Felischak et al., 2019], the total number of feasible reactions increases to $J_{II} = 24$ when it is limited to the highest analyzable olefin hexene. Due to the inclusion of ethane, the number of species considered is now $L_{II} = 8$. All isomers of pentene and hexene are lumped together as C_5H_{10} and C_6H_{12} pseudo-species, to reduce the complexity.

The set of reaction equations quantified in the modified Network II consists of eqs. (6.1) to (6.6) as part of Network I and maintained here. The metathesis reactions (eqs. (6.7) to (6.16)) considered in Network I are replaced by eqs. (6.17) to (6.34) corresponding to the cracking mechanism (Network II). [Felischak et al., 2020]

Cracking

$$C_6H_{12} \longrightarrow 2C_3H_6 \tag{6.17}$$

$$C_6H_{12} \longrightarrow 1-C_4H_8 + C_2H_4 \tag{6.18}$$

$$C_6H_{12} \longrightarrow cis-C_4H_8 + C_2H_4 \tag{6.19}$$

$$C_6H_{12} \longrightarrow trans-C_4H_8 + C_2H_4 \tag{6.20}$$

$$cis-C_4H_8 \longrightarrow 2C_2H_4 \tag{6.21}$$

$$trans-C_4H_8 \longrightarrow 2C_2H_4 \tag{6.22}$$

$$1-C_4H_8 \longrightarrow 2C_2H_4 \tag{6.23}$$

$$C_6H_{12} \xrightarrow{2H} 1-C_4H_8 + C_2H_4 \tag{6.24}$$

$$C_6H_{12} \xrightarrow{2H} cis-C_4H_8 + C_2H_4 \tag{6.25}$$

$$C_6H_{12} \xrightarrow{2H} trans-C_4H_8 + C_2H_4 \tag{6.26}$$

$$1-C_4H_8 \xrightarrow{2H} C_2H_4 + C_2H_6 \tag{6.27}$$

$$cis-C_4H_8 \xrightarrow{2H} C_2H_4 + C_2H_6 \tag{6.28}$$

$$trans-C_4H_8 \xrightarrow{2H} C_2H_4 + C_2H_6 \tag{6.29}$$

$$1-C_4H_8 \xrightarrow{4H} 2C_2H_6 \tag{6.30}$$

$$cis-C_4H_8 \xrightarrow{4H} 2C_2H_6 \tag{6.31}$$

$$trans-C_4H_8 \xrightarrow{4H} 2C_2H_6 \tag{6.32}$$

$$C_2H_4 \xrightarrow{2H} 2C_2H_6 \tag{6.33}$$

$$C_6H_{12} \xrightarrow{2H} C_5H_{10} + CH_4 \tag{6.34}$$

Hydrogen is not an expected molecule in this network. From literature [Argyle and Bartholomew, 2015], it is clear that the high-temperature hydrocarbon reaction does present the possibility to form polyenes or cyclic molecules. With this, hydrogen is released and immediately interacts with occurring unsaturated hydrocarbons to form alkanes. This is supported by the observation in previous publications, where the content of saturated hydrocarbon from olefin feedstock increased with increasing temperature and time-on-stream, while the coking is enhanced. Coke is believed to be of long-chain olefinic, polyenic and cyclic nature.

The different reaction networks introduced above (Network I, eqs. (6.1) to (6.16), and the modified Network II, eqs. (6.1) to (6.6) and eqs. (6.17) to (6.34)) are evaluated and compared using the extensive set of experimental data acquired. The kinetic model applied was based on the LHHW approach and mechanistic modeling.

6.1.2 Data Analysis

Each of the 120 experiments (n = 1,...,Nex = 120) performed, generated m specific outputs (m = 1,...,M_{Out}). The outputs defined by eqs. (2.12) to (2.14), were evaluated for the involved components i ($i = 1,...,L_I = 7; L_{II} = 8$).

This large data set was used to estimate kinetic parameters assuming the two reaction networks described below in conjunction with two types of models quantifying the rates of j reactions characteristic for each of the two networks of j (j=1,...,J_I = 16 or J_{II} = 24) applying two different modeling approaches (see below).

To generate theoretical predictions corresponding to the experimental observations, the steady-state balance of the plug flow tubular reactor (PFTR) model (eq. (6.35)) was solved numerically.

$$\frac{d\dot{n}_i}{dz} = \frac{m_{Cat}}{L}\sum_{j}^{J_{Net}} \nu_{i,j}\, r_j\left(T,\overline{p},\overline{P}_j\right) \qquad i = 1,...,L_I = 7; L_{II} = 8 \tag{6.35}$$

The entity of performed experiment presented varying temperature, feed composition and W/F. Thus, each of the experiments (n = 1,...,Nex = 120) generated a maximum of specific outputs (m = 1,..., $M_{Out,I}$ = 13 and $M_{Out,II}$ = 15). These correspond to the performance parameters conversion of the reactant ethene, the selectivity and yield of the intermediate seven products (propene, ethane, the three butene isomers (n-, cis- and trans-butene), pentene and hexene), defined by eqs. (2.12) to (2.14) and indicated as $Z^{ex}_{m,n}$. Analysis of all reactions assumed (j), dependent on the parameter vector $\overline{P}_j$, was performed by minimizing the following objective function (OF), based on eq. (2.71):

$$OF = \sum_{n}^{Nex=120}\sum_{m}^{M_{Out,Net}}\left(Z^{exp}_{m,n} - Z^{sim}_{m,n}\left(T,\overline{p},\overline{P}_{j=1},...,\overline{P}_{j=J_{Net}}\right)\right)^2 \tag{6.36}$$

In the models, described in more detail below (mod = LHHW or MM), the temperature-dependent rate constants (part of the parameter vectors $\overline{P}_j^{mod}$) were formulated by conventional Arrhenius expressions for the possible reactions, as shown in eq. (2.38).

Two solvers offered by MATLAB2016a (Version 9.0.0.341360 [27]) were used, namely "ODE15s" for solving eq. (6.35) and "lsqnonlin" for minimizing the OF (eq. (6.36)) with the trust-region-reflective algorithm. This optimizer is based on the Levenberg-Marquardt algorithm, solving ordinary differential equations (ODEs). However, it approximates the objective function to a simpler function, with the estimated parameters being varied with a limited step-size.

6.1.3 Model Derivation

Typically only simple reaction mechanisms such as power-laws have been used in previous publications [Froment, 2013; von Aretin and Hinrichsen, 2014; Epelde et al., 2014b]. In this thesis, a detailed kinetic model has been applied and evaluated for the reaction network based on Iwamoto (Network

I) and the proposed network, including cracking (Network II).

6.1.3.1 LHHW

A method mathematically quantifying rate laws of heterogeneously catalyzed reactions is based on LHHW models [Langmuir, 1916]. The approach exploits the Langmuir adsorption isotherm model, which is explained in section 2.3.1. Applying the general procedure for LHHW rate expressions for reactions: dimerization, isomerization, metathesis and cracking can be treated in a straightforward manner [Słomkiewicz, 2004]. It is assumed that all the molecules, reactants and products, participating in the individual reactions can adsorb onto the catalyst sites. For that reason, applying the LHHW procedure for the catalytic reaction steps, shown in Figures 5.6 and 5.7, the following general rate equation is obtained for an exemplary dimerization reaction (eq. (6.1)), considered irreversible. The assumption of irreversibility is appropriate, since the backward reaction, the formation of short-chain hydrocarbons from a long-chain molecule equals a cracking reaction. This reaction requires a separate, specialized catalytic active center and modified reaction conditions.

Dimerization

$$r_{dim}^{LHHW} = \frac{k_{Dim}^{LHHW} \cdot K_{C_2H_4,LHHW}^2 \cdot p_{C_2H_4}^2}{\left(1 + K_{C_2H_4,LHHW} \cdot p_{C_2H_4} + K_{1-C_4H_8,LHHW} \cdot p_{1-C_4H_8}\right)^2} \tag{6.37}$$

The K_i represents the component specific adsorption equilibrium constants, in eq. (6.37) for ethene $K_{C_2H_4}$ and 1butene $K_{1-C_4H_8}$.

In accordance with this procedure, the following equations can be derived for the rates of the isomerization (eq. (6.4)), metathesis (eq. (6.7)), which correlates to network I, and cracking (eq. (6.17)), which is the subsequent step following dimerization and isomerization in network II. Hereby, based on the results of preliminary research [Haag and Pines, 1960; Cramer, 1966; Herisson and Chauvin, 1971; Baird and Lunsford, 1972; Grubbs, 2004; Wang et al., 2011; Andrei et al., 2016], the isomerization and the metathesis reactions are considered to be reversible reactions, which is implemented as the backward reaction in the equations, implying the equilibrium constant K_P for better representation.

Isomerization

$$r_{iso}^{LHHW} = \frac{k_{Iso}^{LHHW} \cdot K_{1-C_4H_8,LHHW} \cdot p_{1-C_4H_8} - \frac{1}{K_{P,Iso}} \cdot K_{trans-C_4H_8,LHHW} \cdot p_{trans-C_4H_8}}{1 + K_{1-C_4H_8,LHHW} \cdot p_{1-C_4H_8} + K_{trans-C_4H_8,LHHW} \cdot p_{trans-C_4H_8}} \tag{6.38}$$

Metathesis

$$r_{met}^{LHHW} = \frac{k_{Met}^{LHHW} \cdot K_{C_2H_4,LHHW} \cdot p_{C_2H_4} \cdot K_{trans-C_4H_8,LHHW} \cdot p_{trans-C_4H_8} - \frac{1}{K_{P,Met}} \cdot K_{C_3H_6,LHHW}^2 \cdot p_{C_3H_6}^2}{\left(1 + K_{C_2H_4,LHHW} \cdot p_{C_2H_4} + K_{trans-C_4H_8,LHHW} \cdot p_{trans-C_4H_8} + K_{C_3H_6,LHHW} \cdot p_{C_3H_6}\right)^2} \tag{6.39}$$

Cracking

$$r_{crack}^{LHHW} = \frac{k_{Crack}^{LHHW} \cdot K_{lump-C_6,LHHW} \cdot p_{lump-C_6}}{1 + K_{lump-C_6,LHHW} \cdot p_{lump-C_6H_{12}} + K_{C_3H_6,LHHW} \cdot p_{C_3H_6}} \tag{6.40}$$

The temperature dependence of the adsorption equilibrium constants K_i^{LHHW} is typically less pronounced compared to the dependence of the corresponding reaction rate constants $k_{LHHW}(T)$. Thus, the former is often ignored, as done in the present work.

6.1.3.2 Mechanistic modeling

The methodology of mechanistic modeling has already been developed in sec. 2.3.1 and is applied in this section to the specific reaction types that can be assumed as occurring reaction steps on individual active sites.

The catalytic cycle of dimerization, shown in Figures 5.6 and 5.7, is initiated with the addition of ethene onto the nickel active side. In the next step, the oxidative coupling leads to a metallacyclopentane and via β-hydride transfer, the 1-butene is obtained [Speiser et al., 2005]. It can be assumed that the dimerization is an irreversible reaction, with the oxidative coupling being not reversible. Therefore, the frequency of λ_{32}, as introduced in Figure 2.1, is equal to zero and can be eliminated from eq. (2.49). This simplification results in the following equation applied for the analysis of the reaction rate given by eq. (6.1).

$$r_{Dim}^{MM} = \frac{k_{Dim}^{MM} p_{C_2H_4}^2}{1 + K_\alpha^{Dim,MM} + K_\beta^{Dim,MM} \cdot p_{C_2H_4}^2 + K_\gamma^{Dim,MM} \cdot p_{1-C_4H_8}} \tag{6.41}$$

It is noteworthy; that this final equation for the mechanistic description of the dimerization is similar to the corresponding equation derived using the LHHW model (eq. (6.37)). However, it differs in the number of constants in the denominator.

In an analogous manner, the following mechanistically based general rate equation can be derived for the isomerization:

$$r_{Iso}^{MM} = \frac{k_{Iso}^{MM} p_{Reac} - \frac{1}{K_{P,Iso}} p_{Prod}}{1 + K_\alpha^{Iso,MM} + K_\beta^{Iso,MM} \cdot p_{Reac} + K_\gamma^{Iso,MM} \cdot p_{Prod}} \,. \tag{6.42}$$

When applying the isomerization of 1-butene to its trans-isomer (eq. (6.4)) the following expression is obtained (to be compared with eq. (6.38)):

$$r_{Iso}^{MM} = \frac{k_{Iso}^{MM} p_{1-C_4H_8} - \frac{1}{K_{P,Iso}} p_{trans-C_4H_8}}{1 + K_\alpha^{Iso,MM} + K_\beta^{Iso,MM} \cdot p_{1-C_4H_8} + K_\gamma^{Iso,MM} \cdot p_{trans-C_4H_8}} \,. \tag{6.43}$$

To quantify the rate of the metathesis reactions (as used in Network I) the mechanism of Herisson and Chauvin [Herisson and Chauvin, 1971] (see Figure 5.6) is applied. The four-step catalytic cycle involves two addition and two elimination steps. A complete general mechanistic model for such a catalytic reaction cycle introduces a vast amount of new variables. The rate expression has the following structure.

$$\begin{aligned} r_{Met}^{MM} = \frac{k_{Met}^{MM} p_{Reac1} p_{Reac2} - \frac{1}{K_{P,Met}} p_{Prod1} p_{Prod2}}{\begin{aligned} &1 + K_\alpha^{Met,MM} \cdot p_{Reac1} + K_\beta^{Met,MM} \cdot p_{Reac2} + K_\gamma^{Met,MM} \cdot p_{Reac1} p_{Reac2} \\ &+ K_\delta^{Met,MM} \cdot p_{Reac1} p_{Prod1} + K_\epsilon^{Met,MM} \cdot p_{Reac2} p_{Prod2} \\ &+ K_\zeta^{Met,MM} \cdot p_{Prod1} + K_\eta^{Met,MM} p_{Prod2} + K_\theta^{Met,MM} p_{Prod1} p_{Prod2} \end{aligned}} \end{aligned} \tag{6.44}$$

Exemplary, the rate equation for the metathesis of ethene with 2-butene to produce propene (eq. (6.8)) is presented. Since the metathesis is assumed fully reversible, no simplification can be applied. To obtain a simplified expression of the parameter set for this type of equation, the determination of a rate-determining step is necessary. So far, spectroscopic analysis has not yet identified a limiting step. Therefore, the reaction rate cannot be further simplified, resulting in eq. (6.45), which is more complex than the obtained corresponding equation for the LHHW (eq. (6.39)).

$$r_{Met}^{MM} = \frac{k_{Met}^{MM} p_{C_2H_4} p_{trans-C_4H_8}}{\begin{aligned} 1 &+ K_{\alpha}^{Met,MM} \cdot p_{C_2H_4} + K_{\beta}^{Met,MM} \cdot p_{C_2H_4} p_{trans-C_4H_8} \\ &+ K_{\gamma}^{Met,MM} \cdot p_{trans-C_4H_8} + K_{\delta}^{Met,MM} \cdot p_{trans-C_4H_8} p_{C_3H_6} + K_{\epsilon}^{Met,MM} \cdot p_{C_3H_6}^2 \\ &+ K_{\zeta}^{Met,MM} \cdot p_{C_2H_4} p_{C_3H_6} + K_{\eta}^{Met,MM} p_{C_3H_6} \end{aligned}} \tag{6.45}$$

In a similar manner, the other derived rate expressions for the reactions of the modified reaction network (Figure 5.7 and eqs. (6.1) to (6.6) and (6.17) to (6.34)) can be quantified.

In contrast to Network I the rates of catalytic cracking reactions need to be incorporated. The application of the mechanistic model concept results in the following general expression:

$$r_{Crack}^{MM} = \frac{k_{Crack}^{MM} p_{Reac} - \frac{1}{K_{P,Crack}} p_{Prod1} p_{Prod2}}{\begin{aligned} 1 &+ K_{\alpha}^{Crack,MM} \cdot p_{Reac} + K_{\beta}^{Crack,MM} \cdot p_{Reac} p_{Prod1} \\ &+ K_{\gamma}^{Crack,MM} \cdot p_{Prod1} + K_{\delta}^{Crack,MM} \cdot p_{Prod2} + K_{\epsilon}^{Crack,MM} \cdot p_{Prod1} p_{Prod2} \end{aligned}} . \tag{6.46}$$

With the assumption of an irreversible step in the catalytic cycle, e.g. the β-scission as shown in Figure 5.7, the following equation can be derived for the cracking of hexene into two propene molecules (eq. (6.17)):

$$r_{Crack}^{MM} = \frac{k_{Crack}^{MM} p_{C_6}}{\begin{aligned} 1 &+ K_{\alpha}^{Crack,MM} \cdot p_{C_6} + K_{\beta}^{Crack,MM} \cdot p_{C_6} p_{C_3H_6} \\ &+ K_{\gamma}^{Crack,MM} \cdot p_{C_3H_6} + K_{\delta}^{Crack,MM} \cdot p_{C_3H_6}^2 \end{aligned}} . \tag{6.47}$$

Regarding the description of the proposed modified reaction Network II (Figure 5.7) it is important to note that the two sub-networks of isomerization and cracking share an active catalyst species. In such cases, the mutual active catalyst species needs to be incorporated into the mechanistic formulas [Helfferich, 2004]. However, in our example, an excess of active catalyst centers present is assumed, compared to the reactive molecules. Therefore, the mentioned influence on the rates is neglected. Additionally, acidic sites could also be involved in the oligomerization of the short-chain olefins [Henkel, 2013]. Their quantitative incorporation would further increase the complexity of rate expressions. In case of lacking information regarding the nature of the active sites involved, further uncertainties remain.

In comparison to the LHHW models, the derivation of the mechanistic models assumes a larger number of elementary steps and free parameters. Thus, in principle, the approach provides more flexibility. Due to possible and reasonable lumping of parameters, reduced rate expressions can be derived, which are, regarding their structure, similar to LHHW expressions. The results of the comparison will be reported in the next section for the specific reaction system investigated applying both networks postulated.

6.1.4 Evaluation of Kinetic Reaction Models

In this section, the comprehensive parity plots given in Figure 6.1 will be discussed, which compares the two postulated reaction networks and the presented kinetic modeling approaches considered in this work.

The results obtained for Network I (eqs. (6.1) to (6.16)) by applying the mechanistic modeling in Figure 6.1a with 152 fitting parameters and for the LHHW model shown in the parity plot given in Figure 6.1b with 39 fitting parameters are presented.

The experimentally obtained data, particularly the ethene conversions, are represented well in the case of the LHHW approach. For the reaction network based on the conclusions of Iwamoto, significant differences between the two kinetic approaches are apparent. In the case of mechanistic modeling (MM), no ethene conversion is predicted for the entire experimental data set, which is an unsatisfactory result. At the same time, the selectivity to propene is overestimated for low experimental values and underestimates the highest propene selectivity. Similar results can be observed for 2-butene. Here, the low values for cis-butene are overestimated and for the maximal experimental selectivity values of 30 %, the simulative values fluctuate between 10 and 40 %. Only 1-butene is well within the narrow error range of ± 5 %.

In contrast, the LHHW better reflects the conversion of ethene (Figure 6.1) and the selectivity of the butene isomers. Although low ethene conversions are overestimated, the increased values are close to the optimum line. In the case of 1- and cis-butene, a certain number of experimental points are overestimated, but even here the majority of the parity points are within the selected error range. For trans-butene, individual values are slightly overestimated for the spectrum from 20 to 40 % of selectivity. Experimental results around 50 % are underestimated. Only the selectivity to propene shows a significantly worse result for the simpler calculation system with only 39 parameters compared to 152 for the mechanistic approach. According to the simulation, propene is not formed in any experiment. The converted ethene is presumably used for isomerization. Subsequent steps, such as metathesis, are not included. This means that the assumed metathesis does not have any influence on the product spectrum. Accordingly, the assumption is confirmed that this reaction network is less likely to occur than network II, which includes cracking.

As explained above, based on Iwamoto's conclusions, the network is not in a position to explain the entire product range and the above simulations show that the desired product propene is not included. Therefore, it is believed that the described phenomena can be explained with the corresponding parity plots for the modified reaction Network II (eqs. (6.1) to (6.6) and (6.17) to (6.34)). Applying the mechanistic modeling approach (Figure 6.1c) 162 fitting parameters and the LHHW model (Figure 6.1d) with 56 parameters for network involving cracking reaction are used.

In contrast to the previously used network I (Figure 6.1a), the mechanistic modeling (Figure 6.1c) shows an improvement for the ethene conversion, even if the values in the parity plot lie within and around the error range. The selectivity of the main products displays a different picture. Here, except for 1-butene, the main products are considered by the model to be almost constant over the entire range of varying experimental conditions. The data points run on a horizontal line, with the greatest deviation being obtained for higher values. Striking is the apparent agreement of 1-butene selectivity, where few points are marginally overestimated and otherwise are ideally represented. Though, it must be stressed that 162 were estimated.

The result for the implementation of the LHHW approach for network II (Figure 6.1d) indicates significant improvement with only 56 parameters. This model is capable of fitting all estimated conversion, selectivity and yield values within a ±5 % margin compared to the experimental data. These results are similar to the results of the LHHW model for Network I (Figure 6.1b). However, the incorporation of cracking reactions can represent the conversion of ethene and the selectivity of propene significantly better. The distribution of high selectivity values is limited, which implies better agreement and better applicability. The individual butene isomers, namely n-, cis- and trans-butene, are entirely within the narrow error margin of ±5 %. Interestingly, the formerly underestimated desired products are now sufficiently matched, giving appropriate estimated values.

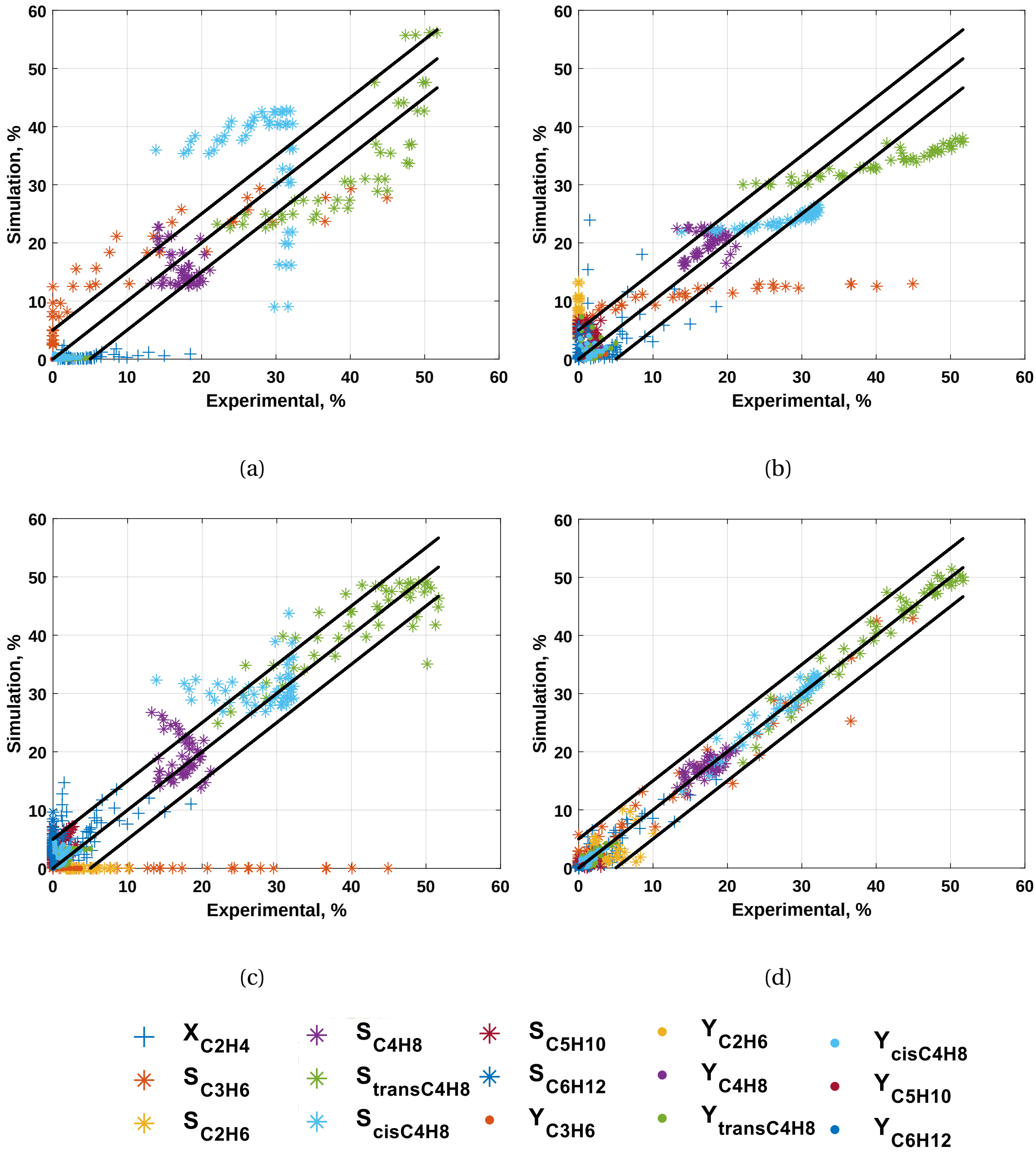

(a) (b)

(c) (d)

Figure 6.1: Comparison of (a) Iwamoto with mechanistic modeling, (b) Cracking network with mechanistic modeling, (c) Iwamoto with LHHW and (d) Cracking network with LHHW.

In the following, the data points obtained here in the parity diagram are presented specifically as temperature-dependent functions for the respective reaction conditions and the respective networks and kinetic approaches are compared in detail.

6.1.4.1 Iwamoto Mechanism

Detailed information for considering Network I using the LHHW model (Figure 6.2) and mechanistic modeling (Figure A.12) are provided in the following sections.

Mechanistic modeling

The approach of mechanistic modeling was applied, which increases complexity. Though, earlier publications [Kiedorf et al., 2014; Jörke et al., 2015; Mueller et al., 2018] have proven the suitability of this method.

Therefore, the formulas, derived before for oligomerization (eqs. (6.1) to (6.3)), isomerization (eqs. (6.4) to (6.6)) and metathesis (eqs. (6.7) to (6.16)), were applied. From the parity plot for the mechanistic modeling (Figure 6.1a) of the reaction network proposed by Iwamoto, fitting of experimental and calculated values observed with a least-square value of 82.7 % was achieved.

For the ethene conversion (Figure A.12a), an underestimation in the entire temperature range is obtained. Though, the model is capable of meeting the point of an increased slope at around 300 °C. The differences, however, are severe and the expected order of the reaction conditions is not met. For propene, the trend of its selectivity is poorly represented by the simulation (Figure A.12b). The estimation shows a linearly inclining trend with the rising temperature, which is accurate.

Furthermore, the experimental data are, below 300 °C, overestimated by the mechanistic model and above underestimated. This is insufficient, especially for the desired product propene. According to simulation, the propene production is independent of the ethene conversion and is produced when the necessary temperature to overcome the existing kinetic barriers are exceeded.

A better fitting is seen for the butene isomers (Figure A.12c and d). In the case of the trans-butene (Figure A.12d), a steady decrease in selectivity is observed, as it is observed in the experiments. The simulation follows a linear function. Each set of reaction conditions has its slope, which are of similar magnitude. This result becomes obvious in the range of high temperatures, where, following the experimental data, the selectivity differs. The experiment with a feed concentration of 2.5 % is not well represented at all. Below 300 °C the linear decrease is opposite to the slight increase of the obtained data. This experiment shows a point of inflection, shifting to a negative slope. Yet, the simulation has a linear trend and is overestimating this set of reaction conditions in the entire temperature range.

For the terminal butene, the derived mechanistic model is capable of following an increasing and above 275 °C a decreasing slope. Nevertheless, the negative slope after the inflection point is too small. All the experimental conditions are overestimated, except for the condition of 2.5 % ethene feed concentration, which was first under- and then overestimated.

Nevertheless, with these results a major question arises: Why this methodology is insufficient for the present case? This question can be answered with a quote by Helfferich [Helfferich, 2004, p.275].

> *We may ask why Christiansen's so convenient formula is hardly ever used in heterogeneous catalysis. Apart from most engineers not being familiar with it, there are two reasons: The formula is for a single catalytic cycle and therefore not applicable to reactions in which adsorbed species react with one another, and the coefficients in the resulting rate equations are composites of rate coefficients of adsorption, desorption, and reaction, making it hard to separate the effects of these phenomena. Nevertheless, for reactions involving only a sin-*

> *gle catalytic site, Christiansen's formula leads more quickly and simply to a rate equation.*

A possibility could be the agglomeration of an intermediate catalyst species, due to rate-determining steps. Such species have to be accounted for. Investigations by different research groups, regarding the catalytic active species, for instance, acidic sites or the oxidation state of the nickel species, and the actual reaction type are still ongoing. So far, it is not possible to propose a rate-determining step or whether a species within the catalytic sub-cycles could be agglomerating.

A deep spectroscopic analysis is necessary to identify such species. This analysis would be beneficial to verify which and how many species are actively participating in the overall reaction network. For multiple active sites, a loop factor is needed that would account for a distribution of active sites and the reactant concentration for each sub-cycle. In the pursuit of a fully resolved mechanism, in-situ spectroscopy is needed to track single reactions. Therefore, parallel reactions must be suppressed to allow for accurate tracking of a sub-network. Here, the biggest challenge for the presented heterogeneous application is clear. Besides potentially multiple active species, the reaction products can further adsorb and react on the catalyst surface. As a result, the reaction network extends to an immense number of molecules and reaction steps. Additionally, one must ask with the coupled effect of adsorption and the resulting equilibrium constant is needed. Possibly, a simplification leading to a similar expression like the LHHW approach [Kiedorf, 2017].

Due to the insufficient adaptation of the reaction network, based on a metathesis reaction, using the mechanistic kinetics, as seen in Figure 6.1, a detailed analysis will be waived in the following and the simpler model based on LHHW will be used.

LHHW

Immediately, when analyzing the corresponding parity plot (Figure 6.1b) it becomes evident that the use of LHHW is beneficial. The least-square method shows the fitting of 83.5 % and most of the plotted data points lie within the range of ±5 % variation from the experimental value.

In Figure 6.2, the simulation correlated to the analyzed experimental conditions is presented. For the conversion of ethene, the least coinciding of theoretical and experimental values is obtained. The computation presents a slight linear increase with elevated temperature. At the same time, the differences are intensified. Below 300 °C, the theoretically determined linear behavior follows the trend of the experimental data. Nevertheless, the prediction is not resulting in the same order magnitude as the experimental data. Above 300 °C, the conversion rises significantly, which is not met by the simulation, leading to higher disagreement.

The generation of propene is assumed to occur not at all by the simulation (Figure 6.2b). The selectivity is entirely at 0 % for all different reaction conditions in the entire temperature range. This is contrary to the experimental observations.

When observing the butene isomers, a favorable outcome is seen with the application of the LHHW. For the terminal C_4-olefin, the model allows elucidating the turning point at 300 °C, which correlates with the increase in propene selectivity. Even though the assumptions underestimate the selectivity below 275 °C, the points of the highest temperature are in good agreement with the experimentally obtained data. Thereby, the order and magnitude are consistently matched. In accordance, the trans-isomer (Figure 6.2d) is well represented by the parameters estimated. The spreading of the values is well represented for increasing temperature and the order of magnitude is in good agreement.

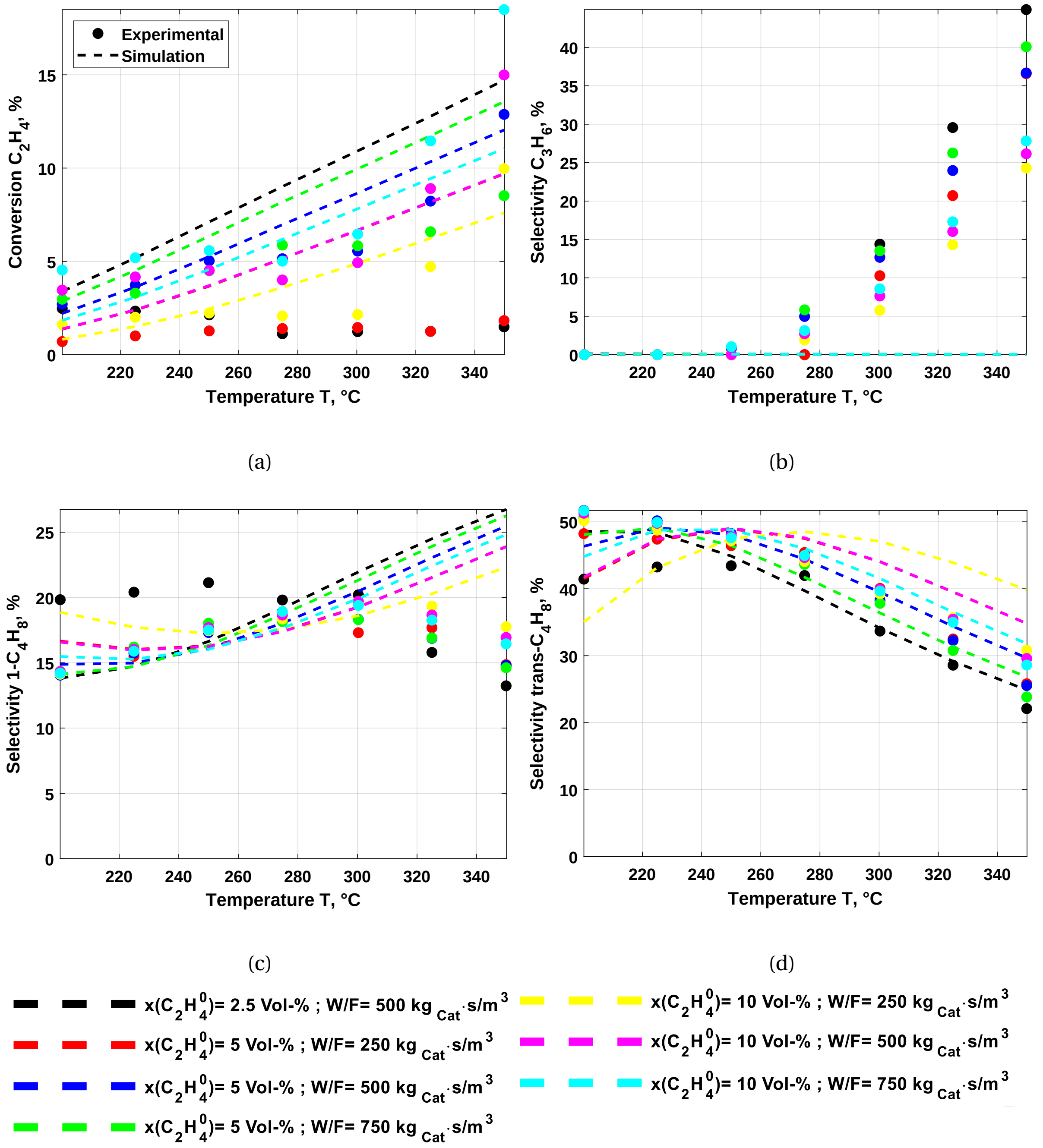

(a) (b)

(c) (d)

Figure 6.2: Detailed representation of simulative results to experimental values for Iwamoto applying LHHW.

However, the same reaction conditions do not represent 1-butene well (Figure 6.2c). Its selectivity is mainly overestimated and for the highest temperature investigated no ideal fitting is obtained.
The limitation of preexisting equilibrium by adsorption is advantageous for the prediction of the data. Additionally, the adsorption is helpful, because it accounts for the blockage of free adsorptive positions on the catalyst surface. As a result, shifts in the selectivity are accurately simulated. However, it seems that ongoing backward reactions are unfavorable for the simulative representation. Especially for the butene isomers, the trend of the theoretical results is inappropriate. Their involvement in the rate equations and the obstacle due to adsorption is not met.

From the analysis, it is evident that Network I with the kinetic LHHW approach is not capable to depict the ETP's response when metathesis seems to not affect the resulting product spectrum. It is therefore doubtful that this reaction takes place as a reaction of the network. Therefore, in the following, the newly postulated network including catalytic cracking with LHHW kinetics is applied.

6.1.4.2 Extended Mechanism including catalytic cracking

The results of parametrizing the rate expression according to the LHHW model applied to the modified Network II based on minimizing the objective function given in eq. (6.36) with 56 Parameters. As discussed above, this combination provided the most satisfying results. The estimated 56 model parameters of the 24 equations (eqs. (6.1) to (6.6) and eqs. (6.17) to (6.34)) formulated for Network II and the LHHW approach are summarized in Table A.3. Experimentally determined and simulated conversion and selectivity data are shown in Figure 6.3.

In Figure 6.3a, the improved agreement can be seen first hand for the conversion of ethene. Even though the initial activity at 200 °C is not met for higher feed concentrations, the model captures the essential features of the ethene conversion trends for varying reaction conditions covered. More details regarding the quality of describing the ethene conversion with this model are shown for varying W/F in Figure A.9, as well as the concentration in Figure A.10 and Figure A.11. The modeled results represent the W/F ratio dependency well. For an ethene feed concentration of 10 %, the conversion is predicted accurately. Limitations are in the case of lower feed concentrations (Figure A.10). The limited quality of the ethene conversion predictions indicates the limits of the model.

The model prediction is improved regarding propene selectivity (Figure 6.3b). The selectivity begins to increase at a temperature of approximately 250 °C. At higher temperatures, the predictions follow the wide-ranging reaction conditions of the measured trends. However, not all individual reaction conditions can be separated. That is why the propene selectivity in Figure 6.1b shows minimal differences between simulation and experiment for high temperatures.

The butene isomers are crucial for comparing Networks I and II since they are considered differently. Their selectivity is predicted quite well, assuming Network II and the LHHW modeling approach for the entire reaction conditions and the temperature range. For 1-butene (Figure 6.2c), in agreement with the observed experimental results, the model is capable of predicting an increase until an inflection point is reached around 275 °C. The influence of feed concentration is well described.

A reasonable agreement between measurements and prediction is also observed for trans-butene as shown in Figure 6.3d. In particular, the trends observed and predicted regarding the butenes support the application of the modified reaction Network II, incorporating a catalytic cracking on acidic sites. Thus, these sites are considered to be significant and relevant for the enhanced production of propene from ethene feedstock.

It could be shown, that the mathematical description of the ethene to propene (ETP) on a mesoporous and nickel impregnated MCM-41 catalyst a reaction network consisting of dimerization, isomerization and cracking in combination with a kinetic approach according to LHHW provides adequate results. A complete reaction network consisting of 24 reactions was used and 56 parameters in total were adjusted for a broad experimental spectrum.

With the knowledge of the reaction kinetics, the significantly occurring deactivation of the catalytic system can be investigated in the following. For this purpose, simple integration of a time-dependent

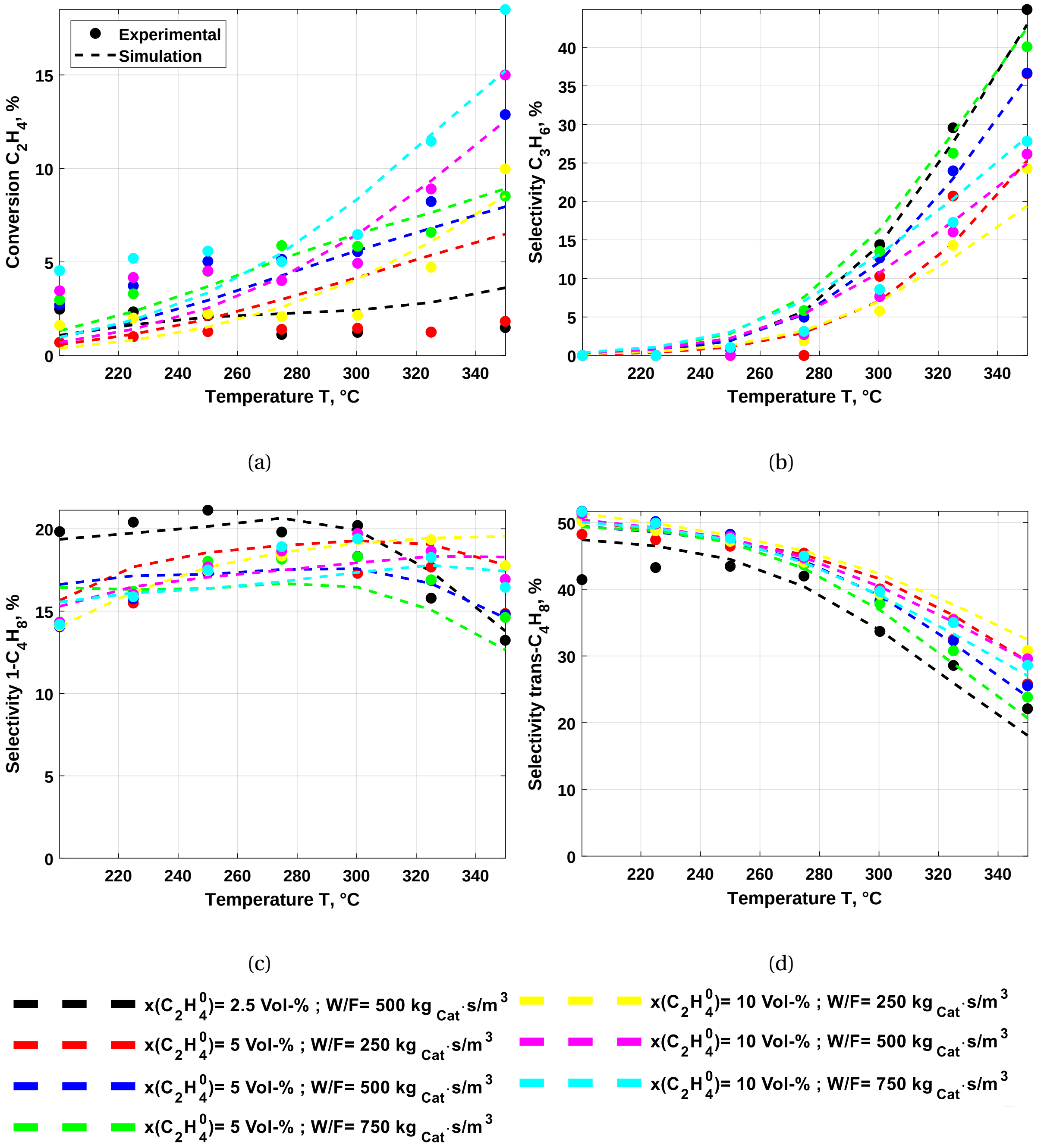

(a)

(b)

(c)

(d)

Figure 6.3: Detailed analysis of simulative results to experimental values for the extended network applying the LHHW.

activity function will be carried out first and then a model approach is used to establish a temporal relationship between the variable conversion and the reaction conditions, residence time and concentration used.

6.2 Kinetics of Deactivation (step 2)

As one of the existing sub-processes of the inherently dynamic operation, kinetic parameters for the deactivation of the aluminized MCM-41 with added nickel for the ETP reaction are now estimated.

Using the deactivation experiments described before (sec. 5.3.3). These are adapted to the activity using a power-law approach (eq. (2.55)) initially. The results for the kinetic estimation are given in Figure 6.4.

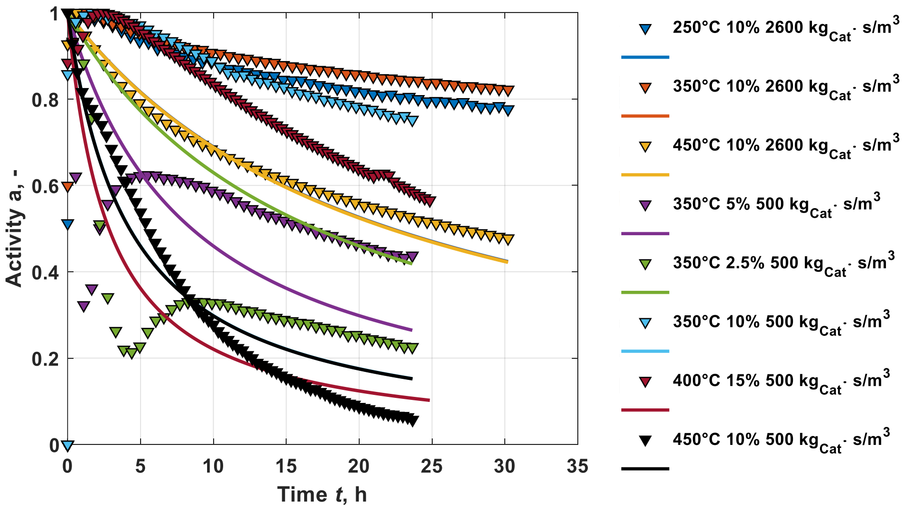

Figure 6.4: Parameter estimation and fitting of the performed deactivation experiments employing a simple exponential deactivation approach (eq. (2.55)).

It is distinct that insufficient fitting is obtained for the adaptation of the kinetic model for the majority of deactivation experiments. This model includes the activity and the input concentration of the reactant, as presented in eq. (2.55). Consequently, the effects obtained from the experiments are not reflected. For example, the experiment with an input concentration of 2.5 % shows an initial substantial decay that cannot be represented. Although the order of the calculated decay in activity is consistent with the applied model (eq. (2.55)), depending on the W/F ratio and the concentration, it almost completely excludes the effect of temperature at this point.

The assumed model for the activity is consistent, but it is known from previous investigations that an increase of the reaction temperature enhances the loss in activity. Further, it appears as if the feed concentration is crucial. Nevertheless, with Figure 5.12 different configurations of carbon form seem to be present at different temperatures, which have a varying influence on the activity decrease of the present system and which cannot be illustrated with the simple model.

Due to the inadequate applicability of the simple use of the temporal course of the activity, an alternative is used in the following to increase the effectiveness of the modeling, with the methodology according to Janssens [Janssens, 2009] applied.

For this, the eq. (2.66) for the change of the ethene conversion is verified. The equation is solved and gives information about the outgoing ethene concentration. For the reaction rate r, different approaches were evaluated and here an LHHW approach showed suitable results, which are presented in Figure 6.5.

This approach shows the significant influence of the reaction temperature on the deactivation process. Since the experiments with high temperatures present the most significant changes in conversion, this is a logical consequence. At the same time, it is a necessary consequence of the Arrhenius approach that the temperature has such a meaning.

The influence of the residence time is now recognizable by the W/F ratio. A reduction of the W/F ratio

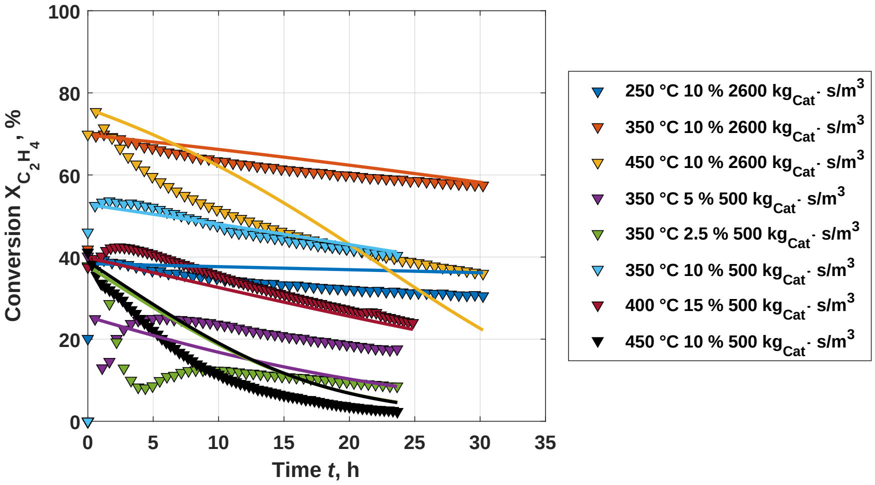

Figure 6.5: Parameter estimation and fitting of the performed deactivation experiments employing the approach by Janssens eq. (2.66).

causes the model to reduce the conversion faster, analogous to the experiment. As explained above, this is due to the fast supply of new reaction material and a lower concentration gradient along the length of the bed.

However, the influence of the input concentration is again of subordinate importance, resulting in no effective changes in the slopes. Thus, with the model approach, which is still easy to handle, the initial dynamics cannot be mapped due to strong deactivation or a necessary initialization of the catalyst. Furthermore, it seems necessary to follow the formation of activated catalyst sites and deactivating species through in-situ analysis. The components involved in the formation of such species cannot be unambiguously defined and, accordingly, the mechanism leading to deactivation is unclear. Thus, the deposition on active catalyst centers, in mono- and poly-layers, as well as the blocking of the pore system, are realistic and conceivable reasons for the obtained results. However, the extent to which each of these effects contributes to deactivation must be included, otherwise, the process of deactivation cannot be validated properly. Based on these new findings, specific models can be adapted which specifically depict intermediate products.

Nevertheless, a simplified model based on the methodology by Janssens [Janssens, 2009] is capable to verify the change in conversion directly. The values of the obtained deactivation kinetics are given below in Table 6.1.

Table 6.1: Deactivation kinetic parameters for the method of Janssens.

Parameter	**Unit**	**Value**
a_0	kg/m^3	$3.724\cdot10^4$
E_D	kJ/mol	47.67
K_1	$1/Pa$	$1.178\cdot10^5$
K_2	$1/Pa$	$6.82\cdot10^5$
σ_1	-	1.058
σ_2	-	1.316

In the next step, it is necessary to model the regeneration as the last sub-process of the inherent cyclic reactor operation.

6.3 Kinetics of Regeneration (step 3)

The use of the experimental data obtained for the estimation of suitable kinetics of regeneration of the Ni/AlMCM-41 (Si/Al = 60) catalyst was used for the direct conversion of ethene to propene (ETP) using two models. For the assumption of a simplified power-law approach (eq. (2.68)) and a hyperbolic model (eq. (2.70)). The optimized parameters are given in Table 6.2.

The comparison of the two models shows that the hyperbolic approach can, in principle, be reduced to the simplified model. In the case of the equilibrium constants for the adsorption of oxygen and carbon, the determined values are close to zero and have a large confidence interval. Furthermore, the newly introduced parameter υ has an equivalent confidence level. In contrast to the orders for oxygen and carbon, with confidence intervals of less than 10 % for the hyperbolic approach and less than 2 % for the power approach, this parameter is not valid. Further, the reaction orders of σ and ψ are similar in their value.

Table 6.2: Kinetic parameters for the regeneration of Ni/AlMCM-41 implying the power-law approach.

Parameter	**Model 1 (eq. (2.68))**		**Model 2 (eq. (2.70))**	
	Value	**KI, %**	**Value**	**KI, %**
$k_{400\,°C}$, $\frac{1}{mg^{\alpha-1}\cdot min}$	0.1062	-	0.0889	-
$k_{450\,°C}$, $\frac{1}{mg^{\alpha-1}\cdot min}$	0.445	-	0.3793	-
$k_{500\,°C}$, $\frac{1}{mg^{\alpha-1}\cdot min}$	1.5667	-	1.3571	-
ξ	0.85	1.38	0.91	7.67
ψ	0.87	1.23	0.88	5.05
υ	-	-	0.38	150160
K_{O_2}	-	-	$3.09{\cdot}10^{-4}$	339810
K_C, $\frac{1}{mg}$	-	-	$4.96{\cdot}10^{-4}$	153680
E_A, $\frac{kJ}{mol}$	133.2	0.59	134.9	0.64
k_∞, $\frac{1}{mg^{\alpha-1}\cdot min}$	$4.4\cdot10^{9}$	14.12	$4.9\cdot10^{9}$	25.44

For comparison, Model 1 (2.68) can be calculated with great certainty. Both oxygen and carbon have a reaction order of equal size with 0.87 and 0.85. Thus, both are significant for the duration of the regeneration process, significantly influencing the kinetics. The quality of the estimation for a set of experiments is given in Figure 6.6 graphically.

The Ni/AlMCM-41 catalyst has a specific kinetic barrier to the activation energy. One reason for this aspect is the large specific surface of the mesoporous catalyst used, with a BET greater than 1000 $\frac{m^2}{g}$. Accordingly, coke can be deposited widely scattered in the pore system and block the pore channels. As a result, these areas are not entirely accessible and may be heavily compressed. This blockage can result in increased necessary energy for the regeneration with 133.2 kJ/mol.

The graphs show that the curves with a constant oxygen concentration of 10 % and varying regeneration temperature (Figure 6.6a) are well represented by the model. In the case of constant regeneration temperature and varying oxygen concentration in the system (Figure 6.6b), this can be fundamentally confirmed if there is a sufficient oxygen concentration for regeneration available. In the case of regeneration with 5 % oxygen in nitrogen, the fitting is slightly different, since the slope of the simulative result is smaller and the flattening of the experimental curve begins earlier. Nevertheless, it can be

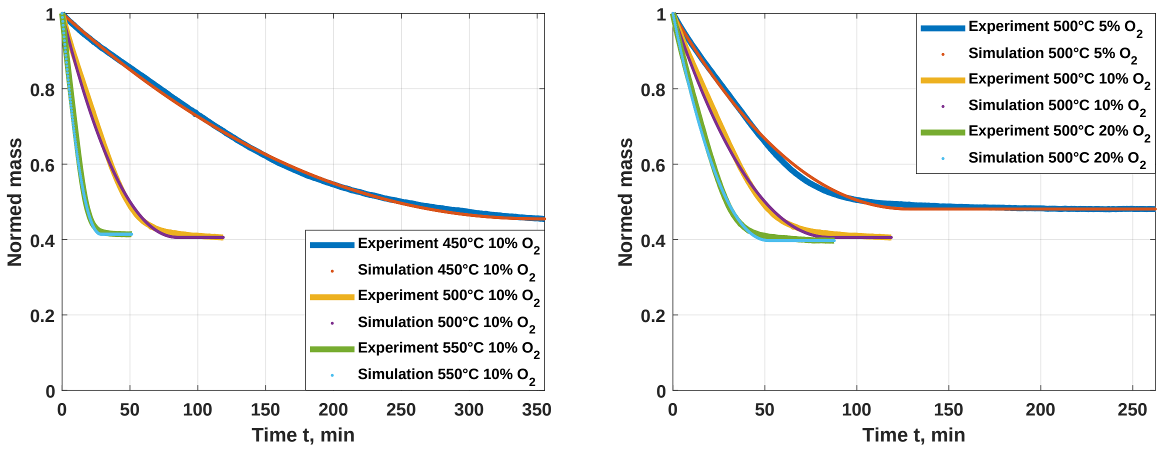

(a) (b)

Figure 6.6: Experimental and predicted results of the regenerative results for model 1 (eq. (2.68)) of (a) varying temperature and (b) varying oxygen concentration.

stated that these results can also be represented satisfactorily. Possibly, an extension of the coke removal concerning two model ranges is expedient at this point. Thereby, an outer coke layer and the amount of coke in it have to be considered with separate kinetics.

6.4 Conclusion

For the heterogeneously catalyzed synthesis of propene from ethene feedstock on a Ni/AlMCM-41 catalyst, kinetic models for the individual process steps of reaction (step 1), deactivation (step 2) and regeneration (step 3) were evaluated and the necessary parameters were estimated.
The following findings based on kinetic modeling can be summarized:

(a) Suitable computational results were achieved for the reaction kinetics applying Langmuir-Hinshelwood-Hougen-Watson in combination with the catalytic cracking network.

(b) Kinetics for the deactivation and regeneration were evaluated using reduced model approaches based on the obtained data from longtime experiments and thermogravimetric analysis (TGA).

The necessary effort required for a quantitative statement for the deactivation and regeneration process steps exceeded the scope of this work, due to the complexity of the overall network with more than 20 reactions occurring simultaneously. Consequently, a methodology for decoupling the reaction network was developed focusing on the reactor level rather than the catalyst level (appendix A.4). It can be concluded that the individual steps of an inevitably dynamic reactor operation must be well understood to enhance the overall process. It is obviously desired to minimize deactivation as far as possible to have long production phases at suitable rates. The regeneration should be as fast as possible, to reduce the length of the phase without production. The resulting switch events cause inlet operating parameters to behave as rectangular functions. Their specification offers possibilities for optimization.

Changing the topic, in the next section a quantitative evaluation of the forced dynamic reactor operation mode using the NFR method is presented (Part III). This powerful and flexible approach predicts the outcome of periodic operation and allows determining optimal parameters for enhanced operation.

Part III

Forced Dynamic Reactor Operation

Preface to Part III

> *We tell people to follow their dreams, but you can only dream of what you can imagine, and, depending on where you come from, your imagination can be quite limited.*
>
> —Trevor Noah

The present part focuses on the validation of forced dynamic operation, Necessarily, the kinetic modeling of the hydrolysis of acetic anhydride (chapter 7) with the derived kinetic parameters is presented. As described initially, the performance of single and simultaneous forced dynamic operation based on predictions by the nonlinear frequency response (NFR) method is analyzed (chapter 8). Parts of the results have been published previously:

1. D. Nikolic, M. Felischak, A. Seidel-Morgenstern, M. Petkovska, *Periodic Operation with Modulation of Inlet Concentration and Flow Rate: Part II. Adiabatic Continuous Stirred-Tank Reactor*, Chemical Engineering & Technology, 39 (2016) 2126-2134, DOI: 10.1002/ceat.201600187. [Nikolić et al., 2016a]
2. M. Felischak, L. Kaps, C. Hamel, D. Nikolic, M. Petkovska, A. Seidel-Morgenstern, *Analysis and experimental demonstration of forced periodic operation of an adiabatic stirred tank reactor: Simultaneous modulation of inlet concentration and total flow-rate*, Chemical Engineering Journal, 410 (2021) 128197, DOI: 10.1016/j.cej.2020.128197. [Felischak et al., 2021]

The author of this thesis contributed to the results presented in these papers. For the first publication, the author provided the kinetic and thermodynamic data, as well as the boundary conditions for the reactive system. In the second publication, the author realized and evaluated the experimental setup for the single and simultaneous modulation of multiple inlet parameters. Based on predicted periodic outputs desirable dynamic parameters were chosen for experimental validation. These experiments were performed and the obtained results were compared to the theoretical values.

In the present thesis, the developed and installed experimental setup for the implementation of the forced dynamic mode of operation is described. After the evaluation of the system, stationary experiments are carried out to re-evaluate the existing kinetic models. The NFR methodology is applied to the hydrolysis of acetic anhydride in an adiabatic CSTR and the corresponding analytical solutions are derived by the collaborators of the group of Prof. Petkovska at the University of Belgrade. Predictions for single and multiple dynamic input parameter variations are obtained and interesting operational regimes for beneficial systemic behavior are determined.

Kinetic parameters face uncertainties on grounds of imperfect experimental data and optimization approaches. Hence, varying kinetic parameters are implemented and the resulting dynamic changes are compared. Afterward, the mentioned forced periodic operations are presented.

7 Kinetics of the Hydrolysis of Acetic Anhydride

As described in section 3.2, the hydrolysis of acetic anhydride is an interesting reaction to evaluate new methodologies. Accordingly, this reaction is used for the forced dynamic operation. It has already been demonstrated that various measurement methods are available for the analysis of the reaction. Conductivity measurement is used as the analytic. Thus, it is possible to represent the temporal changes in the system. First, the experimental setup will be explained and second, the procedure for kinetic model derivation is illustrated.

7.1 Experimental Setup and Procedure

For the evaluation of the hydrolysis of acetic anhydride, a setup was designed and build. The setup was thought of to perform reliable kinetic experiments and implement single and multiple periodic input parameter modulations accordingly. The experimental equipment consists of a multi-channel peristaltic pump for the water inlet stream (Heidolph Hei-Flow Precision), a gear pump for acetic anhydride (ISMATEC BVP-Z), two thermostats controlling the inlet temperature (Huber CC-308 and CC-K12), a multi-port gas chromatography (GC) valve (VICI Valco 4 position flow-through), a custom-made double-jacked glass vessel (Witeg Labortechnik) and an arbitrary function generator (Rigol DG-1032z). The measurement is performed in-operando using a conductivity meter (Ahlborn Almemo 2490-1). The reactor volume is kept constant, using a hydrostatic overflow. The setup is schematically illustrated in a simplified form in Figure 7.1 and presented in operation in Figure 7.2. A detailed schematic drawing of the setup is displayed in the Appendix (Figure B.2).

The system is designed to fluctuate a variety of parameters, such as inlet concentration, total volumetric flow and inlet temperature. These can be implemented as a single modulation or as combinations of multiple parameters, simultaneously. In this work, the focus is on the experimental validation of simultaneous inlet concentration and volumetric flow modulation. Besides, influences of two Temperature levels, differing from room temperature, with the help of the six-way valve from VICI Valco (Type: 4 position flow-through selectors - 1/4 inch fittings) is possible.

The two reactants are pumped from separate storage tanks into the double-jacked glass reactor. The pump of the acetic anhydride is an electrically controlled gear pump from Ismatec (type: BVP-Z), which provides the necessary precision, even for small volumetric flows. Distilled water is pumped by a Heidolph multi-channel hose pump (type: Hei-Flow). This pump is also electrically controlled and provides the required volumetric flow for the reactor operation precisely.

The material flows are a prerequisite for both pumps operated with the help of the function generator by Rigol (type: DG-1032z). Therefore, both pumps are accurately calibrated initially. The whole process was automated using Siemens Simatec S7 and MATLAB. For initiation and data collection by the

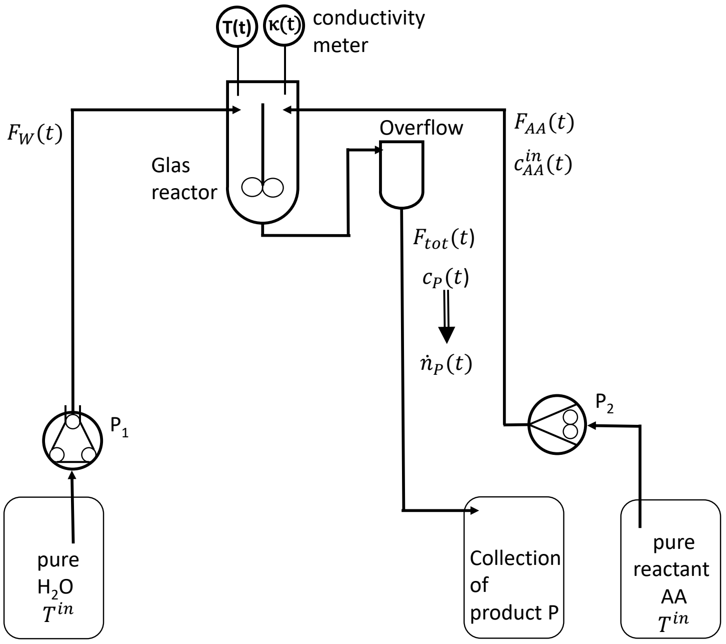

Figure 7.1: Flow sheet of the realized experimental setup for forced dynamic parameter perturbation.

individual units, Siemens control software was used. MATLAB generated the functions for the individual input modulations that were implemented into the reaction system. Such implementation is realized by the conversion of the desired parameter variation into voltage as functions of bytes. The function generator has two separate voltage outlets that can be controlled individually and allow for precise setting of periodic parameters, like frequency, amplitude and phase difference. An oscilloscope was used to check the implemented function.

Huber thermostats (type: CC-308 and CC-K12) are available for temperature control of the material flows, which can be controlled by employing a thermocouple. The measurement was performed right before the reactant enters the reactor. Accordingly, the heating and cooling are controlled for exact inlet parameters. A variation of the input temperature is realized by the use of a further thermostat.

The glass reactor (CSTR) by Witeg (maximum reaction volume 400 mL) is a double-jacket configuration. For mixing, a stirring fish is used, which is brought into motion by a magnetic stirring plate of the company IKA (type: RCT Basic). The outlet of the reactor is configured as a hydrostatic overflow, which results in a constant reaction volume.

All measurement data and parameters are recorded using a digital control and measurement system. The temperatures of the input stream of water and the internal temperature of the reactor can be measured. Also, a conductivity probe from Ahlborn (type: Almeo 2490-1) in the reactor offers a fast indirect recording of the product concentration via conductivity.

The storage tanks are refilled with the respective chemicals for each experiment. With this, preexisting reactions of acetic anhydride with humid air is avoided. The acetic anhydride by the company Grüssing with a purity of 99 % is used. Deionized water is taken from the in-house filter system.

A conductivity probe is used to determine the basic conductivity κ. Between two graphite electrodes, a high-frequency electromagnetic field is generated, which measures the conductivity with the help of free charge carriers in the liquid. The definition of conductivity is the reciprocal of electrical resistance, depending on the surface and distance of both graphite electrodes. To have measurements independent of the probe, a specific conductivity is introduced, which indicates the conductivity of standardized surfaces to a standardized distance. The typical unit of specific conductivity in mS/cm.

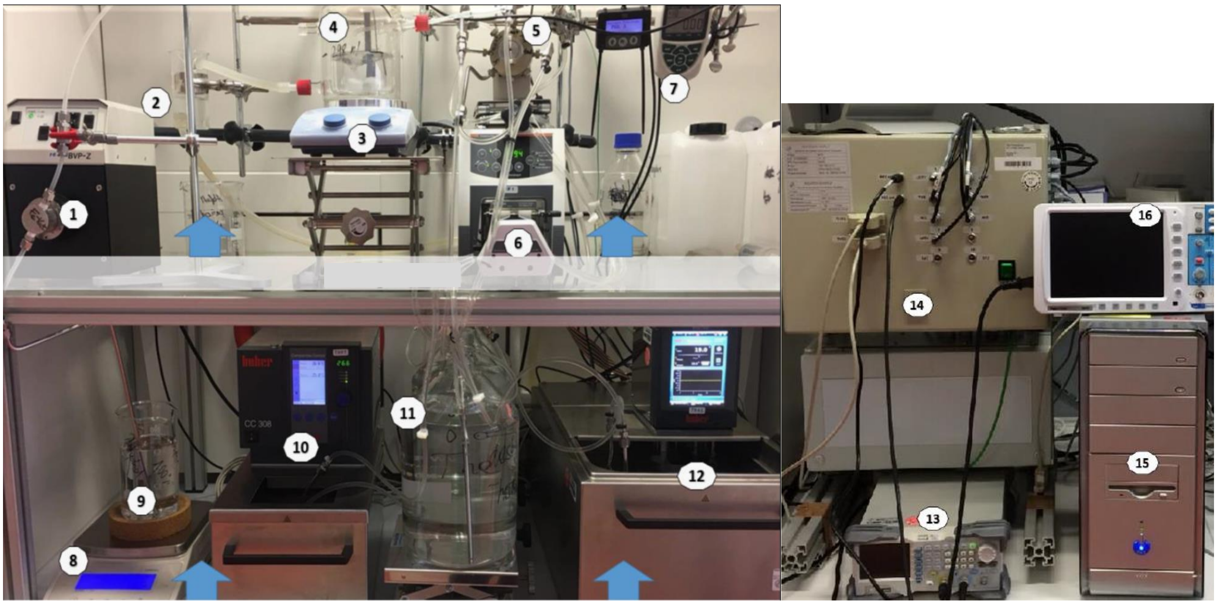

Figure 7.2: Experimental Setup for the implementation of forced dynamic reactor operation for the hydrolysis of acetic anhydride.

1. Gear pump
2. Overflow vessel
3. Stirring plate
4. Double-jacked glass reactor
5. GC valve
6. Multi-channel peristaltic pump
7. Conductivity meter
8. Scale
9. Acetic anhydride tank
10. Cooling thermostat
11. Water tank
12. Heating thermostat
13. Arbitrary function generator
14. Electrical cabinet for Siemens SPS
15. PC
16. Oscilloscope

Aging processes of the conductivity probe are unavoidable due to the concentrations obtained during the experimental procedure. Therefore, it is recommended to determine the cell constant before each experiment to prevent influences on the results. The cell constant is determined by measuring the conductivity of a calibrated standard solution supplied by the manufacturer. Thus, the measured conductivities are to be converted into a specific conductivity κ and the effects of aging are to be compensated.

Acetic acid does not follow a linear dependence between concentration and conductivity so that a model is required for calibration. Due to the fast and straightforward recording of conductivity and temperature, an extensive data set with different temperatures and concentrations can be generated. This data set is used to provide an accurate calibration with "machine learning". MATLAB's regression learner was used, with the Gaussian Process Regression model suggesting to be the most accurate for the problem at hand. This fitting is based on an interpolation of multidimensional Gaussian distributions.

7.2 Experimentally Obtained Kinetic Data

Therefore, the general mass and energy balance have to be implemented and analyzed to represent the chemical system mathematically. Below the two mentioned and applied balances are given, eq. (7.1) and eq. (7.2), based on the eqs. (2.22) and (2.24) for the adiabatic CSTR.

$$V_R \frac{dc_{AA}}{dt} = F\left(c_{AA}^0 - c_{AA}\right) - V_R \cdot r \tag{7.1}$$

$$V_R \overline{\rho c_P} \frac{dT}{dt} = F(t)\overline{\rho c_P}\left(T_i(t) - T\right) + \left(-\Delta_R H\right) V_R \cdot r \tag{7.2}$$

Both equations (eqs. (7.1) and (7.2)) are coupled via the reaction rate r. The reaction rate is in this case generally described using a simple power-law approach, presented in the section below (sec. 7.3). Within this equation, the k(T) is calculated using the Arrhenius equation (eq. (2.38)).

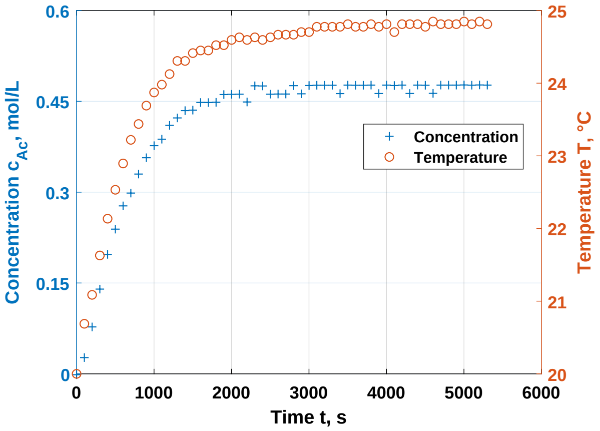

Figure 7.3: Example reaction under constant feed conditions for an adiabatic CSTR approaching steady-state, with 0.74 $\frac{mol}{l}$ of concentration, a flow rate of 43 $\frac{ml}{min}$ and an inlet temperature of 20 °C.

Based on previous kinetic investigations by others, Table 7.1 lists the resulting collision factors and activation energies in combination with the concentration ranges and measurement methods. A first-order reaction is assumed in most of the shown cases. The data indicates that a wide range of concentrations has been investigated, but most publications were conducted for a constant concentration.

For the estimation of kinetic parameters, it is necessary to have a broad database within the experimental boundaries, for accurate parameters. Therefore, the initial conditions are given in Table 7.2 were covered during the experiments. Based on the wide concentration and temperature range, it is possible to include the adiabatic behavior of the CSTR and thus, estimate reliable parameters.

Table 7.1: Kinetic Data for the Hydrolysis of acetic anhydride from literature.

Reference	**Analytic Method**	**Initial Conc.,** $\frac{mol}{l}$	E_A, $\frac{kJ}{mol}$	**ln(k_∞)**	**Unit**
[Wilsdon and Sidgwick, 1913]	Conductivity	0.34	50.6	18.52	1/s
[Wilsdon and Sidgwick, 1913]	Conductivity	1.1	56.2	20.45	1/s
[Gold, 1948]	Conductivity	0.0001 - 0.00035	47.45	5.75	1/s
[Cleland and Wilhelm, 1956]	Titration	0.02 - 0.06	44.4	16.05	1/s
[Janssen et al., 1957]	Caliometry	1.24 - 2.59	57.53	3.85	1/s
[Dyne et al., 1967]	Caliometry	0.17	48.89	17.7	1/s
[Takashima et al., 1971]	Caliometry	0.25	66.76	7.77	1/s
[Glasser and Williams, 1971]	Caliometry	0.25	45.19	16.04	1/s
[Bisio and Kabel, 1985]	Caliometry	0.22	46.5	12.8	1/s
[Haldar and Phaneswara Rao, 1991]	Caliometry	0.002 - 0.007	93.47	44.36	1/s
[Shatynski and Hanesian, 1993]	Caliometry	0.27	46.86	12.74	$\frac{l}{g \cdot mol \cdot s}$
[Asprey et al., 1996]	Conductivity	1	45.61	7.66	$\frac{l}{g \cdot mol \cdot s}$
[Haji and Erkey, 2005]	FTIR	0.85 - 2.12	53.41	19.58	1/s
[Kralj, 2007]	Conductivity	0.41	50.1	18.31	1/s
[Hirota et al., 2010]	Caliometry	4	67.23	15.56	1/s
[Asiedu et al., 2013]	Caliometry	1	50.57	16.56	1/s
[Fritzler et al., 2014]	Caliometry	0.02 - 10.1	52.89	6.72	$\frac{m^3}{kg \cdot mol \cdot s}$

For the parametrization of mathematical reaction kinetics models based on the power-law approach, a sufficiently large data set is necessary. Though, because of the aging of the measuring probe, only a limited number of experiments is possible. Nevertheless, the experiments are validated among each other.

Table 7.2: List of kinetic experiments performed for parameter estimation for the Hydrolysis of acetic anhydride.

c, mol/l **T, °C**	**0.1**	**0.5**	**0.74**	**0.85**	**1.2**
10	1	-	2	-	3
20	4	5	6	7	8
25	9	10	11	12	13
35	14	-	15	-	16

Each experiment has a duration of 90 minutes to ensure that the stationary behavior of the CSTR used is achieved. Figure 7.4a presents the experimental results of the kinetic experiments. Concentration and temperature show no changes toward the end of the experiment. This provides proof that steady-state behavior is reached.

Comparison of the experiments with each other shows that the concentration and temperature profiles proceed as expected. For the same input concentrations, the concentration of product increases with increasing temperature. Moreover, an increase in the concentration profile at constant temperatures and increasing inlet concentration can be seen. These findings indicate that the assumption of a power-law approach is valid. Figure 7.4 shows these processes at a constant inlet temperature (left) and a constant concentration (right).

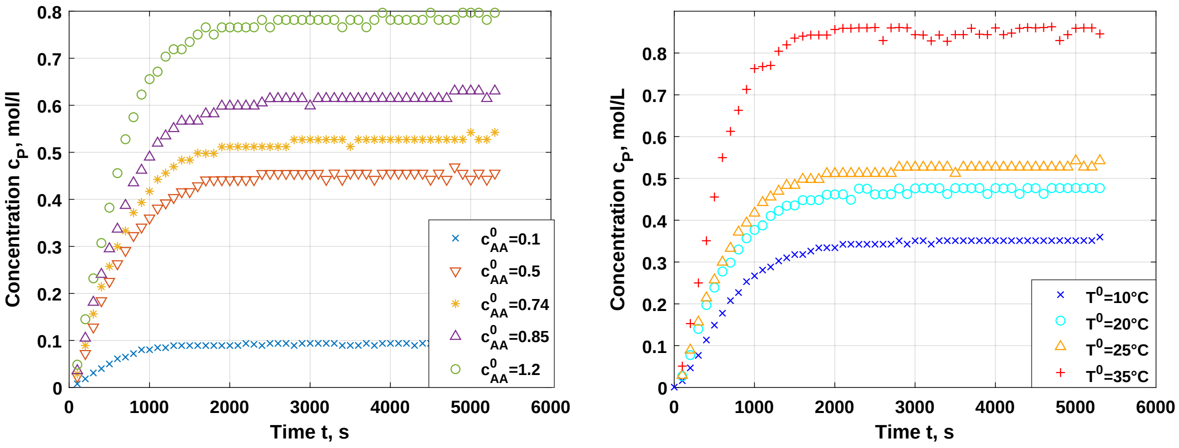

(a) (b)

Figure 7.4: Kinetic experiments approaching steady-state for the hydrolysis of acetic anhydride for (a) constant inlet temperature of 22 °C and varying inlet concentration; (b) constant inlet concentration of 0.74 $\frac{mol}{l}$ and varying inlet temperature.

Kinetic parameters are determined based on these experimental data points in the latter part of this present chapter. Besides, further information can be obtained from the measured values, as described below in an evaluation of the adiabatic process control.

The concentrations are to be converted into conversions according to eq. (2.12). The temporal course is recorded along a trajectory for varying inlet temperature. At the end of this trajectory, temperature and conversion are in steady-state (Figure 7.5). The variation of the input concentration at the same inlet temperatures in the stationary state shows a linear dependency. This allows for the assumption of adiabatic reactor behavior.

Based on the obtained and valid experimental data, kinetic models can now be evaluated and kinetic parameters estimated.

7.3 Kinetic Model Derivation

For each experiment, as initial values of the differential equations, the concentration of reactant A in the reactor is considered to be zero, because initially the reactor does not contain any acetic anhydride nor acetic acid. The temperature is the value of the inlet temperature of the water. The inlet concentration and the inlet temperature are assigned to the corresponding value from Table 7.2. The time vector for solving the differential equations (eqs. (2.22) and (2.23)) depends on the duration of the experiment and is solved up to 80 % of the time needed for obtaining the steady-state $t_{0.8SS;i}$. The reason for this is the importance of the initial kinetic range. The initial rates of concentration changes are highly relevant for the kinetic modeling, due to the high information density considerable for op-

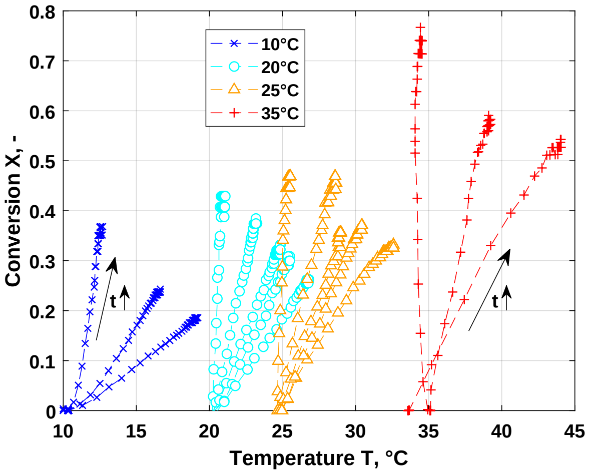

Figure 7.5: Conversion of acetic anhydride as function of temperature for the set of performed kinetic approaching steady-state experiments with varying feed concentration and inlet temperature.

timization. Therefore, this range is defined as 80 % of the maximum value of the adapted parameters in steady-state. Besides, the stationary value is of interest as well. But not the course reaching this point, because of the minor changes occurring.

For the calculation of the steady-state behavior, the differential equations (eqs. (7.1) and (7.2)) are calculated by minimization of the objective function (eq. (7.10)), employing the lsqnonlin solver. The initial kinetic values result from the final value of the previous solution of the differential equation.

To evaluate the objective function fmincon is used, whose response is minimized. A criterion for this heuristic is the compliance of boundary conditions. Thus, it is ensured that the results are within the physical limits and impracticable values are systematically excluded. However, fmincon converges only to local minima and hence is extended by multistart. Initial values are required for this global minimizer, from which internal algorithms define further initial values for an improved solution by fmincon.

The experiments are carried out in an adiabatic CSTR, the heat of reaction can be exploited as an additional source of information. The adiabatic behavior of the reactor setup used could be demonstrated in advance in section 7.2, so that the temperature can be used validly as an additional parameter in the objective function.

The following kinetic models are evaluated based on the power-law approach. These include the typical reaction system assuming a reaction order of one (eq. (7.3)), a variable order u (eq. (7.4)) and a model that additionally implements the concentration of water with a specific reaction order v (eq. (7.5)).

Model 1:

$$r = k_\infty \cdot exp\left(-\frac{E_A}{R \cdot T}\right) \cdot c_{AA} \tag{7.3}$$

Model 2:

$$r = k_\infty \cdot exp\left(-\frac{E_A}{R \cdot T}\right) \cdot c_{AA}^u \tag{7.4}$$

Model 3:

$$r = k_{\infty} \cdot exp\left(-\frac{E_A}{R \cdot T}\right) \cdot c_{AA}^{u} \cdot c_{W}^{v} \tag{7.5}$$

The steady-state value of the theoretical concentration $c_{P,ss,i}^{sim}$ and temperature $T_{ss,i}^{sim}$ are determined numerically by solving eqs. (2.22) and (2.24), while excluding the terms of the accumulation. For this purpose, the solution algorithm lsqnonlin used.

Adjusting steady-states of different values, for equal evaluation, the differences between experimental and simulated concentrations and temperatures are normalized to the respective mean steady-state point (eqs. (7.6) and (7.7)). The squaring of the values avoids that negative and positive differences balance each other out and thus, inappropriate adjustments are made.

$$\Delta \overline{c}_{P,ss} = \left(\frac{\overline{c}_{P,ss}^{exp} - \overline{c}_{P,ss}^{sim}}{\overline{c}_{P,ss}^{exp}}\right)^2 \tag{7.6}$$

$$\Delta \overline{T}_{ss} = \left(\frac{\overline{T}_{ss}^{exp} - \overline{T}_{ss}^{sim}}{\overline{T}_{ss}^{exp}}\right)^2 \tag{7.7}$$

The difference between the theoretical and experimental values of the range in approaching steady-state is determined analogously to the stationary state. The difference accumulated over the dynamic time range (eqs. (7.8) and (7.9)) is considered. By the normalization, the variable values are adapted in the same measure and represented equally, as the stationary results lying on a higher level.

$$\Delta \overline{c}_{P}^{dyn} = \sum_{t}^{t_{0.8 \cdot ss}} \left(\frac{\overline{c}_{P}^{exp}(t) - \overline{c}_{P}^{sim}(t, \vec{x})}{\overline{c}_{P}^{exp}(t)}\right)^2 \tag{7.8}$$

$$\Delta \overline{T}^{dyn} = \sum_{t}^{t_{0.8 \cdot SS}} \left(\frac{\overline{T}_{SS}^{exp}(t) - \overline{T}_{ss}^{sim}(t, \vec{x})}{\overline{T}_{ss}^{exp}(t)}\right)^2 \tag{7.9}$$

These expressions result in the following objective function (eq. (7.10)). The result of the objective functions describes a summed distance between theory and experiment, which is minimized accordingly.

$$min(OF) = min\left[\sum_{j} \Delta c_{P,j}^{dyn} + \Delta T_{j}^{dyn} + \Delta \overline{c}_{P,ss,j} + \Delta \overline{T}_{ss,j}\right] \tag{7.10}$$

The derived objective function and the established evaluation parameters, as well as the assumed kinetic models with the adjustable variables, are available to represent the kinetic experiments adequately.

7.4 Parameter Estimation

The presented reaction models (eqs. (7.3) to (7.5)) can be parametrized for the objective function explained in the previous section and the calculation of the individual parameters for optimization of the CSTR.

Figure 7.6 illustrates the parity plots for model 1 (eq. (7.3)). The theoretically calculated concentration of acetic acid against the experimentally obtained value is shown in Figure 7.6a. The range of ±20 % shows that especially the small concentrations are below this limit and, therefore, underestimated. For most of the data points, the concentrations are underestimated, while the steady-state points are within or slightly beyond the upper boundary, for the kinetic model with a reaction order of one. Nevertheless, the majority of stationary points can be found within the deviation.

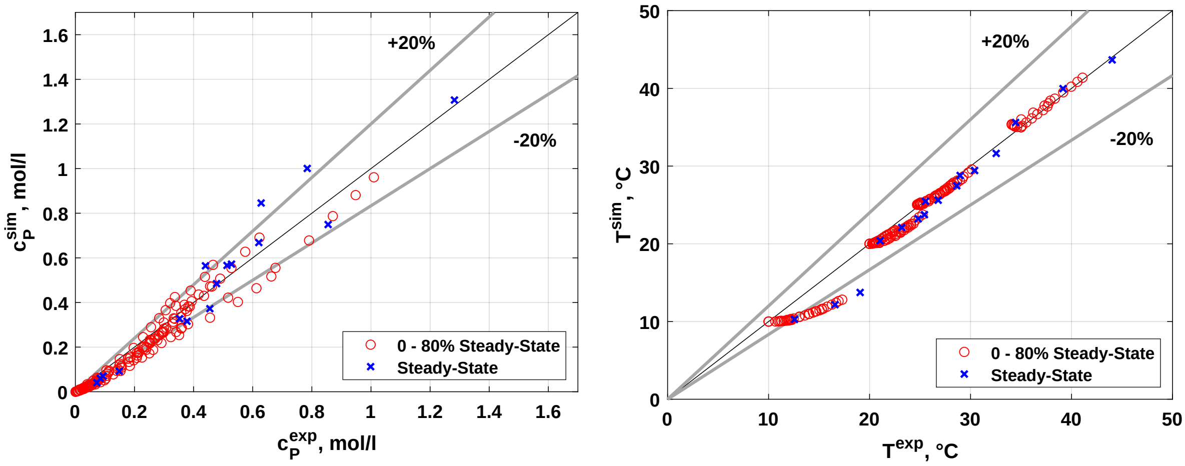

(a)

(b)

Figure 7.6: Parity plots of (a) concentration and (b) temperature employing kinetic model 1 (eq. (7.3)).

Figure 7.6b presents the theoretical temperature against the experimentally determined reactor temperature. Except for the experiments at an input temperature of 10 °C, all the measured experimental points are within the range of 20 %. The temperature is, therefore, more accurately represented by the model than is the case in comparison to the product concentration. In the case of 10 °C, both the measured points and the stationary values are underestimated. This result indicates that other effects seem to occur, like changes in the physical properties.

Next, model 2 (eq. (7.4)) introduces the reaction order for acetic anhydride as an additional fitting parameter. In Figure 7.7, an improvement can be seen for the concentration of the product in comparison to the first model. All stationary operating points within the defined interval are in good agreement. Furthermore, the measuring points in the transient range are found entirely within the chosen tolerances. Correspondingly, the course towards steady-state behavior is well represented by the adaptation of the reaction order.

With this model, the reactor temperature can be represented sufficiently well, shown in Figure 7.7b. Even the stationary points are located close to the main diagonal. Again, the inlet temperature of 10 °C is insufficiently described. This effect supports the assumption of property changes in the chemical system at different temperatures. The representation of the temperature is similarly accurate as the first model, but it represents the concentration better.

For the last and most complex model considered (eq. (7.5)), the concentration of water is included with a variable reaction order as a fitting parameter. However, both the concentration curve (Figure 7.8a) and the measured reactor temperature (Figure 7.8b) show a broader scattering in their respective parity diagram. In the lower concentration range (up to 0.4 mol/l) more downward outliers occur, but the higher concentration points are in good agreement.

For the temperature in the reactor, the picture is hardly changed to the previous cases. Only the

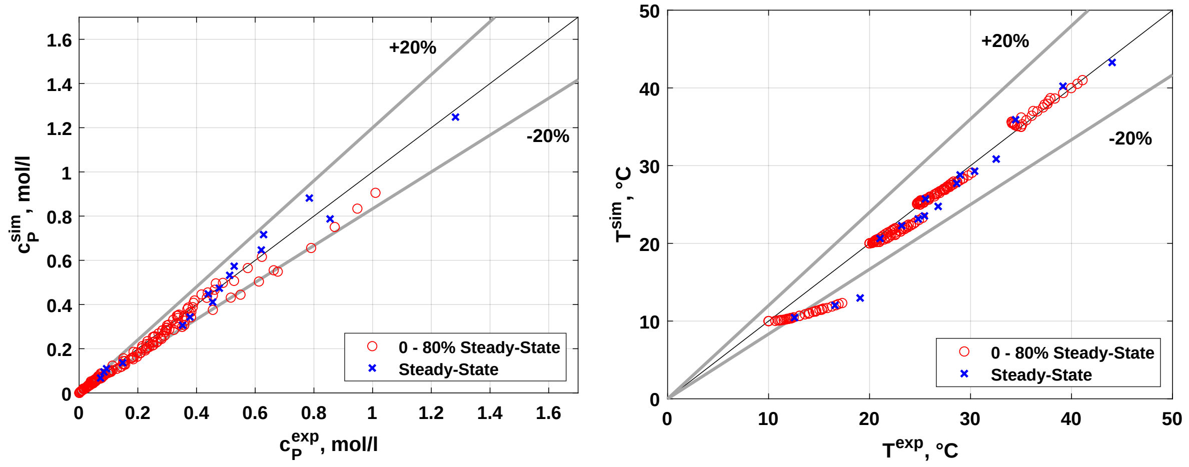

(a) (b)

Figure 7.7: Parity plots of (a) concentration and (b) temperature employing kinetic model 2 (eq. (7.4)).

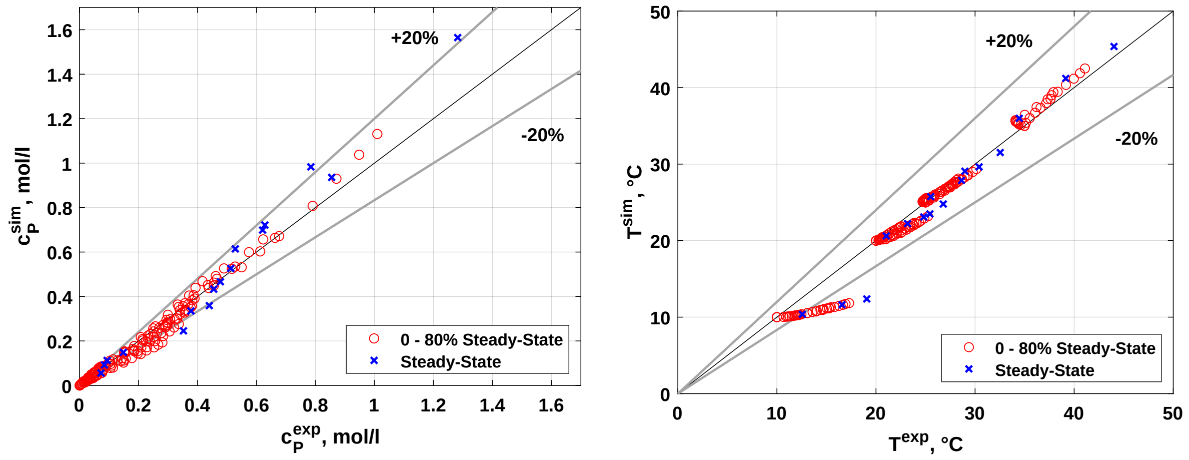

(a) (b)

Figure 7.8: Parity plots of (a) concentration and (b) temperature employing kinetic model 3 (eq. (7.5)).

lowest temperatures seem to be somewhat underestimated, analogous to the obtained values at the highest temperatures in the stationary course. The reason for this seems to be the low reaction order of water, which reduces the influence of the parameter. This means that the influence of the water concentration can in principle be removed from the reaction rate and thus reduces the approach to model 2. The specific kinetic parameters are shown in the following Table 7.3.

Model 1 and 2 have similar values of the collision factor k_∞ and the activation energy E_A. But model 3 is far off, because of the low value of the reaction order ν. Though, it can be concluded that the obtained derivation is based on a local minimum. Therefore, it is believed that the global optimum is not obtained. Nevertheless, this model was not further enhanced, because the first results indicated that a reduction of model 3 to the assumptions of model 2 is sufficient. Model 3 is over-parametrized because water is always in excess and a biphasic system was not observed. For the optimization of the forced periodic operation, the second model is considered.

Table 7.3: Estimated kinetic parameters for the applied kinetic model approaches for the hydrolysis of acetic anhydride.

Model	**ln(k_∞)**	E_A, $\frac{kJ}{mol}$	**u**	**v**
1 (eq. (7.3))	$1.31 \cdot 10^3$	34.32	1[I]	-
2 (eq. (7.4))	904	34.06	0.66	-
3[II](eq. (7.5))	$1.73 \cdot 10^5$	47.06	0.65	$8.35 \cdot 10^{-5}$

[I] Fixed value
[II] Convergence issues

7.5 Conclusion

Preliminary steady-state experiments were carried out and analyzed to evaluate kinetic models for the hydrolysis of acetic anhydride. For this, an adiabatically operated continuously stirred tank reactor (CSTR) was used. The following conclusions can be drawn:

(a) The transient coupled material and energy balance were successfully used for estimating kinetic parameters.

(b) Assuming water to be in excess a reduced power-law approach with a reaction order with respect to anhydride of 0.66was found to be suitable.

(c) Experimentally determined temperatures differed more significantly than the concentration from the theoretical values, indicating slight deviation from adiabatic behavior.

The obtained kinetic parameters are available for predicting output variables by forced periodic operation using nonlinear frequency response (NFR). This will be subject of the next chapter.

8 Analysis and Demonstration of Forced Periodic Operation

8.1 Nonlinear Frequency Response

The presence of dynamic behavior requires the necessity to predict the output behavior of the system, essentially. A possibility is the nonlinear frequency response (NFR) method. This approach will be explained below for the modulation of single and multiple input parameter modulations, based on the models derived by the co-operation partner at the University of Belgrade [Nikolic Paunic, 2016].
As previously mentioned, the forced periodic operation is based on the modulation of input parameters around a steady-state. The implementation of periodically changing the input parameter x will result in a fluctuation of the corresponding output variable y, shown in Figure 8.1. Additionally, another input z could be varied with corresponding forcing parameters (amplitude, frequency and phase shift).

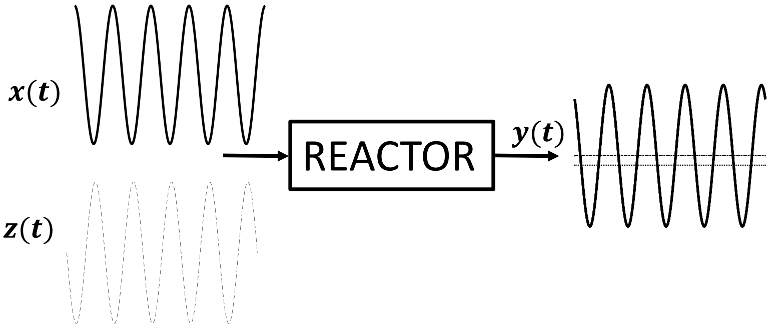

Figure 8.1: Schematic illustration of input modulations and the resulting output function.

Prediction of dynamic behavior is essential because processes can be difficult to start-up and maintain. Therefore, reaction conditions have to be chosen appropriately. The NFR method aims to predict the achievable time-average of the periodic operation modes for single and simultaneous modulation of dynamic parameters. Either the desired product or the reactant can be evaluated. They differ in the definition of beneficial reactor operation. For the product, the change (Δ_P) should be greater than zero, meaning that the time-average at the outlet is higher compared to its steady-state. Vice versa, the reactant outlet concentration must be lower to have a higher conversion, resulting in an adverse change (Δ_A).
This predictive method has been applied for different chemical systems, e.q. adsorption [Ilić et al., 2007a; Ilić et al., 2007b; Ilić et al., 2007c; Ilić et al., 2009], Sabatier reactor [Currie et al., 2018] and hydrolysis of acetic anhydride [Nikolić et al., 2014a; Nikolić et al., 2014b; Nikolić et al., 2016a; Nikolić

et al., 2016b; Petkovska et al., 2018]. A detailed derivation of the here presented functions is given in the thesis of Daliborka Nikolic [Nikolic Paunic, 2016].

For the implementation of forced dynamics, an inlet parameter x is modulated around a previously established stable steady-state. The fluctuation with a specific frequency ω and an amplitude A_x will result in a change of the output y(t). This signal is dependent on the transfer function of the systems, as shown in eq. 8.1.

$$x(t) = x_S + A_x \cdot cos(\omega t) \xrightarrow{t \to \infty} y(t) = y_S + \sum_{n=1}^{\infty} y_n(t) \tag{8.1}$$

The nonlinear frequency response method is based on the Volterra series [Volterra, 2005]. This type of series expansion, shown in eq. (8.2), for the harmonic output functions of different orders, consists of the Volterra kernels g_n and memory terms $x(t-\tau_n)$.

$$y_n(t) = \int_{-\infty}^{\infty} ... \int_{-\infty}^{\infty} g_n(\tau_1, ..., \tau_n) x(t-\tau_1)...x(t-\tau_n) d\tau_1 ... d\tau_n \tag{8.2}$$

These kernels include linear models of different orders and contain the necessary information, such as the reactor model, applied kinetics and process parameters. When applying multidimensional Fourier transformation [Weiner and Spina, 1980] the output functions are transferred to a periodic array. The resulting frequency response functions (FRF) are obtained (eq. (8.3)), which correspond to the transfer functions of the input variables to the output.

$$G_n(\omega_1, ..., \omega_n) = \int_{-\infty}^{\infty} ... \int_{-\infty}^{\infty} g_n(\tau_1, ..., \tau_n) e^{j(\omega_1\tau_1 + ...\omega_n\tau_n)} d\tau_1 ... d\tau_n \tag{8.3}$$

In this way, the nonlinear model G of a weakly nonlinear system with polynomial nonlinearities can be replaced by an infinite sequence of frequency response function (FRF) of different orders. These are directly related to the nonperiodic contribution, the DC component and different harmonics of the response [Weiner and Spina, 1980], as presented below.

The FRF of the n-th order is used to derive the output contributions using transfer functions connected to the reactor.

$$y_n(t) = \sum_{i=0}^{n} \frac{n!}{i!(n-i)!} G_n(\underbrace{\omega, ..., \omega}_{n-i} \underbrace{-\omega, ..., -\omega}_{i}) \cdot \left(\frac{A}{2}\right)^n e^{j(n-2i)\pi t} \tag{8.4}$$

The overall procedure of the NFR method can be summarized in the following steps [Petkovska and Seidel-Morgenstern, 2013].

1. Postulate nonlinear model of the (reactive) system
2. Check system stability (method applicable only for stable systems)
3. Define the modulated inputs and the outputs of interest
4. Derive with the standard procedure the needed FRFs (only the first and asymmetrical second-order functions needed)
5. Analyze signs of the FRFs (can change with frequency)
6. Calculate approximate relevant time-average of the output(s)

Based on this procedure, the method will be applied in the following for single and simultaneous modulation of input parameters.

8.1.1 Single Input Modulation using NFR

For the single input parameter modulation, the frequency response functions have to be calculated as described earlier. By collecting the terms of the same frequency, it can be shown that the response of a weakly nonlinear system to a single harmonics input is obtained as a sum of the basic harmonic, which have the same frequency as the input, a nonperiodic DC term and an infinite number of higher harmonics [Petkovska and Seidel-Morgenstern, 2013], as follows

$$y = y_S + y_{DC} + B_I \cdot cos(\omega t + \phi_I) + B_{II} \cdot cos(2\omega t + \phi_{II}) + \dots\ . \tag{8.5}$$

Within, the subscript DC denotes the nonperiodic component and I, II to the first and second harmonics.

$$y = y_S + y_{DC} + y_I(t) + y_{II}(t) + \dots \tag{8.6}$$

After collecting the terms of ω (the terms with $e^{j\omega t}$ and $e^{-j\omega t}$), the first harmonic of output is obtained.

$$\begin{aligned} y_I =& B_I \cdot cos(\omega t + \phi_I) \\ =& \left\{\left(\frac{A_x}{2}\right) G_1(\omega) + 3\left(\frac{A_x}{2}\right)^3 G_3(\omega,\omega,-\omega) + \dots\right\} e^{j\omega t} \\ &+ \left\{\left(\frac{A_x}{2}\right) G_1(-\omega) + 3\left(\frac{A_x}{2}\right)^3 G_3(\omega,-\omega,-\omega) + \dots\right\} e^{-j\omega t} \end{aligned} \tag{8.7}$$

The second harmonic of the output can be obtained by collecting the terms of frequency 2ω (the terms with $e^{2j\omega t}$ and $e^{-2j\omega t}$)

$$\begin{aligned} y_{II} =& B_{II} \cdot cos(2\omega t + \phi_{II}) \\ =& \left\{\left(\frac{A_x}{2}\right)^2 G_2(\omega,\omega) + 4\left(\frac{A_x}{2}\right)^4 G_4(\omega,\omega,\omega,-\omega) + \dots\right\} e^{2j\omega t} \\ &+ \left\{\left(\frac{A_x}{2}\right)^2 G_2(-\omega,-\omega) + 4\left(\frac{A_x}{2}\right)^4 G_4(\omega,-\omega,-\omega,-\omega) + \dots\right\} e^{-2j\omega t} \end{aligned} \tag{8.8}$$

The DC component of the output is obtained by collecting the nonperiodic terms (the terms with e^0) from the Volterra series and can be expressed as the following infinite series [Weiner and Spina, 1980].

$$\boxed{y_{DC} = 2\left(\frac{A_x}{2}\right)^2 G_2(\omega,-\omega)} + 6\left(\frac{A_x}{2}\right)^4 G_4(\omega,\omega,-\omega,-\omega) + \dots \tag{8.9}$$

In general, the time-average performance of the reactor is determined by the nonperiodic term, the DC component [Nikolic Paunic, 2016]. This value can be sufficiently approximated using the asymmetrical second-order FRF $G_2(\omega,-\omega)$, determining the value of change Δ by the dynamic operation.

$$y_{DC} \equiv \Delta = 2\left(\frac{A_x}{2}\right)^2 G_2(\omega, -\omega) \tag{8.10}$$

This analytic solution is a simple expression, capable of evaluating the change of single input parameter modulation.

8.1.2 Simultaneous Modulation of Multiple Input Parameters using NFR

Further, the aim of the present work is the simultaneous modulation of two input parameters, displayed in Figure 8.2. Each input can be modulated with an individual amplitude A and frequency f , as well as a phase difference ϕ for one of the parameters. Investigations have shown that the best results can be obtained when both inputs have the same frequency $\omega_i = u_i = \omega$ [Nikolic Paunic, 2016].

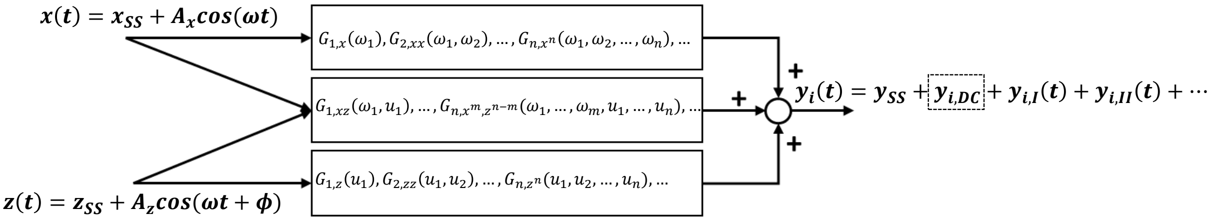
$x(t) = x_{SS} + A_x cos(\omega t)$
$G_{1,x}(\omega_1), G_{2,xx}(\omega_1, \omega_2), \dots, G_{n,x^n}(\omega_1, \omega_2, \dots, \omega_n), \dots$
$G_{1,xz}(\omega_1, u_1), \dots, G_{n,x^m,z^{n-m}}(\omega_1, \dots, \omega_m, u_1, \dots, u_n), \dots$
$G_{1,z}(u_1), G_{2,zz}(u_1, u_2), \dots, G_{n,z^n}(u_1, u_2, \dots, u_n), \dots$
$z(t) = z_{SS} + A_z cos(\omega t + \phi)$
+
+
+
$y_i(t) = y_{SS} + \boxed{y_{i,DC}} + y_{i,I}(t) + y_{i,II}(t) + \cdots$

Figure 8.2: Presentation of multiple input modulations and their influence on the output function.

The application of two input modulation results in a more complicated case. Every individual input generates transfer functions of its own, further both combine to a cross term, illustrated in Figure 8.2. Each output is a sum of harmonic output functions of a different order (eq. (8.11)).

$$y(t) = \sum_{n=1}^{\infty} y_{x,n}(t) + \sum_{n=1}^{\infty} y_{z,n}(t) + \sum_{n=1}^{\infty} y_{xz,n}(t) \tag{8.11}$$

All the single FRF's contribute to the output y, which is again mainly determined by the nonperiodic term y_{DC}. For the assumption of the present work, the DC component itself is dependent on the separate contributions by the individual inputs and their cross effect (eq. (8.12)).

$$y_{DC} = y_{DC,x} + y_{DC,z} + y_{DC,xz} \tag{8.12}$$

Here, the asymmetrical second-order frequency response function is dominantly determining the value of each contribution, since the higher harmonic functions contribute less to the overall outcome. As for the cross term, $G_{2,xz}(\omega, -\omega)$ and $G_{2,xz}(-\omega, \omega)$ are considered as complex conjugates and can be written as follows (eq. (8.13)) by further transformation:

$$\Delta = y_{DC} \approx 2\left(\frac{A_x}{2}\right)^2 G_{2,x}(\omega, -\omega) + 2\left(\frac{A_z}{2}\right)^2 G_{2,z}(\omega, -\omega) + 2\left(\frac{A_x}{2}\right)\left(\frac{A_z}{2}\right) G_{2,xz}(\omega, \phi) \quad . \tag{8.13}$$

Further, the second asymmetrical FRF of the cross term is expressed by eq. (8.14).

$$G_{2,xz}(\omega, \phi) = Re\left(G_{2,xz}(\omega, -\omega)\right) cos(\phi) + Im\left(G_{2,xz}(\omega, -\omega)\right) sin(\phi) \tag{8.14}$$

In previous investigations [Nikolić et al., 2014a; Nikolić et al., 2014b], it was shown that the single modulation can result in detrimental behavior of the system. However, when multiple inputs are simultaneously perturbed, a beneficial output could be generated [Nikolić et al., 2016a; Nikolić et al., 2016b] when optimal phase differences are applied. Such performance can be attributed to the cross effect. With the proper choice of an optimal phase difference (eq. (8.15)), it is possible to maximize the cross effect and thereby, the outcome of the dynamically operated reactor.

$$\phi_{opt,y_P}(\omega, A_C, A_F) = 2 \cdot arctan\left(\frac{a^* \pm \sqrt{a^{*2} - c^{*2} + b^{*2}}}{c^* + b^*}\right) \tag{8.15}$$

with

$$a^* = 1 + 2\left(\frac{A_C}{2}\right)^2 H_{P2,CC}(\omega, -\omega) + 2\left(\frac{A_F}{2}\right)^2 H_{P2,FF}(\omega, -\omega) - Re\big(H_{P2,CF}(\omega, -\omega)\big) \tag{8.16}$$

$$b^* = Im\big(H_{P2,CF}(\omega, -\omega)\big) \tag{8.17}$$

$$c^* = -2\left(\frac{A_C}{2}\right)\left(\frac{A_F}{2}\right) Im\big(H_{P2,FF}(\omega, -\omega)\big) \tag{8.18}$$

With the help of these findings, an output change can now be evaluated.

Output change

The different cases of input modulation result in individual output change functions Δ_P. For variation of the input concentration, this is determined by the asymmetrical FRF, depending on the concentration $G_{2,CC}$.

$$\text{Modulation of inlet concentration: } \Delta_P \equiv y_{DC} = N_{P,DC} \approx 2\left(\frac{A_x}{2}\right)^2 G_{2,CC}(\omega, -\omega) \tag{8.19}$$

If, on the other hand, the total flow is excited periodically, the G function can no longer be used, since it refers to concentrations and this value is influenced by the volumetric flow. It is, therefore, necessary to express the asymmetrical FRF by H in the case of occurring volumetric flow rate modulation for calculation of molar flow rates.

$$\text{Modulation of total flow rate: } \Delta_P \equiv y_{DC} = N_{P,DC} \approx 2\left(\frac{A_z}{2}\right)^2 H_{2,FF}(\omega, -\omega) \tag{8.20}$$

This condition is necessary for simultaneous variation of input concentration and total flow, as shown below. Here, the individual variations and the respective parameters in a mixed form influence the change of the system through a dynamic operation.

Simultaneous modulation of inlet concentration and total flow rate:

$$\begin{aligned}\Delta_P \equiv y_{DC} = N_{P,DC} \approx & 2\left(\frac{A_x}{2}\right)^2 H_{2,CC}(\omega, -\omega) + 2\left(\frac{A_z}{2}\right)^2 H_{2,FF}(\omega, -\omega) \\ & + 2\left(\frac{A_x}{2}\right)\left(\frac{A_z}{2}\right)\Big(Re\big(H_{2,CF}(\omega, -\omega)\big)cos(\phi) + Im\big(H_{2,CF}(\omega, -\omega)\big)sin(\phi)\Big)\end{aligned} \tag{8.21}$$

Based on the NFR methodology presented here, part III of this work considers the hydrolysis of acetic anhydride for forced dynamic operation. The derived equations are used to make predictions regarding the output of the reaction system and to validate them experimentally.

8.1.3 Reactor model evaluated by the NFR

Based on the stationary experiments kinetic parameters could be estimated, which are summarized in Table 8.1. These process parameters were used for the calculations of the NFR method. The necessary equations for the evaluation of dynamic operations were derived at the University of Belgrade and checked by the author. Furthermore, the selected reference parameters are listed, which were selected to allow a study of parameter variations. It is possible to periodically modulate single input parameters as well as multiple parameters simultaneously.

Table 8.1: Kinetic and thermodynamic parameters for the model reaction investigated eq. (3.4).

Parameter	**Symbol**	**Value**	**Unit**
Reaction Order	n	0.66	-
Activation Energy	E_A	34.06	kJ/mol
Collision Factor	k_∞	904	$mol^{0.34}/(s \cdot l^{0.34})$
Heat of reaction	$\Delta_R H$	-55.5	kJ/mol
Heat capacity	ρc_P	4.186	$kJ/(K \cdot l)$
Miscibility limit of AA in W	c_{AA}^{max}	1.4	mol/l
Molar Mass Anhydride	M_{AA}	102.09	g/mol
Density Anhydride	ρ_{AA}	1082	g/l

Before the periodic operation, it is necessary to operate the continuously stirred tank reactor (CSTR) at steady-state. Therefore, the previously calibrated pumps were set to constant voltages correlating to the desired steady-state values of the flow rate F and the volume of the reactor V_R. After 90 minutes, a steady-state was obtained and the voltages were adjusted according to eqs. (8.22) and (8.23), varying the individual flow rates that are part of the anhydride concentration c_{AA} and the total flow rate F.

$$c_{AA}(t) = c_{AA,s}\big(1 + A_C \cdot cos(\omega t)\big) \tag{8.22}$$

$$F_{tot}(t) = F_s\left(1 + A_F \cdot cos(\omega t + \phi)\right) \tag{8.23}$$

Within these equations, c_{AA} represents the inlet concentration of acetic anhydride, with the subscript s for the steady-state value, F the total flow rate, A_C forcing amplitude of inlet concentration modulation, A_F forcing amplitude of flow rate modulation, ω for the desired period and ϕ for the phase difference between the input modulations. Nevertheless, these are not the functions implemented by the individual pumps. A representation of the individual flow rates must be derived.

The corresponding total flow is the sum of the time-dependent individual flows of acetic anhydride (AA) and water (W) fed into the reactor, eq. 8.24.

$$F_{tot}(t) = F_{AA}(t) + F_W(t) \tag{8.24}$$

The time-dependent inlet concentration is calculated, as shown in eq. 8.25.

$$c_{AA}(t) = \frac{F_{AA}(t)}{F_{tot}(t)} \cdot \frac{\rho_{AA}}{M_{AA}} \tag{8.25}$$

Rearrangement of eq. (8.25) gives the flow rate of acetic anhydride as follows eq. (8.26):

$$F_{AA}(t) = c_{AA}(t) F_{tot}(t) \frac{M_{AA}}{\rho_{AA}} \tag{8.26}$$

When incorporating the eqs. (8.22) and (8.23) into eq. (8.26), the flows are modulated accordingly for acetic anhydride (eq. (8.27)) and water (eq. (8.28)).

$$F_{AA}(t) = c_{AA,s} F_{tot,s} \frac{M_{AA}}{\rho_{AA}} \big(1 + A_C \cdot cos(\omega t)\big)\big(1 + A_F \cdot cos(\omega t + \phi)\big) \tag{8.27}$$

$$F_W(t) = F(t) - F_{AA}(t) = F_{tot}(t) - c_{AA,s} F_{tot,s} \frac{M_{AA}}{\rho_{AA}} \big(1 + A_C \cdot cos(\omega t +)\big)\big(1 + A_F \cdot cos(\omega t + \phi)\big) \tag{8.28}$$

During the experiment, conductivity and temperature were continuously recorded within the reactor vessel and in the thermostats, respectively.

It should be mentioned, that in conventional steady-state operation performance can be enhanced e.g. by decreasing the flow rates (offering more residence time) or increasing the inlet concentration of R (within the miscibility limit). Thus, it needs to be noted, that the reference situation corresponding to the parameters in Table 8.2 does not represent a fully optimized steady-state operation. Results of optimization calculations were described in [Nikolić et al., 2014a; Nikolić et al., 2014b; Nikolić et al., 2016a], however, slightly different kinetics were used. Furthermore, the existing miscibility constraint was not respected and the usage of unrealistically high reactant feed concentrations was suggested.

Table 8.2: Reference parameters of eqs. (7.1) and (7.2) in accordance with constraints and restrictions originating from the reaction system and possibilities for the experimental study for the optimization and the steady-state conditions assuming kinetic model 2 (eq. (7.4)).

Parameter	**Symbol**	**Value**	**Unit**
Reaction volume	V_R	298	ml
Inlet temperature	T^{in}	294.15	K
Water Flow (steady)	F_W	40	ml/min
Anhydride Flow (steady)	F_{AA}	3	ml/min
Total Flow (steady)	F_{tot}	43	ml/min
Inlet concentration (steady)	c^0_{AA}	0.74	mol/l
Adiabatic temperature rise	ΔT_{ad}	19.6	K

Below, the expected periodic outputs and the sensitivity of the NFR method based on the kinetic parameters collision factor k_∞, activation energy E_A and reaction order n are evaluated. Subsequently, the implementation of individual input parameter variations of the input concentration and the total flow rate are presented. At this point, the possibility of the exact imprint of dynamic input modulations shall be demonstrated. Subsequently, the simultaneous implementation of two input variables with an optimal phase shift. The influences of the individual amplitudes and the phase shift on the reactive system will be experimentally demonstrated.

As the objective function, the yield of product is chosen (eq. (2.14)). For the fluctuating range, the objective function (OF) must be adjusted, whereby the time-averaged values for the product P and the input variable AA must be considered.

$$\overline{Y_P(t)} = \frac{\overline{\dot{n}_P(t)}}{\dot{n}^0_{AA}(t)} \cdot \frac{|\nu_{AA}|}{\nu_P} \tag{8.29}$$

To compare between steady-state and periodic operation an absolute yield difference:

$$\Delta Y_P = \overline{\dot{Y}_P(t)} - Y_{P,s} \tag{8.30}$$

and a normalized criterion will be evaluated below.

$$Y_P^{norm} = \frac{\overline{\dot{Y}_P(t)}}{Y_{P,s}} \tag{8.31}$$

8.2 Simulative Results

For a demonstration of the potential by forced dynamic operation, the simulative results of the NFR method are given and explained here. Subsequently, the sensitivity of the kinetic parameters to the NFR is evaluated. The obtained results are based on the derived functions, presented in section 8.1.2 and in more detail in the Ph.D. thesis of Daliborka Nikolic [Nikolic Paunic, 2016]. The kinetic parameters are derived by implying the experiments carried out and it is therefore questionable to what extent a global optimum could be found. Nevertheless, a multitude of initial values and boundary conditions are implemented, to minimize the evaluated objective function. As a result, an optimal set of parameters is obtained. In most cases, extrapolation from a defined range of reaction conditions is carried out. Accordingly, the kinetics used can never be completely correct. Therefore, the influence of the variation of the collision factor, activation energy and reaction order on the output by forced dynamic modes is investigated in the following in detail.

After deriving the functions with the help of the NFR method by the collaborators in Belgrade [Nikolic Paunic, 2016], algebraic equations are obtained, which can evaluate periodic parameters and the corresponding time-average values. The NFR was evaluated for simultaneous dynamic excitation of two input parameters, because this approach has shown the great potential of dynamic operation, compared to simple transient modulation with an arbitrary switching time. For this purpose, the respective amplitudes were selected by previous investigations [Nikolić et al., 2016a] and the limits of the experimental setup.

The predicted changes due to dynamic operation are given in Figure 8.3. In Figure 8.3a the single and simultaneous variation of the input concentration (A_C = 85 %) and the total volumetric flow (A_F = 55 %) is analyzed. To have a direct link to the following experimental study the predicted normalized yields are presented in Figure 8.3 as a function of the period of the modulation P, which is related to the inverse of the frequency f as follows:

$$P = \frac{1}{f} \tag{8.32}$$

In Figure 8.3b the variations of input concentration and input temperature (A_T = 7 %) as single and simultaneous dynamic operation are displayed.

The normalized yield (eq. (8.31)) is regarded as a function of the period duration. In the case of the in-

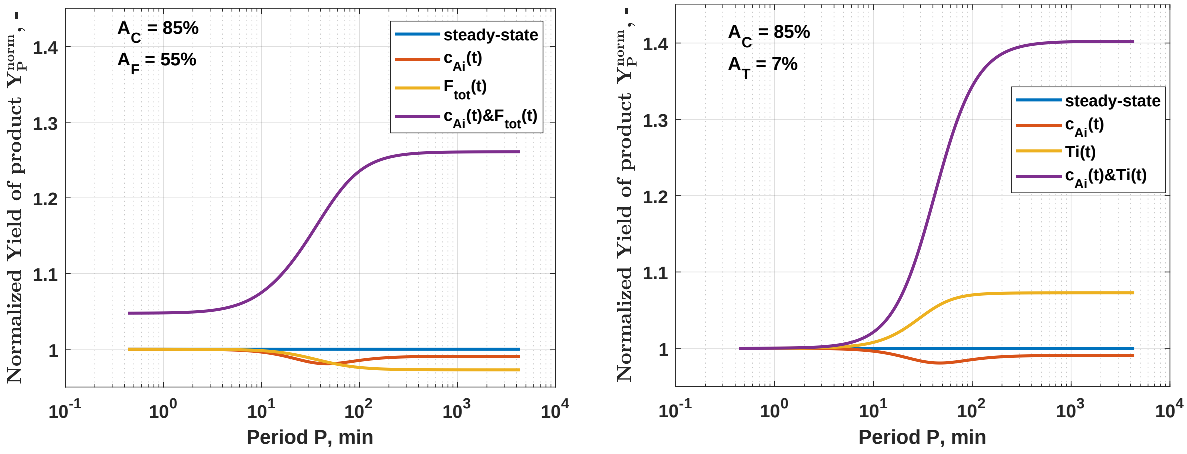

(a) (b)

Figure 8.3: Normalized yield (eq. (8.31)) as a function of period calculated using the NFR method with the defined standard values for (a) perturbation of inlet concentration A_C = 85 % and total flow rate A_F = 55 % and (b) perturbation of inlet concentration A_C = 85 % and inlet temperature A_T = 7 %.

dividual modulations in Figure 8.3a it is evident that these correspond to the stationary state for small periods. This condition is a logical consequence of the low-pass filter behavior a CSTR presents. Beginning at a period duration of 10 min, a trend towards detrimental response behavior occurs. In case of the total volumetric flow rate variation, the trend tends towards a constant value, which represents a slight deterioration when a dynamic operation is implied. The modulation of the input concentration also has a negative tendency. However, it reaches a minimum in the range of around 40 min and then approaches the stationary value again without reaching it for longer periods.

An opposite behavior can be seen for the simultaneous modulation of both parameters with a period-specific optimal phase shift. This graph lies above the stationary point in the entire period range. There are two stable value ranges, below 4 min at 1.05 and above 400 min period duration with 1.26. This indicates a new stationary state as a result of too high or too low frequencies. Correspondingly, the response behavior is not observed before switching to low values of period or the modulation exceeds multitudes of the residence time and an entirely new steady-state is reached.

In the period range between 10 and 100 minutes, the performance of periodic operation changes rather strongly. This range is well suited for laboratory investigations of liquid-phase reactions. To fix a promising and easy to apply reference period for the experimental study the following aspects were considered. A longer period is, for the reaction system considered, beneficial to increase the potential of dynamic operation. However, performing experiments with longer periods is time-consuming and causes conflicts with constraints imposed by the lengths of working days. Thus, based on the results of the preliminary theoretical analysis performed together with the mentioned rational considerations a reference period P of 40 min was selected for simultaneously perturbing the input flow rate and the reactant concentration around the mean values given in Table 8.2. This period corresponds to a frequency of $f = 4.167 \cdot 10^{-4}$ Hz.

Related to this reference period, an optimal theoretical reference phase shift for modulating both inputs simultaneously could be calculated based on eq. (8.15). The obtained optimal reference phase shift is ϕ_{opt} = 157.33°. The predicted improvement of periodic operation in terms of the normalized product yield (eq. 8.30) is for the reference condition $Y_P^{norm} = 1.17$. This corresponds according to eq. 8.30 to an absolute increase of 5.91 %.

In comparison to the modulation of inlet concentration and total flow rate, a similar picture can be obtained for the variation of the input concentration and the input temperature (Figure 8.3b). The single variation of the temperature is for low periods equal to the steady-state. However, the normalized yield increases from 10 min and reaches about 1.07 at 100 min period duration. The simultaneous modulation of the two input parameters with an optimal phase shift indicates the highest potential for a period duration higher than 10 min. With a maximum value of 1.4 for the normalized yield. The effect of simultaneous variation from Figure 8.3a is exceeded. The even higher effect is caused by the higher nonlinear influence of the temperature via the Arrhenius equation (eq. (2.38)). Furthermore, the single modulation is already beneficial, which means that the caused change is increased by the cross term of the transfer function. Given the difficulty of sinusoidal variation of the temperature, due to thermal inertia of the system, further investigation of this parameter is refrained from.

For a group of different period lengths, the optimal phase shifts and the time-averaged yield for the dynamic change of inlet concentration and total flow rate were determined and summarized in Table 8.3.

Table 8.3: Predicted dynamic results by the NFR method for a varying period time, with fixed amplitudes for inlet concentration A_C = 85 % and total flow rate A_F = 55 %, for the yield obtained by dynamic operation implying an optimal phase difference.

Period, [min]	**Forcing frequency,** [10^{-4}Hz]	**Amplitudes**		**Optimal phase difference,** [rad]	**Product yield, Y_P** [%]
		Inlet concentration, [%]	**Total flow rate,** [%]		
13.89	12	85	55	2.5673	38.06
20	8.33			2.5899	38.87
40	4.17			2.7459	40.88
60	2.77			2.8533	42.06
100	1.66			2.9606	43.12
120	1.39			2.9897	43.36

The optimum offset in the range is for the assumed reactive system slightly below 180° (3.14 rad). Accordingly, the mountains and valleys of the function are superimposed for the periodic excitation of the input concentration and the total volumetric flow rate. For very high frequencies, the period duration is correspondingly short and the changes are significantly faster than the residence time in the reactor. As a result, there will be no dynamic operation because the time for the response behavior is not considered. In contrast, different stationary points occur if the residence time is shorter than the period duration. Improvements can thus be achieved by the favorable shift of the input parameters to each other.

This interesting result is however only valid for the assumed kinetic parameters. By variation of kinetic parameters, the steady-state is fundamentally varied. It becomes apparent that a reduced stationary yield can be more significantly affected in terms of improvement or process intensification. This enhancement is a logical conclusion, since analogous to the *Pareto principle* an increase of the system from a higher state of quality can only be realized with significantly more effort.

Figure 8.4 reveals the variation of the activation energy with ±20 % (a) from the value shown in Table 8.1, as well as the variation of the collision factor by 20 % (b) and the reaction order n between 0 and 1.5 (c). The chosen 20 % of the variation is selected according to uncertainties in the estimation of kinetic parameters. In the legend extended information is given, indicating what the steady-state yield Y_{ss} for the corresponding kinetic set of parameters is. Further, it must be stressed that only one parameter was varied at a time.

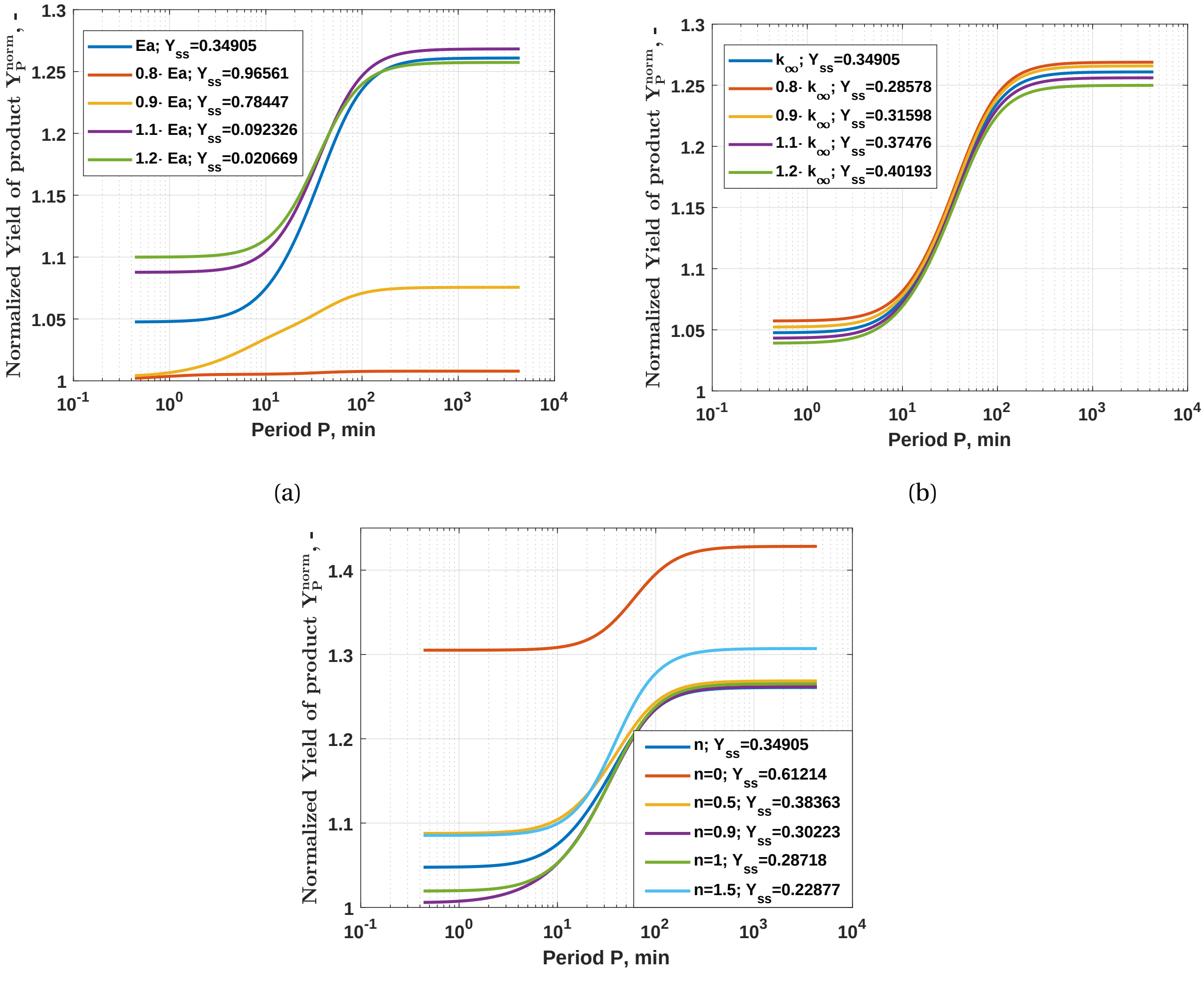

(a)

(b)

(c)

Figure 8.4: Influence of the (a) activation energy E_A, (b) the collision factor k_∞ and (c) the reaction order n on the normalized product yield (eq. (8.31)) for the simultaneous modulation of inlet concentration and total flow with amplitudes of A_C = 85 % and A_F = 55 % with individual optimal phase differences.

Despite the changed stationary state, the period duration range in which the front of the improvement its maximum increase remains equivalent. The range in which enhancement is achievable is dependent on the reaction conditions, the reactor model and the boundary conditions seem to overlap the kinetics. Though, it appears as if the reactor parameters define the interesting ranges in which changes from the steady-state behavior are achievable.

Further, industrial interest has a different focus. Instead of predicting periodic parameters, one might have dynamic operation through temperature changes in the feed or changes in the inlet concentration, which consequently result in fluctuation. Therefore, the prediction, if the system is robust, meaning its output varies within a defined range would be of interest to validate.

In the case of lowered activation energy, the energetic barrier is significantly decreased, which leads to significantly higher yields. Accordingly, the nominal change of the time-average yield of the dynamic operation is less pronounced. As a result, the course of the lowest activation energy graph is strongly flattened, with a marginal increase between 10 and 100 minutes period duration. In contrast, the curves for the activation energies higher than the ones calculated in this thesis are very similar to it. Some deviation is apparent, especially at low periods. With increasing value the graphs differ less, with the order of the plot changing, interestingly.

A similar result is obtained for the variation of the collision factor. In this case, the influence on the stationary yield is less concisely influenced. The curves of the individual graphs are fanned out for periods of less than 10 and greater than 100 minutes, but closer to each other as in the case of E_A. Within the range in which a significant improvement can be expected, the curves overlap. Further, the order of the plots remains the same. Nevertheless, the influence of the collision factor is negligible.

Contrary results are observed for the variation of the reaction order. According to theory, forced dynamic variation of a single input parameter can always be expected, to result in deterioration, if the reaction order is between zero and one, as in the model reaction selected [Schädlich et al., 1983]. Though, two input parameters can be varied simultaneously. Improvement is achieved with the optimal phase shift. This detail is applied here and the results are shown in Figure 8.4c. For low periods, all considered reaction regimes are below a nominal improvement of 10 %, except for the reaction order of zero. This fact will be discussed later on. Here, the kinetics with orders close to one have the least beneficial influence. An increase of the curves, with an increasing period duration, begins in a range at 10 min, whereby the assumed model with $n \approx 1$ initializes before this limit. With increasing periodic time, only the system with an order of 1.5 rises stronger than the others. In comparison, all reaction orders between zero and one converge to an approximately equal value.

As mentioned, the reaction order zero is an exception. The reaction rate is only dependent on the reaction rate constant k. Its plot is above all the other curves for all period durations. With this kinetic approach, the reaction speed and conversion are independent of the concentrations of the components involved. At the same time, the resulting stationary yield is almost twice as high as for the determined kinetic parameters (section 7.3). This result can be justified by the constant linear increase in yield over time. Therefore, the yield with the same residence time is higher than the reaction orders greater than zero. If the reaction order is of negative values, the system would even accelerate with increasing time and the amount of converted reactant, subsequently less amount in the reactor. The effects of forced, dynamic operation would become further intensified.

In the following, the performed forced dynamic experiments will be presented and the results are validated.

8.3 Single Input Modulation

First, it must be mentioned that the conditions selected here and listed in Table 8.1 do not reflect the optimal parameters. To stay within the necessary boundary conditions of the system (solubility limits) and at the same time to enable the implementation of correspondingly intensive input parameter modulations, the parameters for amplitude, concentration, reactor volume and the single streams were selected. For the validation of the simulative results, the simpler case of the single input parameter variation is considered. Two exemplary experiments at a reference frequency $f = 4.167 \cdot 10^{-4}$ Hz in combination with an input concentration amplitude of $A_C = 85$ % and an amplitude of the total flow of $A_F = 55$ % are shown. The steady-state values are offered in Table 8.1, with 0.74 $\frac{mol}{l}$ and 43 $\frac{ml}{min}$. Further, a stable steady-state was established, before dynamically varying the input parameters.

Variation of Inlet concentration

As the simplest case, the inlet of concentration was modulated individually (Figure 8.5). To illustrate the periodic modulations implied to the reactor, Figure 8.6 presents the implemented temporal values of c^0_{An}, F_{tot}, F_W and F_{An}. The period of the parameters considered here is only given for the range of dynamic operation.

In contrast, a sinusoidal oscillation in the range of 0.11 and 1.37 $\frac{mol}{l}$ is realized for the concentration, as required. Thus, the conceptual imprint of periodic behavior has been realized. The volume flow is constant over the entire time horizon. This is managed by the shift of 180° between H_2O and anhydride.

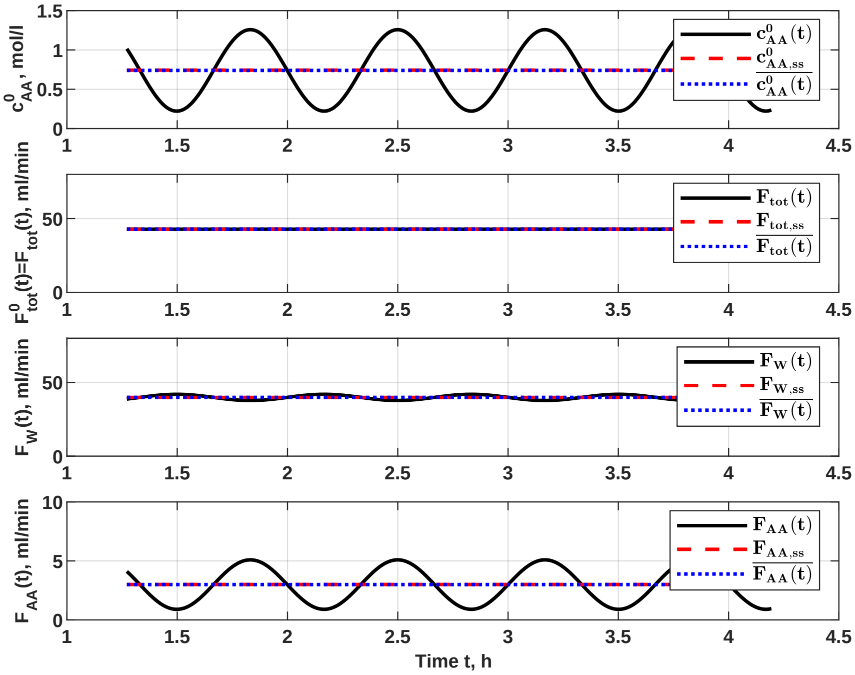

Figure 8.5: Input signals for the single input modulation of the concentration for the dynamic experimental part with inlet concentration of anhydride (top), total volumetric flow rate (second), water flow rate (third) and acetic anhydride flow rate (bottom).

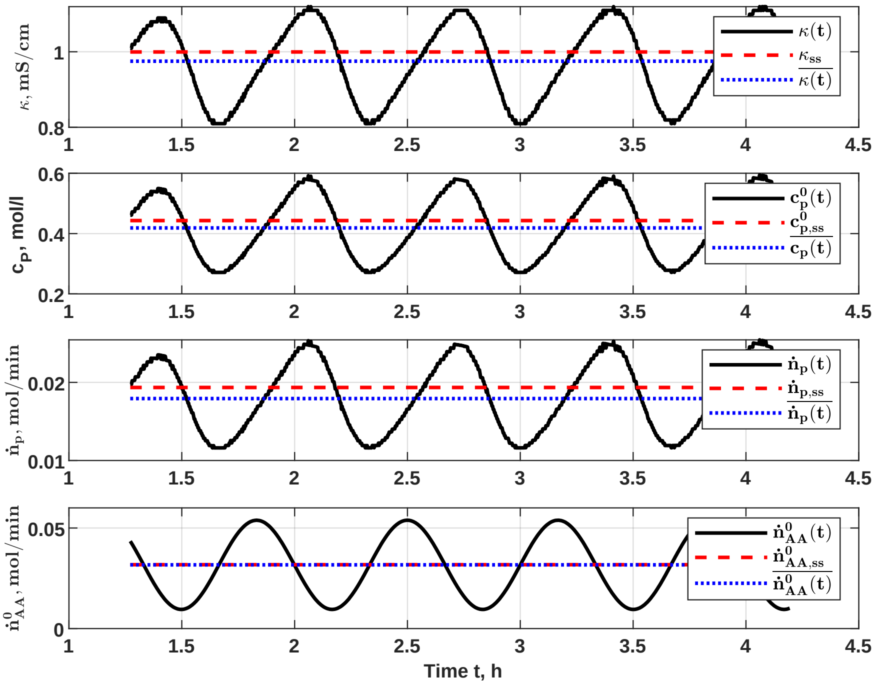

Figure 8.6: Single modulation of inlet concentration $A_C = 85$ % and a period of 40 min, presenting conductivity at the outlet (top), product concentration at the outlet (second), molar product flow (third) and inlet molar product flow (bottom).

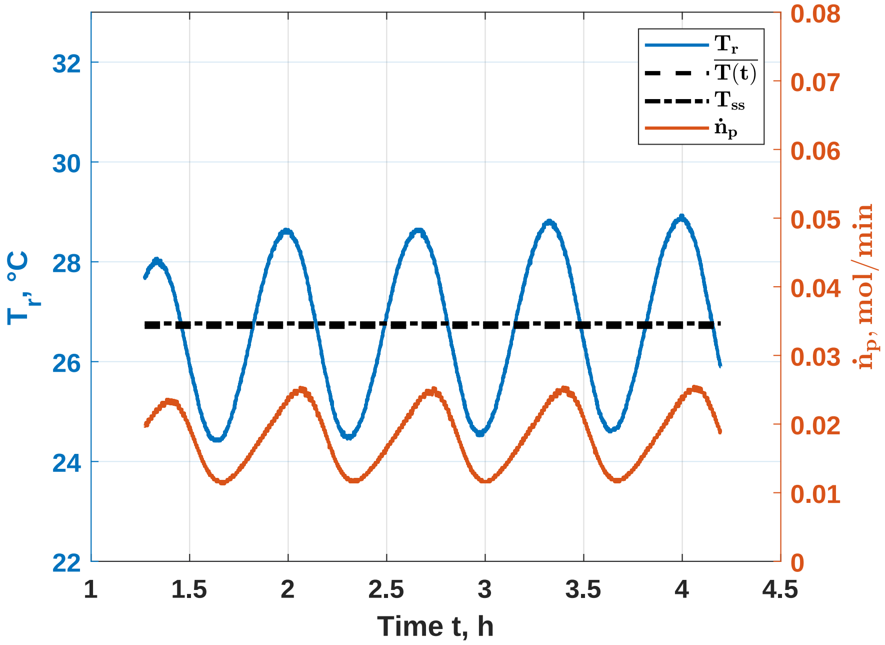

Figure 8.7: Single modulation of inlet concentration $A_C = 85$ % and a period of 40 min, presenting reactor temperature (blue) and molar product flow (orange) over the time of periodic operation.

Accordingly, the measured signal of the product, shown in Figure 8.6 and Figure 8.7 together with the reactor temperature is to be discussed. It becomes evident that the modulation of the input concentration generates a fronting of the output. As the concentration increases, the measured molar flow linearly reaches its peak slightly later than the maximum concentration. Next, the signal drops significantly faster to its minimum than the concentration, which is a result of the kinetics. Compared to the maximum, the minimum is now less delayed than the valley of the concentration course. A similar effect is also recorded for the temperature. However, the course is in phase with the oscillating molar flow.

This smeared profile appears to result from the non-ideal mixing of the system and the resulting response behavior by kinetics. Nevertheless, the implementation of a periodic harmonic modulation of a single input parameter was experimentally realized. Though, resulting in a detrimental output of the time-average as predecited.

Variation of Total Flow

In the next step, the single variation of the total volumetric flow is analyzed (Figure 8.8). In analogy to the previous analysis in Figure 8.9 the inlet parameters are shown.

The experiment illustrates that in this case, the input concentration of acetic anhydride is constant at the stationary value as desired. At the same time, the volumetric flow is varied sinusoidally in the range from 19.35 to 66.65 $\frac{ml}{min}$. The two individual flows are approximately in phase since the concentration remains constant, a slight shift is necessary. It must be mentioned that in Figure 8.9 only the experimental range for dynamic operation is displayed.

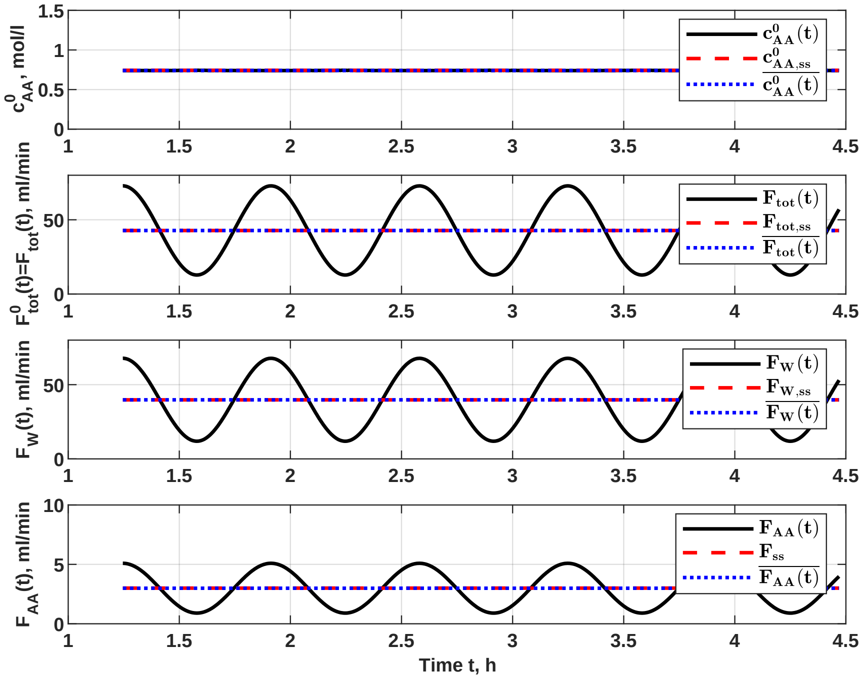

Figure 8.8: Input signals for the single input modulation of the total flow rate for the dynamic experimental part with inlet concentration of anhydride (top), total volumetric flow rate (second), water flow rate (third) and acetic anhydride flow rate (bottom).

In Figure 8.9 the output signal in combination with the converted values and Figure 8.10 the reactor temperature with the molar flow of the product (b) are shown. In contrast to the fronting for the

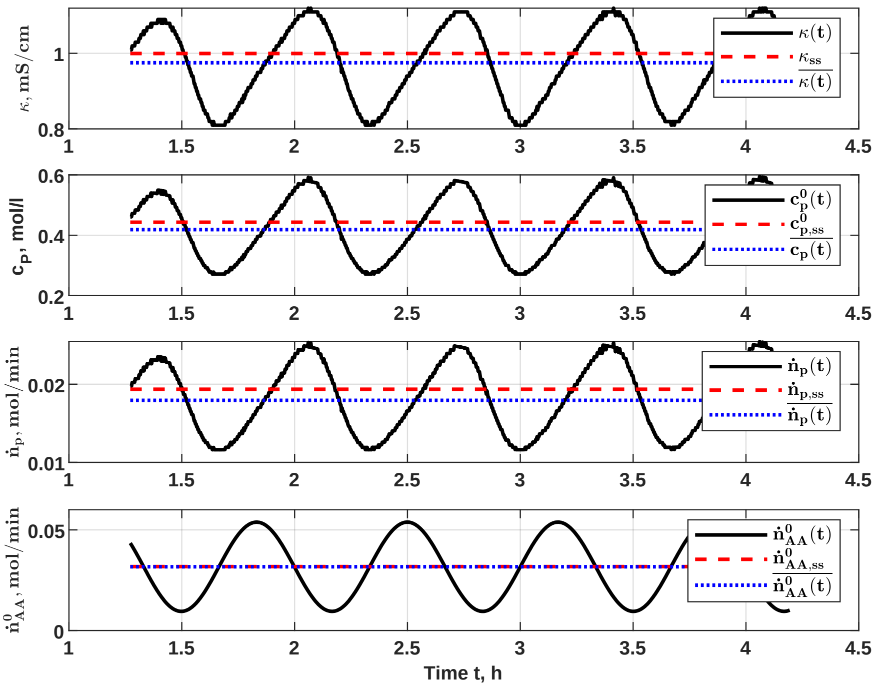

Figure 8.9: Single modulation of total flow rate A_F = 55 % and a period of 40 min, presenting conductivity at the outlet (top), product concentration at the outlet (second), molar product flow (third) and inlet molar product flow (bottom).

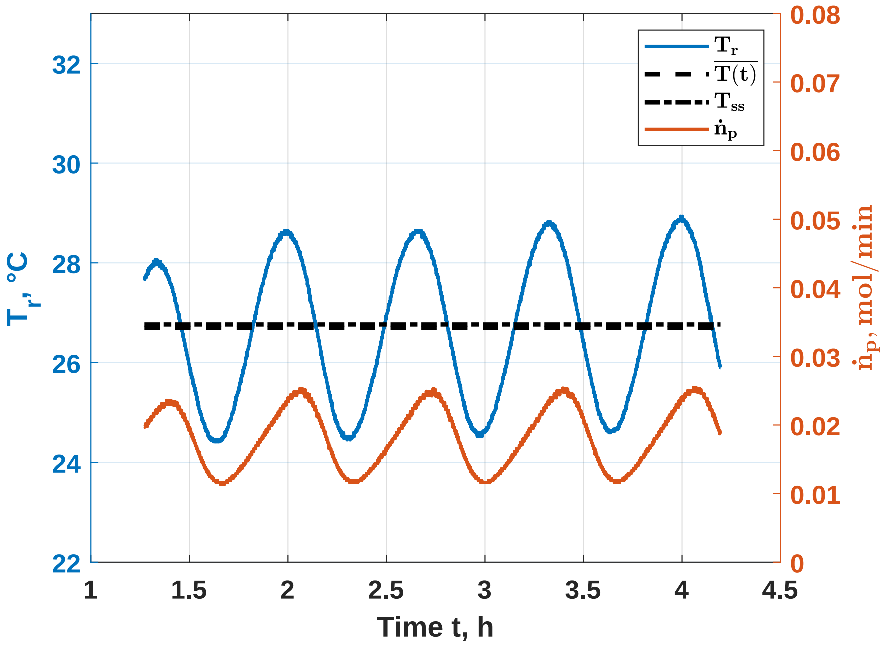

Figure 8.10: Single modulation of total flow rate A_F = 55 % and a period of 40 min, presenting reactor temperature (blue) and molar product flow (orange) over the time of periodic operation.

concentration modulation, a tailing can be seen in the case of the total volumetric flux. Furthermore, the extremes (maximum and minimum) of the molar product flow are upstream of those of the total volumetric flow variation. The maximum is reached earlier, while due to the tailing the valleys of the progressions match almost ideally. This behavior is a logical consequence since the conversion in the system is inversely proportional to the volumetric flow. At a constant reactor volume, a high flow rate corresponds to a shortened residence time in the system and correspondingly to a lower product conversion. As already mentioned, a CSTR needs a certain time to react to changes at the inlet. This so-called response behavior, based on residence time, causes a time delay. Thus, after the minimum flow rate value, the product molar flow rises steeply and flattens with the decreasing residence time. At the tipping point, the highly concentrated system with high conversion is replaced again, which results in a delay, and is almost caught up by the volumetric flow. However, the reactant accumulates in the reactor, due to low conversion, and a high reaction rate is initiated when the residence time drops below a certain limit.

Interestingly, the resultant product signal follows a sinusoidal profile. Though, the molar flow is shifted by 90°, since this value is the combination of concentration and flow rate. A further indication is the course of the reactor temperature in Figure 8.10. The reactor temperature is a sine function shifted by 180° to the volumetric flow variation. At the points of lowest residence time, corresponding to the highest flow rate, the temperature is at the minimum, due to the lowest conversion and residence time. At the same time, the reaction rate r is reduced by the influence of the temperature on the reaction rate constant k. Thus, the reactant is accumulated at this point. If the reactant is continuously fed and the volumetric flow rate is lowered, consequently, below a limit value, the reaction initiates itself and thus causes the molar flow rate to rise. This rate results in the maximum temperature in the reactor, which first has to be discharged again by the convective flow and accordingly can continue to promote the reaction to achieve the maximum of the molar flow with a slight offset.

The experiments carried out are valid for the modulation of a single input parameter and that the results obtained provide meaningful values. Especially the modulation of the input volumetric flow, shown in Figure 8.15 with the first data point for $A_C = 0\,\%$, matches the predicted values with excellent agreement.

The implementation of the single parameter variations showed the possibility to perturb input parameters periodically in a targeted and reliable way. The mean product yields determined in this way correspond satisfactorily to the predictions of the NFR methodology. Thus, the simultaneous modulation of several input variables can be examined.

8.4 Simultaneous Input Modulation of Inlet Concentration and Total Flow Rate

With the successful demonstration of stationary operation and the imprinting of single input parameter modulations, the simultaneous variation of multiple parameters can now be observed. For this purpose, the boundary conditions are considered analogous to the values from Table 8.1. Each experimental series was conducted separately, with the reference case being remeasured each time, which resulted in deviations in the observed output changes.

At first, the experiment is kept under constant conditions for 90 min to reach a stable stationary point (Figure 8.11). It can be seen that the temperature in the reactor and the molar product flow follow the expected course. The expected theoretical steady-state molar flow value is not reached by the experiment, but they are in an approximately equal range. Interestingly, the adiabatic temperature increase

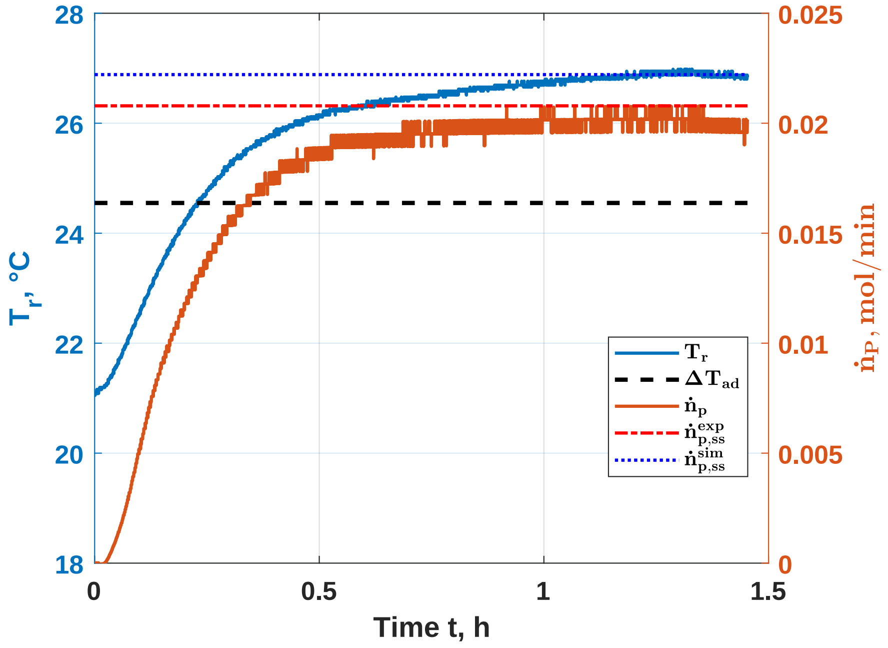

Figure 8.11: Experimental data of reactor temperature (left) and molar flow of the product acetic acid (right) with first stationary conditions ($V_R = 298$ ml, $F_W = 40$ ml/min and $F_{AA} = 3$ ml/min).

ΔT_{ad} is in the correct range for a conversion of 0.349.

The steady-state temperature monitored is slightly below the expected value for complete adiabatic behavior. Therefore the heat losses of the laboratory reactor used are not significant but should be specified more precisely. Nevertheless, the simple adiabatic reactor model can be used. The reduced experimentally obtained temperature relative to the predicted temperature is consistent with the observed lower steady-state conversion and yield.

Subsequently, predefined values of amplitudes, frequency and phase shift were applied for the periodic operation. Following the chosen and applied conditions, a frequency of $4.167 \cdot 10^{-4}$ Hz and a phase shift of 157.33°, as well as amplitudes for the input concentration of 85 % and the total flow rate of 55 % were applied. The functions were implemented by voltage transmission to the respective pump.

The volumetric flows of the individual components, acetic anhydride and water, were calculated based on the transferred signals and the specific calibration. Using this set of data, the curves for the variation of the total flow and the input concentration could be calculated, as shown in Figure 8.12 as top and second graph.

The volumetric flow fluctuates around the stationary value of 43 ml/min in the desired range of 19.35 and 66.65 ml/min. Besides, this input parameter is shifted by the desired phase shift value in comparison to inlet concentration. This is seen in the shift of the maxima and minima to one another in Figure 8.12. Both input parameters follow an ideal sinusoidal function, while the individual inlet flow rates are combinations of these functions (eqs. (8.27) and (8.28)). By means of value, the water flow rate does not differ from the ideal periodic function. Whereas, the anhydride visualizes the change intensively.

In Figure Figure 8.13, the output signals for periodic operation are shown. With an established stationary state, the reactor is disturbed. Though, the system needs some time to compensate for tran-

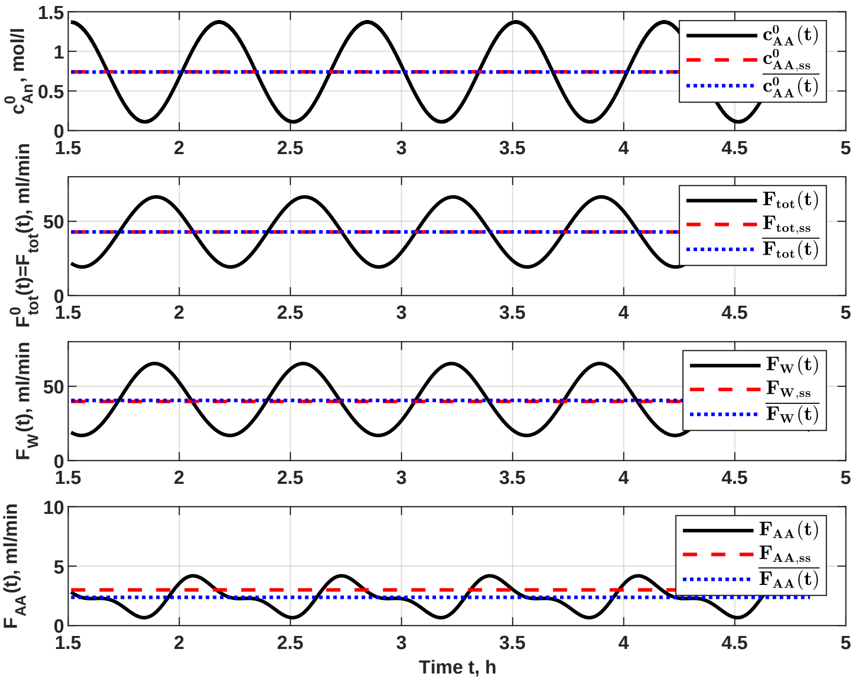

Figure 8.12: Input signals for multiple input parameter modulation of inlet concentration and total flow rate for the dynamic experimental part with inlet concentration of anhydride (top), total volumetric flow rate (second), water flow rate (third) and acetic anhydride flow rate (bottom) for dynamic operation with a frequency f = $4.167 \cdot 10^{-4}$ Hz, amplitude of inlet concentration A_C = 85 %, amplitude of total flow A_F = 55 % and phase difference ϕ = 157.33 °.

sient behavior and stabilize the fluctuation around the new operating point. This intermediate phase can be seen from 1.5 to 2.5 h of the experiment, after switching to dynamic operation. For the evaluation of the time-average, only the periods of the stable periodic range are used. Such transient behavior is apparent for all the output values. The measured conductivity κ and reactor temperature T_R, and subsequently, the calculated product concentration c_P and molar outlet flow $\dot{n}_P$ present a constant profile.

Figure 8.14 illustrates the interconnection of the output with the input. The temperature is not in phase with the molar product flow, but with the concentration. The exothermic behavior of the reaction generates heat. With increased concentration and residence time, the reaction rate is enhanced, leading to a higher energetic release. In the following, the total flow rate increases, which leads to a change in $\dot{n}_P$ and a reduced residence time. In parallel, the inlet concentration decreases and consequently the temperature, due to less energy being released.

In this experiment, the relevant mean value of the desired product is lower than the mean value of the steady-state operation due to the dynamic operating mode. Furthermore, it is shown that the molar flow does not follow an ideal sine function. This result is due to the shifted functions for input concentration and total flow. Nevertheless, an increase in yield is achieved. This yield is based on the combination of concentration and total flow to calculate, as shown in eq. 8.29, the average input molar flow in the periodic operating range. For the case shown here, with a frequency of $4.167 \cdot 10^{-4}$ Hz, a phase shift of 157.33°, and the amplitudes for concentration of 85 % and total flow rate of 55 %, an absolute change ΔY of 4.1 % from periodic operation to steady-state operation could be achieved. This change in yield is in good agreement with the prediction of the NFR method, with 5.95 % of increased yield.

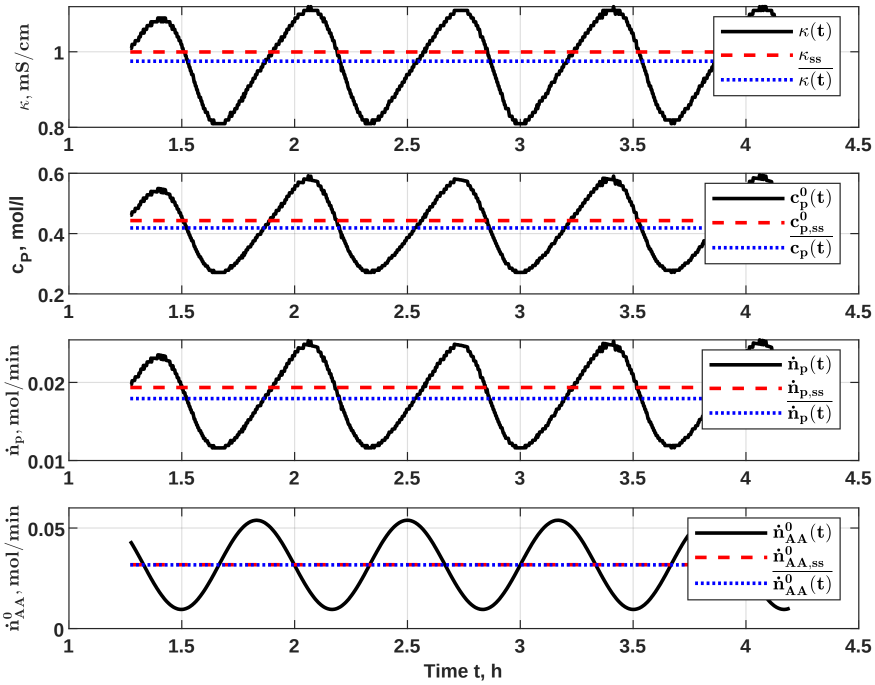

Figure 8.13: Multiple input parameter modulation of inlet concentration A_C = 85 %, total flow rate A_F = 55 % and a period of 40 min, presenting conductivity at the outlet (top), product concentration at the outlet (second), molar product flow (third) and inlet molar product flow (bottom) for a phase difference ϕ = 157.33 °.

It could be shown that implementation of multiple simultaneous input parameter variations is possible and that the achieved absolute change ΔY of the average yield $\overline{Y}$ during dynamic operation, concerning the steady-state value $Y_{P,s}$, is in good agreement with the predicted changes by the NFR method.

As the next step, an experimental study of the predictions by the NFR method for individually varying amplitudes and the phase shift is presented.

8.4.1 Variation of Inlet Concentration Amplitude

Table 8.4 summarizes the time-average yield for periodic operation with a varying amplitude of the input concentration. At the same time, the total flow rate variation is kept constant and a respective optimum phase shift is applied in each case.

Following the theory (section 8.1.2), the variation of a single input variable has presented a detrimental influence on the desired target variable, the yield. However, the NFR method derived by the collaborators at the University of Belgrade for the present chemical system, indicated that you multiple input parameter variations applied simultaneously, significant improvements can be achieved. This was shown above under the chosen standard dynamic conditions.

For the variation of A_C, interestingly, the optimal phase shift varies in an approximately constant

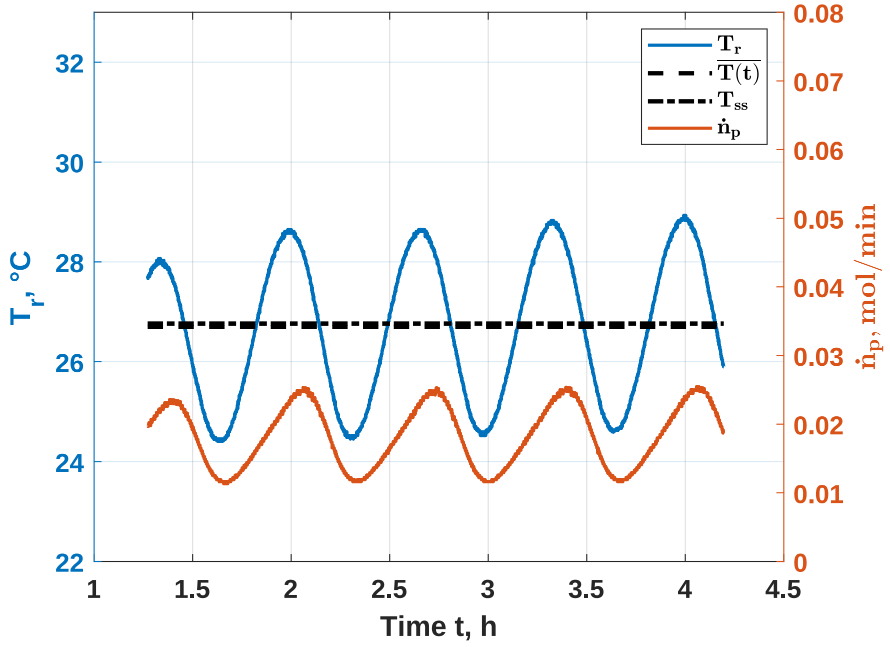

Figure 8.14: Multiple input parameter modulation of inlet concentration A_C = 85 %, total flow rate A_F = 55 % and a period of 40 min, presenting reactor temperature (blue) and molar product flow (orange) over the time of periodic operation with a phase difference ϕ = 157.33 °.

Table 8.4: Predicted dynamic results by the NFR method for varying inlet concentration amplitude A_C, with fixed amplitudes for total flow rate A_F = 55 % and period of 40 min, for the yield obtained by dynamic operation implying an optimal phase difference ϕ_{opt}.

Period [min]	**Amplitudes**		**Phase difference** [rad]	**Product yield,** Y_P **[%], NFR**	**Absolute change,** ΔY_P **[%], NFR**
	Inlet concentration [%]	**flow rate [%]**			
40	0	55	0	34.38	-0.52
	10		2.6575	35.07	0.17
	20		2.6702	35.78	0.88
	30		2.6825	36.50	1.66
	40		2.6945	37.24	2.34
	50		2.7063	38.00	3.10
	60		2.7179	38.79	3.89
	70		2.7292	39.61	4.71
	80		2.7404	40.45	5.55
	90		2.7514	41.33	6.43
	100		2.7623	42.24	7.34

range just below a complete shift of the minima and maxima, with 152 to 158°. This corresponds to a periodic switch in the range of $5/6\pi$. As the amplitude of the input concentration increases, the phase difference increases insignificantly and the improvement is linearly enhanced. This observation presents the fact that for higher fluctuations in concentration, corresponding to higher dynamic modulations, intensified output changes can be expected.

Figure 8.15 shows the absolute change in yield ΔY of the theoretical predictions by the NFR method

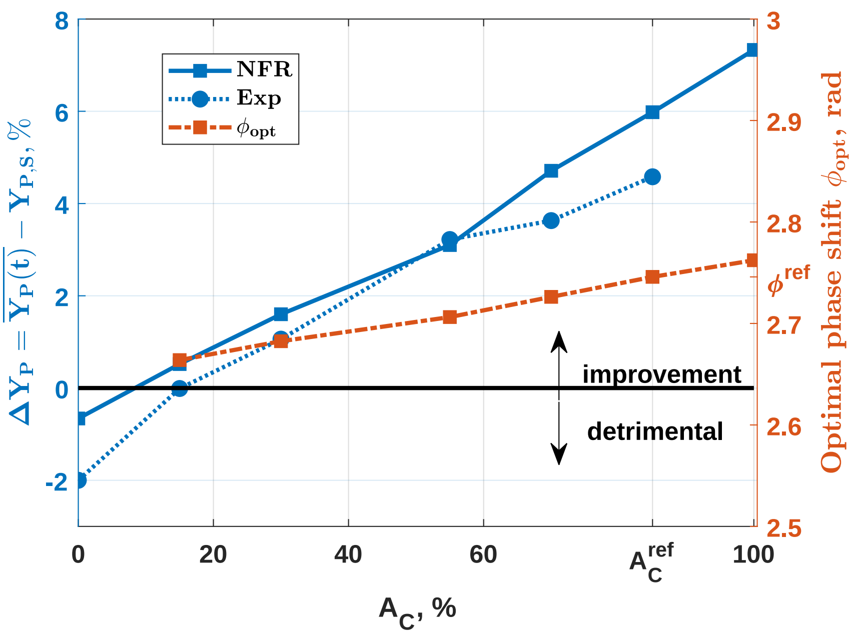

Figure 8.15: Results of predicted and experimental of absolute change in product yield (eq. (8.30)) by dynamic operation for varying inlet concentration amplitude A_C, with a fixed amplitude for total flow rate A_F = 55 % and period of 40 min, for the yield obtained by dynamic operation implying an optimal phase difference ϕ_{opt}.

(triangles) and the experimental values (circles) for varying amplitude of the input concentration A_c. The two graphs show that the absolute changes obtained experimentally are in good agreement with the predictions. For the areas in which deterioration is expected, these also occur in reality. The experiments confirm the linearly increasing course of the improvement. Especially, in the range from 30 to 60 % amplitude, a great agreement can be seen.

Only the highest amplitude of 90 % differs significantly. This result is assumed to be the reason for the limitation of the equipment, with the flow rates being too small for the pumps to sufficiently supply the desired operating parameters.

8.4.2 Variation of Total Flow Rate Amplitude

In the case of a variation of the amplitude for the total flow, a similar trend is observable with increasing amplitude value. As the value of the amplitude increases, both the value of the phase shift increases towards a shift of π, and the expected mean yield increases as well, see Table 8.5. Again, this effect is ascribed to the intensified periodic behavior due to higher fluctuations.

What is striking here, the theoretically achievable mean yield for an amplitude of zero, corresponding to the single modulation of the amplitude for the concentration, predicts a slight deterioration and then continues to increase linearly with a significantly larger slope than for the concentration amplitude. In the case of a hundred percent oscillation of the total flux, up to 14 % improvement is predicted compared to 8 % for inlet concentration. Accordingly, selected points were approached analogous to the previous experiments and are shown in Figure 8.16.

In the range of low amplitudes, the prediction is below the values obtained experimentally. Thus, the effective improvement by the forced dynamic operation is stronger than predicted. As the amplitude

Table 8.5: Predicted dynamic results by the NFR method for varying inlet concentration amplitude A_F, with fixed amplitudes for inlet concentration A_C = 85 % and period of 40 min, for the yield obtained by dynamic operation implying an optimal phase difference.

Period **[min]**	**Amplitudes**		**Phase difference [rad]**	**Product yield, Y_P [%], NFR**	**Absolute change, ΔY_P [%], NFR**
	Inlet concentration [%]	**flow rate [%]**			
40	85	0	0	34.24	-0.66
		10	2.6619	35.31	0.41
		20	2.6814	36.43	1.53
		30	2.7003	37.61	2.71
		40	2.7188	38.86	3.96
		50	2.7370	40.19	5.29
		60	2.7548	41.61	6.71
		70	2.7725	43.13	8.23
		80	2.7900	44.80	9.90
		90	2.8074	46.62	11.72
		100	2.8248	48.63	13.73

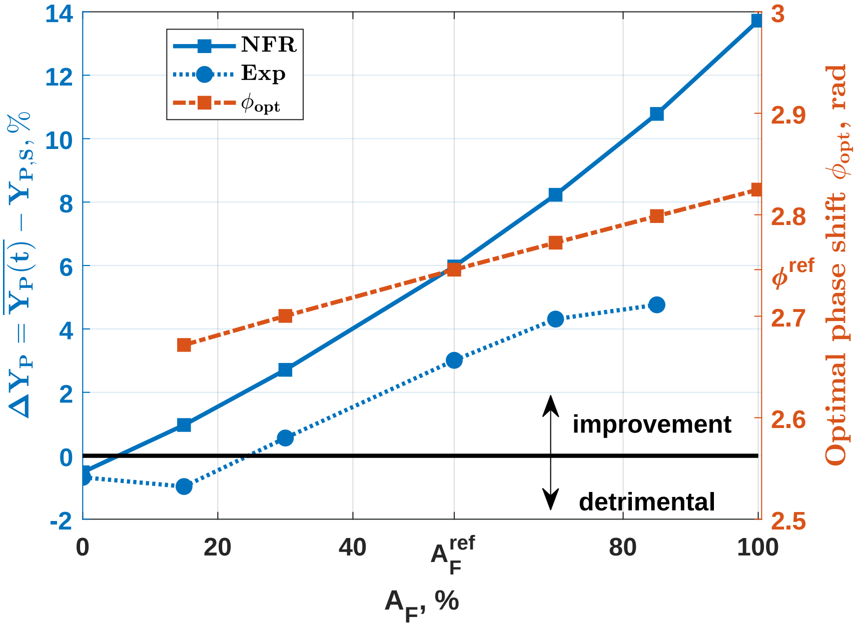

Figure 8.16: Results of predicted and experimental of absolute change in product yield (eq. (8.30)) by dynamic operation for varying total flow rate amplitude A_F, with a fixed amplitude for inlet concentration A_C = 85 % and period of 40 min, for the yield obtained by dynamic operation implying an optimal phase difference.

value increases, the course of the experimental results flattens. The two curves intersect in the middle range of the amplitude, which corresponds to the conditions selected for a standardized test. Over the further course, the curve of the experiments is completely flattened and shows no analogously increasing values and even a decreasing course.

Effects seem to occur within the reaction system that are to be considered by the predictions of the NFR. Furthermore, apparatus aspects are also conceivable. The aging process of the probe may have been advanced at this point, leading to irregularities. Moreover, it is realistic that the pumps used could have had problems with low flow rates due to strong fluctuations. Necessary minimal flows or voltages may have been undercut. It is conceivable that in these cases no component was temporarily introduced into the system, leading to different chemical behavior. Speculation is not appropriate at this point, because it could be shown that improvements can be achieved and this is an interesting and relevant measure. However, further limits by the experimental setup must be considered for implementable dynamic parameters.

8.4.3 Variation of Phase Difference

Last, both amplitudes are kept constant and the influence of the phase shift is evaluated. A different course is predicted for the variation of the phase shift, presented in Table 8.6. If the two fluctuated parameters oscillate in the same phase, then the highest reaction rate, due to the highest concentration in the maximum, corresponds to the lowest residence time in the reactor by the highest flow rate. Accordingly, the system is not given enough time to convert the reactants to the desired product sufficiently, corresponding to a deterioration in the yield change.

Table 8.6: Predicted dynamic results by the NFR method for varying phase difference ϕ, with fixed amplitudes for inlet concentration A_C = 85 % and total flow rate A_F = 55 %, for the yield obtained by dynamic operation implying.

Period	**Amplitudes**		**Phase difference [rad]**	**Phase difference [°]**	**Product yield, Y_P [%], NFR**	**Absolute change, ΔY_P [%], NFR**
[min]	**Inlet concentration [%]**	**flow rate [%]**				
40	85	55	0	0	29.73	-5.17
			0.7854	45	32.41	-2.49
			1.5708	90	36.48	1.58
			2.3562	135	40.24	5.34
			2.5714	147.33	40.75	5.85
			2.7459	157.33	40.88	5.98
			2.9205	167.33	40.74	5.84
			3.1416	180	40.16	5.26
			3.9270	225	35.57	0.67
			4.7124	270	30.97	-3.93
			5.4978	315	29.06	-5.84
			5.9690	324	29.00	-5.90

According to theory, an improvement can be achieved with an increasing phase shift, as given in Table 8.6. The optimal value is in close range of the complete shift of the extrema of the input parameters to each other. Accordingly, a high concentration is associated with a lower flow rate. Thus, the high reaction rate based on high concentration has significantly more time to react and thus achieves higher yields. If the yield is at its maximum, the concentration is lowered and in parallel, the volumetric flow is increased. Meaning that the concentration front is quickly moving out of the reactor. As the process progresses, the reaction rate is minimal and the reactor only has little time to react at this point. As a result, an average value can be calculated, which can result in a beneficial outcome for the selected amplitudes and frequency. The table also shows that further increase in the phase shift results in a deterioration of the change compared to the optimum phase shift. Thus, a clear maximum is recognizable, with a Gaussian-like distribution curve.

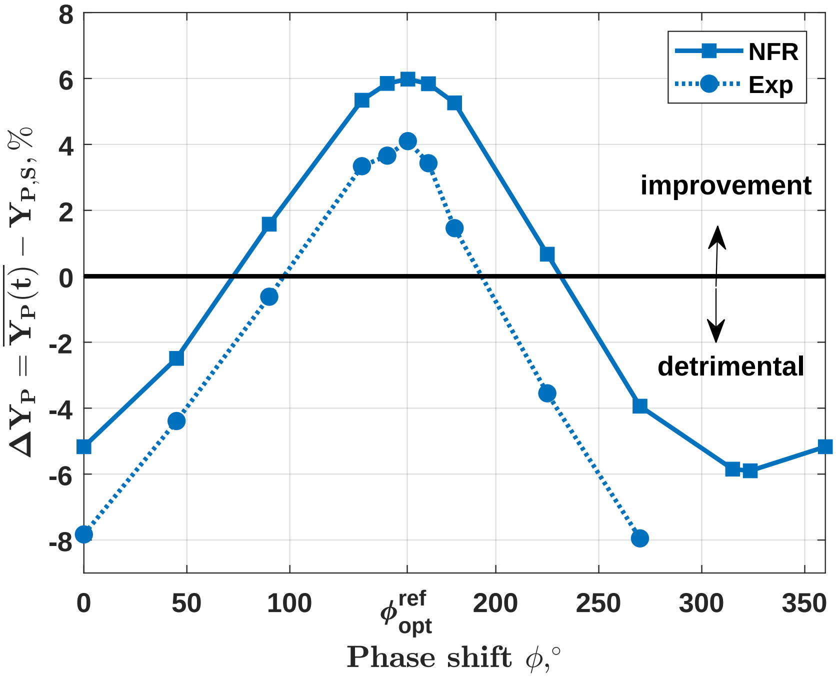

Figure 8.17: Results of predicted and experimental of absolute change in product yield (eq. (8.30)) by dynamic operation for varying phase difference ϕ, with fixed amplitudes for inlet concentration A_C = 85 % and total flow rate A_F = 55 %, for the yield obtained by dynamic operation implying.

The experimental implementation (Figure 8.17) reveals that the trend of the NFR predictions can be represented by the experiments in the case of the variation of the phase shift. In areas with low phase shift, a negative influence on the change of what becomes apparent. Compared to the theoretical prediction, the effect is further enhanced. In contrast to the expected 3 - 5 % losses, -8 % is realized in the experiment. With an increasing phase shift, the value of the absolute change also increases analogously. A good agreement of the experimentally obtained and the predicted absolute change in yield can be determined for the optimal phase angle. However, with a further increase, the improvement increases even further. This result contradicts the NFR predictions. Though, the trend is valid.

At the presented optimum, an improvement in the normalized product yield of periodic operation of ΔY_P^{exp} = 4.1 % is achieved (Figure 8.17) under the chosen reference conditions. This corresponds to a $Y_P^{norm,exp}$ of 1.11 This improvement is slightly lower than predicted by the NFR method, ΔY_P^{NFR} = 5.9 % and $Y_P^{norm,NFR}$ = 1.17 (see Figures 8.3a and 8.17). The reduced experimentally observed yield gain agrees with the fact, that the reactor appears to be not fully adiabatic and is, thus, characterized by a conversion loss.

Additionally, the predicted trend of resulting absolute change in yield illustrates that, according to the formula for the optimal phase shift (eq. 8.15), a value exists which maximizes the detrimental behavior. This point is achieved when the phase shift is further increased. After reaching this minimum at 324° the trend is again increasing and results consequently for 360° in the same change as for 0°.

There seem to be effects that are currently not covered by the kinetic model. Furthermore, anhydride may have already reacted in advance with moisture in the air to form the product, or aging of the probe that cannot be precisely described has an influence on the values. However, this was corrected by checking with a standard solution, which minimized the error as far as possible. Repetition measurements always showed approximately the same result as previously measured.

8.5 Conclusion

In the present chapter, forced dynamic reactor operation was investigated theoretically and experimentally. Nonlinear frequency response (NFR) analysis was applied to evaluate periodic operating parameters and predict mean values of desired parameters for single and simultaneous modulation of multiple input parameters. The hydrolysis of acetic anhydride in an adiabatic continuously stirred tank reactor (CSTR) was applied as an example reaction. The following results were derived:

(a) A reactor setup for the dynamic operation was realized for the accurate implementation of single and simultaneous modulation of multiple input parameters.

(b) Predictions of the nonlinear frequency response (NFR) identified interesting operational regions and forcing parameters with beneficial time-average output changes.

(c) The trends of the experimentally obtained output changes by excitation with harmonic input functions are in good agreement with the prediction by the nonlinear frequency response method.

(d) The results stress the importance of the applied forcing parameters, particularly of the optimal phase difference ϕ_{opt}.

In summary, the NFR method can predict whether and to what extent an output change will occur under forced periodic operation. The quantitative projection of the mean output signals were validated in corresponding experiments. For the first time, the simultaneous modulation of two input parameters with a specific phase shift was studied in such a systematic way revealing a high potential to improve the performance of a chemical reactor.

Part IV

Concluding Remarks

9 Concluding Remarks and Outlook

> *Imagination is more important than knowledge. Imagination is the language of the soul. Pay attention to your imagination and you will discover all you need to be fulfilled.*
>
> —Albert Einstein

9.1 Conclusions

In the present work investigations of dynamically operated chemical reactors were performed based on detailed experimental and simulative studies. Inherent and forced dynamic operations were considered and evaluated for two case studies.

Decisive for the performance of respective continuously operated processes is the time-averaged value of desired output parameters, such as activity, yield or molar product flow. It is desirable to quantify the influence of the dynamic operation for a chemical system on the desired parameter in advance. Suitable parameters and operating conditions for dynamic operation need to be identified. In this thesis, methodological approaches have been developed, applied and evaluated to predict the output of different systems. For the inherent dynamics a heterogeneous reaction and for the forced dynamic operation a homogenous process were employed.

Inherent Dynamic Reactor Operation Part (II)

As an example of inherent dynamic operation, the direct conversion of ethene to propene was investigated using a heterogeneous catalyst (Ni/AlMCM-41). In the case of heterogeneously catalyzed reactions, the dynamics are introduced by the deactivating catalyst itself, leading to multiple process steps. The catalyst loses activity with time-on-stream and regeneration is required for continued application of the catalyst.

Based on the results of a performed preliminary theoretical study, it could be shown that optimization of the cyclic operation is possible by identification of suitable termination criteria (**chapter 4**). For a proper reactor operation, significantly faster regeneration than deactivation is desirable to increase the performance. This reduces the time-frame without any product generated and increases the process productivity.

Employing an aluminized and nickel-incorporated MCM-41, the reaction network for the ETP reaction could be validated (**chapter 5**). Catalytic cracking was considered to occur in addition to di-/oligomerization and isomerization based on product spectrum analysis for varying reaction conditions. This conclusion explains the selective formation of propene at elevated temperatures (>300 °C). Based on these findings, extended catalytic cycles were postulated and ongoing individual reactions (step 1) were quantified.

The effect of catalyst deactivation (step 2) can be described adequately using simplified models. According to the literature, different coke species form, resulting in blockage of the active catalyst sites. The temperature significantly influences the rate at which carbon is deposited. The necessary removal of the distributed coke was analyzed by thermogravimetric analysis (TGA) measurements. With these results, a suitable regeneration (step 3) strategy was developed. The rate of the regeneration step is considerably dependent on the temperature as well. Under optimized regeneration conditions, the catalysts operation time could be extended to more than 2000 h.

For the mentioned steps of reaction, deactivation and regeneration in the investigated case study, kinetic approaches were applied for mathematical evaluation and parametrization (**chapter 6**). Based on the experiments performed, the postulated catalytic cycles could be validated. The reaction network connected to cracking and the Langmuir-Hinshelwood-Hougen-Watson (LHHW) approach result in the highest qualitative agreement of the theoretical values with the experimental data. The deactivation can be represented, by proportionally coupling the conversion with a time-dependent activity function. Furthermore, a kinetic model for the regeneration could be derived and kinetic parameters were determined that represent the experiments well using thermogravimetric analysis (TGA) data. Thus, it is possible to predict all three partial steps of the production cycle. The ratio of reaction time to regeneration time can be maximized to improve the overall process.

Forced Dynamic Reactor Operation Part (III)

A recently developed method for predicting the time-average of forced periodic modulations of input parameters is the nonlinear frequency response (NFR). Analytical equations can be obtained and optimal dynamic parameters can be predicted. The NFR method is capable of predicting the change in parameter outputs for the variation of one as well as the simultaneous modulation of multiple inlets. The periodic analysis was applied to the homogeneous hydrolysis of acetic anhydride. Based on simple power-law kinetics (**chapter 7**), interesting operating conditions and forcing parameters could be determined (**chapter 8**). A dynamically operated experimental setup was developed in which both steady-state and dynamic experiments could be performed. The plant automation allowed the perturbation of several input parameters according to the desired specifications. Both, single parameter variation and the simultaneous modulation of multiple input parameters (inlet concentration and total volumetric flow rate) were investigated were performed. A highlight result is the realization of simultaneous fluctuation of two input parameters with adequate precision and an applied optimal phase shift. The obtained improvements are in good agreement with the predictions of the NFR method. As a key result, the particular importance of the phase shift was identified. For values far away from the optimum, deteriorations were verified. The maximum improvement was found exactly in the range of the optimum value predicted by the NFR method.

Summary

The availability of precise models and parameters for the dynamic reactor behavior and the individual process steps allows for the identification of optimized inherent and forced dynamic operation. Significant process intensification can be achieved for homogeneous and heterogeneous processes, compared to conventional steady-state approaches.

For the inherently dynamic process mode, enhancement can be realized by increasing the ratio of production time to regeneration time. The determination of suitable operating parameters is straightforward, but the exact implementation of termination criteria is complex.

Forced dynamic operation offers the possibility to precisely predict the output changes and determine optimal parameters, using the NFR method. These parameters can be imposed and reveal a potential for improvement, in particular when multiple inlets are perturbed simultaneously.

The methodological approaches developed and applied in the present work should promote the broader use of optimized dynamic reactor operation. The author hopes that the methodology of exploiting the dynamic operation of chemical reactors, especially against the background of the energy turnaround, will be used in the future to improve existing processes and inspire innovative new operational approaches.

9.2 Outlook

With the help of the models derived and the approaches developed here, prediction and evaluation of dynamic operation can be transferred to other reactions.

Considering the inherent dynamic reactor operation with the ETP, it is necessary to have an improved synthesis pathway of the AlMCM-41 carrier material. For larger quantities, reliable production is desired. It seems essential to verify the changing catalyst properties with spectroscopic analysis.

A further improvement of inherent dynamic reactor operation requires a significantly higher effort to analyze all relevant kinetic effects in detail. This effort is not necessarily justifiable in every case.

Concerning the forced dynamic mode of operation, it is of particular interest to modulate the temperature of the system in addition to the input concentration and the total volumetric flow. Further, a change of the shape of the input function for periodic modulation is of interest, using for example rectangular or other suitable functions instead of sinusoidal harmonics. This can exploit the effect of nonlinearities in the model even more. The NFR method can be applied also to analyse more complex reaction systems.

Furthermore, it is useful to apply forced periodic operation to reactions that have a reaction order higher than one. For example, dimerization or esterification would be potentially interesting, since all reactants contribute to the reaction rate. In this context, within the framework of the priority program (SPP2080), funded by the German Science Foundation (DFG), the forced dynamic mode of operation is currently applied to the mechanistically complex and heterogeneously catalyzed methanol synthesis. The nonlinear frequency response (NFR) will be used to evaluate the forced dynamic operation. In an ideal continuously stirred tank reactor (CSTR), of the Berty-type a periodic perturbation of the system will be induced. Methanol is currently of large interest in connection with the storage of renewable energies due to its application in the production of paraffins, olefins and other organics.

Bibliography

[Aaron and Tsouris, 2005] Aaron, D. and Tsouris, C. (2005). Separation of co_2 from flue gas: A review. *Separation Science and Technology*, 40(1-3):321–348.

[Afandizadeh and Foumeny, 2001] Afandizadeh, S. and Foumeny, E. A. (2001). Design of packed bed reactors: guides to catalyst shape, size and loading selection. *Applied Thermal Engineering*, 21:669–682.

[Aguayo et al., 1999] Aguayo, A. T., Sanchez del Campo, Ana E., Gayubo, A. G., Tarrío, A. M., and Bilbao, J. (1999). Deactivation by coke of a catalyst based on a sapo-34 in the transformation of methanol into olefins. *J. Chem. Tech. Biotechnol.*, 74:315–321.

[Alvarado Perea, 2014] Alvarado Perea, L. (28.03.2014). *Direct conversion of ethene to propene on Ni-alumino-mesostructured catalysts: synthesis, characterization and catalytic testing.* PhD thesis, Otto-von-Guericke Universität, Magdeburg.

[Alvarado Perea et al., 2017] Alvarado Perea, L., Felischak, M., Wolff, T., Hamel, C., and Seidel-Morgenstern, A. (2017). Experimental investigation of the reaction network of ethene to propene over ni/almcm-41 catalysts. *Chemie Ingenieur Technik*, 89(7):903–914.

[Alvarado Perea et al., 2021] Alvarado Perea, L., Felischak, M., Wolff, T., López Gaona, J. A., Hamel, C., and Seidel-Morgenstern, A. (2021). Propene production at low temperature by bimetallic ni-mo and ni-re catalysts on mesoporous mcm-41 prepared using template ion exchange. *Fuel*, 284:119031.

[Alvarado Perea et al., 2017] Alvarado Perea, L., Wolff, T., Hamel, C., and Seidel-Morgenstern, A. (2017). Experimental study of the deactivation of ni/almcm-41 catalyst in the direct conversion of ethene to propene. *Applied Catalysis A: General*, 533:121–131.

[Alvarado Perea et al., 2013] Alvarado Perea, L., Wolff, T., Veit, P., Hilfert, L., Edelmann, F. T., Hamel, C., and Seidel-Morgenstern, A. (2013). Alumino-mesostructured ni catalysts for the direct conversion of ethene to propene. *Journal of Catalysis*, 305:154–168.

[Alvarez et al., 1996] Alvarez, F., Ribeiro, F. R., Perot, G., Thomazeau, C., and Guisnet, M. (1996). Hydroisomerization and hydrocracking of alkanes: 7. influence of the balance between acid and hydrogenating functions on the transformation of n-decane on pthy catalysts. *Journal of Catalysis*, 162:179–189.

[Alwahabi and Froment, 2004] Alwahabi, S. M. and Froment, G. F. (2004). Single event kinetic modeling of the methanol-to-olefins process on sapo-34. *Industrial & Engineering Chemistry Research*, 43(17):5098–5111.

[Amakawa et al., 2012] Amakawa, K., Wrabetz, S., Kröhnert, J., Tzolova-Müller, G., Schlögl, R., and Trunschke, A. (2012). In situ generation of active sites in olefin metathesis. *Journal of the American Chemical Society*, 134(28):11462–11473.

[Amenaghawon et al., 2013] Amenaghawon, N. A., Osagie, E. I., Osemwengie, S. O., Ogbeide, S. E., and Okieimen, C. O. (2013). Modelling acetic anhydride synthesis. *Nigerian Journal of Technology*, 32(3):386–392.

[Amghizar et al., 2017] Amghizar, I., Vandewalle, L. A., van Geem, K. M., and Marin, G. B. (2017). New trends in olefin production. *Engineering*, 3(2):171–178.

[Amigues et al., 1991] Amigues, P., Chauvin, Y., Commereuc, D., Hong, C. T., Lai, C. C., and Liu, Y. H. (1991). Methathesis of ethylene-butene mixtures to propylene with rhenium on alumina catalysts. *Journal of Molecular Catalysis*, 65(1-2):39–50.

[Amin and Anggoro, 2003] Amin, N. and Anggoro, D. D. (2003). Characterization and activity of cr, cu and ga modified zsm-5 for direct conversion of methane to liquid hydrocarbons. *Journal of Natural Gas Chemistry*, 12:123–134.

[Ampelli et al., 2005] Ampelli, C., Di Bella, D., Lister, D. G., and Maschio, G. (2005). Fitting isoperibolic calorimeter data for reactions with pseudo-first order chemical kinetics. *Journal of Thermal Analysis and Calorimetry*, 79:89–94.

[Ampelli et al., 2003] Ampelli, C., Di Bella, D., Lister, D. G., Maschio, G., and Parisi, J. (2003). The integration of an ultraviolet-visible spectrometer and a reaction calorimeter. *Journal of Thermal Analysis and Calorimetry*, 72:875–883.

[Andrei et al., 2016] Andrei, R. D., Popa, M. I., Cammarano, C., and Hulea, V. (2016). Nickel and molybdenum containing mesoporous catalysts for ethylene oligomerization and metathesis. *New J. Chem.*, 40(5):4146–4152.

[Andrei et al., 2015] Andrei, R. D., Popa, M. I., Fajula, F., Cammarano, C., Khudhair, A. A., Bouchmella, K., Mutin, P. H., and Hulea, V. (2015). Ethylene to propylene by one-pot catalytic cascade reactions. *ACS Catalysis*, 5(5):2774–2777.

[Antic, 2014] Antic, D. (2014). Hydrolysis of acetic anhydride with heavy water (d2o).

[Argyle and Bartholomew, 2015] Argyle, M. and Bartholomew, C. (2015). Heterogeneous catalyst deactivation and regeneration: A review. *Catalysts*, 5(1):145–269.

[Argyle et al., 2014] Argyle, M. D., Frost, T. S., and Bartholomew, C. H. (2014). Cobalt fischer–tropsch catalyst deactivation modeled using generalized power law expressions. *Topics in Catalysis*, 57(6-9):415–429.

[Asiedu et al., 2013] Asiedu, N., Hildebrandt, D., and Glasser, D. (2013). Kinetic modeling of the hydrolysis of acetic anhydride at higher temperatures using adiabatic batch reactor (thermos-flask). *Journal of Chemical Engineering & Process Technology*, 04(09).

[Asprey et al., 1996] Asprey, S. P., Wojciechowski, B. W., Rice, N. M., and Dorcas, A. (1996). Applications of temperature scanning in kinetic investigations: The hydroylsis of acetic anhydride. *Chemical Engineering Science*, 51(20):4681–4692.

[Atanga et al., 2018] Atanga, M. A., Rezaei, F., Jawad, A., Fitch, M., and Rownaghi, A. A. (2018). Oxidative dehydrogenation of propane to propylene with carbon dioxide. *Applied Catalysis B: Environmental*, 220:429–445.

[Baerns, 2013] Baerns, M. (2013). *Technische Chemie*. Wiley, Hoboken, 2nd ed. edition.

[Baerns et al., 1992] Baerns, M., Hofmann, H., and Renken, A., editors (1992). *Lehrbuch der technischen Chemie*. Thieme, Stuttgart, 2., durchges. aufl. edition.

[Bailey and Horn, 1972a] Bailey, J. E. and Horn, F. (1972a). Cyclic operation of reaction systems: the influence of diffusion on catalyst selectivity. *Chemical Engineering Science*, 27(1):109–119.

[Bailey and Horn, 1972b] Bailey, J. E. and Horn, F. (1972b). Cyclic operation of reaction systems: the influence of diffusion on catalyst selectivity. *Chemical Engineering Science*, 27:109–119.

[Bailey and Horn, 1969] Bailey, J. E. and Horn, F. J. M. (1969). Catalyst selectivity under steady-state and dynamic operation. *Berichte der Bunsengesellschaft*, 73(3):274–279.

[Bailey and Horn, 1971a] Bailey, J. E. and Horn, F. J. M. (1971a). Comparison between two sufficient conditions for improvement of an optimal steady-state process by periodic operation. *Journal of Optimization Theory and Applications*, 7(5):378–384.

[Bailey and Horn, 1971b] Bailey, J. E. and Horn, J. M. (1971b). Comparison between two sufficient conditions for improvement of an optimal steady-state process by periodic operation. *Journal of Optimization Theory and Applications*, 7(5):378–384.

[Baird and Lunsford, 1972] Baird, M. J. and Lunsford, J. H. (1972). Catalytic sites for the isomerization of 1-butene over magnesium oxide. *Journal of Catalysis*, 26:440–450.

[Bakala et al., 2008] Bakala, P., Briot, E., Millot, Y., Piquemal, J., and Bregeault, J. (2008). Comparison of olefin metathesis by rhenium-containing γ-alumina or silica–aluminas and by some mesoporous analogues. *Journal of Catalysis*, 258(1):61–70.

[Balcar et al., 2007] Balcar, H., Hamtil, R., Žilková, N., Zhang, Z., Pinnavaia, T. J., and Čejka, J. (2007). Re(vii) oxide on mesoporous alumina of different types—activity in the metathesis of olefins and their oxygen-containing derivatives. *Applied Catalysis A: General*, 320:56–63.

[Balcar et al., 2004] Balcar, H., Hamtil, R., and Zilková, Nadezda, Cejka, Jiri (2004). Rhenium oxide supported on mesoporous organised alumina as a catalyst for metathesis of 1-alkenes. *Catalysis Letters*, 97(1-2):25–29.

[Balcar et al., 2009] Balcar, H., Mishra, D., Marceau, E., Carrier, X., Žilková, N., and Bastl, Z. (2009). Molybdenum oxide catalysts for metathesis of higher 1-alkenes via supporting moo2(acetylacetonate)2 and moo2(glycolate)2 on sba-15 mesoporous molecular sieves. *Applied Catalysis A: General*, 359(1-2):129–135.

[Bartholomew, 1982] Bartholomew, C. H. (1982). Carbon deposition in steam reforming and methanation. *Catalysis Reviews*, 24(1):67–112.

[Bates and Watts, 2007] Bates, D. M. and Watts, D. G. (2007). *Nonlinear regression analysis and its applications.* Wiley-Interscience paperback series. Wiley, New York, NY.

[Beirnaert et al., 2001] Beirnaert, H. C., Alleman, J. R., and Marin, G. B. (2001). A fundamental kinetic model for the catalytic cracking of alkanes on a usy zeolite in the presence of coke formation. *Industrial & Engineering Chemistry Research*, 40(5):1337–1347.

[Bell et al., 1998] Bell, W. C., Booksh, K. S., and Myrick, M. L. (1998). Monitoring anhydride and acid conversion in supercritical/hydrothermal water by in situ fiber-optic raman spectroscopy. *Analytical Chemistry*, 70(2):332–339.

[Bellare and Dadyburjor, 1993] Bellare, A. and Dadyburjor, D. B. (1993). Evaluation of modes of catalyst deactivation by coking for cumene cracking over zeolites. *Journal of Catalysis*, 140:510–525.

[Beller, 2012] Beller, M., editor (2012). *Catalysis: From principles to applications.* Wiley-VCH-Verl., Weinheim.

[Bhuiyan et al., 2013] Bhuiyan, T. I., Arudra, P., Akhtar, M. N., Aitani, A. M., Abudawoud, R. H., Al-Yami, M. A., and Al-Khattaf, S. S. (2013). Metathesis of 2-butene to propylene over w-mesoporous molecular sieves: A comparative study between tungsten containing mcm-41 and sba-15. *Applied Catalysis A: General*, 467:224–234.

[Bisio and Kabel, 1985] Bisio, A. and Kabel, R. L. (1985). *Scaleup of chemical processes: Conversion from laboratory scale tests to successful commercial size design.* J. Wiley, New York (etc.).

[Blackwell et al., 2000] Blackwell, H. E., O'Leary, D. J., Chatterjee, A. K., Washenfelder, R. A., Bussmann, D. A., and Grubbs, R. H. (2000). New approaches to olefin cross-metathesis. *Journal of the American Chemical Society*, 122(1):58–71.

[Bonneviot et al., 1983] Bonneviot, L., Olivier, D., and Che, M. (1983). Dimerization of olefins with nickel-surface complexes in x-type zeolite or on silica. *Journal of Molecular Catalysis A: Chemical*, 21:415–430.

[Bortnovsky et al., 2005] Bortnovsky, O., Sazama, P., and Wichterlova, B. (2005). Cracking of pentenes to c2–c4 light olefins over zeolites and zeotypes. *Applied Catalysis A: General*, 287(2):203–213.

[Bouchmella et al., 2013] Bouchmella, K., Hubert Mutin, P., Stoyanova, M., Poleunis, C., Eloy, P., Rodemerck, U., Gaigneaux, E. M., and Debecker, D. P. (2013). Olefin metathesis with mesoporous rhenium–silicium–aluminum mixed oxides obtained via a one-step non-hydrolytic sol–gel route. *Journal of Catalysis*, 301:233–241.

[Broene et al., 2005] Broene, R. D., Brookhart, M., Lamanna, W. M., and Volpe, A. F. (2005). Cobalt-catalyzed dimerization of α-olefins to give linear α-olefin products. *Journal of the American Chemical Society*, 127(49):17194–17195.

[Buchanan et al., 1996] Buchanan, J. S., Santiesteban, J. G., and Haag, W. O. (1996). Mechanistic considerations in acid-catalyzed cracking of olefins. *Journal of Catalysis*, 158:279–287.

[Buluchevskiy et al., 2014] Buluchevskiy, E. A., Lavrenov, A. V., and Sayfulina, L. F. (2014). Kinetics of direct synthesis of ethylene to propylene on pdo-re2o7-b2o3-al2o3 in liquid phase. *Journal of Siberian Federal University*, 3(7):424–430.

[Bunimovich et al., 2008] Bunimovich, G., Silveston, P. L., and Matros, Y. S. (2008). "unsteady-state reactor operation" in: Handbook of heterogeneous catalysis online. In Ertl, G., Knözinger, H., Schüth, F., and Weitkamp, J., editors, *Handbook of heterogeneous catalysis*, pages 2156–2174. Wiley-VCH, Weinheim.

[Busca et al., 1998] Busca, G., Lietti, L., Ramis, G., and Berti, F. (1998). Chemical and mechanistic aspects of the selective catalytic reduction of nox by ammonia over oxide catalysts: A review. *Applied Catalysis B: Environmental*, 18:1–36.

[Butt, 1980] Butt, J. B. (1980). Catalyst poisoning and chemical process dynamics. In *Catalyst Deactivation*, volume 6 of *Studies in Surface Science and Catalysis*, pages 21–41. Elsevier.

[Butt, 1984] Butt, J. B. (1984). Catalyst deactivation and regeneration. *Catalysis Science and Technology*, 6:1–63.

[Cavani et al., 2007] Cavani, F., Ballarini, N., and Cericola, A. (2007). Oxidative dehydrogenation of ethane and propane: How far from commercial implementation? *Catalysis Today*, 127(1-4):113–131.

[Chaemchuen et al., 2012] Chaemchuen, S., Phatanasri, S., Verpoort, F., Sae-ma, N., and Suriye, K. (2012). The structure-reactivity relationship for metathesis reaction between ethylene and 2-butene on wo3/sio2 catalysts calcinated at different temperatures. *Kinetics and Catalysis*, 53(2):247–252.

[Chauvin and Commereuc, 1992] Chauvin, Y. and Commereuc, D. (1992). Chemical counting and characterization of the active sites in the rhenium oxide/alumina metathesis catalyst. *J. Chem. Soc., Chem. Commun.*, pages 462–464.

[Chen et al., 2014] Chen, C.-J., Rangarajan, S., Hill, I. M., and Bhan, A. (2014). Kinetics and thermochemistry of c 4 –c 6 olefin cracking on h-zsm-5. *ACS Catalysis*, 4(7):2319–2327.

[Chen et al., 2013] Chen, S.-L., Wang, Y., Yuan, G., Hua, D., Zheng, M., and Zhang, J. (2013). Metathesis of ethene and decene to propene over a wo 3 /sio 2 catalyst. *Chemical Engineering & Technology*, 36(5):795–800.

[Cleland and Wilhelm, 1956] Cleland, F. A. and Wilhelm, R. H. (1956). Diffusion and reaction in viscous-flow tubular reactor. *AIChE Journal*, 2(4):489–497.

[Conn et al., 1942] Conn, J. B., Kistiakowsky, G. B., Roberts, R. M., and Smith, E. A. (1942). Heats of organic reactions. xiii. heats of hydrolysis of some acid anhydrides. *Journal of the American Chemical Society*, 64(8):1747–1752.

[Corma et al., 2005] Corma, A., Melo, F. V., and Sauvanaud, L. (2005). Kinetic and decay cracking model for a microdowner unit. *Applied Catalysis A: General*, 287(1):34–46.

[Corma and Orchillés, 2000] Corma, A. and Orchillés, A. V. (2000). Current views on the mechanism of catalytic cracking. *Microporous and Mesoporous Materials*, 35-36:21–30.

[Coronas et al., 1995] Coronas, J., Menendez, M., and Santamaria, J. (1995). Use of a ceramic membrane reactor for the oxidative dehydrogenation of ethane to ethylene and higher hydrocarbons. *Ind. Eng. Chem. Res.*, 34:4229–4234.

[Cortright et al., 1997] Cortright, R. D., Dumesic, J. A., and Madon, R. J. (1997). Catalytic cycles for hydrocarbon cracking on zeolites. *Topics in Catalysis*, 4:15–26.

[Cramer, 1966] Cramer, R. (1966). Olefin coordination compounds of rhodium. iii. the mechanism of olefin isomerization. *Journal of the American Chemical Society*, 88(10):2272–2282.

[Currie et al., 2018] Currie, R., Nikolic, D., Petkovska, M., and Simakov, D. S. (2018). Co 2 conversion enhancement in a periodically operated sabatier reactor: Nonlinear frequency response analysis and simulation-based study. *Israel Journal of Chemistry*, 58(6-7):762–775.

[Dai et al., 2014] Dai, W., Sun, X., Tang, B., Wu, G., Li, L., Guan, N., and Hunger, M. (2014). Verifying the mechanism of the ethene-to-propene conversion on zeolite h-ssz-13. *Journal of Catalysis*, 314:10–20.

[Debecker et al., 2014] Debecker, D. P., Stoyanova, M., Rodemerck, U., Colbeau-Justin, F., Boissère, C., Chaumonnot, A., Bonduelle, A., and Sanchez, C. (2014). Aerosol route to nanostructured wo3-sio2-al2o3 metathesis catalysts: Toward higher propene yield. *Applied Catalysis A: General*, 470:458–466.

[Dejavifve, 1980] Dejavifve, P. (1980). Reaction pathways for the conversion of methanol and olefins on h-zsm-5 zeolite. *Journal of Catalysis*, 63(2):331–345.

[Ding et al., 2009] Ding, X., Geng, S., Li, C., Yang, C., and Wang, G. (2009). Effect of acid density of hzsm-5 on the oligomerization of ethylene in fcc dry gas. *Journal of Natural Gas Chemistry*, 18(2):156–160.

[Douglas, 1972a] Douglas, J. M. (1972a). *Process Dynamic and Control: Analysis of dynamic systems*, volume / James M. Douglas ; Vol. 1 of *Process dynamics and control.* Prentice-Hall, Englewood Cliffs, NJ.

[Douglas, 1972b] Douglas, J. M. (1972b). *Process dynamics and control: Control System Synthesis*, volume / James M. Douglas ; Vol. 2 of *Prentice-Hall International series in the physical and chemical engineering sciences.* Prentice-Hall, Englewood Cliffs, NJ.

[Douglas and Rippin, 1966] Douglas, J. M. and Rippin, D. (1966). Unsteady state process operation. *Chemical Engineering Science*, 21:305–315.

[Dumez and Froment, 1976] Dumez, F. J. and Froment, G. F. (1976). Dehydrogenation of 1-butene into butadiene. kinetics, catalyst coking, and reactor design. *Ind. Eng. Chem. Prod. Res. Dev.*, 15(2):291–301.

[Dyne et al., 1967] Dyne, S. R., Glasser, D., and King, R. P. (1967). Automatically controlled adiabatic reactor for reaction rate studies. *Review of Scientific Instruments*, 38(2):209–214.

[Eichel et al., 2020] Eichel, R.-A., Leitner, W., and Wagemann, K. (2020). Editorial - warum wir uns mit power-to-x beschäftigen. *Chemie Ingenieur Technik*, 92(1-2):3.

[Elnashaie and ElShishini, 1996] Elnashaie, S. S. E. H. and ElShishini, S. S. (1996). *Dynamic modelling, bifurcation and chaotic behaviour of gas-solid catalytic reactors*, volume 9 of *Topics in chemical engineering*. Gordon & Breach, [South Yarra, Victoria].

[Epelde et al., 2014a] Epelde, E., Aguayo, A. T., Olazar, M., Bilbao, J., and Gayubo, A. G. (2014a). Kinetic model for the transformation of 1-butene on a k-modified hzsm-5 catalyst. *Industrial & Engineering Chemistry Research*, 53(26):10599–10607.

[Epelde et al., 2014b] Epelde, E., Aguayo, A. T., Olazar, M., Bilbao, J., and Gayubo, A. G. (2014b). Modifications in the hzsm-5 zeolite for the selective transformation of ethylene into propylene. *Applied Catalysis A: General*, 479:17–25.

[Farhad Pour, 1976] Farhad Pour, A. (1976). *The unsteady State operation of chemical reactors*. Doktorarbeit, University College London, London.

[Farhadpour and Gibilaro, 1981] Farhadpour, F. A. and Gibilaro, L. G. (1981). On the optimal unsteady state operation of the continuous stirred tank reactor. *Chemical Engineering Science*, 36:143–147.

[Felischak et al., 2021] Felischak, M., Kaps, L., Hamel, C., Nikolic, D., Petkovska, M., and Seidel-Morgenstern, A. (2021). Analysis and experimental demonstration of forced periodic operation of an adiabatic stirred tank reactor: Simultaneous modulation of inlet concentration and total flowrate. *Chemical Engineering Journal*, 410:128197.

[Felischak et al., 2019] Felischak, M., Wolff, T., Alvarado Perea, L., Seidel-Morgenstern, A., and Hamel, C. (2019). Influence of process parameters on single bed ni/(al)mcm-41 for the production of propene from ethene feedstock. *Chemical Engineering Science*, 210:115246.

[Felischak et al., 2020] Felischak, M., Wolff, T., Alvarado Perea, L., Seidel-Morgenstern, A., and Hamel, C. (2020). Detailed kinetic model for the reaction of ethene to propene on ni/almcm-41. *Chemie Ingenieur Technik*, 92(5):564–574.

[Feng et al., 1993] Feng, W., Vynckier, E., and Froment, G. F. (1993). Single event kinetics of catalytic cracking. *Industrial & Engineering Chemistry Research*, 32(12):2997–3005.

[Fichtl et al., 2015] Fichtl, M. B., Schlereth, D., Jacobsen, N., Kasatkin, I., Schumann, J., Behrens, M., Schlögl, R., and Hinrichsen, O. (2015). Kinetics of deactivation on cu/zno/al2o3 methanol synthesis catalysts. *Applied Catalysis A: General*, 502:262–270.

[Fogler, 2006] Fogler, H. S. (2006). Catalyst decay. In *Elemenst of Chemical Reaction Engineering*, volume 4. Pearson Education.

[Frei et al., 2019] Frei, M. S., Mondelli, C., García-Muelas, R., Kley, K. S., Puértolas, B., López, N., Safonova, O. V., Stewart, J. A., Curulla Ferré, D., and Pérez-Ramírez, J. (2019). Atomic-scale engineering of indium oxide promotion by palladium for methanol production via co2 hydrogenation. *Nature communications*, 10(1):3377.

[Frey and Hinrichsen, 2012] Frey, A. S. and Hinrichsen, O. (2012). Comparison of differently synthesized ni(al)mcm-48 catalysts in the ethene to propene reaction. *Microporous and Mesoporous Materials*, 164:164–171.

[Fritzler et al., 2014] Fritzler, B. C., Dharmavaram, S., Hartrim, R. T., and Diffendall, G. F. (2014). Acetic anhydride hydrolysis at high acetic anhydride to water ratios. *International Journal of Chemical Kinetics*, 46(3):151–160.

[Froment, 2013] Froment, G. F. (2013). Fundamental kinetic modeling of catalytic hydrocarbon conversion processes. *Reviews in Chemical Engineering*, 29(6):385–412.

[Gascon et al., 2003] Gascon, J., Tellez, C., Herguido, J., and Menendez, M. (2003). Propane dehydrogenation over a cr2o3/al2o3 catalyst: transient kinetic modeling of propene and coke formation. *Applied Catalysis A: General*, 248(1-2):105–116.

[Gayubo et al., 2010] Gayubo, A. G., Alonso, A., Valle, B., Aguayo, A. T., and Bilbao, J. (2010). Kinetic model for the transformation of bioethanol into olefins over a hzsm-5 zeolite treated with alkali. *Industrial & Engineering Chemistry Research*, 49(21):10836–10844.

[Gerlach et al., 2017] Gerlach, M., Abdul Wajid, D., Hilfert, L., Edelmann, F. T., Seidel-Morgenstern, A., and Hamel, C. (2017). Impact of minor amounts of hydroperoxides on rhodium-catalyzed hydroformylation of long-chain olefins. *Catalysis Science & Technology*, 7(7):1465–1469.

[Glasser and Williams, 1971] Glasser, D. and Williams, D. F. (1971). The study of liquid-phase kinetics using temperature as a measured variable. *Industrial & Engineering Chemistry Fundamentals*, 10(3):516–519.

[Gmehling and Kolbe, 1992] Gmehling, J. and Kolbe, B. (1992). *Thermodynamik*. VCH, Weinheim, 2., überarb. aufl. edition.

[Golay et al., 1998] Golay, S., Doepper, R., and Renken, A. (1998). In-situ characterization of the surface intermediates for the ethanol dehydration reaction over γ-alumina under dynamic conditions. *Applied Catalysis A: General*, 172:97–106.

[Gold, 1948] Gold, V. (1948). Hydrolysis of acetic anhydride. *Trans. Farraday Soc.*, 44:506–518.

[Gomez et al., 2018] Gomez, E., Kattel, S., Yan, B., Yao, S., Liu, P., and Chen, J. G. (2018). Combining co2 reduction with propane oxidative dehydrogenation over bimetallic catalysts. *Nature communications*, 9(1):1398.

[Grabmüller et al., 1985] Grabmüller, H., Hoffmann, U., and Schädlich, K. (1985). Prediction of conversion improvements by periodic operation for isothermal plug-flow reactors. *Chemical Engineering Science*, 40(6):951–960.

[Grabowski and Słoczyński, 2005] Grabowski, R. and Słoczyński, J. (2005). Kinetics of oxidative dehydrogenation of propane and ethane on vox/sio2 pure and with potassium additive. *Chemical Engineering and Processing: Process Intensification*, 44(10):1082–1093.

[Grande and Rodrigues, 2005] Grande, C. A. and Rodrigues, A. E. (2005). Propane/propylene separation by pressure swing adsorption using zeolite 4a. *Industrial & Engineering Chemistry Research*, 44(23):8815–8829.

[Grubbs, 2003] Grubbs, R. H. (2003). *Handbook of metathesis.* Wiley-VCH, Weinheim Germany.

[Grubbs, 2004] Grubbs, R. H. (2004). Olefin metathesis. *Tetrahedron*, 60(34):7117–7140.

[Grubbs, 2006] Grubbs, R. H. (2006). Olefin-metathesis catalysts for the preparation of molecules and materials (nobel lecture). *Angewandte Chemie (International ed. in English)*, 45(23):3760–3765.

[Grubbs and Chang, 1998] Grubbs, R. H. and Chang, S. (1998). Recent advances in olefin metathesis and its application in organic synthesis. *Tetrahedron*, 54:4413–4450.

[Grubbs and Stanley, 1991] Grubbs, R. H. and Stanley, H. P. (1991). Comprehensive organic synthesis: Alkene metathesis and related reactions. *Reference Module in Chemistry, Molecular Sciences and Chemical Engineering*, 5:1115–1127.

[Guisnet et al., 2009] Guisnet, M., Costa, L., and Ribeiro, F. R. (2009). Prevention of zeolite deactivation by coking. *Journal of Molecular Catalysis A: Chemical*, 305(1-2):69–83.

[Guisnet and Magnoux, 1997] Guisnet, M. and Magnoux, P. (1997). Deactivation by coking of zeolite catalysts. prevention of deactivation. optimal conditions for regeneration. *Catalysis Today*, 36(4):477–483.

[Güttel, 2013] Güttel, R. (2013). Study of unsteady-state operation of methanation by modeling and simulation. *Chemical Engineering & Technology*, 36(10):1675–1682.

[Güttel et al., 2020] Güttel, R., Freund, H., Sauer, J., Krewer, U., and Horn, R. (2020). Trendbericht - technische chemie. *Nachrichten aus der Chemie*, 68:46–53.

[Gwyn, 1969] Gwyn, J. E. (1969). On the particle size distribution function and the attrition of cracking catalysts. *AIChE Journal*, 15(1):35–39.

[Haag and Pines, 1960] Haag, W. O. and Pines, H. (1960). Alumina catalyst and support iii 1a the kinetics and mechanisms of olefin isomerization1b. *Journal of the American Chemical Society*, 82:2488–2494.

[Hahn et al., 2014] Hahn, T., Kondratenko, E. V., and Linke, D. (2014). The effect of supported moo(x) structures on the reaction pathways of propene formation in the metathesis of ethylene and 2-butene. *Chemical communications (Cambridge, England)*, 50(65):9060–9063.

[Haji and Erkey, 2005] Haji, S. and Erkey, C. (2005). Kinetics of hydrolysis of acetic anhydride by insitu ftir spectroscopy. *ChE Laboratory*, pages 56–61.

[Haldar and Phaneswara Rao, 1991] Haldar, R. and Phaneswara Rao, D. (1991). Experimental studies on limit cycle behaviour of the sulphuric acid catalysed hydrolysis of acetic anhydride in a cstr. *Chemical Engineering Science*, 46(4):1197–1200.

[Hamel, 2015] Hamel, C. (13.11.2015). *Beeinflussung der Produktselektivität homgen und heterogen katalysierter Reaktionen.* Habilitationsschrift, Otto-von-Guericke Universität, Magdeburg.

[Hamel et al., 2010] Hamel, C., Tóta, Á., Klose, F., Tsotsas, E., and Seidel-Morgenstern, A. (2010). Packed-bed membrane reactors. In *Membrane Reactors: Distributing Reactant to Improve Selectivity and Yield*, pages 133–165. Wiley-VCH, Weinheim.

[Hartmann et al., 1996] Hartmann, M., Pöppl, A., and Kevan, L. (1996). Ethylene dimerization and butene isomerization in nickel-containing mcm-41 and. *Journal of Physical Chemistry C*, 100:9906–9910.

[Hegedus, 1978] Hegedus, L. (1978). Phosphorus accumulation in automotive catalysts. *Journal of Catalysis*, 54(2):115–119.

[Helfferich, 2004] Helfferich, F. G. (2004). *Kinetics of multistep reactions*, volume v. 40 of *Comprehensive chemical kinetics.* Elsevier, Amsterdam and Boston, 2nd ed. edition.

[Henkel, 2013] Henkel, A. S. (2013). *Direkte Umsetzung von Ethen zu Propen mit Nickelkatalysatoren.* Dissertation, Technische Universität München, München.

[Herisson and Chauvin, 1971] Herisson, P. J.-L. and Chauvin, Y. (1971). Catalyse de transformation des oléfines par les complexes du tungstène. ii. télomérisation des oléfines cycliques en présence d'oléfines acycliques. *Die Makromolekulare Chemie*, 141(1):161–176.

[Hertwig et al., 2018] Hertwig, K., Martens, L., and Hamel, C. (2018). *Chemische Verfahrenstechnik: Berechnung, Auslegung und Betrieb Chemischer Reaktoren.* De Gruyter Studium Ser. De Gruyter Inc, Berlin/Boston, 3rd ed. edition.

[Hirota et al., 2010] Hirota, W. H., Rodrigues, R. B., Sayer, C., and Giudici, R. (2010). Hydrolysis of acetic anhydride: Non-adiabatic calorimetric determination of kinetics and heat exchange. *Chemical Engineering Science*, 65(12):3849–3858.

[Hoffmann and Schädlich, 1986] Hoffmann, U. and Schädlich, H.-K. (1986). The influence of reaction orders and of changes in the total number of moles on the conversion in a periodically operated cstr. *Chemical Engineering Science*, 41(11):2733–2738.

[Horn and Lin, 1967] Horn, F. and Lin, R. C. (1967). Periodic processes: A variational approach. *I&ES Process Design and Development*, 6(1):21–30.

[Horn, 1970] Horn, F. J. M. (1970). Optimale reaktoren für reaktionen erster ordnung. *Chemie Ingenieur Technik*, 42(19):1185–1240.

[Horn and Bailey, 1968] Horn, F. J. M. and Bailey, J. E. (1968). An application of the theorem of relaxed control to the problem of increasing catalyst selectivity. *Journal of Optimization Theory and Applications*, 2(6):441–449.

[Hua et al., 2011] Hua, D., Chen, S.-L., Yuan, G., Wang, Y., Zhao, Q., Wang, X., and Fu, B. (2011). Metathesis of butene to propene and pentene over wo3/mts-9. *Microporous and Mesoporous Materials*, 143(2-3):320–325.

[Huang et al., 2005] Huang, S., Liu, S., Xin, W., Bai, J., Xie, S., Wang, Q., and Xu, L. (2005). Metathesis of ethene and 2-butene to propene on w/al2o3–hy catalysts with different hy contents. *Journal of Molecular Catalysis A: Chemical*, 226(1):61–68.

[Ilić et al., 2007a] Ilić, M., Petkovska, M., and Seidel-Morgenstern, A. (2007a). Nonlinear frequency response functions of a chromatographic column—a critical evaluation of their potential for estimation of single solute adsorption isotherms. *Chemical Engineering Science*, 62(5):1269–1281.

[Ilić et al., 2007b] Ilić, M., Petkovska, M., and Seidel-Morgenstern, A. (2007b). Nonlinear frequency response method for estimation of single solute adsorption isotherms. part i. theoretical basis and simulations. *Chemical Engineering Science*, 62(16):4379–4393.

[Ilić et al., 2007c] Ilić, M., Petkovska, M., and Seidel-Morgenstern, A. (2007c). Nonlinear frequency response method for estimation of single solute adsorption isotherms. part ii. *Chemical Engineering Science*, 62(16):4394–4408.

[Ilić et al., 2009] Ilić, M., Petkovska, M., and Seidel-Morgenstern, A. (2009). Determination of competitive adsorption isotherms applying the nonlinear frequency response method. part i. theoretical analysis. *Journal of chromatography. A*, 1216(33):6098–6107.

[Iwamoto, 2008] Iwamoto, M. (2008). Conversion of ethene to propene on nickel ion-loaded mesoporous silica prepared by the template ion exchange method. *Catalysis Surveys from Asia*, 12(1):28–37.

[Iwamoto, 2011] Iwamoto, M. (2011). One step formation of propene from ethene or ethanol through metathesis on nickel ion-loaded silica. *Molecules (Basel, Switzerland)*, 16(9):7844–7863.

[Janssen et al., 1957] Janssen, H. J., Haydel, C. H., and Greathouse, L. H. (1957). Hydrolysis of acetic anhydride in concentrated acetic acid without catalysis. *Industrial and Engineering Chemistry*, 49(2).

[Janssens, 2009] Janssens, T. V. (2009). A new approach to the modeling of deactivation in the conversion of methanol on zeolite catalysts. *Journal of Catalysis*, 264(2):130–137.

[Jayakumar et al., 2010] Jayakumar, N. S., Hashim, M. A., and Thomas, M. T. (2010). Input multiplicity analysis in a non-isothermal cstr for acid-catalyzed hydrolysis of acetic anhydride. *Chemical Engineering & Technology*, 33(3):499–507.

[Jayakumar et al., 2014] Jayakumar, N. S., Thomas, M., and Sahu, J. N. (2014). Experimental and modeling of a non-isothermal cstr to find out parameter regions and conditions causing input multiplicity for acid catalyzed hydrolysis of acetic anhydride. *Chemometrics and Intelligent Laboratory Systems*, 135:213–222.

[Jiang et al., 2016] Jiang, W., Huang, R., Li, P., Feng, S., Zhou, G., Yu, C., Zhou, H., Xu, C., and Xu, Q. (2016). Metathesis and isomerization of n-butene and ethylene over wo3/sio2 and mgo catalysts: Thermodynamic and experimental analysis. *Applied Catalysis A: General*, 517:227–235.

[Jörke et al., 2015] Jörke, A., Triemer, S., Seidel-Morgenstern, A., and Hamel, C. (2015). Kinetic investigation exploiting local parameter subset selection: Isomerization of 1-decene using a rh-biphephos catalyst. *Chemie Ingenieur Technik*, 87(6):713–725.

[Joshi, 2007] Joshi, M. (2007). *Statistical analysis of models and parameters in chemical and biochemical reaction networks: Zugl.: Magdeburg, Univ., Fak. für Verfahrens- und Systemtechnik, Diss., 2007.* Logos-Verl., Berlin.

[Kapteijn et al., 1981] Kapteijn, F., Bredt, Hubert L. G., Homburg, E., and Mol, J. C. (1981). Kinetics of the metathesis of propene over re2o7al2o3. *Ind. Eng. Chem. Prod. Res. Dev.*, 20:457–466.

[Kelling et al., 2012] Kelling, R., Kolios, G., Tellaeche, C., Wegerle, U., Zahn, V. M., and Seidel-Morgenstern, A. (2012). Development of a control concept for catalyst regeneration by coke combustion. *Chemical Engineering Science*, 83:138–148.

[Kern and Jess, 2005] Kern, C. and Jess, A. (2005). Regeneration of coked catalysts - modelling and verification of coke burn-off in single particles and fixed bed reactors. *Chemical Engineering Science*, 60(15):4249–4264.

[Kern and Jess, 2006] Kern, C. and Jess, A. (2006). Verkokung und koksabbrand in heterogenen katalysatoren. *Chemie Ingenieur Technik*, 78(8):1033–1048.

[Kiedorf, 2017] Kiedorf, G. (2017). *Mechanistic and kinetic analysis of homogeneously and heterogeneously catalyzed reactions.* Dissertation, Shaker Verlag GmbH.

[Kiedorf et al., 2014] Kiedorf, G., Hoang, D. M., Müller, A., Jörke, A., Markert, J., Arellano-Garcia, H., Seidel-Morgenstern, A., and Hamel, C. (2014). Kinetics of 1-dodecene hydroformylation in a thermomorphic solvent system using a rhodium-biphephos catalyst. *Chemical Engineering Science*, 115:31–48.

[Kiedorf et al., 2016a] Kiedorf, G., Wolff, T., Seidel-Morgenstern, A., and Hamel, C. (2016a). Adsorption measurements on a crox/γ-al2o3 catalyst for parameter reduction in kinetic analysis. *Chemical Engineering Science*, 149:266–276.

[Kiedorf et al., 2016b] Kiedorf, G., Wolff, T., Seidel-Morgenstern, A., and Hamel, C. (2016b). Kinetic analysis of the hydrocarbon total oxidation using individually measured adsorption isotherms. *Chemie Ingenieur Technik.*

[Kim et al., 2017] Kim, K.-M., Lee, J. W., Kim, S., Santos da Silva, F. V., Seidel-Morgenstern, A., and Lee, C.-H. (2017). Advanced operating strategies to extend the applications of simulated moving bed chromatography. *Chemical Engineering & Technology*, 40(12):2163–2178.

[Kissin, 1996] Kissin, Y. V. (1996). Chemical mechanism of hydrocarbon cracking over solid acidic catalysts. *Journal of Catalysis*, 163:50–62.

[Kissin, 2001] Kissin, Y. V. (2001). Chemical mechanisms of catalytic cracking over solid acidic catalysts: Alkanes and alkenes. *Catalysis Reviews*, 43(1-2):85–146.

[Kogan and Herskowitz, 2001] Kogan, S. B. and Herskowitz, M. (2001). Selective propane dehydrogenation to propylene on novel bimetallic catalysts. *Catalysis Communications*, 2:179–185.

[Kralj, 2007] Kralj, A. K. (2007). Checking the kinetics of acetic acid production by measuring the conductivity. *J. Ind. Eng. Chem.*, 13(4):631–636.

[Kuczynski, 1975] Kuczynski, G. C., editor (1975). *Sintering and Catalysis*. Springer US, Boston, MA.

[Kustov et al., 2016] Kustov, L. M., Furman, D. B., and Barkova, A. P. (2016). Metathesis of c5–c8 terminal olefins on re2o7/al2o3 catalysts. *Catalysis Letters*, 146(6):1033–1039.

[Laidler and Meiser, 1982] Laidler, K. J. and Meiser, J. H. (1982). *Physical chemistry*. Benjamin-Cummings Publishing Company, Menlo Park, California.

[Lamia et al., 2007] Lamia, N., Wolff, L., Leflaive, P., Sá Gomes, P., Grande, C. A., and Rodrigues, A. E. (2007). Propane/propylene separation by simulated moving bed i. adsorption of propane, propylene and isobutane in pellets of 13x zeolite. *Separation Science and Technology*, 42(12):2539–2566.

[Lange et al., 1999] Lange, R., Gutsche, R., and Hanika, J. (1999). Forced periodic operation of a trickle-bed reactor. *Chemical Engineering Science*, 54(13-14):2569–2573.

[Langmuir, 1916] Langmuir, I. (1916). The constitution and fundamental properties of solids and liquids. part i. solids. *Journal of the American Chemical Society*, 38(11):2221–2295.

[Lavrenov et al., 2016] Lavrenov, A. V., Karpova, T. R., Buluchevskii, E. A., and Bogdanets, E. N. (2016). Heterogeneous oligomerization of light alkenes: 80 years in oil refining. *Catalysis in Industry*, 8(4):316–327.

[Lavrenov et al., 2015] Lavrenov, A. V., Saifulina, L. F., Buluchevskii, E. A., and Bogdanets, E. N. (2015). Propylene production technology: Today and tomorrow. *Catalysis in Industry*, 7(3):175–187.

[Lee, 2020] Lee, J. W. (2020). Expanding simulated moving bed chromatography into ternary separations in analogy to dividing wall column distillation. *Industrial & Engineering Chemistry Research*, 59(20):9619–9628.

[Lehmann et al., 2012] Lehmann, T., Wolff, T., Hamel, C., Veit, P., Garke, B., and Seidel-Morgenstern, A. (2012). Physico-chemical characterization of ni/mcm-41 synthesized by a template ion exchange approach. *Microporous and Mesoporous Materials*, 151:113–125.

[Lehmann et al., 2011] Lehmann, T., Wolff, T., Zahn, V. M., Veit, P., Hamel, C., and Seidel-Morgenstern, A. (2011). Preparation of ni-mcm-41 by equilibrium adsorption — catalytic evaluation for the direct conversion of ethene to propene. *Catalysis Communications*, 12(5):368–374.

[Levenberg, 1944] Levenberg, K. (1944). A method for the solution of certain non-linear problems in least squares. *Quart. Appl. Math. 2*, 2:164–168.

[Levenspiel, 1999] Levenspiel, O. (1999). *Chemical reaction engineering*. Wiley, Hoboken, NJ, 3. ed. edition.

[Li et al., 2013] Li, L., Palcheva, R. D., and Jens, K.-J. (2013). Conversion of ethene to propene by a dual function niso4/re2o7/γ-al2o3 catalyst. *Topics in Catalysis*, 56(9-10):783–788.

[Li et al., 2011] Li, Q., Sui, Z., Zhou, X., and Chen, D. (2011). Kinetics of propane dehydrogenation over pt–sn/al2o3 catalyst. *Applied Catalysis A: General*, 398(1-2):18–26.

[Li et al., 2009a] Li, X., Zhang, W., Li, X., Liu, S., Huang, H., Han, X., Xu, L., and Bao, X. (2009a). Insights into the deactivation mechanism of heterogeneous $mo/h\beta - al_2o_3$ catalysts for olefin metathesis. *The Journal of Physical Chemistry C*, 113(19):8228–8233.

[Li et al., 2009b] Li, X., Zhang, W., Liu, S., Xie, S., Zhu, X., Bao, X., and Xu, L. (2009b). Promoting effect of mg in supported mo/hbeta–al2o3 catalyst for cross-metathesis of ethene and butene-2 to propene. *Journal of Molecular Catalysis A: Chemical*, 313(1-2):38–43.

[Li et al., 2007] Li, X., Zhang, W., Liu, S., XU, L., Han, X., and Bao, X. (2007). The role of alumina in the supported mo/hbeta–al2o3 catalyst for olefin metathesis: A high-resolution solid-state nmr and electron microscopy study. *Journal of Catalysis*, 250(1):55–66.

[Liao and Shiang, 1991] Liao, Y. S. and Shiang, L. C. (1991). Computer simulation of self-excited and forced vibrations in the external cylindrical plunge grinding process. *Journal of Engineering for Industry*, 113(3):297.

[Limsangkass et al., 2013] Limsangkass, W., Phatanasri, S., Praserthdam, P., Panpranot, J., Jareewatchara, W., Na Ayudhya, Sirachaya Kunjara, and Suriye, K. (2013). Effect of nano-sized tio2 additional support in wo3/sio2 catalyst systems on metathesis of ethylene and trans-2-butene to propylene. *Catalysis Letters*, 143(9):919–925.

[Lin et al., 2009] Lin, B., Zhang, Q., and Wang, Y. (2009). Catalytic conversion of ethylene to propylene and butenes over h−zsm-5. *Industrial & Engineering Chemistry Research*, 48(24):10788–10795.

[Lin et al., 2014] Lin, C., Tao, K., Yu, H., Hua, D., and Zhou, S. (2014). Enhanced catalytic performance of molybdenum-doped mesoporous sba-15 for metathesis of 1-butene and ethene to propene. *Catal. Sci. Technol.*, 4(11):4010–4019.

[Lin et al., 1983] Lin, C. C., Park, S. W., and Hatcher Jr., William J. (1983). Zeolite catalyst deactivation by coking. *Ind. Eng. Chem. Prod. Res. Dev.*, 22:609–614.

[Liu et al., 2016] Liu, B., Slocombe, D., AlKinany, M., AlMegren, H., Wang, J., Arden, J., Vai, A., Gonzalez-Cortes, S., Xiao, T., Kuznetsov, V., and Edwards, P. P. (2016). Advances in the study of coke formation over zeolite catalysts in the methanol-to-hydrocarbon process. *Applied Petrochemical Research*, 6(3):209–215.

[Liu et al., 2009a] Liu, H., Huang, S., Zhang, L., Liu, S., Xin, W., and XU, L. (2009a). The preparation of active wo3 catalysts for metathesis between ethene and 2-butene under moist atmosphere. *Catalysis Communications*, 10(5):544–548.

[Liu et al., 2015] Liu, H., Tao, K., Yu, H., Zhou, C., Ma, Z., Mao, D., and Zhou, S. (2015). Effect of pretreatment gases on the performance of wo3/sio2 catalysts in the metathesis of 1-butene and ethene to propene. *Comptes Rendus Chimie*, 18(6):644–653.

[Liu et al., 2009b] Liu, H., Zhang, L., Li, X., Huang, S., Liu, S., Xin, W., Xie, S., and Xu, L. (2009b). Production of propene from 1-butene metathesis reaction on tungsten based heterogeneous catalysts. *Journal of Natural Gas Chemistry*, 18(3):331–336.

[Liu et al., 2004] Liu, S., Huang, S., Xin, W., Bai, J., Xie, S., and Xu, L. (2004). Metathesis of ethylene and butylene-2 to propylene with mo on hβ-al2o3 catalysts. *Catalysis Today*, 93-95:471–476.

[Liu et al., 2010] Liu, S., Li, X., Xin, W., Xie, S., Zeng, P., Zhang, L., and Xu, L. (2010). Cross metathesis of butene-2 and ethene to propene over mo/mcm-22-al2o3 catalysts with different al2o3 contents. *Journal of Natural Gas Chemistry*, 19(5):482–486.

[Liwu et al., 1990] Liwu, L., Tao, Z., Jingling, Z., and Zhusheng, X. (1990). Dynamic process of carbon deposition on pt and pt–sn catalysts for alkane dehydrogenation. *Applied Catalysis*, 67(1):11–23.

[Lu et al., 2006] Lu, J., Zhao, Z., Xu, C., Duan, A., and Zhang, P. (2006). Crhzsm-5 zeolites – highly efficient catalysts for catalytic cracking of isobutane to produce light olefins. *Catalysis Letters*, 109(1-2):65–70.

[Lunsford et al., 1998] Lunsford, J. H., Qiu, P., Rosynek, M. P., and Yu, Z. (1998). Catalytic conversion of methane and ethylene to propylene. *The Journal of Physical Chemistry B*, 102(1):167–173.

[Lwin et al., 2016] Lwin, S., Li, Y., Frenkel, A. I., and Wachs, I. E. (2016). Nature of wo x sites on sio 2 and their molecular structure–reactivity/selectivity relationships for propylene metathesis. *ACS Catalysis*, 6(5):3061–3071.

[Maksasithorn et al., 2014] Maksasithorn, S., Debecker, D. P., Praserthdam, P., Panpranot, J., Suriye, K., and Ayudhya, Sirachaya Kunjara Na (2014). Naoh modified wo3/sio2 catalysts for propylene production from 2-butene and ethylene metathesis. *Chinese Journal of Catalysis*, 35(2):232–241.

[Mance et al., 2017] Mance, D., van der Zwan, J., Velthoen, M. E. Z., Meirer, F., Weckhuysen, B. M., Baldus, M., and Vogt, E. T. C. (2017). A dnp-supported solid-state nmr study of carbon species in fluid catalytic cracking catalysts. *Chemical communications (Cambridge, England)*, 53(28):3933–3936.

[Marin and Yablonsky, 2011] Marin, G. B. and Yablonsky, G. S. (2011). *Kinetics of chemical reactions: Decoding complexity*. Wiley-VCH, Weinheim, 1st reprint edition.

[Marković et al., 2008] Marković, A., Morgenstern, A.-S., and Petkovska, M. (2008). Evaluation of the potential of periodically operated reactors based on the second order frequency response function. *Chemical Engineering Research and Design*, 86(7):682–691.

[Marquardt, 1963] Marquardt, D. W. (1963). An algorithm for least-squares estimation of nonlinear parameters | journal of the society for industrial and applied mathematics | vol. 11, no. 2 | society for industrial and applied mathematics. *Journal of the Society for Industrial and Applied Mathematics*, 2:431–441.

[Mathworks, 2004] Mathworks (2004). Genetic algorithm and direct search toolbox user's guide. Documentation of optimization algortithms.

[Matros, 1985] Matros, Y. S. (1985). *Unsteady processes in catalytic reactors*, volume 22 of *Studies in Surface Science and Catalysis*. Elsevier Science Publishers, Amsterdam and New York.

[Mazoyer et al., 2014] Mazoyer, E., Szeto, K. C., Merle, N., Thivolle-Cazat, J., Boyron, O., Basset, J.-M., Nicholas, C. P., and Taoufik, M. (2014). Insights into the deactivation mechanism of supported tungsten hydride on alumina (w-h/al2o3) catalyst for the direct conversion of ethylene to propylene. *Journal of Molecular Catalysis A: Chemical*, 385:125–132.

[Mazzotti et al., 1997] Mazzotti, M., Storti, G., and Morbidelli, M. (1997). Optimal operation of minulated moving bed units for nonlinear chromatographic separations. *Journal of chromatography. A*, 769:3–24.

[Meyer et al., 2017] Meyer, D., Friedland, J., Kohn, T., and Güttel, R. (2017). Transfer functions for periodic reactor operation: Fundamental methodology for simple reaction networks. *Chemical Engineering & Technology*, 40(11):2096–2103.

[Mol, 2004] Mol, J. (2004). Industrial applications of olefin metathesis. *Journal of Molecular Catalysis A: Chemical*, 213(1):39–45.

[Mol, 1999] Mol, J. C. (1999). Eratum to "olefin metathesis over supported rhenium oxide catalysts". *Catalysis Today*, 52:377.

[Mol and can Leeuwen, 2008] Mol, J. C. and can Leeuwen, P. W. (2008). "metathesis of alkenes" in: Handbook of heterogeneous catalysis online. In Ertl, G., Knözinger, H., Schüth, F., and Weitkamp, J., editors, *Handbook of heterogeneous catalysis*, pages 3240–3256. Wiley-VCH, Weinheim.

[More and Sorensen, 1983] More, J. J. and Sorensen, D. C. (1983). Computing a trust region step. *SIAM Journal on Scientific and Statistical Computing*, 4(3):553–572.

[Moulijn et al., 2001] Moulijn, J., van Diepen, A. E., and Kapteijn, F. (2001). Catalyst deactivation: is it predictable? what to do? *Applied Catalysis A: General*, 212:3–16.

[Mousavi et al., 2017] Mousavi, S. H., Fatemi, S., and Razavian, M. (2017). Kinetic modeling of the methanol to olefins process in the presence of hierarchical sapo-34 catalyst: parameter estimation, effect of reaction conditions and lifetime prediction. *Reaction Kinetics, Mechanisms and Catalysis*, 122(2):1245–1264.

[Moustafa and Froment, 2003] Moustafa, T. M. and Froment, G. F. (2003). Kinetic modeling of coke formation and deactivation in the catalytic cracking of vacuum gas oil. *Industrial & Engineering Chemistry Research*, 42(1):14–25.

[Mueller et al., 2018] Mueller, I., Kiedorf, G., Runne, E., Pottratz, I., Seidel-Morgenstern, A., and Hamel, C. (2018). Process control and yield enhancement of the galacto–oligosaccharide formation. *Chemie Ingenieur Technik*, 90(5):725–730.

[Murzin, 2013] Murzin, D. (2013). *Engineering catalysis*. De Gruyter Graduate. Walter de Gruyter GmbH, Berlin.

[Murzin and Salmi, 2005] Murzin, D. and Salmi, T. (2005). *Catalytic kinetics*. Elsevier, Amsterdam.

[Murzin, 2010] Murzin, D. Y. (2010). Kinetic analysis of cluster size dependent activity and selectivity. *Journal of Catalysis*, 276(1):85–91.

[Nawaz et al., 2010] Nawaz, Z., Tang, X., Cui, Y., and Wei, F. (2010). 1-hexene catalytic cracking to propylene using shape selective molecular sieve sapo-34 zeolite. *Arabian Journal for Science and Engineering*, 35(1B):15–24.

[Nawaz et al., 2009] Nawaz, Z., Tang, X., and Wei, F. (2009). Hexene catalytic cracking over 30% sapo-34 catalyst for propylene maximization: Influence of reaction conditions and reaction pathway exploration. *Brazilian Journal of Chemical Engineering*, 26(4):705–712.

[Netzsch Thermal Analysis, 2018] Netzsch Thermal Analysis (2018). Sta 449 f3 jupiter.

[Nikolić et al., 2016a] Nikolić, D., Felischak, M., Seidel-Morgenstern, A., and Petkovska, M. (2016a). Periodic operation with modulation of inlet concentration and flow rate part ii: Adiabatic continuous stirred-tank reactor. *Chemical Engineering & Technology*, 39(11):2126–2134.

[Nikolić and Petkovska, 2016] Nikolić, D. and Petkovska, M. (2016). Evaluation of performance of periodically operated reactors for single input modulations of general waveforms. *Chemie Ingenieur Technik*, 88(11):1715–1722.

[Nikolić et al., 2014a] Nikolić, D., Seidel-Morgenstern, A., and Petkovska, M. (2014a). Nonlinear frequency response analysis of forced periodic operation of non-isothermal cstr using single input modulations. part i: Modulation of inlet concentration or flow-rate. *Chemical Engineering Science*, 117:71–84.

[Nikolić et al., 2014b] Nikolić, D., Seidel-Morgenstern, A., and Petkovska, M. (2014b). Nonlinear frequency response analysis of forced periodic operation of non-isothermal cstr using single input modulations. part ii: Modulation of inlet temperature or temperature of the cooling/heating fluid. *Chemical Engineering Science*, 117:31–44.

[Nikolić et al., 2015] Nikolić, D., Seidel-Morgenstern, A., and Petkovska, M. (2015). Nonlinear frequency response analysis of forced periodic operation of non-isothermal cstr with simultaneous modulation of inlet concentration and inlet temperature. *Chemical Engineering Science*, 137:40–58.

[Nikolić et al., 2016b] Nikolić, D., Seidel-Morgenstern, A., and Petkovska, M. (2016b). Periodic operation with modulation of inlet concentration and flow rate. part i: Nonisothermal continuous stirred-tank reactor. *Chemical Engineering & Technology*, 39(11):2020–2028.

[Nikolic Paunic, 2016] Nikolic Paunic, D. S. (2016). *Forced Periodically Operated Chemical Reactors-Evaluation and Analysis by the Nonlinear Frequency Response Method*. Dissertation, University of Belgrade, Belgrad.

[Noreña-Franco et al., 2002] Noreña-Franco, L., Hernandez-Perez, I., Aguilar-Pliego, J., and Maubert-Franco, A. (2002). Selective hydroxylation of phenol employing cu–mcm-41 catalysts. *Catalysis Today*, 75(1-4):189–195.

[Norinaga and Deutschmann, 2007] Norinaga, K. and Deutschmann, O. (2007). Detailed kinetic modeling of gas-phase reactions in the chemical vapor deposition of carbon from light hydrocarbons. *Industrial & Engineering Chemistry Research*, 46(11):3547–3557.

[Norinaga et al., 2009] Norinaga, K., Deutschmann, O., Saegusa, N., and Hayashi, J.-i. (2009). Analysis of pyrolysis products from light hydrocarbons and kinetic modeling for growth of polycyclic aromatic hydrocarbons with detailed chemistry. *Journal of Analytical and Applied Pyrolysis*, 86(1):148–160.

[Norinaga et al., 2008] Norinaga, K., Janardhanan, V. M., and Deutschmann, O. (2008). Detailed chemical kinetic modeling of pyrolysis of ethylene, acetylene, and propylene at 1073-1373 k with a plug-flow reactor model. *International Journal of Chemical Kinetics*, 40(4):199–208.

[Oakenfull, 1974] Oakenfull, D. G. (1974). Kinetics of the hydrolysis of acetic anhydride and the reaction of 4-nitrophenyl acetate with imidazole in aqueous-organic mixed solvents. *Australian Journal of Chemistry*, 27(7):1423.

[Oikawa et al., 2006] Oikawa, H., Shibata, Y., Inazu, K., Iwase, Y., Murai, K., Hyodo, S., Kobayashi, G., and Baba, T. (2006). Highly selective conversion of ethene to propene over sapo-34 as a solid acid catalyst. *Applied Catalysis A: General*, 312:181–185.

[Olah, 2005] Olah, G. A. (2005). Beyond oil and gas: the methanol economy. *Angewandte Chemie (International ed. in English)*, 44(18):2636–2639.

[Olah et al., 2009] Olah, G. A., Goeppert, A., and Prakash, G. K. S. (2009). *Beyond Oil and Gas: The Methanol Economy*. Wiley.

[Olah and Molnár, 2003] Olah, G. A. and Molnár, Á. (2003). *Hydrocarbon chemistry*. Wiley-Interscience, Hoboken, N.J., 2nd ed. edition.

[Onken et al., 1996] Onken, U., Behr, A., and Baerns, M., editors (1996). *Lehrbuch der technischen Chemie*. Thieme, Stuttgart.

[Orton and Jones, 1912] Orton, K. and Jones, M. (1912). Hydrolysis of acetic anhydride. *Journal of the Chemical Society*, 101:1708–1720.

[Osakada, 2014] Osakada, K. (2014). *Organometallic reactions and polymerization*, volume volume 85 of *Lecture Notes in Chemistry*. Springer, Heidelberg.

[Ovesen et al., 1997] Ovesen, C. V., Clausen, B. S., Schiotz, J., Stoltze, P., Topsoe, H., and Norskov, J. K. (1997). Kinetic implications of dynamical changes in catalyst morphology during methanol synthesis over cu/zno catalysts. *Journal of Catalysis*, 168:133–142.

[P. Desai and J.T. Richardson, 1980] P. Desai and J.T. Richardson (1980). Support effects during sintering of nickel catalysts. In *Catalyst Deactivation*, Studies in Surface Science and Catalysis, pages 149–158. Elsevier.

[Papageorgiou et al., 2012] Papageorgiou, M., Leibold, M., and Buss, M. (2012). *Optimierung*. Springer Berlin Heidelberg, Berlin, Heidelberg.

[Pariya et al., 1998] Pariya, C., Jayaprakash, K. N., and Sakar, A. (1998). Alkene metathesis: new developments in catalyst design and application. *Coordination Chemistry Review*, 168:1–48.

[Pérez-Uriarte et al., 2016] Pérez-Uriarte, P., Ateka, A., Aguayo, A. T., Gayubo, A. G., and Bilbao, J. (2016). Kinetic model for the reaction of dme to olefins over a hzsm-5 zeolite catalyst. *Chemical Engineering Journal*, 302:801–810.

[Petkovska and Do, 1998] Petkovska, M. and Do, D. D. (1998). Nonlinear frequency response of adsorption systems: isothermal batch and continuous flow adsorbers. *Chemical Engineering Science*, 53(17):3081–3097.

[Petkovska et al., 2018] Petkovska, M., Nikolić, D., and Seidel-Morgenstern, A. (2018). Nonlinear frequency response method for evaluating forced periodic operations of chemical reactors. *Israel Journal of Chemistry*, 58(6-7):663–681.

[Petkovska and Seidel-Morgenstern, 2013] Petkovska, M. and Seidel-Morgenstern, A. (2013). Evaluation of periodic processes. In Silveston, P. L., editor, *Periodic Operation of Chemical Reactors*, pages 387–413. Elsevier.

[Pinto et al., 2004] Pinto, R. R., Borges, P., Lemos, M., Lemos, F., and Ribeiro, F.Ramôa,mur (2004). Kinetic modelling of the catalytic cracking of n-hexane and n-heptane over a zeolite catalyst. *Applied Catalysis A: General*, 272(1-2):23–28.

[Rabeah et al., 2016] Rabeah, J., Radnik, J., Briois, V., Maschmeyer, D., Stochniol, G., Peitz, S., Reeker, H., La Fontaine, C., and Brückner, A. (2016). Tracing active sites in supported ni catalysts during butene oligomerization by operando spectroscopy under pressure. *ACS Catalysis*, 6(12):8224–8228.

[Rahimi and Karimzadeh, 2011] Rahimi, N. and Karimzadeh, R. (2011). Catalytic cracking of hydrocarbons over modified zsm-5 zeolites to produce light olefins: A review. *Applied Catalysis A: General*, 398(1-2):1–17.

[Regenass, 1985] Regenass, W. (1985). Calorimetric monitoring of industrial chemical processes. *Thermochimica Acta*, 95:351–368.

[Renken, 1972] Renken, A. (1972). The use of periodic operation to improve the performance of continuous stirred tank reactors. *Chemical Engineering Science*, 27:1925–1932.

[Renken, 1974] Renken, A. (1974). Verbesserung von selektivität und ausbeute durch periodische prozeßführung. *Chemie Ingenieur Technik*, 46(3):113.

[Renken, 1982] Renken, A. (1982). Instationäre prozeßführung kontinuierlicher reaktoren. *Chemie Ingenieur Technik*, 54(6):571–580.

[Renken, 1983] Renken, A. (1983). Periodische betriebsweise kontinuierlicher chemischer reaktoren. *Dechema-Monographien*, 94:313–333.

[Rivett and Sidgwick, 1910] Rivett, A. and Sidgwick, N. V. (1910). The rate of hydration of acetic anhydride. *Journal of the Chemical Society*, 97:732–741.

[Rostom and de Lasa, 2018] Rostom, S. and de Lasa, H. (2018). High propylene selectivity via propane oxidative dehydrogenation using a novel fluidizable catalyst: Kinetic modeling. *Industrial & Engineering Chemistry Research*, 57(31):10251–10260.

[Sang et al., 2012] Sang, L., Chen, S.-L., Yuan, G., Zheng, M., You, J., Chen, A., Li, R., and Chen, L. (2012). Metathesis of 1-butene and 2-butene to propene over re2o7 supported on macro-mesoporous γ-alumina prepared via a dual template method. *Journal of Natural Gas Chemistry*, 21(2):105–108.

[Schädlich et al., 1983] Schädlich, K., Hoffmann, U., and Hofmann, H. (1983). Periodical operation of chemical processes and evaluation of conversion improvements. *Chemical Engineering Science*, 38(9):1375–1384.

[Schrock, 2004] Schrock, R. (2004). Recent advances in olefin metathesis by molybdenum and tungsten imido alkylidene complexes. *Journal of Molecular Catalysis A: Chemical*, 213(1):21–30.

[Schrock, 1986] Schrock, R. R. (1986). On the trail of metathesis catalysts. *Journal of Organometallic Chemistry*, 300:249–262.

[Schrock, 1999] Schrock, R. R. (1999). Olefin metathesis by molybdenum imido alkylidene catalysts. *Tetrahedron*, 55:8141–8153.

[Schrock, 2006] Schrock, R. R. (2006). Multiple metal-carbon bonds for catalytic metathesis reactions (nobel lecture). *Angewandte Chemie (International ed. in English)*, 45(23):3748–3759.

[Schrock and Hoveyda, 2003] Schrock, R. R. and Hoveyda, A. H. (2003). Molybdenum and tungsten imido alkylidene complexes as efficient olefin-metathesis catalysts. *Angewandte Chemie (International ed. in English)*, 42(38):4592–4633.

[Schrock et al., 1990] Schrock, R. R., Murdzek, J. S., Bazan, G. C., Robbins, J., DiMare, M., and O'Regan, M. (1990). Synthesis of molybdenum imido alkylidene complexes and some reactions involving acyclic olefins. *Journal of the American Chemical Society*, 112(10):3875–3886.

[Schwaab and Pinto, 2007] Schwaab, M. and Pinto, J. C. (2007). Optimum reference temperature for reparameterization of the arrhenius equation. part 1: Problems involving one kinetic constant. *Chemical Engineering Science*, 62(10):2750–2764.

[Shatynski and Hanesian, 1993] Shatynski, J. J. and Hanesian, D. (1993). Adiabatic kinetic studies of the. *Ind. Eng. Chem. Res.*, 32:594–599.

[Shen and Okamoto, 2016] Shen, J. and Okamoto, Y. (2016). Efficient separation of enantiomers using stereoregular chiral polymers. *Chemical reviews*, 116(3):1094–1138.

[Silveston et al., 1995] Silveston, P., Hudgins, R. R., and Renken, A. (1995). Periodic operation of catalytic reactors—introduction and overview. *Catalysis Today*, 25(2):91–112.

[Silveston, 2013] Silveston, P. L., editor (2013). *Periodic Operation of Chemical Reactors*. Elsevier.

[Silveston et al., 2008] Silveston, P. L., Budman, H., and Jervis, E. (2008). Forced modulation of biological processes: A review. *Chemical Engineering Science*, 63(20):5089–5105.

[Słomkiewicz, 2004] Słomkiewicz, P. M. (2004). Determination of the langmuir–hinshelwood kinetic equation of synthesis of ethers. *Applied Catalysis A: General*, 269(1-2):33–42.

[Soerensen, 2017] Soerensen, M. D. P. (2017). The establishment of a coke-burn kinetic model for zeolite catalysts. *Chemical Engineering Science*, 168:465–479.

[Sohn and Park, 2000] Sohn, J. R. and Park, W. C. (2000). Ethylene dimerization catalyst of nickel sulfate supported on silica-alumina. *Korean J. Chem. Eng.*, 17(6):727–730.

[Sohn et al., 2006] Sohn, J. R., Park, W. C., and Shin, D. C. (2006). Characterization of nickel sulfate supported on sio2 for ethylene dimerization and promoting effect of al2o3 on catalytic activity. *Journal of Molecular Catalysis A: Chemical*, 256(1-2):156–163.

[Speiser et al., 2005] Speiser, F., Braunstein, P., and Saussine, L. (2005). Catalytic ethylene dimerization and oligomerization: recent developments with nickel complexes containing p,n-chelating ligands. *Accounts of chemical research*, 38(10):784–793.

[Spiegel, 1974] Spiegel, M. R. (1974). *Schaum's outline of theory and problems of Fourier analysis: With applications to boundary value problems.* Schaum's outline series. McGraw-Hill, New York.

[Stankiewicz and Kuczynski, 1995] Stankiewicz, A. and Kuczynski, M. (1995). An industrial view on the dynamic operation of chemical converters. *Chemical Engineering and Processing: Process Intensification*, 34(4):367–377.

[Summers and Hegedus, 1979] Summers, J. C. and Hegedus, L. L. (1979). Modes of catalyst deactivation in stoichiometric automobile exhaust. *Ind. Eng. Chem. Prod. Res. Dev.*, 18(4):318–324.

[Sundmacher et al., 2005] Sundmacher, K., Kienle, A., and Seidel-Morgenstern, A. (2005). *Integrated chemical processes: Synthesis, operation, analysis, and control.* Wiley-VCH, Weinheim.

[Takashima et al., 1971] Takashima, I., Nishida, A., Ogita, K., and Uchida, N. (1971). Computer aided reaction analysis on twin calorimetry. *Kog Kagaku Zasshi*, 74(7):1293–1297.

[Tang et al., 2008] Tang, X., Zhou, H., Qian, W., Wang, D., Jin, Y., and Wei, F. (2008). High selectivity production of propylene from n-butene: Thermodynamic and experimental study using a shape selective zeolite catalyst. *Catalysis Letters*, 125(3-4):380–385.

[Taoufik et al., 2007] Taoufik, M., Le Roux, E., Thivolle-Cazat, J., and Basset, J.-M. (2007). Direct transformation of ethylene into propylene catalyzed by a tungsten hydride supported on alumina: Trifunctional single-site catalysis. *Angewandte Chemie International Edition*, 46(38):7202–7205.

[Tiong Sie, 1992] Tiong Sie, S. (1992). Acid catalyzed cracking of paraffinic hydrocarbons discussion of existing mechanisms and proposal of a new mechanism. *Industrial & Engineering Chemistry Research*, 31:1881–1889.

[Trimm, 2001] Trimm, D. (2001). The regeneration or disposal of deactivated heterogeneous catalysts. *Applied Catalysis A: General*, 212(1-2):153–160.

[Trnka and Grubbs, 2001] Trnka, T. M. and Grubbs, R. H. (2001). The development of $l_2x_2ru = chr$ olefin metathesis catalysts: An organometallic success story. *Accounts of Chemical Research*, 34(1):18–29.

[Truffer and Renken, 1986] Truffer, M. A. and Renken, A. (1986). Transient behavior of heterogeneous catalytic reactions with educt inhibition. *AIChE Journal*, 32(10):1612–1621.

[Tsakoumis et al., 2010] Tsakoumis, N. E., Rønning, M., Borg, Ø., Rytter, E., and Holmen, A. (2010). Deactivation of cobalt based fischer–tropsch catalysts: A review. *Catalysis Today*, 154(3-4):162–182.

[van Grieken et al., 2008] van Grieken, R., Escola, J. M., Moreno, J., and Rodríguez, R. (2008). Nitrogen and sulphur poisoning in alkene oligomerization over mesostructured aluminosilicates (al-mts, al-mcm-41) and nanocrystalline n-hzm-5. *Applied Catalysis A: General*, 337(2):173–183.

[van Santen, 2017] van Santen, R. A. (2017). *Modern heterogeneous catalysis: An Introduction.* Wiley-VCH Verlag GmbH & Co. KGaA, Weinheim, Germany.

[Van Speybroeck et al., 2014] Van Speybroeck, V., de Wispelaere, K., Van der Mynsbrugge, J., Vandichel, M., Hemelsoet, K., and Waroquier, M. (2014). First principle chemical kinetics in zeolites: the methanol-to-olefin process as a case study. *Chemical Society reviews*, 43(21):7326–7357.

[Visentin et al., 2004] Visentin, F., Gianoli, S. I., Zogg, A., Kut, O. M., and Hungerbühler, K. (2004). A pressure-resistant small-scale reaction calorimeter that combines the principles of power compensation and heat balance (crc.v4). *Organic Process Research & Development*, 8(5):725–737.

[Volterra, 2005] Volterra, V. (2005). *Theory of functionals and of integral and integro-differential equations.* Dover, Mineola.

[von Aretin and Hinrichsen, 2014] von Aretin, T. and Hinrichsen, O. (2014). Single-event kinetic model for cracking and isomerization of 1-hexene on zsm-5. *Industrial & Engineering Chemistry Research*, 53(50):19460–19470.

[von Aretin et al., 2017a] von Aretin, T., Standl, S., Tonigold, M., and Hinrichsen, O. (2017a). Optimization of the product spectrum for 1-pentene cracking on zsm-5 using single-event methodology. part 1: Two-zone reactor. *Chemical Engineering Journal*, 309:886–897.

[von Aretin et al., 2017b] von Aretin, T., Standl, S., Tonigold, M., and Hinrichsen, O. (2017b). Optimization of the product spectrum for 1-pentene cracking on zsm-5 using single-event methodology. part 2: Recycle reactor. *Chemical Engineering Journal*, 309:873–885.

[Vougioukalakis and Grubbs, 2010] Vougioukalakis, G. C. and Grubbs, R. H. (2010). Ruthenium-based heterocyclic carbene-coordinated olefin metathesis catalysts. *Chemical reviews*, 110(3):1746–1787.

[Wang et al., 2004] Wang, B., Gao, Q., Gao, J., Ji, D., Wang, X., and Suo, J. (2004). Synthesis, characterization and catalytic c4 alkene cracking properties of zeolite zsm-23. *Applied Catalysis A: General*, 274(1-2):167–172.

[Wang et al., 2011] Wang, C.-M., Wang, Y.-D., Dong, J., Liu, S., and Xie, Z.-K. (2011). Structure sensitivity of double bond isomerization of butene over mgo surfaces: A periodic dft study. *Computational and Theoretical Chemistry*, 974(1-3):52–56.

[Wedler and Freund, 2012] Wedler, G. and Freund, H.-J. (2012). *Lehrbuch der physikalischen Chemie*. Wiley VCH Lehrbuchkollektion 1. Wiley-VCH, Weinheim, 6., vollst. überarb. und aktualisierte aufl. edition.

[Weiner and Spina, 1980] Weiner, D. D. and Spina, J. F. (1980). *Sinusoidal analysis and modeling of weakly nonlinear interference effects*. Van Nostrand Reinhold electrical/computer science and engineering series. Van Nostrand Reinhold, New York.

[Werther and Reppenhagen, 1999] Werther, J. and Reppenhagen, J. (1999). Catalyst attrition in fluidized–bed systems. *AIChE Journal*, 45(9):2001–2010.

[William A. Cupples and Rodger D. Loutzenhiser, 1998] William A. Cupples and Rodger D. Loutzenhiser (1998). Dynamic autoregulation in the in vitro perfused hydronephrotic rat kidney. *American Journal of Physiology*, 275(1):126–130.

[Wilsdon and Sidgwick, 1913] Wilsdon, B. H. and Sidgwick, N. V. (1913). The rate of hydration of acid anhydrides acetic, propionic, butyric, and benzoic. *Journal of the Chemical Society, Transactions*, 103:1959–1973.

[Wiseman, 2012] Wiseman, F. L. (2012). New insight on an old reaction - the aqueous hydrolysis of acetic anhydride. *Journal of Physical Organic Chemistry*, 25(12):1105–1111.

[Wittcoff et al., 2013] Wittcoff, H. A., Reuben, B. G., and Plotkin, J. S. (2013). *Industrial organic chemicals, third edition*. Wiley, Hoboken, N.J., 3rd ed. edition.

[Wu et al., 2015] Wu, D., Gu, Z., and Li, Y. (2015). Attrition of catalyst particles in a laboratory-scale fluidized-bed reactor. *Chemical Engineering Science*, 135:431–440.

[Xu and Wang, 2007] Xu, L. and Wang, Y. (2007). Dynamic modeling and control of dfig-based wind turbines under unbalanced network conditions. *IEEE Transactions on Power Systems*, 22(1):314–323.

[Yaws, 1999] Yaws, C. L. (1999). *Chemical properties handbook: Physical, thermodynamic, environmental, transport, and health related properties for organic and inorganic chemicals*. McGraw-Hill handbooks. McGraw-Hill, New York.

[Zhou et al., 2008] Zhou, H., Wang, Y., Wei, F., Wang, D., and Wang, Z. (2008). Kinetics of the reactions of the light alkenes over sapo-34. *Applied Catalysis A: General*, 348(1):135–141.

[Zhu et al., 2009] Zhu, X., Li, X., Xie, S., Liu, S., Xu, G., Xin, W., Huang, S., and Xu, L. (2009). Two new on-purpose processes enhancing propene production: Catalytic cracking of c4 alkenes to propene and metathesis of ethene and 2-butene to propene. *Catalysis Surveys from Asia*, 13(1):1–8.

[Zhu et al., 2005a] Zhu, X., Liu, S., Song, Y., Xie, S., and Xu, L. (2005a). Catalytic cracking of 1-butene to propene and ethene on mcm-22 zeolite. *Applied Catalysis A: General*, 290(1-2):191–199.

[Zhu et al., 2005b] Zhu, X., Liu, S., Song, Y., and Xu, L. (2005b). Butene catalytic cracking to propene and ethene over potassium modified zsm-5 catalysts. *Catalysis Letters*, 103(3-4):201–210.

[Zhu et al., 2005c] Zhu, X., Liu, S., Song, Y., and Xu, L. (2005c). Catalytic cracking of c4 alkenes to propene and ethene: Influences of zeolites pore structures and si/al_2 ratios. *Applied Catalysis A: General*, 288(1-2):134–142.

[Ziaka et al., 1993] Ziaka, Z. D., Minet, R. G., and Tsotsis, T. T. (1993). Propane dehydrogenation in a packed–bed membrane reactor. *AIChE Journal*, 39(3):526–529.

[Zimmermann, 2013] Zimmermann, H. (2013). Propene. In *Ullmann's Encyclopedia of Industrial Chemistry*, volume 3, page 00. Wiley-VCH Verlag GmbH & Co. KGaA, Weinheim, Germany.

[Zogg et al., 2003] Zogg, A., Fischer, U., and Hungerbühler, K. (2003). A new small-scale reaction calorimeter that combines the principles of power compensation and heat balance. *Industrial & Engineering Chemistry Research*, 42(4):767–776.

[Zogg et al., 2004] Zogg, A., Fischer, U., and Hungerbühler, K. (2004). A new approach for a combined evaluation of calorimetric and online infrared data to identify kinetic and thermodynamic parameters of a chemical reaction. *Chemometrics and Intelligent Laboratory Systems*, 71(2):165–176.

Nomenclature

Latin Symbols

a	Activity	–
a^*	Parameter in eq. (8.15)	–
A	Amplitude	–
b^*	Parameter in eq. (8.15)	–
$B_{P,s}$	Stability parameter (eq. (B.5))	–
c	Concentration	mol/l
c^*	Parameter in eq. (8.15)	–
CO	Carbon Monoxide	–
CO_2	Carbon Dioxide	–
c_P	Heat capacity	$J/(mol \cdot K)$
E_A	Activation energy	kJ/mol
F	Volumetric Flow Rate	ml/min or l/h
f	Frequency	Hz
$\Delta_F G$	Gibb's enthalpy of formation	kJ/mol
$\Delta_R G$	Gibb's enthalpy of reaction	kJ/mol
G_n	n-th order frequency response function correlating the concentration with a single and multiple input modulation(s)	–
$\Delta_F H$	Enthalpy of formation	kJ/mol
$\Delta_R H$	Enthalpy of reaction	kJ/mol
H_n	n-th order frequency response function correlating the molar flow with a single and multiple input modulation(s)	–
K_i	Lumped inhibition coefficient in mechanistic rate approach	–
K_P	Equilibrium constant	–

k_∞	Collision of factor	$varies$
k	Reaction rate constant	$varies$
L	Length	m
M	Molar mass	g/mol
m_{Cat}	Catalyst mass	kg or g
n	Number of moles	mol
N_P	Molar flow of product	mol/s
$\dot{n}$	Molar flux	mol/s
O_2	Oxygen	–
p	Pressure	Pa
$p^{\oslash}$	Reference pressure	Pa
R	Universal Gas constant	$J/(mol \cdot K)$
S	Selectivity of product	% or –
SSR	Objective function	–
$\Delta_F S$	Entropy of formation	$J/(mol \cdot K)$
$\Delta_R S$	Entropy of reaction	$J/(mol \cdot K)$
T	Temperature	K or $^\circ C$
t	Time	s or h
V_R	Reactor volume	ml
w	Velocity	m/s
X	Conversion of reactant	% or –
$x(t)$	Time dependent input signal	–
Y	Yield of product	% or –
$y(t)$	Time dependent output signal	–
z	Spatial coordinate	m
$z(t)$	Time dependent input signal	–

Greek symbols

α^*	Dimensionless parameter for process evaluation (eq. (B.2))	–

α	Specification of catalyst crystalline structure as α-Type	–
β^*	Dimensionless parameter for process evaluation (eq. (B.3))	–
β	Specification of catalyst crystalline structure as β-Type	–
γ^*	Dimensionless parameter for process evaluation (eq. (B.4))	–
γ	Specification of catalyst crystalline structure as γ-Type	–
Δ	Difference of two values	varies
η	Efficiency	-
θ_{free}	Free adsorption sites	–
θ_i	Surface coverage by component i	–
Θ_{opt}	Optimization parameter vector	–
κ	Conductivity	mS/cm
λ	Frequency in Christiansen Matrix	–
ν	Stoichiometric coefficient	–
π	ratio of circumference of circle to its diameter	–
ρ	Density	kg/m^3 or
τ	Residence time	s or h
ϕ	Phase shift between two harmonic functions	° or rad
χ	Volumetric fraction of oxygen	–
ω	Dimensionless frequency	–

Glossary

Acronyms

BET	Brunauer-Emmett-Teller analysis
BR	batch reactor
CSTR	continuously stirred tank reactor
D	Christiansen Matrix
DSC	differential scanning calorimetry
DTA	differential thermal analysis
EDX	energy dispersive X-ray spectroscopy
EPR	electron paramagnetic resonance
ETP	ethene to propene
FCC	fluid catalytic cracking
FRF	frequency response function
FTIR	Fourier Transformed Infrared Spectroscopy
GC	gas chromatography
HTKR	high temperature kinetic reactor
IWI	incipient wet impregnation
LHHW	Langmuir-Hinshelwood-Hougen-Watson
MCM	mobil composition of matter
MFC	mass flow controller
MOF	metal organic framework
MPZM	Miniplant Zapfstellen- und Membranreaktor
NFR	nonlinear frequency response
NMR	nuclear magnetic resonance
OCT	Olefin Conversion Process
ODE	ordinary differential equation
ODH	oxidative dehydrogenation
OF	objective function
OLS	ordinary least square
PFTR	plug flow tubular reactor
PSA	pressure swing adsorption
RCM	ring closing metathesis
RE	rare earth
ROMP	ring opening metathesis polymerization
SAPO	Small-pore molecular sieves
SBA	Santa Barbara Amorphous material

SEM	scanning electron microscope
SHOP	Shell higher olefin process
SMB	simulated moving bed
SSR	squares of residues
STA	simultaneous thermal analysis
TCD	thermal conductivity detector
TDH	thermal dehydrogenation
TGA	thermogravimetric analysis
TOS	time-on-stream
TPR	Temperature Programmed Reduction
US	ultra stable
W/F	weight to flow ratio
WHSV	weight hourly space velocity
WLS	weighted least square
XRD	powder x-ray diffraction
ZSM	zeolite socony mobil

Subscripts

$1-C_4H_8$	n-Butene
C_2H_4	Ethene
C_3H_6	Propene
C_5H_{10}	Pentene
C_6H_{12}	Hexene
α	Subscript for lumped parameter K in the Christiansen-Matrix
β	Subscript for lumped parameter K in the Christiansen-Matrix
δ	Subscript for lumped parameter K in the Christiansen-Matrix
ϵ	Subscript for lumped parameter K in the Christiansen-Matrix
η	Subscript for lumped parameter K in the Christiansen-Matrix
γ	Subscript for lumped parameter K in the Christiansen-Matrix
ι	Reaction order for the reaction ι
μ	Reaction order for the deactivation μ
ψ	Reaction order of oxygen for the regeneration ψ
σ	Reaction order for the deactivation σ
θ	Subscript for lumped parameter K in the Christiansen-Matrix
υ	Fitting parameter for regeneration υ

ξ	Reaction order of oxygen for the regeneration carbon mass ξ
ζ	Subscript for lumped parameter K in the Christiansen-Matrix
$cis-C_4H_8$	cis-Butene
$trans-C_4H_8$	trans-Butene
0	Initial value
A	Reactant of the reaction
AA	Acetic Anhydride
C	Single modulation of inlet concentration
cat	Catalyst
CF	Simultaneous Modulation of inlet concentration and total flow
crack	Type of involved reaction step, as cracking
cycle	Cycle of one whole period
d	Deactivation step and kinetics
DC	Nonperiodic component
dim	Type of involved reaction step, as dimerization
dyn	Dynamic operation
exp	Experimental Value
F	Single modulation of total flow
I	First harmonic of output
i	Component i
II	Second harmonic of output
in	Input value
iso	Type of involved reaction step, as isomerization
j	Reaction j
k	Product k
LHHW	Langmuir-Hinshelwood-Hougen-Watson approach
m	Output value m
met	Type of involved reaction step, as metathesis
MM	Mechanistic Modeling approach
mod	Modeled parameter or data
n	Experimental run n
P	Product of the reaction
R	Reactor
ref	Reference value
reg	Regeneration step and kinetics
sim	Simulated Value
ss	Steady-state operation
T	Single modulation of inlet temperature
u	Reaction order of acetic anhydride u
v	Reaction order of water v

W	Water
x	Fluctated inlet parameter x
xz	Combination of fluctuated inlet parameters x and z
z	Fluctated inlet parameter z

List of Figures

Figure 1.1 Schematic display of an inherent cyclic reactor operation carrying out a catalyzed reaction facing deactivation effects. 6

Figure 1.2 Exemplified display of the forced periodic reactor operation concept with imposed fluctuation of an input parameter. 8

Figure 2.1 Exemplified catalytic cycle for the generation of a product from two reactants. . . . 20

Figure 3.1 Propene selectivity of catalytic systems over the conversion of ethene. 34

Figure 4.1 Illustration of the inherent dynamic operation with maximum and minimum activity, as well as their corresponding time arrays. 47

Figure 4.2 Simulative results for a continuously stirred tank reactor (CSTR) of (a) the yield (blue) and conversion (orange) of the reaction network imposed for different residence times and (b) the efficiency (blue) of the process compared to the ideal system and the yield of product (orange) as functions of the residence time. 49

Figure 4.3 Simulative results of product yield and activity with time for the inherent dynamic operation of a continuously stirred tank reactor (CSTR) with a k_D / k_{Reg} = 1 for (a) a lower boundary of 5 % activity and an upper boundary of 15 % activity, (b) a lower boundary of 85 % activity and an upper boundary of 95 % activity, (c) a lower boundary of 45 % activity and an upper boundary of 55 % activity, (d) a lower boundary of 10 % activity and an upper boundary of 90 % activity. 50

Figure 4.4 Simulative results of product yield and for optimized activity determination values with time for the inherent dynamic operation of a continuously stirred tank reactor (CSTR) for a k_D / k_{Reg} = 1. 51

Figure 4.5 Simulative results of product yield and for optimized activity determination values with time for the inherent dynamic operation of a continuously stirred tank reactor (CSTR) for a k_D / k_{Reg} = 0.2. 52

Figure 4.6 Simulative results for a plug flow tubular reactor (PFTR) of the efficiency (blue) of the process compared to the ideal system and the yield of product (orange) as functions of the residence time. 53

Figure 4.7 Simulative results of product yield and activity with time for the inherent dynamic operation of a plug flow tubular reactor (PFTR) with a k_D / k_{Reg} = 0.2 for (a) a lower boundary of 5 % activity and an upper boundary of 15 % activity, (b) a lower boundary of 10 % activity and an upper boundary of 90 % activity, (c) optimized determination values for activity. 54

Figure 5.1 Experimental setup HTKR for testing catalytic activity. 57

Figure 5.2 Characterization of Ni/AlMCM-41 with (a) XRD patterns for different Si/Al ratios and (b) N_2-physiosoprtion isotherms for Ni/AlMCM-41 for different Si/Al ratios. . . 59
Figure 5.3 Pyridine diffuse-reflectance FTIR spectra of the Ni/MCM-41 and Ni/AlMCM-41 with different Si/Al ratio; a = 5, b = 16, c = 60, d = 150, e = ∞, before (a) and after pyridine adsorption at 50 °C (b) and 150 °C (c). 61
Figure 5.4 Temperature dependent conversion of ethene and selectivity of the main reaction products (propene, 1-butene, trans-butene and cis-butene) with 10 % ethene feed implying a Ni/AlMCM-41 catalyst with a Si/Al = 60 at a W/F ratio of 2600 $\frac{kg_{cat} \cdot s}{m^3}$. . . 62
Figure 5.5 Comparative evaluation of the Ni/AlMCM-41 catalyst with a Si/Al ratio of 60, under varying reaction conditions of (a) conversion of ethene, (b) selectivity of propene, (c) selectivity of 1-butene and (d) selectivity of 2-butene as a function of temperature. 64
Figure 5.6 Catalytic cycle based on the reaction network proposed by Iwamoto [Felischak et al., 2019]. 65
Figure 5.7 Catalytic Cycle of the reaction network implying catalytic cracking [Felischak et al., 2019]. 66
Figure 5.8 24h Spectra of (a) conversion and yield of the main reaction products and carbon balance, (b) the product selectivity, for an ethene feed of 10 %, with a W/F = 500 $\frac{kg_{cat} \cdot s}{m^3}$ and 350 °C. 67
Figure 5.9 Change of catalyst color after regeneration at 500 °C and 500 $\frac{kg_{cat} \cdot s}{m^3}$. 68
Figure 5.10 Varying feed composition (top), reaction temperature (2nd), conversion of ethene (3rd) and propene selectivity (bottom) over time for the verification of the longtime stability of a single catalyst bed. 69
Figure 5.11 Comparative evaluation of the deactivation effect on the Ni/AlMCM-41 catalyst with a Si/Al ratio of 60, under varying reaction conditions of (a) conversion of ethene, (b) selectivity of propene, (c) selectivity of 1-butene and (d) 2-butene over time-on-stream. 71
Figure 5.12 Types of carbonaceous residue and the inter-transformation [Bartholomew, 1982]. 72
Figure 5.13 Exemplified dynamic regeneration experiment of gravimetric mass loss (blue) and differential mass loss (orange) with varying temperature. 73
Figure 5.14 Gaussian peak fitting with (a) two and (b) three peaks of the differential mass loss signal. 75
Figure 5.15 Isothermal regeneration experimental signals exploiting TGA measurement with (a) constant oxygen concentration of 10 % and varying temperature, (b) constant oxygen concentration of 20 % and varying temperature and (a) constant temperature of 500 °C and varying oxygen concentration. 76

Figure 6.1 Comparison of (a) Iwamoto with mechanistic modeling, (b) Cracking network with mechanistic modeling, (c) Iwamoto with LHHW and (d) Cracking network with LHHW. 86
Figure 6.2 Detailed representation of simulative results to experimental values for Iwamoto applying LHHW. 89
Figure 6.3 Detailed analysis of simulative results to experimental values for the extended network applying the LHHW. 91

Figure 6.4 Parameter estimation and fitting of the performed deactivation experiments employing a simple exponential deactivation approach (eq. (2.55)). 92
Figure 6.5 Parameter estimation and fitting of the performed deactivation experiments employing the approach by Janssens eq. (2.66). 93
Figure 6.6 Experimental and predicted results of the regenerative results for model 1 (eq. (2.68)) of (a) varying temperature and (b) varying oxygen concentration. 95

Figure 7.1 Flow sheet of the realized experimental setup for forced dynamic parameter perturbation. 103
Figure 7.2 Experimental Setup for the implementation of forced dynamic reactor operation for the hydrolysis of acetic anhydride. 104
Figure 7.3 Example reaction under constant feed conditions for an adiabatic CSTR approaching steady-state, with 0.74 $\frac{mol}{l}$ of concentration, a flow rate of 43 $\frac{ml}{min}$ and an inlet temperature of 20 °C. 105
Figure 7.4 Kinetic experiments approaching steady-state for the hydrolysis of acetic anhydride for (a) constant inlet temperature of 22 °C and varying inlet concentration; (b) constant inlet concentration of 0.74 $\frac{mol}{l}$ and varying inlet temperature. 107
Figure 7.5 Conversion of acetic anhydride as function of temperature for the set of performed kinetic approaching steady-state experiments with varying feed concentration and inlet temperature. 108
Figure 7.6 Parity plots of (a) concentration and (b) temperature employing kinetic model 1 (eq. (7.3)). 110
Figure 7.7 Parity plots of (a) concentration and (b) temperature employing kinetic model 2 (eq. (7.4)). 111
Figure 7.8 Parity plots of (a) concentration and (b) temperature employing kinetic model 3 (eq. (7.5)). 111

Figure 8.1 Schematic illustration of input modulations and the resulting output function. . . . 113
Figure 8.2 Presentation of multiple input modulations and their influence on the output function. 116
Figure 8.3 Normalized yield (eq. (8.31)) as a function of period calculated using the NFR method with the defined standard values for (a) perturbation of inlet concentration A_C = 85 % and total flow rate A_F = 55 % and (b) perturbation of inlet concentration A_C = 85 % and inlet temperature A_T = 7 %. 121
Figure 8.4 Influence of the (a) activation energy E_A, (b) the collision factor k_∞ and (c) the reaction order n on the normalized product yield (eq. (8.31)) for the simultaneous modulation of inlet concentration and total flow with amplitudes of A_C = 85 % and A_F = 55 % with individual optimal phase differences. 123
Figure 8.5 Input signals for the single input modulation of the concentration for the dynamic experimental part with inlet concentration of anhydride (top), total volumetric flow rate (second), water flow rate (third) and acetic anhydride flow rate (bottom). . . . 125

Figure 8.6 Single modulation of inlet concentration A_C = 85 % and a period of 40 min, presenting conductivity at the outlet (top), product concentration at the outlet (second), molar product flow (third) and inlet molar product flow (bottom). 126

Figure 8.7 Single modulation of inlet concentration A_C = 85 % and a period of 40 min, presenting reactor temperature (blue) and molar product flow (orange) over the time of periodic operation. 126

Figure 8.8 Input signals for the single input modulation of the total flow rate for the dynamic experimental part with inlet concentration of anhydride (top), total volumetric flow rate (second), water flow rate (third) and acetic anhydride flow rate (bottom). . . . 127

Figure 8.9 Single modulation of total flow rate A_F = 55 % and a period of 40 min, presenting conductivity at the outlet (top), product concentration at the outlet (second), molar product flow (third) and inlet molar product flow (bottom). 128

Figure 8.10 Single modulation of total flow rate A_F = 55 % and a period of 40 min, presenting reactor temperature (blue) and molar product flow (orange) over the time of periodic operation. 128

Figure 8.11 Experimental data of reactor temperature (left) and molar flow of the product acetic acid (right) with first stationary conditions (V_R = 298 ml, F_W = 40 ml/min and F_{AA} = 3 ml/min). 130

Figure 8.12 Input signals for multiple input parameter modulation of inlet concentration and total flow rate for the dynamic experimental part with inlet concentration of anhydride (top), total volumetric flow rate (second), water flow rate (third) and acetic anhydride flow rate (bottom) for dynamic operation with a frequency $f = 4.167 \cdot 10^{-4}$ Hz, amplitude of inlet concentration A_C = 85 %, amplitude of total flow A_F = 55 % and phase difference ϕ = 157.33 °. 131

Figure 8.13 Multiple input parameter modulation of inlet concentration A_C = 85 %, total flow rate A_F = 55 % and a period of 40 min, presenting conductivity at the outlet (top), product concentration at the outlet (second), molar product flow (third) and inlet molar product flow (bottom) for a phase difference ϕ = 157.33 °. 132

Figure 8.14 Multiple input parameter modulation of inlet concentration A_C = 85 %, total flow rate A_F = 55 % and a period of 40 min, presenting reactor temperature (blue) and molar product flow (orange) over the time of periodic operation with a phase difference ϕ = 157.33 °. 133

Figure 8.15 Results of predicted and experimental of absolute change in product yield (eq. (8.30)) by dynamic operation for varying inlet concentration amplitude A_C, with a fixed amplitude for total flow rate A_F = 55 % and period of 40 min, for the yield obtained by dynamic operation implying an optimal phase difference ϕ_{opt}. 134

Figure 8.16 Results of predicted and experimental of absolute change in product yield (eq. (8.30)) by dynamic operation for varying total flow rate amplitude A_F, with a fixed amplitude for inlet concentration A_C = 85 % and period of 40 min, for the yield obtained by dynamic operation implying an optimal phase difference. 135

Figure 8.17 Results of predicted and experimental of absolute change in product yield (eq. (8.30)) by dynamic operation for varying phase difference ϕ, with fixed amplitudes for inlet concentration $A_C = 85$ % and total flow rate $A_F = 55$ %, for the yield obtained by dynamic operation implying. 137

Figure A.1 Propene selectivity of catalytic systems with the subsequent conversion for different feed molecules. A4
Figure A.2 Column configuration of the used gas chromatography for the analysis of the product spectrum for the ETP reaction. A5
Figure A.3 Schematic picture of the TGA setup by Netzsch [Netzsch Thermal Analysis, 2018]. . A5
Figure A.4 Comparative evaluation of the Ni/AlMCM-41 catalyst with a Si/Al ratio of 60, under varying reaction conditions of (a) conversion of ethene, (b) yield of propene, (c) yield of 1-butene and (d) yield of 2-butene as a function of temperature. A7
Figure A.5 Comparative evaluation of the deactivation effect on the Ni/AlMCM-41 catalyst with a Si/Al ratio of 60, under varying reaction conditions of (a) conversion of ethene, (b) selectivity of propene, (c) selectivity of 1-butene and (d) selectivity of 2-butene over time-on-stream for the ETP reaction at 250 °C. A8
Figure A.6 Comparative evaluation of the deactivation effect on the Ni/AlMCM-41 catalyst with a Si/Al ratio of 60, under varying reaction conditions of (a) conversion of ethene, (b) selectivity of propene, (c) selectivity of 1-butene and (d) selectivity of 2-butene over time-on-stream for the ETP reaction at 300 °C. A9
Figure A.7 Comparative evaluation of the deactivation effect on the Ni/AlMCM-41 catalyst with a Si/Al ratio of 60, under varying reaction conditions of (a) conversion of ethene, (b) selectivity of propene, (c) selectivity of 1-butene and (d) selectivity of 2-butene over time-on-stream for the ETP reaction at 350 °C. A10
Figure A.8 Concluded over all reaction network occurring on Ni/AlMCM-41. . . . . A11
Figure A.9 Effect of temperature of W/F ratios applying the LHHW approach in combination with the modified reaction Network II (a) Conversion of ethene; (b) Propene selectivity; (c) 1-butene selectivity; d) trans-butene selectivity and $Para_{II} = 56$ estimated parameters. A12
Figure A.10 Effect of temperature for a feed concentration of 5 % ethene applying the LHHW approach in combination with the modified reaction Network II (a) Conversion of ethene; (b) Propene selectivity; (c) 1-butene selectivity; (d) trans-butene selectivity and $Para_{II} = 56$ estimated parameters. A13
Figure A.11 Effect of temperature for a feed concentration of 10 % ethene applying the LHHW approach in combination with the modified reaction Network II (a) Conversion of ethene; (b) Propene selectivity; (c) 1-butene selectivity; (d) trans-butene selectivity and $Para_{II} = 56$ estimated parameters. A14
Figure A.12 Detailed analysis of simulative results to experimental values for mechanistic modeling for the reaction network introduced by Iwamoto. A17
Figure A.13 Detailed analysis of simulative results to experimental values for mechanistic modeling for the reaction network assuming catalytic cracking. A18

Figure A.14 Concept for the reactor configurations as a single catalyst bed in an integrated setup (top) and in a segregated configuration with two distinct catalysts and two separate temperatures (bottom). A19
Figure A.15 Detailed flow diagram of the Miniplant Zapfstellen- und Membranreaktor (MPZM), including two packed-bed reactors in series. A20
Figure A.16 Constructive drawing of the implied reactor for the mini plant setup (MPZM) A21
Figure A.17 Comparative evaluation of the Ni/AlMCM-41 catalyst with a Si/Al ratio of 60, incorporated in a lab scale experimental setup (blue, orange and yellow) and in a miniplant setup (purple and green) at 600 °C. A23
Figure A.18 Temperature dependent conversion via cross-metathesis of ethene and trans-butene (orange) using W/SiO_2 as the catalyst and the corresponding selectivity of the analyzed products (blue). A26
Figure A.19 Resulting conversion (red) and product selectivity (blue) for the retro-metathesis applying W/SiO_2 with 5 % propene feed and W/F = 500 $\frac{kg_{Cat} \cdot s}{m^3}$. A26
Figure A.20 Conversion of trans-butene (top) and ethene (bottom) as a function of time for W/SiO_2 at T = 600 °C, W/F = 500 $\frac{kg_{Cat} \cdot s}{m^3}$, $c_{C_2H_4}$ = 2.5 % and $c_{trans-C_4H_8}$ = 2.5 %. . . . A27
Figure A.21 Product selectivity as a function of time for W/SiO_2 at T = 600 °C, W/F = 500 $\frac{kg_{Cat} \cdot s}{m^3}$, $c_{C_2H_4}$ = 2.5 % and $c_{trans-C_4H_8}$ = 2.5 %. A28
Figure A.22 Influence of the weight to flow ratio for an ethene to trans-butene ratio of 1:1 at 600 °C on (a) conversion of trans-butene (solid line) and ethene (dashed line) and (b) selectivity of propene. A29
Figure A.23 Influence of the Feed ratio of ethene to trans-butene for a W/F of 500 $\frac{kg_{Cat} \cdot s}{m^3}$ and 600 °C on (a) conversion of trans-butene (solid line) and ethene (dashed line) and (b) selectivity of propene. A30
Figure A.24 Comparative evaluation of the integrated setup incorporating Ni/AlMCM-41 catalyst with a Si/Al ratio of 60, for a lab scale (blue) and miniplant experimental setup (orange), with a segregated setup (yellow), incorporating Ni/AlMCM-41 in the first and W/SiO_2 in the second reactor at 600 °C. A32

Figure B.1 Influence of the (a) activation energy E_A, (b) the collision factor k_∞ and (c) the reaction order n on the normalized product yield for the simultaneous modulation of inlet concentration and inlet temperature with amplitudes of A_C = 85 % and A_T = 7 % with individual optimal phase differences. B2
Figure B.2 Flow sheet of the realized experimental setup for forced dynamic parameter perturbation. B4
Figure B.3 Implemented voltages for the individual pumps for acetic anhydride (top) and water (bottom) with previously established steady-state (V_R = 298 ml, F_W = 40 ml/min and F_{AA} = 3 ml/min) and subsequent dynamic operation with the following parameter: frequency f = $4.167 \cdot 10^{-4}$ Hz, amplitude of inlet concentration A_C = 85 %, amplitude of total flow A_F = 55 % and phase difference ϕ = 157.33°). B5
Figure B.4 Graphical display of fourier expansion of different values k. B8

Figure B.5 Predicted yield of product (blue) and optimal phase difference (orange) as function of period, comparing sinusoidal and square wave input modulation for the hydrolysis of acetic anhydride. B8

Figure B.6 Input signals for simultaneous modulation of inlet concentration A_C = 85 % and total flow rate A_F = 55 % for a period of 40 min and with optimal phase difference applied for square wave input function, with inlet concentration of anhydride (top), total volumetric flow rate (second), water flow rate (third) and acetic anhydride flow rate (bottom) with a square wave function. B10

Figure B.7 Output signals for simultaneous modulation of inlet concentration A_C = 85 %, total flow rate A_F = 55 % and a period of 40 min with an optimal phase difference, presenting (a) conductivity at the outlet (top), product concentration at the outlet (second), molar product flow (third) and inlet molar product flow (bottom) B11

Figure B.8 Implemented voltages for the individual pumps for acetic anhydride (top) and water (bottom) with previously established steady-state (V_R = 298 ml, F_W = 40 ml/min and F_{AA} = 3 ml/min) and subsequent dynamic operation with the following parameter for square wave input functions: frequency f = $4.167 \cdot 10^{-4}$ Hz, amplitude of inlet concentration A_C = 85%, amplitude of total flow A_F = 55 % and phase difference ϕ = 157.33°). B12

List of Tables

Table 3.1 Catalytic Systems for the direct conversion of ethene to propene, conversion of the reactant ethene, selectivity of propene and reaction conditions, catalytic system. . . . 34

Table 4.1 Kinetic Parameters for an exemplified reactive system for the cyclic process for inherent dynamic operation. 46

Table 5.1 Specifications of Netzsch's thermogravimetric analysis (TGA). 58
Table 5.2 Nitrogen adsorption data of Ni/AlMCM-41 with different aluminum content. 60
Table 5.3 Highest selectivity and yield data detected of the investigated temperature, feed concentration and W/F ranges covered. 65

Table 6.1 Deactivation kinetic parameters for the method of Janssens. 93
Table 6.2 Kinetic parameters for the regeneration of Ni/AlMCM-41 implying the power-law approach. 94

Table 7.1 Kinetic Data for the Hydrolysis of acetic anhydride from literature. 106
Table 7.2 List of kinetic experiments performed for parameter estimation for the Hydrolysis of acetic anhydride. 106
Table 7.3 Estimated kinetic parameters for the applied kinetic model approaches for the hydrolysis of acetic anhydride. 112

Table 8.1 Kinetic and thermodynamic parameters for the model reaction investigated eq. (3.4). 118
Table 8.2 Reference parameters of eqs. (7.1) and (7.2) in accordance with constraints and restrictions originating from the reaction system and possibilities for the experimental study for the optimization and the steady-state conditions assuming kinetic model 2 (eq. (7.4)). 119
Table 8.3 Predicted dynamic results by the NFR method for a varying period time, with fixed amplitudes for inlet concentration A_C = 85 % and total flow rate A_F = 55 %, for the yield obtained by dynamic operation implying an optimal phase difference. 122
Table 8.4 Predicted dynamic results by the NFR method for varying inlet concentration amplitude A_C, with fixed amplitudes for total flow rate A_F = 55 % and period of 40 min, for the yield obtained by dynamic operation implying an optimal phase difference ϕ_{opt}. 133
Table 8.5 Predicted dynamic results by the NFR method for varying inlet concentration amplitude A_F, with fixed amplitudes for inlet concentration A_C = 85 % and period of 40 min, for the yield obtained by dynamic operation implying an optimal phase difference. . 135
Table 8.6 Predicted dynamic results by the NFR method for varying phase difference ϕ, with fixed amplitudes for inlet concentration A_C = 85 % and total flow rate A_F = 55 %, for the yield obtained by dynamic operation implying. 136

Table A.1 Results of the calculation for the reaction eq. (4.1) for a CSTR with varying residence time. A3

Table A.2 Results of the calculation for the reaction eq. (4.1) for a PFTR with varying residence time. A3

Table A.3 Estimated 56 kinetic parameters for the modified reaction network including catalytic cracking (eqs. (6.1) to (6.6) and (6.17) to (6.34)) and the kinetic model based on the LHHW approach, including the temperature-independent adsorption equilibrium constants for the components involved [Felischak et al., 2019]. A14

Table A.4 References for the cross-metathesis of ethene and butene to propene, conversion of the reactant butene and the selectivity of propene, reaction conditions and employed catalyst. A24

Part V

Appendix

A - Inherent Dynamic Operation

B - Forced Dynamic Operation

A Inherent Dynamic Operation

The inherent dynamic process operation was described in Part II using the case study of the ethene to propene (ETP) for the occurring process steps of reaction (step 1), deactivation (step 2) and regeneration (step 3).
In this appendix, additional data is given for the performed preliminary theoretical study, for the validation of the individual process steps and the reaction kinetics. Furthermore, the possibility of decoupling the reaction network according to Iwamoto [Iwamoto, 2008] into a two-reactor concept for process intensification is presented.

A.1 Theoretical Study of Inherent Dynamic Optimization

As presented in section 4 for a simplified reaction (eq. (4.1)), optimal determination values for the activity exist, depending on the residence time in the reactor. In the following the obtained results for the different residence time in a CSTR (Table A.1) and a PFTR (Table A.2).

Table A.1: Results of the calculation for the reaction eq. (4.1) for a CSTR with varying residence time.

τ, s	η, %	Y_{ideal}, %	$\overline{Y}_{deac}$, %	a_{max}, %	a_{min}, %	Δt_D, s	Δt_R, s	Δt_{cycle}, s
10	8.88	19.91	1.77	66.91	35.05	323	337	660
50	22.85	31.63	7.23	71.29	22.27	582	498	1080
100	23.11	47.15	10.89	66.26	17.37	670	448	1118
500	22.03	76.77	16.91	72.77	3.22	1559	634	2193
1000	19.39	81.98	15.90	77.62	0.78	2298	745	3043

Within the tables, the individual time arrays for the separate process intervals of reaction coupled with deactivation and regeneration are displayed. Subsequently, the sum of these values results in the overall cycle time. When this value increases the resulting time-averaged yield decreases and in the following the efficiency η decreases.

Table A.2: Results of the calculation for the reaction eq. (4.1) for a PFTR with varying residence time.

τ, s	η, %	Y_{ideal}, %	$\overline{Y}_{deac}$, %	a_{max}, %	a_{min}, %	Δt_D, s	Δt_R, s	Δt_{cycle}, s
10	16.93	19.91	3.37	82.71	48.54	266	109	375
50	38.41	31.63	12.15	89.75	25.76	624	198	822
100	37.40	47.15	17.63	88.17	21.16	714	190	904
500	30.10	76.77	23.10	95.68	4.08	1578	310	1888
1000	25.16	81,98	20,62	92,02	1.87	1949	251	2200

A.2 Analysis of the Process steps for the ETP reaction

For the multitude of catalyst systems presented for the selective formation of propene (section 3.1), the selectivity of propene is shown concerning the conversion of the molecules used in Figure A.1. Ethene, 1-butene, 2-butene, longer-chain alkenes and alcohols are considered.

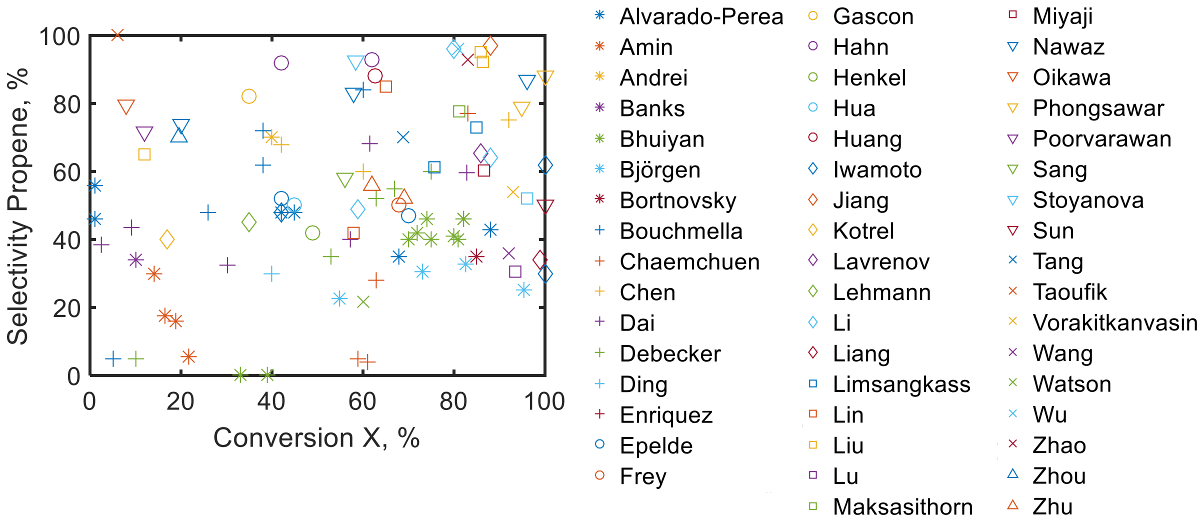

Figure A.1: Propene selectivity of catalytic systems with the subsequent conversion for different feed molecules.

A.2.1 Experimental Configurations

For the quantitative analysis of the product stream composition in the high temperature kinetic reactor (HTKR) a combination of gas chromatography and mass spectrometry was applied. However, only the signals from the chromatograph were used for the evaluation. This allowed the changes in the case of the heterogeneously catalyzed and inherently dynamic direct conversion of ethene to propene to be validated. The following Figure A.2 shows the column configuration and coupling of the columns for the analysis.

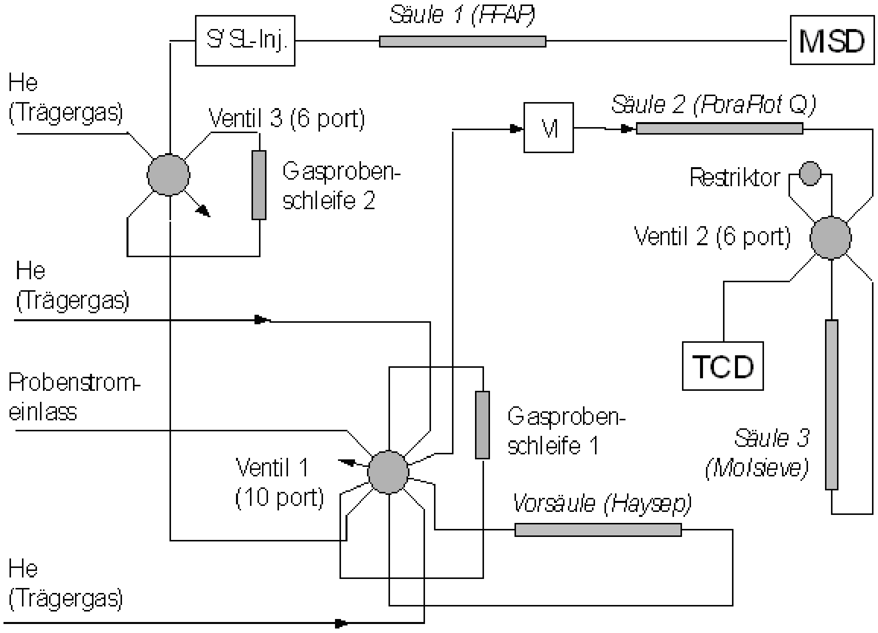
S/SL-Inj.
Säule 1 (FFAP)
MSD
He
(Trägergas)
Ventil 3 (6 port)
Gasproben-
schleife 2
VI
Säule 2 (PoraPlot Q)
Restriktor
Ventil 2 (6 port)
He
(Trägergas)
TCD
Probenstrom-
einlass
Gasproben-
schleife 1
Säule 3
(Molsieve)
Ventil 1
(10 port)
Vorsäule (Haysep)
He
(Trägergas)

Figure A.2: Column configuration of the used gas chromatography for the analysis of the product spectrum for the ETP reaction.

To detect the mass decrease due to coke burn off on a deactivated, heterogeneous catalyst, a thermogravimetric analysis (TGA) from Netzsch was used. A schematic diagram of the equipment used is shown in Figure A.3.

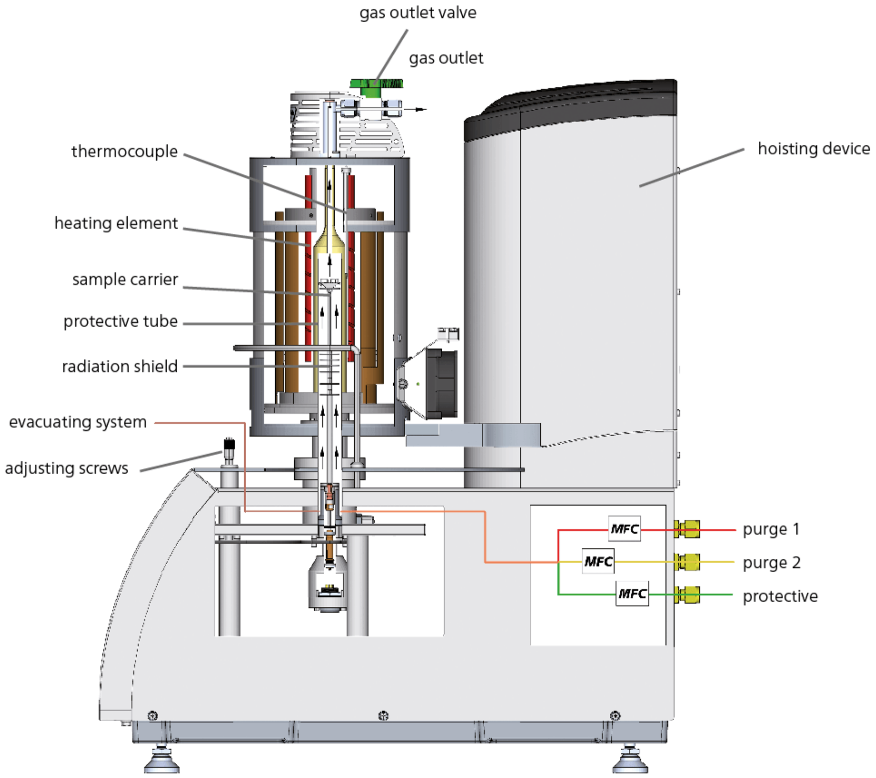
gas outlet valve
gas outlet
thermocouple
hoisting device
heating element
sample carrier
protective tube
radiation shield
evacuating system
adjusting screws
MFC
MFC
MFC
purge 1
purge 2
protective

Figure A.3: Schematic picture of the TGA setup by Netzsch [Netzsch Thermal Analysis, 2018].

A.2.2 Catalyst Characterization

Sorption isotherms and BET

For the determination of the sorption isotherms, the NOVA200e instrument from Quantachrome was used. For pretreatment, the sample was degassed 24 h in a vacuum at 120 °C. The adsorption/desorption of gaseous nitrogen was carried out at low temperatures, which was achieved by cooling with liquid nitrogen at -196 °C. The sample was then degassed in a vacuum at 120 °C. The sorption isotherms were measured in the range from 0 to 0.999 (≈ 1) $\frac{p}{p_0}$.

X-ray diffraction

An X'Pert PRO apparatus from PANalytical was used for this purpose. It was equipped with a copper tube that generates the specific K_α radiation. The equipment consists of a sample holder, a movable radiation source, detector shoulders and a generator PW3040 (mppe). 40 kV and 40 mA are used in operating mode. The finely crushed sample was placed on a silicon wafer. The sample was scanned in the 2θ range from 1.3° to 80° with a step size of 0.008° per 30 s.

Temperature Programmed Reduction (TPR)

The ChemStar TPx from Quantachrome was used for this analysis method. Initially, the material was pretreated with a helium stream of 30 $\frac{ml}{min}$ at 150 °C to remove moisture from the sample. The temperature of 150 °C was maintained for 30 min. Afterward, the sample was cooled to 50 °C under helium. The next step was the measurement in a temperature range of 50-900 °C. The temperature was changed at a rate of $10\frac{K}{min}$, with a total volumetric flow of 50 $\frac{ml}{min}$ from 10 % hydrogen in argon. Finally, the material was cooled again with an inert gas to 50 °C. The difference in the hydrogen volume flow was measured using a TCD.

A.2.3 ETP Activity Evaluation

For further evaluation, the conversion and the yield of the main reaction products for varying reaction temperature are presented for a Ni/AlMCM-41 catalyst in Figure A.4 under varying reaction conditions.

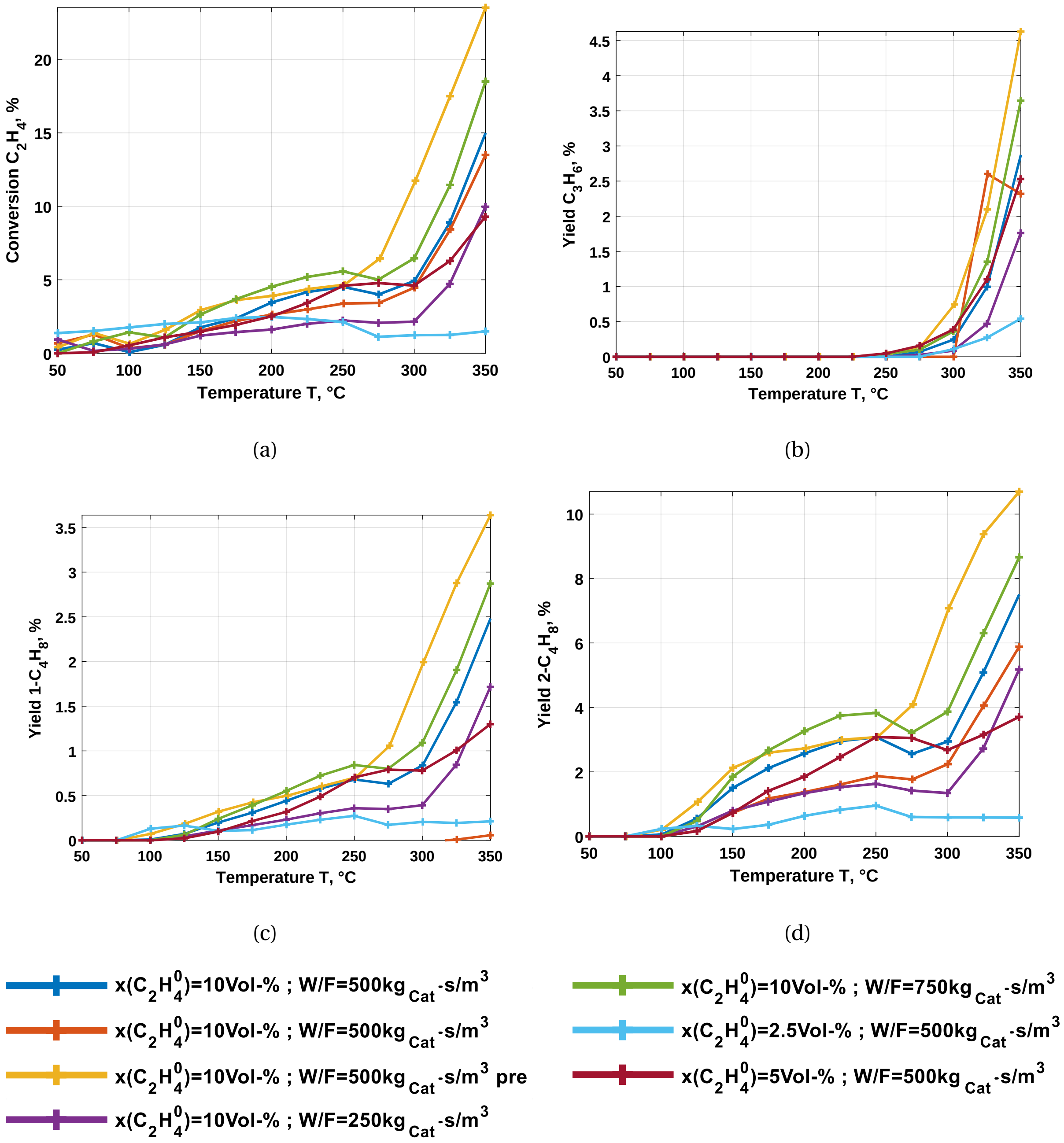

(a) (b)

(c) (d)

Figure A.4: Comparative evaluation of the Ni/AlMCM-41 catalyst with a Si/Al ratio of 60, under varying reaction conditions of (a) conversion of ethene, (b) yield of propene, (c) yield of 1-butene and (d) yield of 2-butene as a function of temperature.

A.2.4 Deactivation

To evaluate the deactivation process for the aluminized, mesoporous MCM-41 catalyst charged with nickel, long-term tests were carried out depending on the input concentration and the reaction temperature. New catalyst beds were prepared and loaded with 5, 10, 15 and 25 % ethene. In addition, the reaction temperature was varied between 250 °C (Figure A.5), 300 °C (Figure A.6) and 350 °C (Figure A.7).

It can be seen that the ethene turnover increases with increasing reaction temperature and input concentration. At the same time, deactivation increases with higher temperature limits, which can be seen from the more pronounced drop in turnover. Furthermore, the formation of propene increases significantly with temperature and is increased with lower input concentration.

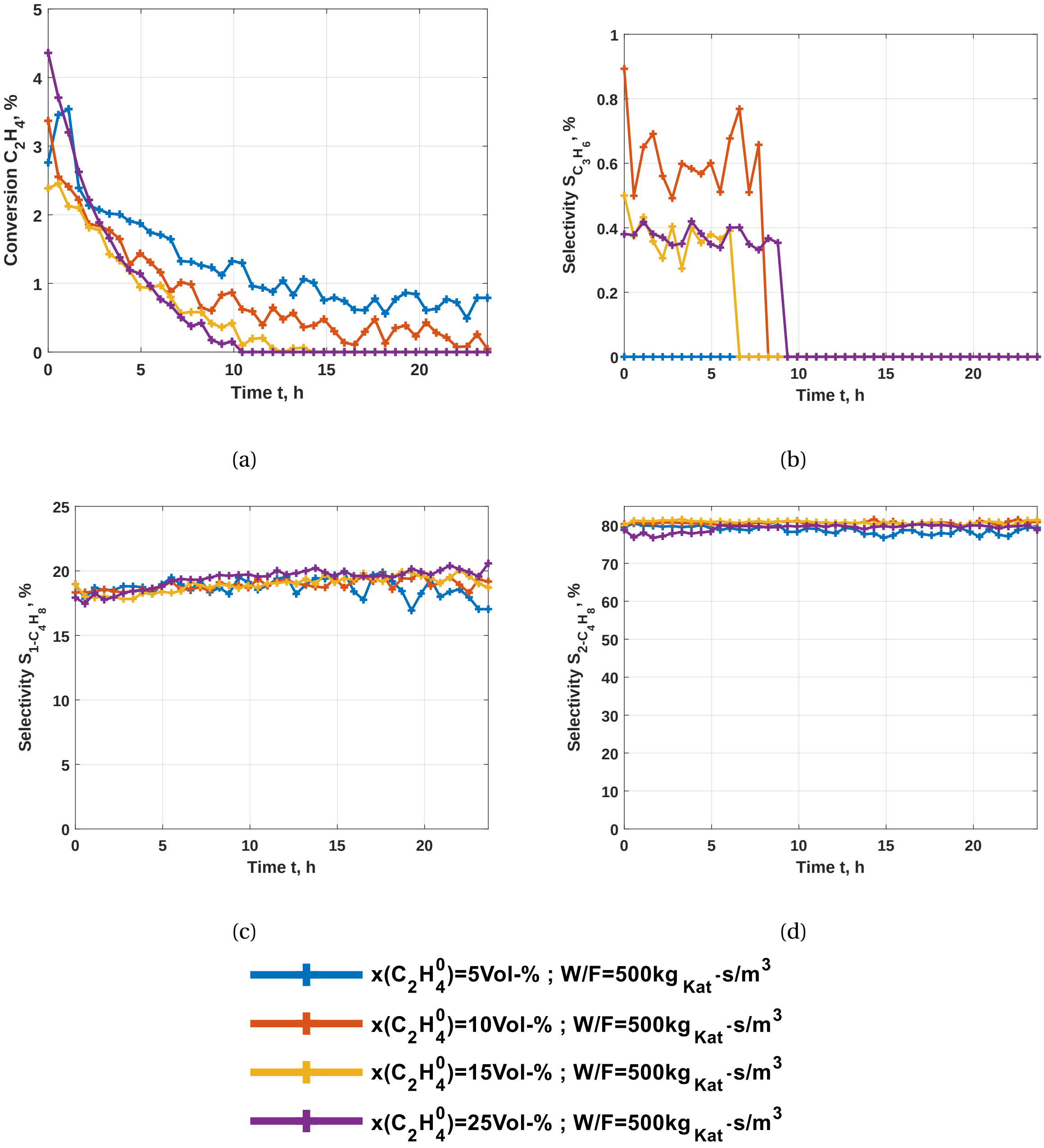

(a) (b)

(c) (d)

Figure A.5: Comparative evaluation of the deactivation effect on the Ni/AlMCM-41 catalyst with a Si/Al ratio of 60, under varying reaction conditions of (a) conversion of ethene, (b) selectivity of propene, (c) selectivity of 1-butene and (d) selectivity of 2-butene over time-on-stream for the ETP reaction at 250 °C.

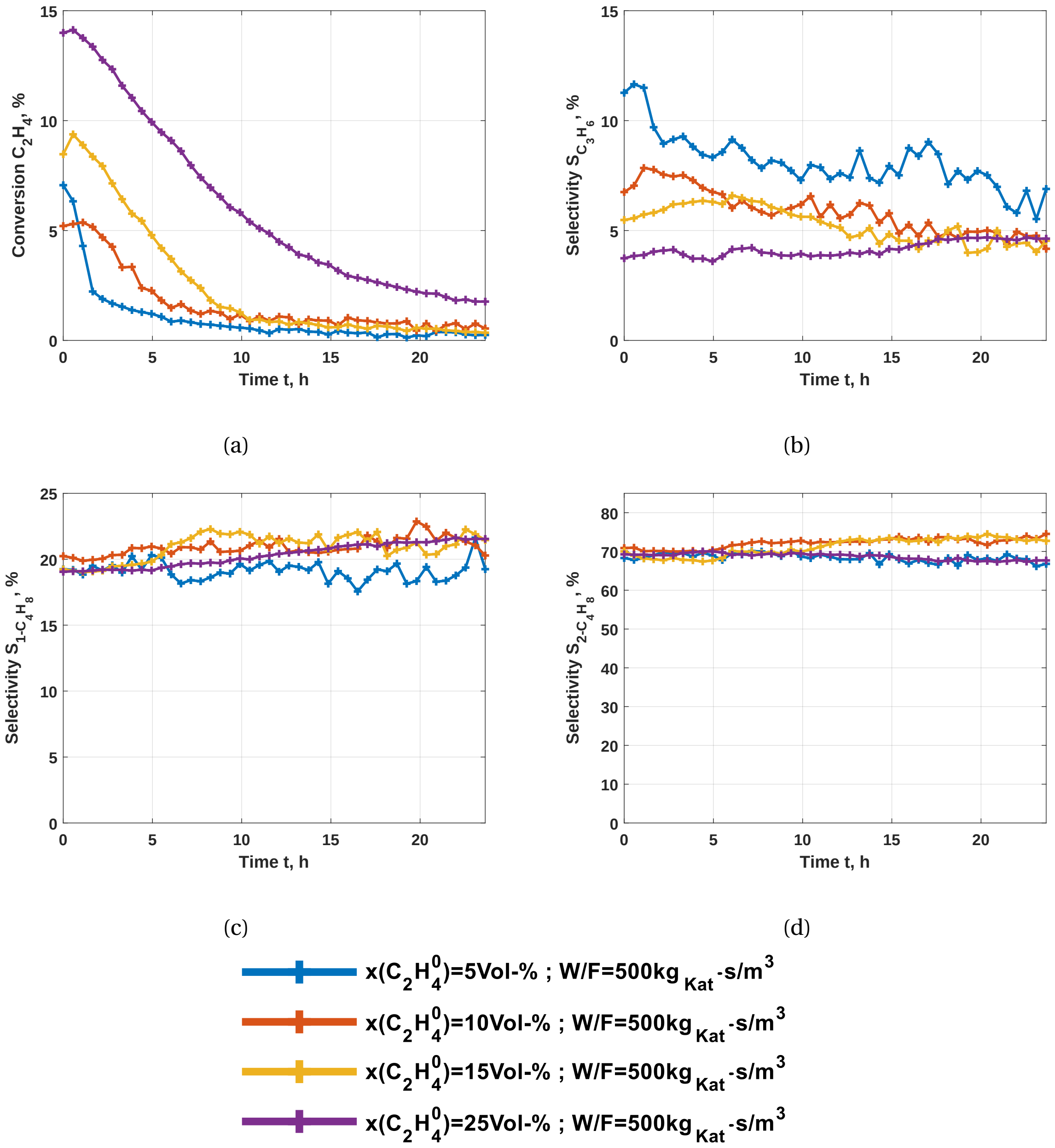

(a) (b)

(c) (d)

Figure A.6: Comparative evaluation of the deactivation effect on the Ni/AlMCM-41 catalyst with a Si/Al ratio of 60, under varying reaction conditions of (a) conversion of ethene, (b) selectivity of propene, (c) selectivity of 1-butene and (d) selectivity of 2-butene over time-on-stream for the ETP reaction at 300 °C.

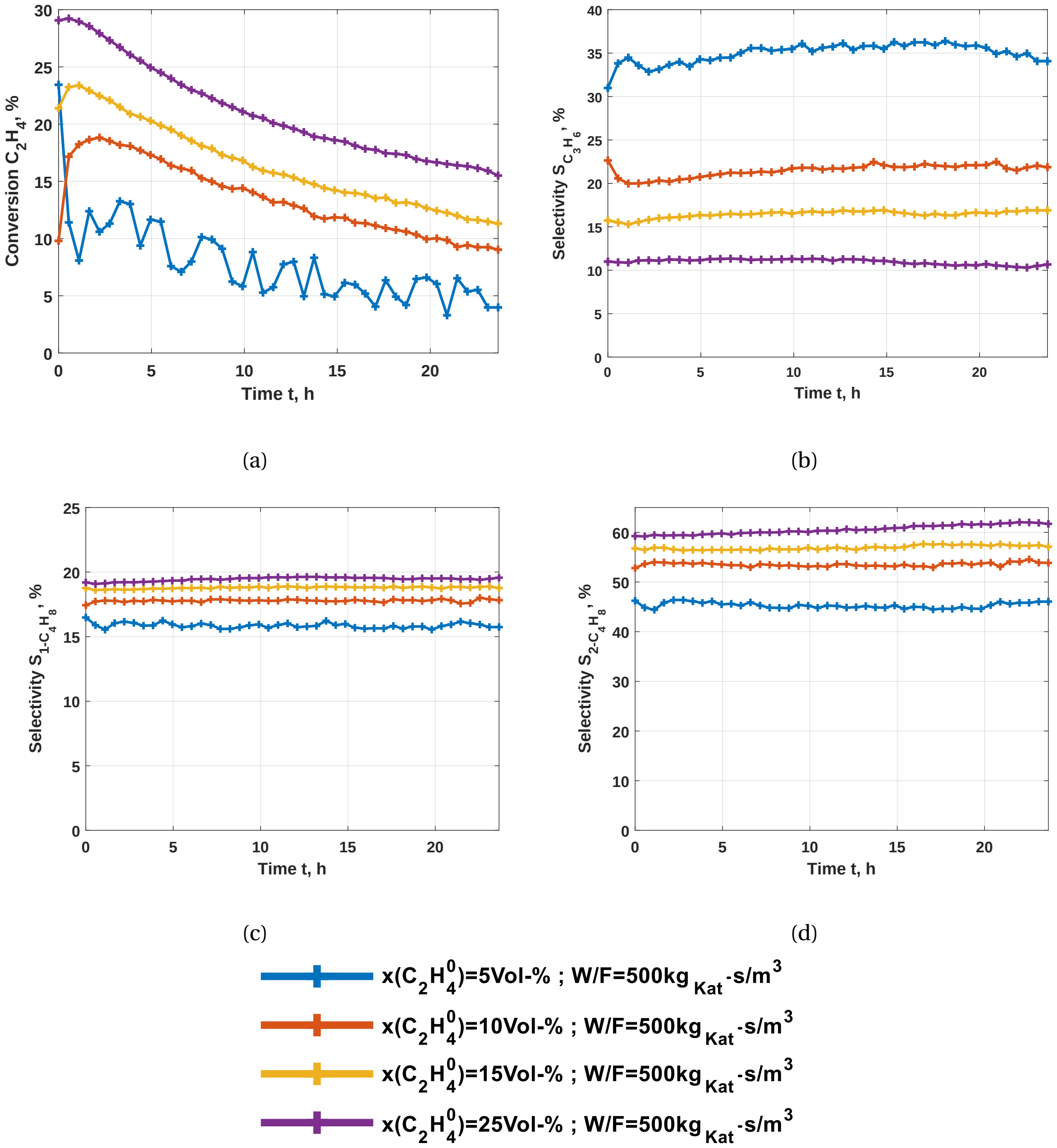

(a) (b)

(c) (d)

Figure A.7: Comparative evaluation of the deactivation effect on the Ni/AlMCM-41 catalyst with a Si/Al ratio of 60, under varying reaction conditions of (a) conversion of ethene, (b) selectivity of propene, (c) selectivity of 1-butene and (d) selectivity of 2-butene over time-on-stream for the ETP reaction at 350 °C.

Another representation of the concluded overall reaction network is shown in Figure A.8. This includes both the reaction network assumed by Iwamoto, based on dimerization, isomerization and metathesis, and the network postulated in this study based on oligomer formation from the feed employed with subsequent cracking reaction. Furthermore, based on the findings of the deactivation study and by literature research, an extension by a possible deactivation pathway is included. Thus, the dehydration of the resulting structures at strongly acidic centers can be used to substantiate the formation of different molecules.

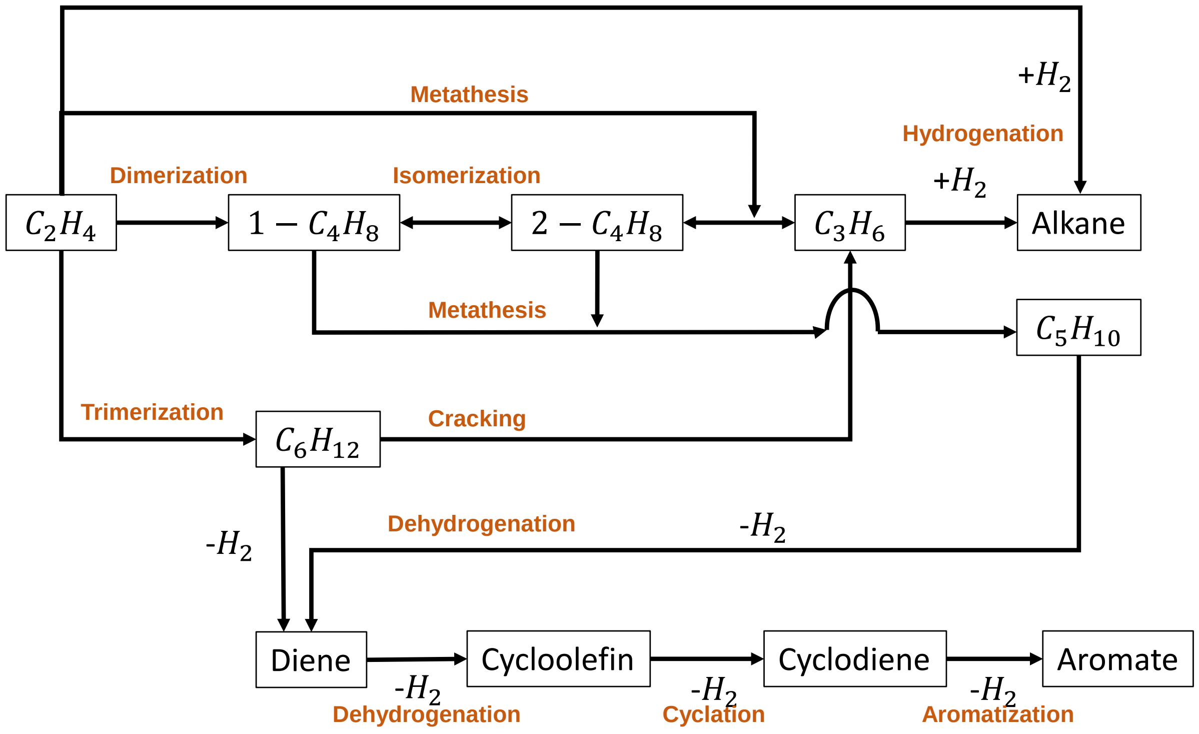

C_2H_4
$1-C_4H_8$
$2-C_4H_8$
C_3H_6
Alkane
C_5H_{10}
C_6H_{12}
Diene
Cycloolefin
Cyclodiene
Aromate
Metathesis
Dimerization
Isomerization
Hydrogenation
$+H_2$
$+H_2$
Metathesis
Trimerization
Cracking
Dehydrogenation
$-H_2$
$-H_2$
$-H_2$
Dehydrogenation
$-H_2$
Cyclation
$-H_2$
Aromatization

Figure A.8: Concluded over all reaction network occurring on Ni/AlMCM-41.

A.3 Reaction Kinetics

As already shown (section 6.1.4.2), with the help of the kinetic approach according to LHHW, the reaction network with cracking can sufficiently represent map the measured values obtained. In the following, the individual courses of the experimental and simulated results are shown in detail as a function of the W/F ratio (Figure A.9), of an input concentration of 5 % (Figure A.10) and for 10 % ethene concentration (Figure A.11).

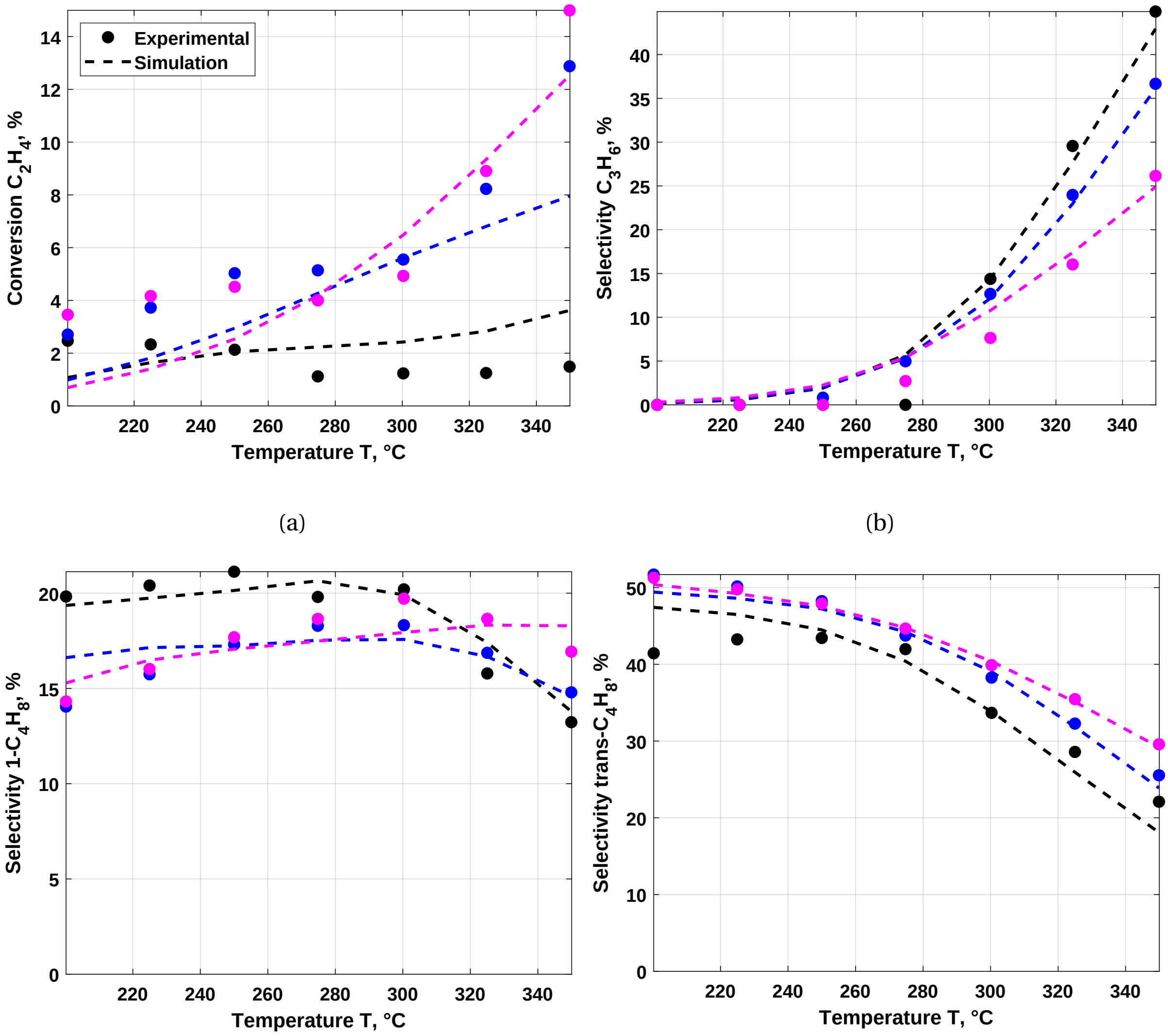

(a)

(b)

(c)

(d)

Figure A.9: Effect of temperature of W/F ratios applying the LHHW approach in combination with the modified reaction Network II (a) Conversion of ethene; (b) Propene selectivity; (c) 1-butene selectivity; d) trans-butene selectivity and $Para_{II} = 56$ estimated parameters.

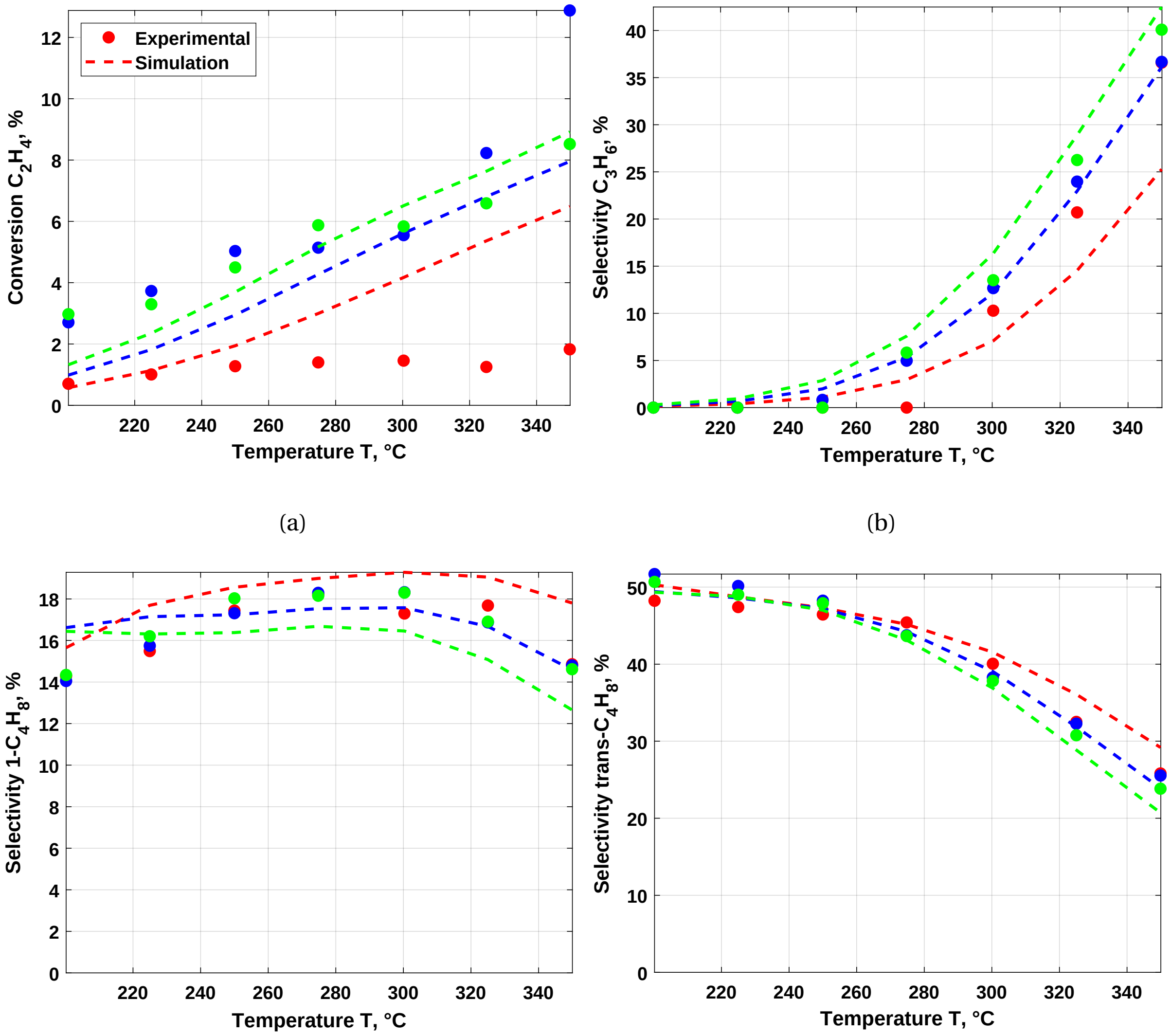

(a)

(b)

(c)

(d)

Figure A.10: Effect of temperature for a feed concentration of 5 % ethene applying the LHHW approach in combination with the modified reaction Network II (a) Conversion of ethene; (b) Propene selectivity; (c) 1-butene selectivity; (d) trans-butene selectivity and $Para_{II}$ = 56 estimated parameters.

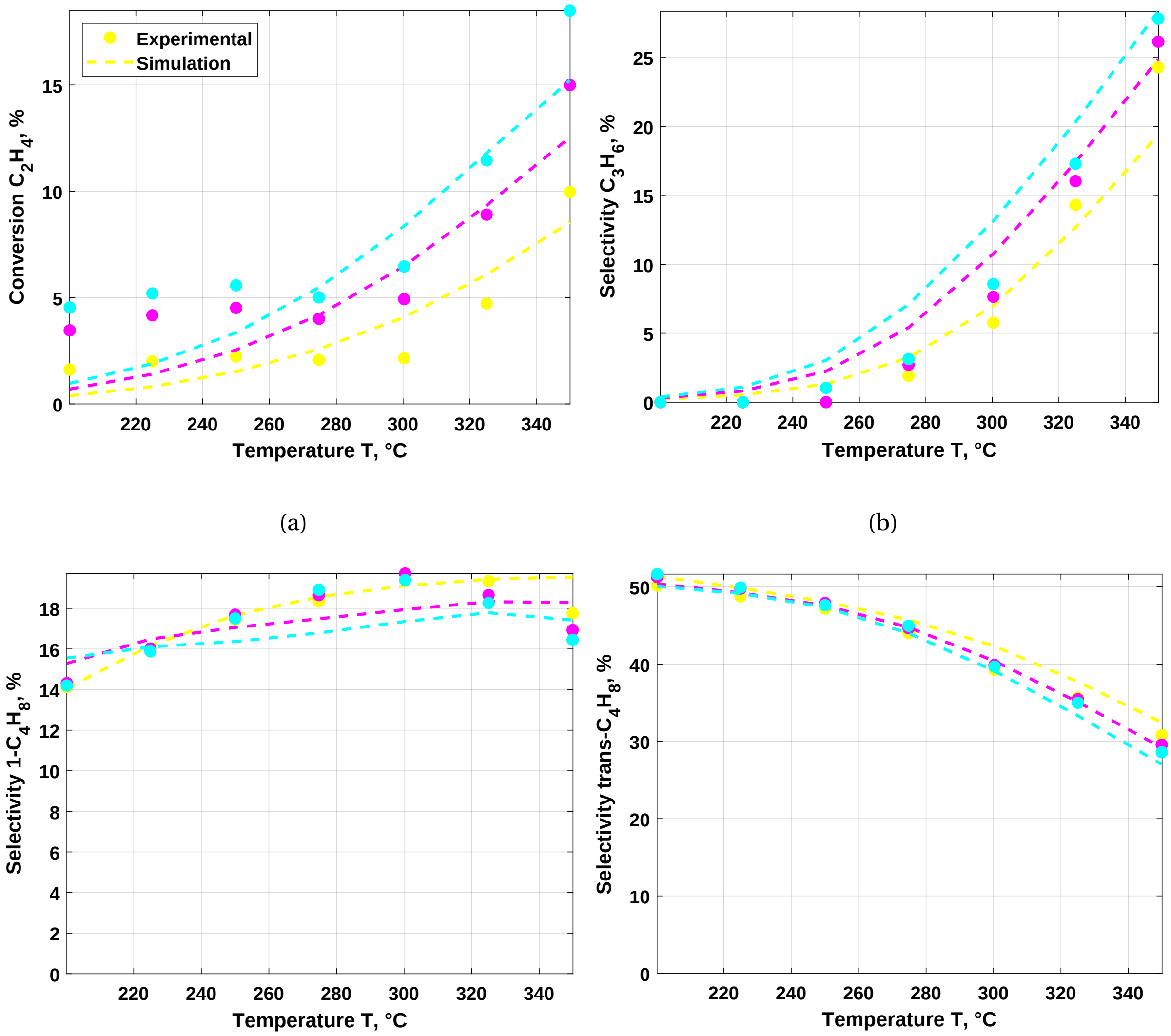

(a)

(b)

(c)

(d)

Figure A.11: Effect of temperature for a feed concentration of 10 % ethene applying the LHHW approach in combination with the modified reaction Network II (a) Conversion of ethene; (b) Propene selectivity; (c) 1-butene selectivity; (d) trans-butene selectivity and $Para_{II}$ = 56 estimated parameters.

The graphs show that the low concentrations result in the greatest deviations, even if only marginally. For this reaction network in combination with the kinetic model, the following kinetic parameters were determined (Table A.3).

Table A.3: Estimated 56 kinetic parameters for the modified reaction network including catalytic cracking (eqs. (6.1) to (6.6) and (6.17) to (6.34)) and the kinetic model based on the LHHW approach, including the temperature-independent adsorption equilibrium constants for the components involved [Felischak et al., 2019].

Equation	**Name**	**Value**	**Unit**
eq. (6.1)	$k_{\infty;(6.1)}$	$9.99{\cdot}10^{+07}$	$mol \cdot s^{-1} \cdot kg_{cat}^{-1} Pa^{-1}$
eq. (6.1)	$E_{A,(6.1)}$	$2.02{\cdot}10^{+02}$	kJ/mol

Table A.3: Estimated 56 kinetic parameters for the modified reaction network including catalytic cracking (eqs. (6.1) to (6.6) and (6.17) to (6.34)) and the kinetic model based on the LHHW approach, including the temperature-independent adsorption equilibrium constants for the components involved [Felischak et al., 2019]. *(continued)*

Equation	**Name**	**Value**	**Unit**
eq. (6.2)	$k_{\infty,(6.2)}$	$1.00 \cdot 10^{+08}$	$mol \cdot s^{-1} \cdot kg_{cat}^{-1} Pa^{-1}$
eq. (6.2)	$E_{A,(6.2)}$	$7.05 \cdot 10^{+01}$	kJ/mol
eq. (6.3)	$k_{\infty,(6.3)}$	$1.00 \cdot 10^{+08}$	$mol \cdot s^{-1} \cdot kg_{cat}^{-1} Pa^{-1}$
eq. (6.3)	$E_{A,(6.3)}$	$6.29 \cdot 10^{+01}$	kJ/mol
eq. (6.4)	$k_{\infty,(6.4)}$	$9.99 \cdot 10^{+05}$	$mol \cdot s^{-1} \cdot kg_{cat}^{-1} Pa^{-1}$
eq. (6.4)	$E_{A,(6.4)}$	$5.69 \cdot 10^{+01}$	kJ/mol
eq. (6.5)	$k_{\infty,(6.5)}$	$9.94 \cdot 10^{+05}$	$mol \cdot s^{-1} \cdot kg_{cat}^{-1} Pa^{-1}$
eq. (6.5)	$E_{A,(6.5)}$	$1.23 \cdot 10^{+02}$	kJ/mol
eq. (6.6)	$k_{\infty,(6.6)}$	$9.92 \cdot 10^{+05}$	$mol \cdot s^{-1} \cdot kg_{cat}^{-1} Pa^{-1}$
eq. (6.6)	$E_{A,(6.6)}$	$4.46 \cdot 10^{+01}$	kJ/mol
eq. (6.17)	$k_{\infty,(6.17)}$	$9.99 \cdot 10^{+07}$	$mol \cdot s^{-1} \cdot kg_{cat}^{-1} Pa^{-1}$
eq. (6.17)	$E_{A,(6.17)}$	$2.73 \cdot 10^{+01}$	kJ/mol
eq. (6.18)	$k_{\infty,(6.18)}$	$1.00 \cdot 10^{+08}$	$mol \cdot s^{-1} \cdot kg_{cat}^{-1} Pa^{-1}$
eq. (6.18)	$E_{A,(6.18)}$	$5.42 \cdot 10^{+01}$	kJ/mol
eq. (6.19)*	$k_{\infty,(6.19)}$	$9.99 \cdot 10^{+07}$	$mol \cdot s^{-1} \cdot kg_{cat}^{-1} Pa^{-1}$
eq. (6.19)*	$E_{A,(6.19)}$	$1.73 \cdot 10^{+01}$	kJ/mol
eq. (6.20)*	$k_{\infty,(6.20)}$	$9.99 \cdot 10^{+07}$	$mol \cdot s^{-1} \cdot kg_{cat}^{-1} Pa^{-1}$
eq. (6.20)*	$E_{A,(6.20)}$	$1.72 \cdot 10^{+01}$	kJ/mol
eq. (6.21)	$k_{\infty,(6.21)}$	$1.00 \cdot 10^{+08}$	$mol \cdot s^{-1} \cdot kg_{cat}^{-1} Pa^{-1}$
eq. (6.21)	$E_{A,(6.21)}$	$7.21 \cdot 10^{+01}$	kJ/mol
eq. (6.22)	$k_{\infty,(6.22)}$	$9.99 \cdot 10^{+07}$	$mol \cdot s^{-1} \cdot kg_{cat}^{-1} Pa^{-1}$
eq. (6.22)	$E_{A,(6.22)}$	$9.27 \cdot 10^{+01}$	kJ/mol
eq. (6.23)*	$k_{\infty,(6.23)}$	$9.99 \cdot 10^{+07}$	$mol \cdot s^{-1} \cdot kg_{cat}^{-1} Pa^{-1}$
eq. (6.23)*	$E_{A,(6.23)}$	$7.87 \cdot 10^{+01}$	kJ/mol
eq. (6.24)*	$k_{\infty,(6.24)}$	$9.99 \cdot 10^{+07}$	$mol \cdot s^{-1} \cdot kg_{cat}^{-1} Pa^{-1}$
eq. (6.24)*	$E_{A,(6.24)}$	$1.14 \cdot 10^{+02}$	kJ/mol
eq. (6.25)*	$k_{\infty,(6.25)}$	$9.99 \cdot 10^{+07}$	$mol \cdot s^{-1} \cdot kg_{cat}^{-1} Pa^{-1}$
eq. (6.25)*	$E_{A,(6.25)}$	$1.10 \cdot 10^{+02}$	kJ/mol
eq. (6.26)*	$k_{\infty,(6.26)}$	$9.99 \cdot 10^{+07}$	$mol \cdot s^{-1} \cdot kg_{cat}^{-1} Pa^{-1}$
eq. (6.26)*	$E_{A,(6.26)}$	$1.20 \cdot 10^{+02}$	kJ/mol
eq. (6.27)	$k_{\infty,(6.27)}$	$9.99 \cdot 10^{+07}$	$mol \cdot s^{-1} \cdot kg_{cat}^{-1} Pa^{-1}$
eq. (6.27)	$E_{A,(6.27)}$	$1.07 \cdot 10^{+02}$	kJ/mol
eq. (6.28)*	$k_{\infty,(6.28)}$	$9.99 \cdot 10^{+07}$	$mol \cdot s^{-1} \cdot kg_{cat}^{-1} Pa^{-1}$
eq. (6.28)*	$E_{A,(6.28)}$	$1.87 \cdot 10^{+02}$	kJ/mol
eq. (6.29)*	$k_{\infty,(6.29)}$	$9.99 \cdot 10^{+07}$	$mol \cdot s^{-1} \cdot kg_{cat}^{-1} Pa^{-1}$
eq. (6.29)*	$E_{A,(6.29)}$	$1.69 \cdot 10^{+02}$	kJ/mol

Table A.3: Estimated 56 kinetic parameters for the modified reaction network including catalytic cracking (eqs. (6.1) to (6.6) and (6.17) to (6.34)) and the kinetic model based on the LHHW approach, including the temperature-independent adsorption equilibrium constants for the components involved [Felischak et al., 2019].*(continued)*

Equation	**Name**	**Value**	**Unit**
eq. (6.30)*	$k_{\infty,(6.30)}$	9.99·10^{+07}	$mol \cdot s^{-1} \cdot kg_{cat}^{-1} Pa^{-1}$
eq. (6.30)*	$E_{A,(6.30)}$	7.27·10^{+01}	kJ/mol
eq. (6.31)*	$k_{\infty,(6.31)}$	9.99·10^{+07}	$mol \cdot s^{-1} \cdot kg_{cat}^{-1} Pa^{-1}$
eq. (6.31)*	$E_{A,(6.31)}$	1.73·10^{+02}	kJ/mol
eq. (6.32)*	$k_{\infty,(6.32)}$	9.99·10^{+07}	$mol \cdot s^{-1} \cdot kg_{cat}^{-1} Pa^{-1}$
eq. (6.32)*	$E_{A,(6.32)}$	1.60·10^{+02}	kJ/mol
eq. (6.33)	$k_{\infty,(6.33)}$	9.99·10^{+07}	$mol \cdot s^{-1} \cdot kg_{cat}^{-1} Pa^{-1}$
eq. (6.33)	$E_{A,(6.33)}$	1.49·10^{+02}	kJ/mol
eq. (6.34)	$k_{\infty,(6.34)}$	9.99·10^{+07}	$mol \cdot s^{-1} \cdot kg_{cat}^{-1} Pa^{-1}$
eq. (6.34)	$E_{A,6.34)}$	6.85·10^{+01}	kJ/mol
	K_{ads}^{Ethene}	1.51·10^{-04}	1/Pa
	$K_{ads}^{1-Butene}$	3.64·10^{-03}	1/Pa
	$K_{ads}^{cis-Butene}$	7.94·10^{-02}	1/Pa
	$K_{ads}^{trans-Butene}$	2.47·10^{-01}	1/Pa
	$K_{ads}^{Propene}$	2.05·10^{-03}	1/Pa
	$K_{ads}^{Pentene}$	2.54·10^{-07}	1/Pa
	K_{ads}^{Hexene}	1.57·10^{-04}	1/Pa
	K_{ads}^{Ethane}	9.902	1/Pa

Furthermore, in Figure A.12the mechanistic modeling approach for the network based on Iwamoto's conclusions and in Figure A.13 for the newly proposed reaction network show a detailed analysis of the experimental and simulated results, depending on the reaction conditions.

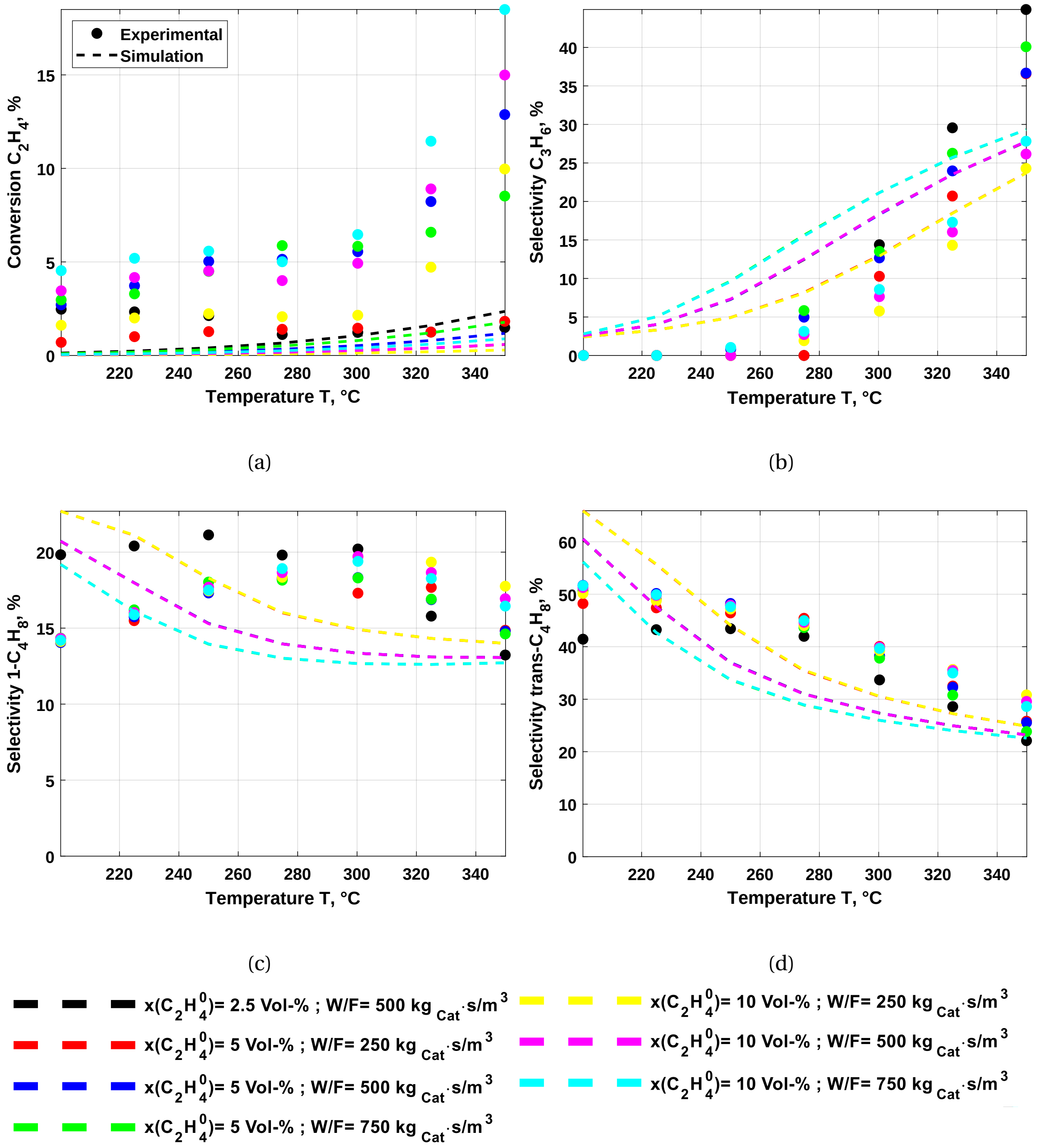

(a) (b)

(c) (d)

Figure A.12: Detailed analysis of simulative results to experimental values for mechanistic modeling for the reaction network introduced by Iwamoto.

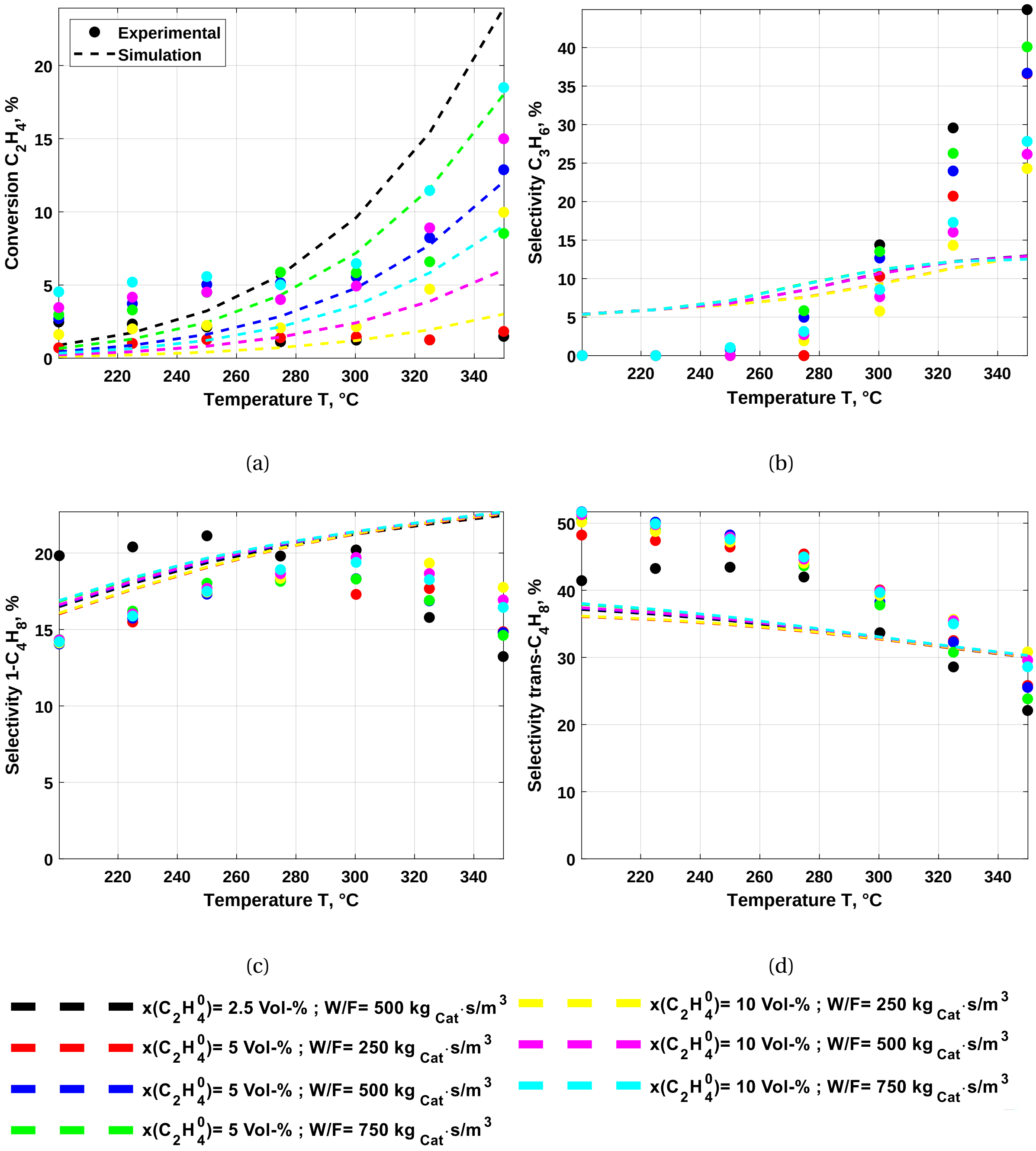

(a)

(b)

(c)

(d)

Figure A.13: Detailed analysis of simulative results to experimental values for mechanistic modeling for the reaction network assuming catalytic cracking.

A.4 Two-Stage Reactor Concept

As mentioned, the NFR method can be used to optimize the heterogeneous catalyzed system with known kinetic parameters. Another possibility is to split the reaction system into two separate reactors. This way it is possible to obtain more degrees of freedom and thus increase the potential of the reaction system. The realization of further increases in the performance parameters of the process is to be achieved by decoupling the reaction network described by Iwamoto [Iwamoto, 2008], which is indicated in Figure A.14. Based on the presented concept, the way can be paved for better industrial applicability and convenience.

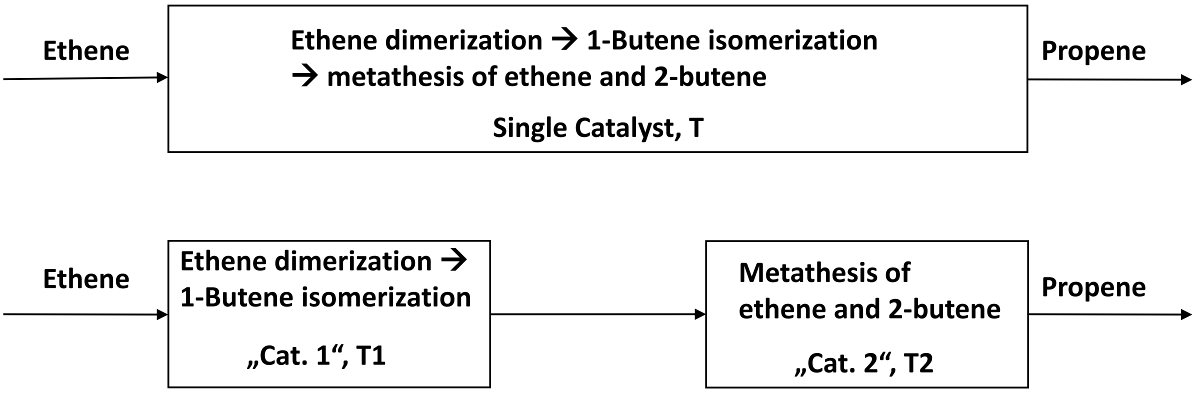
Ethene
Ethene dimerization → 1-Butene isomerization → metathesis of ethene and 2-butene
Single Catalyst, T
Propene
Ethene
Ethene dimerization → 1-Butene isomerization
„Cat. 1“, T1
Metathesis of ethene and 2-butene
„Cat. 2“, T2
Propene

Figure A.14: Concept for the reactor configurations as a single catalyst bed in an integrated setup (top) and in a segregated configuration with two distinct catalysts and two separate temperatures (bottom).

A.4.1 Pilot Plant Setup

To experimentally validate this reactor design approach, a pilot plant, MPZM presented in Figure A.15, existing at the Max Planck Institute Magdeburg (MPI) was applied.

The plant was adapted according to the requirements and thus consists of three primary areas. First, the gas supply, that adjusts the desired compositions of the feed by mixing ethene (purity 99.95 %) with nitrogen (purity 99.9995 %). With the setting of the flow rates, the corresponding contact times are accomplished. The flows of the gaseous media are determined and achieved by MFC's (*Bürkert*). This part of the plant is connected to the second part, with the temperature control by preheaters (*Fabr. Horst* with 230 V / 1000 W and *Inconel* with 110V/9A) and pipe heaters (*Fabr. Horst* with 230 V / 170 W/m). The temperature-controlled and concentrated media are transported to the reactors, as the third part of the plant.

The scale of the plant is characterized by fully glazed, ceramic tubes with an inner diameter of 21 mm and an outer diameter of 32 mm. Compared to the quartz glass tube with 6 mm inner and 10 mm outer diameter on a laboratory scale. This ceramic is housed in a steel jacket that is designed to operate as a fixed-bed reactor membrane reactor. For the present case, this configuration was not used, a rather simplified packed-bed with a fully glazed inner wall. The reactor was tempered employing electric heating sleeves (*Fabr. Horst* with 230 V / 530 W) according to the temperature of the catalyst bed center. Several thermocouples were introduced into the reactor to monitor the temperature distribution along the reactor bed in the axial direction. Due to the size of the setup, the

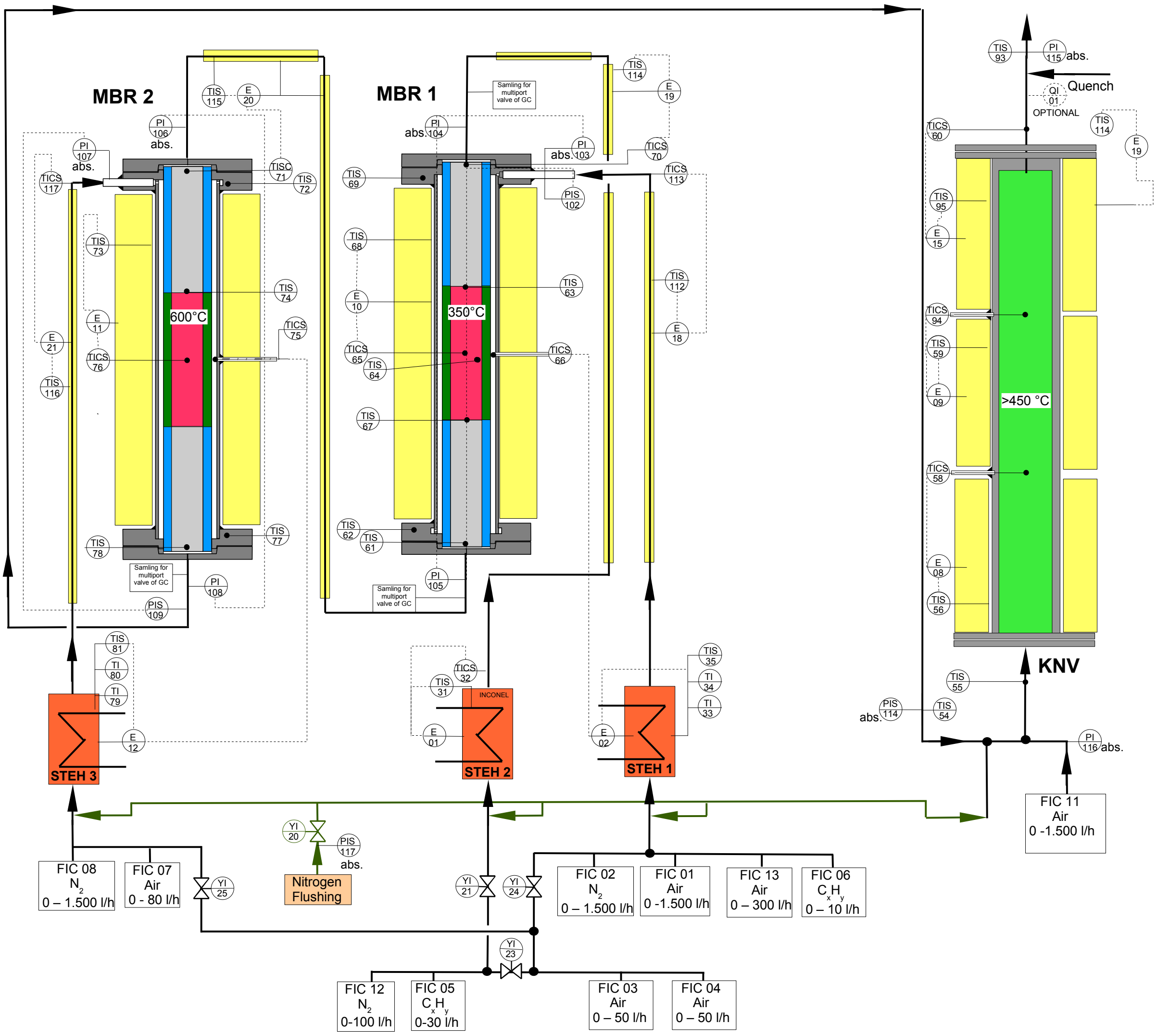
MBR 2
MBR 1
KNV
600°C
350°C
>450 °C
STEH 3
STEH 2
STEH 1
INCONEL
Quench
QI 01 OPTIONAL
Samling for multiport valve of GC
Nitrogen Flushing
FIC 08 N2 0 – 1.500 l/h
FIC 07 Air 0 - 80 l/h
FIC 02 N2 0 – 1.500 l/h
FIC 01 Air 0 -1.500 l/h
FIC 13 Air 0 – 300 l/h
FIC 06 CxHy 0 – 10 l/h
FIC 11 Air 0 -1.500 l/h
FIC 12 N2 0-100 l/h
FIC 05 CxHy 0-30 l/h
FIC 03 Air 0 – 50 l/h
FIC 04 Air 0 – 50 l/h
YI 20
YI 21
YI 23
YI 24
YI 25
PIS 117 abs.
PI 106 abs.
PI 107 abs.
PI 104 abs.
PI 103 abs.
PI 105
PI 108
PIS 109
PIS 102
PI 115 abs.
PI 116 abs.
PIS 114 abs.
TIS 115
E 20
TISC 71
TIS 72
TIS 73
TIS 74
TICS 75
TICS 76
TIS 77
TIS 78
TICS 117
E 21
TIS 116
E 11
TIS 114
E 19
TICS 70
TICS 113
TIS 69
TIS 68
E 10
TICS 65
TIS 64
TIS 67
TIS 63
TICS 66
TIS 62
TIS 61
TIS 112
E 18
TIS 81
TI 80
TI 79
E 12
TICS 32
TIS 31
E 01
TIS 35
TI 34
TI 33
E 02
TIS 93
TICS 60
TIS 95
E 15
TICS 94
TIS 59
E 09
TICS 58
E 08
TIS 56
TIS 55
TIS 54

Figure A.15: Detailed flow diagram of the MPZM, including two packed-bed reactors in series.

effect of disturbances on the flow by these installations is minimal. After the single or cascade reactor setup, the media is transferred to an afterburner that catalytically oxidizes the residue hydrocarbons to carbon dioxide.

For illustration, a constructive drawing of the implemented reactors in the mini plant setup is given in Figure A.16. Within the illustration, all necessary dimensions are given for a realization of the construction.

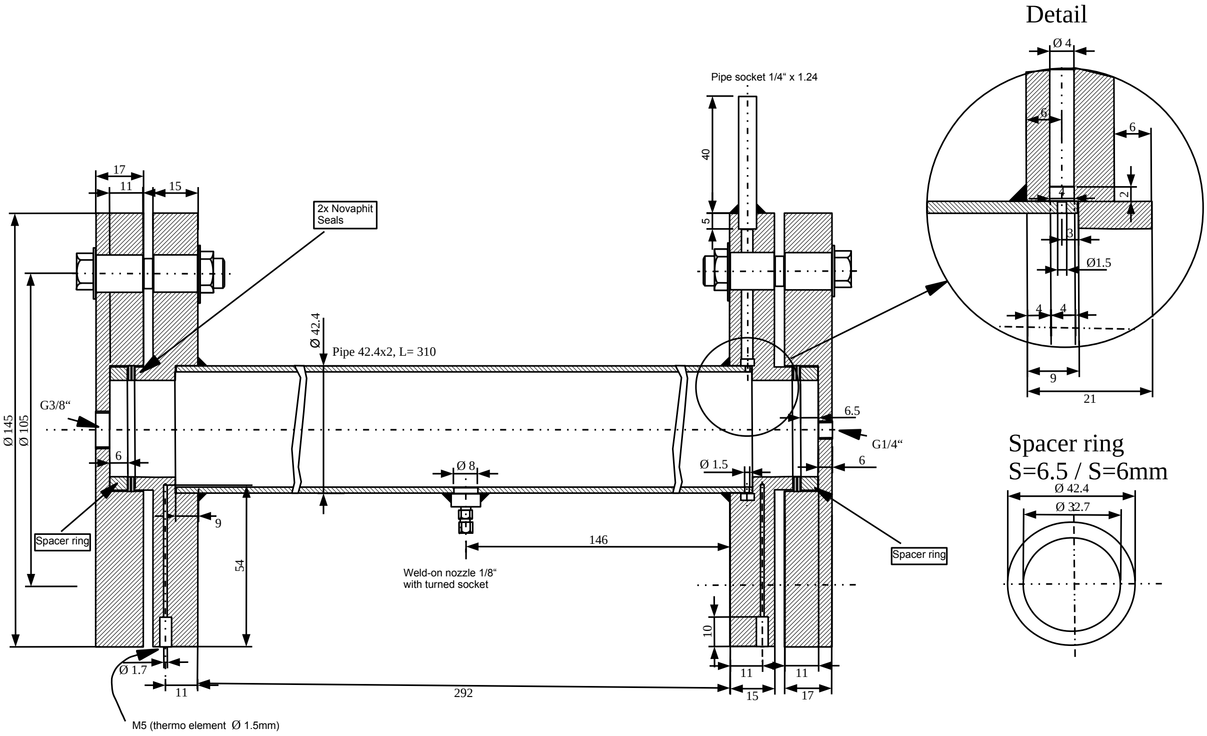
Detail
Ø 4
6
6
4
2
3
Ø1.5
4
4
9
21
Spacer ring
S=6.5 / S=6mm
Ø 42.4
Ø 32.7
Pipe socket 1/4" x 1.24
40
5
17
11
15
2x Novaphit Seals
Ø 42.4
Pipe 42.4x2, L= 310
G3/8"
Ø 145
Ø 105
6
Ø 8
Ø 1.5
6.5
G1/4"
6
9
Spacer ring
146
Spacer ring
54
Weld-on nozzle 1/8" with turned socket
10
Ø 1.7
11
292
11
11
15
17
M5 (thermo element Ø 1.5mm)

Figure A.16: Constructive drawing of the implied reactor for the mini plant setup (MPZM)

Not shown in this constructive drawing is the position and installation of the temperature sensors, which record the temperature at the reactor inlet and outlet, the beginning, the middle and the end of the catalyst bed.

A.4.2 Single-Stage Setup Results

For a suitable and valid comparison of the segregated two-reactor process with the integrated process, it must first be ensured that the scale-up from the laboratory to the pilot plant scale achieves consistent results. The results obtained in the laboratory and pilot plant are then compared with the segregated multi-reactor setup.

As mentioned, the different scales for the integrated, catalyzed system will first be compared, to validate the viability of the pilot plant. In the present case for a laboratory and a pilot plant reactor with a Ni/AlMCM-41 catalyst, Figure A.17 depicts an analogous result. The feed concentration of the used ethene deviates from the standard experiment with 10 % ethene feed and a W/F of 500 $\frac{kg_{Cat} \cdot s}{m^3}$. This deviation is due to the technical limitations of the preexisting mass flow controller configuration in the pilot plant. Further, significant temperature distribution along the reactor can be seen. Such a deviation is the result of the enlarged catalyst bed volume. This influences the resulting performance parameters. However, the adjusted reaction conditions were validated in advance on a laboratory scale, as well.

In a comparison of the laboratory to the pilot plant, a decrease in activity, here illustrated by conversion is observed in Figure A.17a. In contrast to the laboratory, where an initial activation appears, the catalyst starts to deactivate directly. Here, conversion of the ethene feed drops from 22 to 5 % or has only 6 % conversion at the beginning due to a not optimal regeneration and loses the activity completely. The measurements in the laboratory show an initial increase in conversion and drop after 2 h to about 10 % conversion.

The selectivity remains unaffected by the selected conditions. Thus, all measurements in the laboratory and pilot plant are well reproducible and in the same range in terms of selectivity. Throughout the experimental period the values are kept constant, for the three main products 1-butene (Figure A.17b), 2-butene (Figure A.17c) and propene (Figure A.17d) are in the same range. In the case of 1-butene selectivity, the value in the laboratory is higher than the result obtained in the pilot plant. Nevertheless, the difference is only about 2 %. A similar deviation, if not less, can also be observed for the other products 2-butene and propene. The difference in these cases is that the pilot plant generates higher selectivity with 61 % for 2-butene and 18 % for propene to 58 and 17 % for the laboratory reactor.

One reason for the differences could be the possible heterogeneity of the catalyst bed. Due to the self-synthesized catalyst, it cannot be guaranteed that all components of the powder have the same particle size. This synthesis pathway can lead to larger particles, which influence the result of the setup. Besides, concentration gradients and in particular, temperature fluctuations in the catalyst bed can occur due to the increased diameter of the reactor and the length of the catalyst bed. A temperature deviation of 20 to 30 K between the center and the ends of the catalyst bed observed along the bed. A radial temperature profile can also be expected due to the heating of the reactor with a heating sleeve on the outer wall. However, this could not be recorded. Thus, the deviation of the experiments on a pilot-scale from the laboratory test can be justified and the results are in good agreement, nevertheless.

A.4.3 Metathesis Catalysts - Literature Survey

The mentioned and further results are summarized in the table below for illustration, Table A.4.

A.4.4 Catalyst Preparation

The preparation methods are specifically explained for a set of chosen catalysts. As for the applied MCM-41 and its aluminized counterparts, the supports were synthesized following the procedure presented in sec. 5.2. The catalysts were prepared in cooperation by Dr. Tanya Wolff at the Max-Planck-Institute in Magdeburg

W/SiO_2

The tungsten is incorporated on a silicon dioxide catalyst using the incipient wet impregnation (IWI) method. 2.4 g silicon dioxide (SiO_2) is added to a weighed porcelain crucible. As a further component 0.2504 g ammonium paratungstate ($(NH_4)_{10}(H_2W_{12}O_{42})\cdot 4\ H_2O$) is added. Then pipette 3 ml of water into the crucible. The result is a viscous, milky colored slurry which is stirred continuously for 15 minutes. The material is then homogenized for 15 minutes by manual stirring and spreading. The crucible is then covered and dried at room temperature for 24 hours without stirring. After resting for 24 hours, the now white solid is calcined in a muffle furnace at 600 °C for 6 hours.

The experimental investigations and catalyst characterizations were carried out following the methodology and equipment presented in sec. 5.1.1.

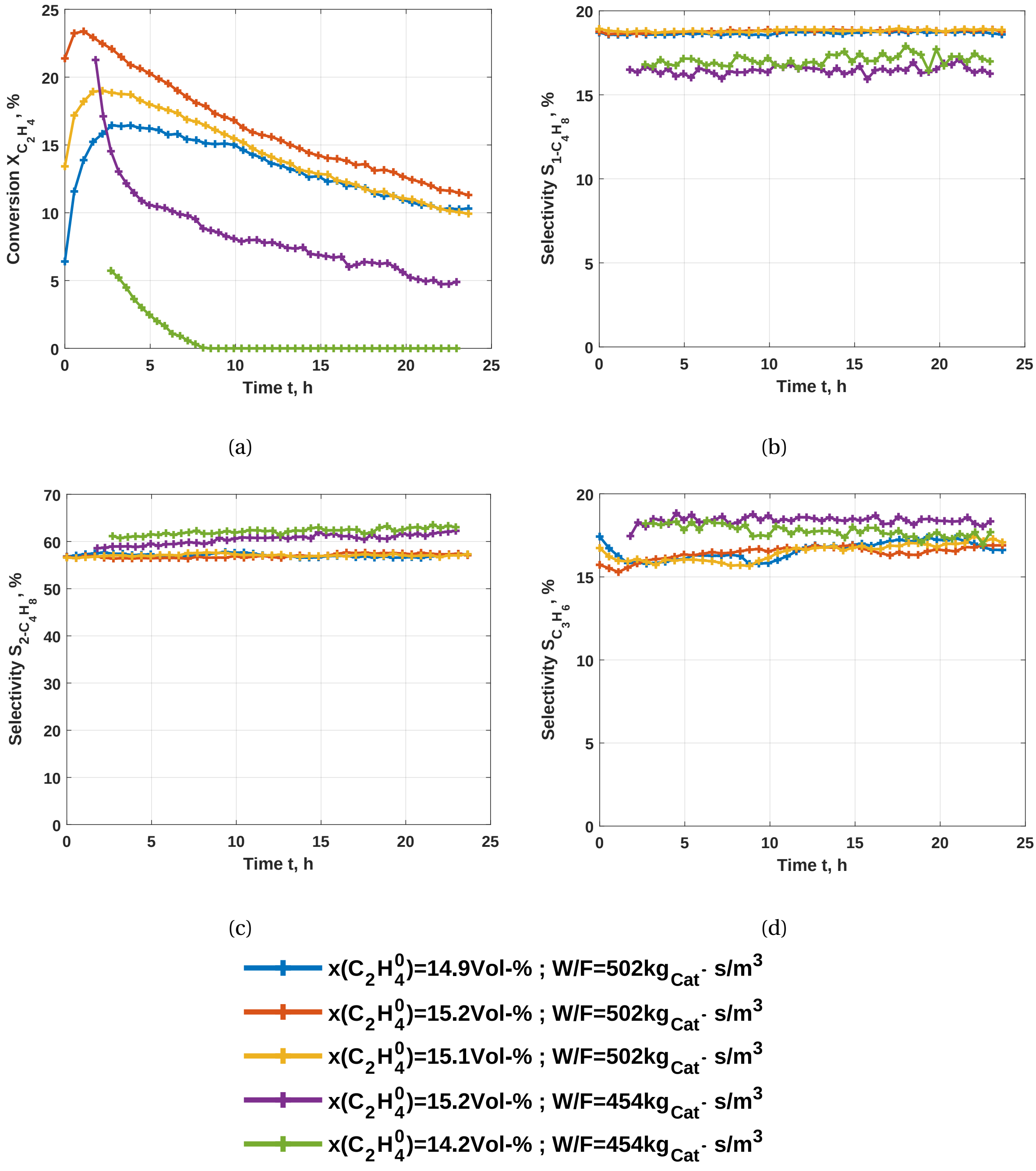

Figure A.17: Comparative evaluation of the Ni/AlMCM-41 catalyst with a Si/Al ratio of 60, incorporated in a lab scale experimental setup (blue, orange and yellow) and in a miniplant setup (purple and green) at 600 °C.

Table A.4: References for the cross-metathesis of ethene and butene to propene, conversion of the reactant butene and the selectivity of propene, reaction conditions and employed catalyst.

Reference	$X_{C_4H_8}$ **%**	$S_{C_3H_6}$ **%**	**Reaction conditions**	**Catalyst**
[Bhuiyan et al., 2013]	82	46	550 °C and GHSV = 900 1/h	$WO_3/SBA-15$
[Bhuiyan et al., 2013]	82	46	550 °C and GHSV = 900 1/h	$WO_3/MCM-41$
[Bouchmella et al., 2013]	60	84	40 °C and 8 ml/min	H-SSZ-13
[Chaemchuen et al., 2012]	83	77	40 °C and calcinated at 550 °C	WO_3/SiO_2
[Debecker et al., 2014]	75	60	250 °C, 10 % Feed and 8 ml/min	$WO_x/SiAl$ aerosol
[Epelde et al., 2014a]	42	52	450 °C and only 1-Butene Feed	K modified HZSM-5
[Hahn et al., 2014]	62	93	150 °C and $C_x : N_2$ 10:1	1.5 $MoO_x/$ $SiO_2 - Al_2O_3$
[Hua et al., 2011]	45	50	342 °C, only butene feed, 0.8 MPa and WHSV = 6.4 1/h	$12\% WO_3/MTS-9$
[Huang et al., 2005]	62.6	88.2	180 °C	$10W/Al_2O_3-70HY$
[Jiang et al., 2016]	88	97	370 °C, WHSV = 4 1/h 2 MPa and $C_2 : C_4 = 2$	WO_3/SiO_2
[Li et al., 2007]	88	64	120 °C, 1 MPa and $C_2 : C_4 = 3$	$4Mo/H\beta-30Al$
[Limsangkass et al., 2013]	85	73	400 °C and WHSV=2.34 1/h	WO_3/SiO_2 with TiO_2
[Lin et al., 2014]	65	85	450 °C, WHSV = 2 1/h and $C_2 : C_4 = 2$	Mo(5.1 %)-SBA-15
[Liu et al., 2010]	86	95	125 °C, WHSV = 1 1/h, 1 MPa and $C_2 : C_4 = 4$	Mo/MCM-22 30Al
[Maksasithorn et al., 2014]	81.2	77.6	400 °C	WO_3/SiO_2 (8W+1NaOH)
[Sang et al., 2012]	56	58	60 °C and only butene feed	$13\% Re_2O_7/MMA$
[Tang et al., 2008]	68.8	70	500 °C, WHSV = 1.96 1/h and only butene feed	SAPO-34
[Zhu et al., 2005a]	69	52	620 °C and WHSV = 3.5 1/h	0.7 % K/ZSM-5

A.4.5 Metathesis Catalyst Evaluation

For the realization of a segregated two-reactor setup, a second catalyst for the metathesis is necessary. A commercially applied tungsten catalyst on SiO_2 was selected and is first validated in more detail.
To evaluate the respective catalytic processes equally, suitable evaluation variables must be selected. Analogous to the previous processes the conversion (eq. (2.12)), the selectivity (eq. (2.13)) and the yield (eq. (2.14)) are chosen. In the case of metathesis, the definition of selectivity remains the same; conversion must be specified for each of the two components used (ethene and trans-butene). Regarding the yield, the equations are adapted to replace the stoichiometric factors. The reason lies in the complexity of the reaction network. As mentioned above, metathesis is a reversible reaction and all alkenes contained in the reaction can, therefore, be used as product and reactant. Since individual reactions cannot be decoupled, in the case of metathesis, the yield of a product is related to the two carbon sources used. Correspondingly, as in eq. (A.1), the total substance quantity of the reactants is used, and stoichiometry is replaced by the carbon numbers of the product and the total reactants.

$$Y_k = \frac{\dot{n}_k^{exp}}{\sum_{i=1}^{2} \dot{n}_i^0} \cdot \frac{\#C_{trans-C_4H_8} + \#C_{C_2H_4}}{\#C_k} \qquad \text{i} = C_2H_4 \ \& \ trans-C_4H_8 \tag{A.1}$$

$$\text{k} = C_2H_6,\ C_3H_6,\ iso-C_4H_8,\ 1-C_4H_8,\ cis-C_4H_8,\ C_5H_{10} \ \& \ C_6H_{12}$$

Although the increase of the reaction temperature is not a desired task, interesting results for W/SiO_2 could be found (Figure A.18) at 600 °C. The commercial SiO_2 carrier was heated to 600 °C and managed to achieve a propene selectivity of 46 %. Besides, there is a significant conversion of ethene with about 20 % and 67.4 % for trans-butene. At temperatures below 350 °C, no conversion of both reactants was analyzed. Merely isomerization was observed. Above 400 °C the metathesis is activated, which linearly increasing propene values.
Tungsten is known to be more robust to reaction conditions and possible impurities than rhenium and molybdenum. Therefore, an increase in temperature does not seem to be negative, especially given the absence of the by-product spectrum. Only minimal amounts of pentene are formed, which is shown in (Figure A.18). The observations indicate that the desired reaction for the formation of propene from ethene and trans-butene takes place preferentially.

Retro-Metathesis

For the experimental implementation of a segregated reactor setup, a suitable metathesis catalyst was selected for the second reactor with W/SiO_2. This catalyst was characterized by its high stability, good regenerability and interesting selectivity to the desired reaction product propene.
To validate the mechanism taking place, it was investigated whether the introduction of the desired product propene as the feed results in the previous reactants with ethene and trans-butene. For this purpose, 5 % propene was set as the input concentration and a temperature profile in the range of 50 to 600 °C was realized. The results of this experiment are shown in Figure A.19.

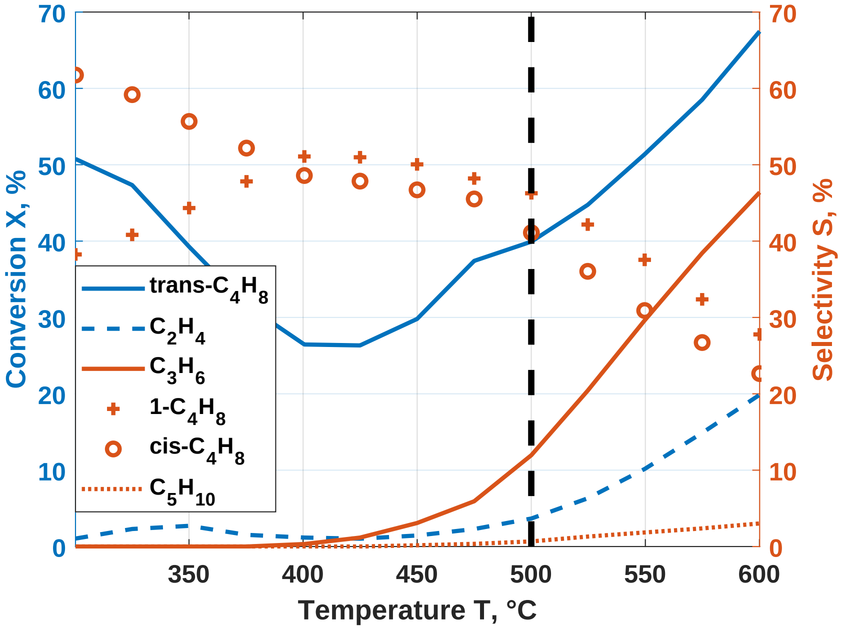

Figure A.18: Temperature dependent conversion via cross-metathesis of ethene and trans-butene (orange) using W/SiO_2 as the catalyst and the corresponding selectivity of the analyzed products (blue).

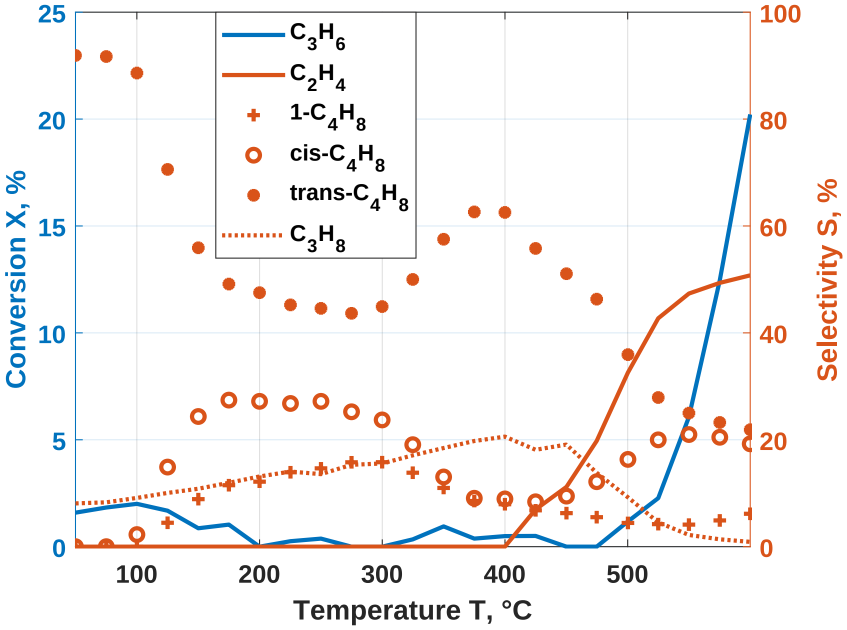

Figure A.19: Resulting conversion (red) and product selectivity (blue) for the retro-metathesis applying W/SiO_2 with 5 % propene feed and W/F = 500 $\frac{kg_{Cat} \cdot s}{m^3}$.

It can be seen that here, too, the catalyst is only actively converting the feed at temperatures above 400 °C. At 500 °C, the conversion increases significantly and reaches 20 % at 600 °C. In this range, the selectivity of ethene increases significantly, while the total amount of butene decreases. Under the optimal conditions at 600 °C, an approximately equimolar composition of C_2 and C_4 olefin is present. Correspondingly, the function of the catalyst as active for the metathesis can be confirmed.

Stability Analysis

Before application in a segregated two-stage setup the stability and regenerability are investigated for the W/SiO_2 catalyst (Figures A.14 and A.15). First, the conversion of the two reactants used is evaluated over the length of three measurement cycles with a respective regeneration. The resulting product spectrum is then analyzed.

Regarding the conversion of trans-butene, shown in Figure A.20, this value undergoes only marginal changes with time-on-stream and the regeneration has no detrimental influence on its value. In contrast, the conversion of ethene initiates at 10 % and increases to 17 % during the first measurement. The regeneration does not deteriorate the activity of the catalyst with 20 % of oxygen at 500 °C. In the second experiment, the catalyst again shows an increasing conversion profile over time. The value rises to 20 %, which remains constant after the second regeneration. During the third experiment, an initially slight decrease in the first 3 h is compensated over the course of the experiment, leasing to the previous 20 %. This value is kept constant until the end of the test.

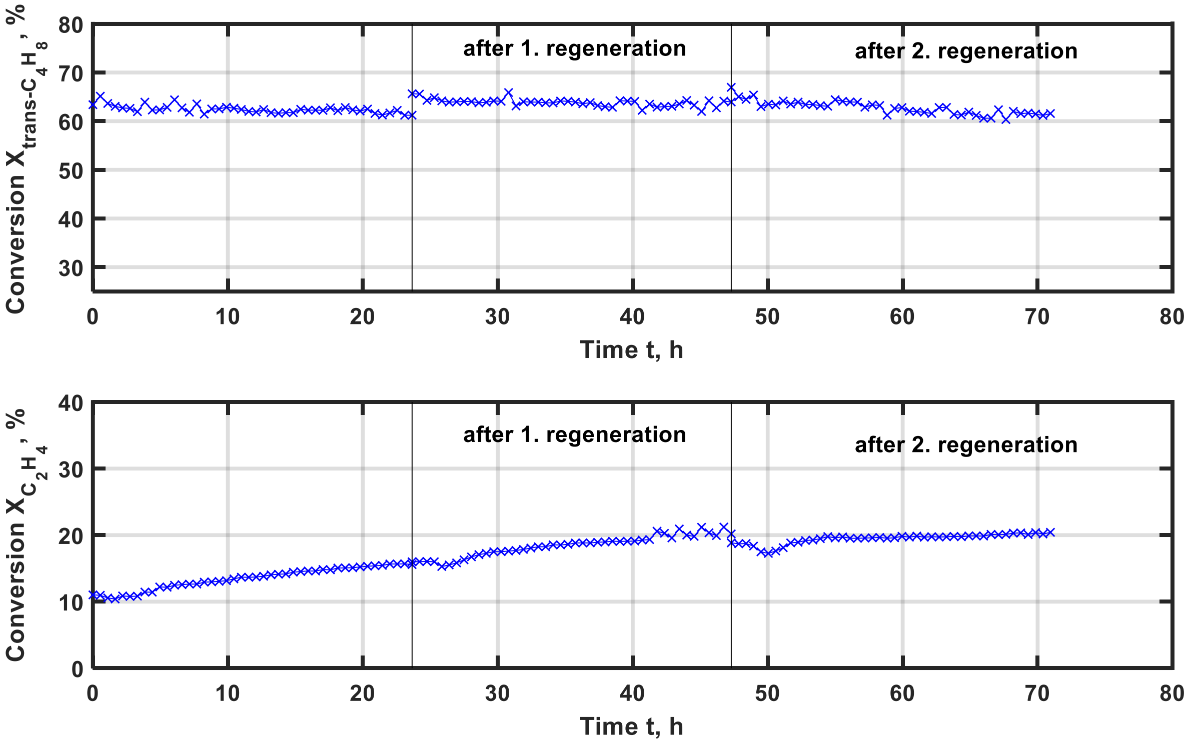

Figure A.20: Conversion of trans-butene (top) and ethene (bottom) as a function of time for W/SiO_2 at T = 600 °C, W/F = 500 $\frac{kg_{Cat}\cdot s}{m^3}$, $c_{C_2H_4}$ = 2.5 % and $c_{trans-C_4H_8}$ = 2.5 %.

With this information, the selectivity of the catalysts throughout the three experiments can now be examined under constant reaction conditions and with respective regeneration. The W/SiO_2 system is analyzed analogously (Figure A.21). The catalyst initially forms 1-butene as the main product, followed by propene, cis-butene and traces of pentene. Following an initial decrease of ethene, the selectivity of propene drops from 32 % to 28 %, with 2-butene isomers increasing concurrent from

37 % and 40 %. After this decreasing phase for ethene, the selectivity of the isomers then drops to 30 % for 1-butene and 23 % for cis-butene. In parallel, the selectivity for pentene remains constant at about 3 % and for propene, this value increases to about 44 %. Propene selectivity is 40 %, after the subsequent regeneration. It then tends to a local minimum of 38 % and afterward increases up to 50 %. The enhanced conversion of ethene is beneficial for the generation of propene, while less butene is obtained. It appears that the metathesis of ethene and 2-butene is enhanced, limiting isomerization and self-metathesis.

In contrast, pentene selectivity is constant for all experimental runs. The butene isomers run parallel to each other, with 1-butene above. The selectivity for 1-butene drop from 30 %, corresponding to maximum ethene conversion, to 27 %. For cis-butene, as mentioned above, the same progression can be seen from 26 % to about 22 %. After the second regeneration, all the selectivity values start at the previous values and follows the same course from the previous experiment. Thus, the butene selectivity drop to 25 % for 1-butene and 21 % for cis-butene. With increases in the ethene conversion the reaction rate generating propene must be enhanced, to explain the observed phenomena.

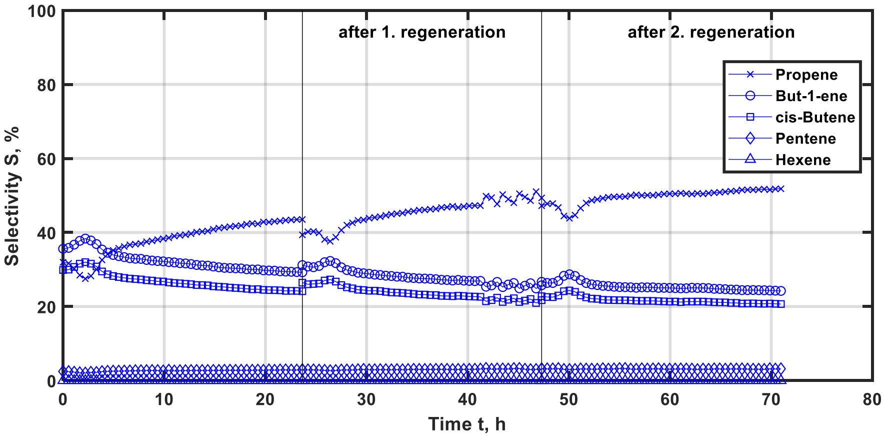

Figure A.21: Product selectivity as a function of time for W/SiO_2 at T = 600 °C, W/F = 500 $\frac{kg_{Cat} \cdot s}{m^3}$, $c_{C_2H_4}$ = 2.5 % and $c_{trans-C_4H_8}$ = 2.5 %.

Analysis of Feed Variation

To implement the catalyst in the overall structure of the reactor setup, a detailed reaction engineering investigation must be carried out. For this purpose, the conversions of ethene and trans-butene, as well as the selectivity of the desired product propene, are evaluated as functions of residence time (Figure A.22) and ethene-to-trans-butene ratio (Figure A.23). By selecting suitable reaction conditions, based on the knowledge gained, the propene formation rate can be controlled and the upstream reactor can be adjusted advantageously.

The first aspect considered is dependence on the ratio of catalyst mass to volume flow (W/F), corresponding to the residence time of the reactants on the catalyst, see Figure A.22. Following the previous stability tests, the conversion (Figure A.22a) of trans-butene remains constant over the entire measurement period. Furthermore, this value is increasing from 55 % for W/F ratio of 330 $\frac{kg_{Cat} \cdot s}{m^3}$ to 72 % for the highest value of 1000 $\frac{kg_{Cat} \cdot s}{m^3}$.

In comparison, the ethene conversion presents a different behavior. The residence times corresponding to 330 and 500 $\frac{kg_{Cat}\cdot s}{m^3}$ are in a range of 11 to 15 % initial conversion and approach a level of 23 % with increasing time on stream. This observation indicates that the catalyst first forms an active catalyst species, the methyl metal compound mentioned above. Less residence time results in an inhibition phase. A different result is seen for the higher W/F ratios, with 750 and 1000 $\frac{kg_{Cat}\cdot s}{m^3}$. These start almost identically and have over the entire time frame a constant value of 23 %. For these cases, the system has enough time to form the active catalyst component and this does not take place with the time-on-stream. Nevertheless, all W/F ratios obtain an approximately equal value.

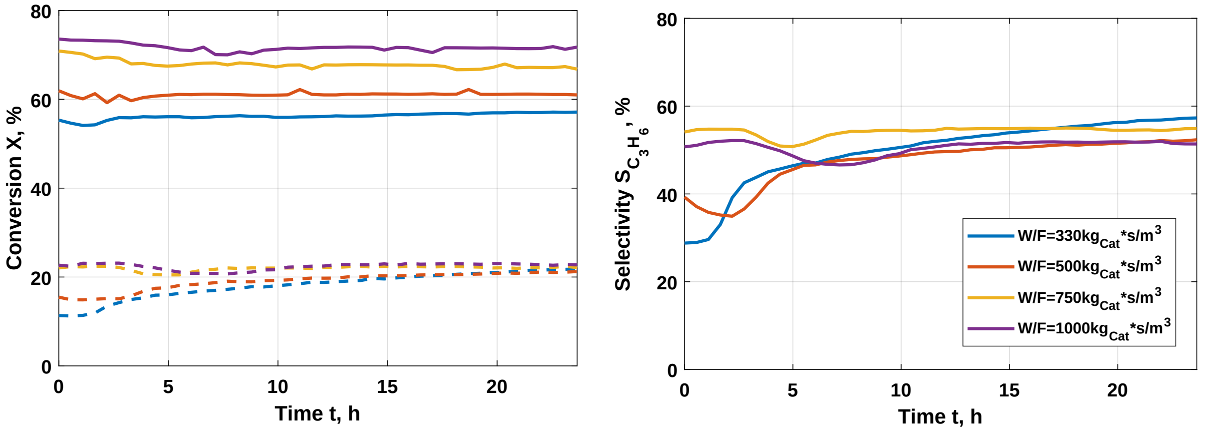

(a)

(b)

Figure A.22: Influence of the weight to flow ratio for an ethene to trans-butene ratio of 1:1 at 600 °C on (a) conversion of trans-butene (solid line) and ethene (dashed line) and (b) selectivity of propene.

The product selectivity achieved from the converted reactants can now be analyzed for the desired target component propene (Figure A.22b). In the first 2 h of the reaction, the order of selectivity is ascending as follows:

$$330\ \frac{kg_{Cat}\cdot s}{m^3} < 500\ \frac{kg_{Cat}\cdot s}{m^3} < 1000\ \frac{kg_{Cat}\cdot s}{m^3} < 750\ \frac{kg_{Cat}\cdot s}{m^3}$$

The results show that shorter contact time, corresponding to a lower W/F ratio initially leads to lower selectivity of 30 and 40 %. Thus, a reversal was observed for 750 and 1000 $\frac{kg_{Cat}\cdot s}{m^3}$, but both are at a value of 50 %. An interesting effect is a temporal minimum of selectivity, which seems to correspond to a drop in ethene conversion. This drop occurs later with increasing W/F ratio. Accordingly, for 330 $\frac{kg_{Cat}\cdot s}{m^3}$ this is already within the first hour, for 550 $\frac{kg_{Cat}\cdot s}{m^3}$ at 2 - 3 h, for 750 $\frac{kg_{Cat}\cdot s}{m^3}$ at 4 - 5 h and for 1000 $\frac{kg_{Cat}\cdot s}{m^3}$ in the range of 7.5 h. For this, an in-operando analysis of the catalyst would be necessary and conceivable, which validates the change of the catalyst material under reaction conditions.

After the mentioned minimum for the respective contact times of the reaction medium on the catalyst the selectivity approaches a value in the range of 52 to 55 %. Only the lowest ratio does not seem to have reached its maximum after 24 h and finally lies with 57 % above the other experimental runs. One assumption for this effect is the fastest supply of new reactive material to the reaction zone. According to this, the trans-butene has not enough time to be isomerized, since new ethene is always available. This would suppress the undesired side reaction to the butene isomers and favor the targeted metathesis to propene.

Concluding the findings for the W/F ratio, initially, the active catalyst species is formed at different rates, depending on the flow rate. After 7 h the catalyst is fully activated and no significant distinction between the different W/F ratios is observable. Further, the ethene conversion and the selectivity of propene follow similar trends.

Next, the influence of the ethene to trans-butene ratio at a constant W/F ratio of 500 $\frac{kg_{Cat}\cdot s}{m^3}$ on the conversion of the reactants (Figure A.23a) and the selectivity to propene (Figure A.23b) is evaluated. In terms of conversion, it increases, for decreasing ethene to the trans-butene ratio. This effect is due to the reduced amount of ethene, which is increasingly converted with trans-butene. The conversion increases from 4 %, for a ratio of 10, to 40 - 43 %, for a reactant feed with a value of 0.25 observed.

In comparison, the conversion of trans-butene is at a higher level and in a narrower window of 59 - 67 % conversion at the beginning of the experiment. The used ratios of ethene to trans-butene occur in pairs. The measurements for the values of one and two (medium), four and ten (high), as well as 0.25 and 0.5 (low), are only marginally different. These pairs are in ascending order for the trans-butene conversion in the following order: low > medium > high. This order corresponds to decreasing trans-butene amounts. The conversion for the middle and high conversions is thereby with temporal progress in each case, increasing by 2 - 3 %. For the low ratios, a reverse effect can be identified in which the system loses 2 - 3 % of conversion. Thus, the differences slightly increase in the range of 54 to 69 %.

Interestingly, the maximum conversion of trans-butene is at an input ratio of 4 and the minimum for the case of 0.5. It can be concluded that the processes on the catalyst surface cannot be assumed profanely as generalized. Thus the adsorption behavior can be influenced by specific relationships with each other.

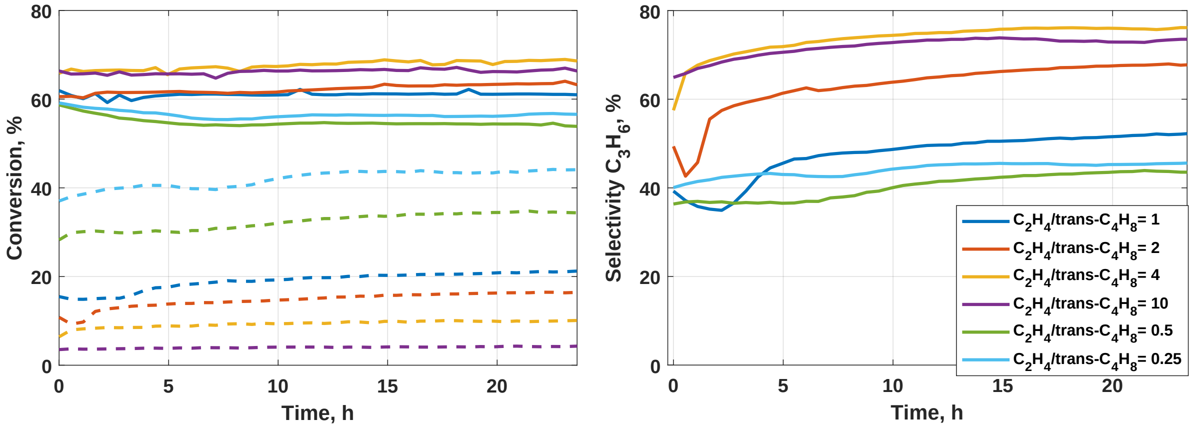

(a)

(b)

Figure A.23: Influence of the Feed ratio of ethene to trans-butene for a W/F of 500 $\frac{kg_{Cat}\cdot s}{m^3}$ and 600 °C on (a) conversion of trans-butene (solid line) and ethene (dashed line) and (b) selectivity of propene.

Similar behavior can be observed for the selectivity of propene. At first, it can be stated that all experiments show an increasing profile over time, but this increase is dismal for the low feed ratios. The high feed ratios obtain values of 57.5 and 65% of propene selectivity for four and ten, initially. Towards the end of the experiment, 76 or 73.5 % for four or ten as the ratio of ethene to trans butene are measured. In the case of the low ratios, the selectivity for the case 0.25 is analogously above 0.5 over the entire time range, at 40 % selectivity, which is approached with experimental time.

The middle ratios of 1 and 2 for the reactants show strikingly different behavior. Thus, within the first five hours of the experiment, they exhibit a decreasing selectivity profile, with a minimum. Afterward, the graph increases again. The experiment with ethene to trans-butene ratio of one initially has a selectivity of 39 %, which is lower than the feed ratio of 0.25. In the first section, the experiment with a ratio of 1 falls below the experiment with 0.5. Up to the mark of 5 h, however, the experiment with an equimolar feed is again above the low ratios. It then goes up to 52 % with an approximately equal increase as the feed ratio of 2. The experiment with two times more ethene than trans-butene has 49 % at the beginning and increases to 68 % selectivity of the desired product.
With the help of the performed reaction analysis, an increased ratio of ethene to trans-butene seems to be advantageous for the W/SiO_2 catalyst with a low W/F ratio to selectively form propene.

A.4.6 Two-Stage Setup

In the following, instructive experiments are compared with the implemented segregated reactor concept, one for a laboratory experiment and the other for a pilot plant experiment for the integrated concept.
The segregated design shows that after the first reactor, comparable conversions are achieved as with the integrated design for the pilot plant, see Figure A.24a. The conclusion could be drawn from the laboratory-scale preliminary tests that the reactor temperature would have to be lowered to not form propene from the nickel-impregnated and aluminized MCM-41. Instead, the main goal was to obtain suitable amounts of 2-butene to allow metathesis to proceed in a targeted manner. The activity corresponding to conversion was too low within the pilot plant to obtain valid results at below 300 °C. Therefore, a temperature of 350 °C had to be used, which resulted in conversions of up to 15 % ethene. However, it was lower than the 20 % achieved in the laboratory. Though, over 80 % total selectivity of butene could be achieved, see Figure A.24b and Figure A.24c. For 1-butene, these results were in the range of the values for the laboratory and in the case of 2-butene, the observations of the smaller scale were even exceeded.
In contrast, propene with 10 - 13 % selectivity is formed significantly less (Figure A.24d). Due to the lower conversion, ethene is present in significant amounts at the outlet of the first reactor and is transferred to the second reactor with the resultant products. The second reactor is filled with the previously described metathesis catalyst W/SiO_2. Based on the obtained outlet spectra values, the ratio of ethene to 2-butene as the inlet of the second reactor is ***5.88***. This value is close to the optimum ratio for W/SiO_2. Thus, sufficient material flow is supplied to the reactor. In the course of the reaction, the first reactor deactivates so that the conversion decreases further and the ratio of trans-butene to ethene increases over time. As shown in the previous chapter, the tungsten catalyst does not tend to lose activity. Also, a ratio significantly greater than one is advantageous for the formation of propene.
Interpretation of the outlet composition of the second reactor (yellow curve after the steep course with higher conversion and spontaneously varying selectivity), the results between integrated and segregated systems differ significantly. First, the conversion of ethene could be increased to 30 - 40 % compared to the first reactor. One possible reason for this result is the preference for metathesis steps in which ethene is used as a reaction partner. These reactions are accelerated by the high "residual concentrations" of ethene. Because the first reactor is continuously deactivating, less conversion is

achieved with time-on-stream (TOS). In the following the ethene concentration at the outlet of the first reactor increases. Besides, reactions with ethene as a product are inhibited according to the principle Le'Chatelier. Metathesis is a reaction limited by equilibrium. Therefore the supply of products causes a shift of the equilibrium to the reactant side. Accordingly, the reactions in which ethene would occur as a product do not take place, or only to a limited extent. As a result, ethene is hardly formed but mainly consumed.

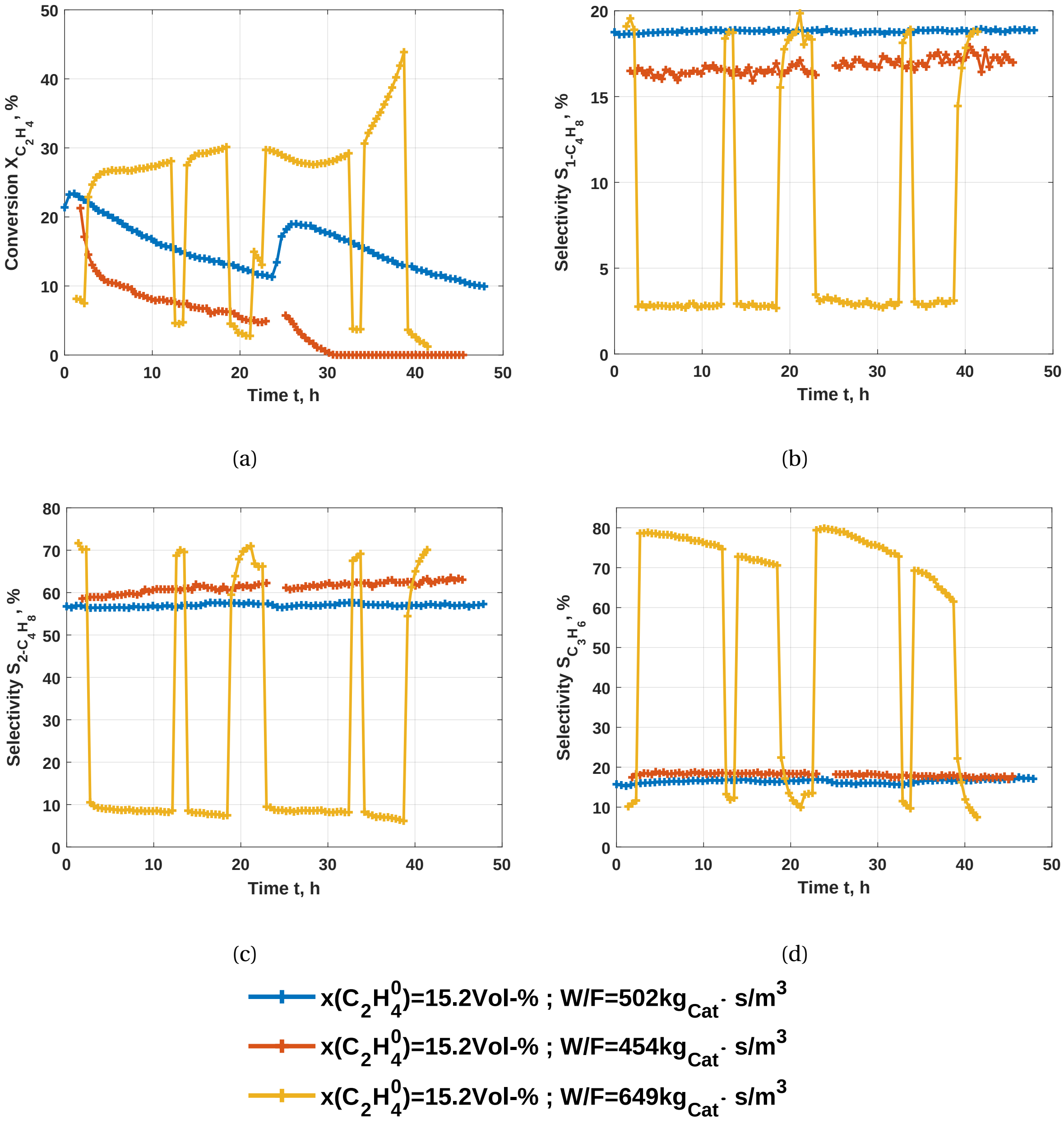

(a)

(b)

(c)

(d)

Figure A.24: Comparative evaluation of the integrated setup incorporating Ni/AlMCM-41 catalyst with a Si/Al ratio of 60, for a lab scale (blue) and miniplant experimental setup (orange), with a segregated setup (yellow), incorporating Ni/AlMCM-41 in the first and W/SiO_2 in the second reactor at 600 °C.

The second essential component in the second reactor is butene, which is the main product of the first reactor. This fact allows the above-described reaction of 2-butene with ethene to propene. In the case of the butenes, the trans modification is the thermodynamically preferential form. Thus, its generation via isomerization is enhanced when the thermodynamic equilibrium is shifted with its use as a reactant for the metathesis towards propene. Besides, the cross and self-metathesis of the butenes are promoted, where propene occurs as a product as well. The selectivity of 1- (Figure A.24b) and 2-butene (Figure A.24c) is reduced below 5 and 10 %, respectively, indicating an significant switch and consequently, an enhancement of the desired reaction.

The conversion of ethene increases over time as more ethene is available for the reaction in the second reactor. In contrast to butenes, the selectivity of the desired product propene increases to 80 % (Figure A.24d). This value decreases over time to a minimum of approximately 77 %. One reason for this seems to be the increased conversion and thus, more byproducts are formed. However, it must be mentioned that this happens to a small extent.

It can be concluded that a process intensification takes place. The decoupling of the reaction network postulated by Iwamoto had the desired effect of increasing the selectivity of the target product propene. The integration of a second, specialized metathesis catalyst and the specific adjustment of the reaction conditions for the respective system increased the conversion of ethene and at the same time, led to a significant increase in selectivity to the target product propene. Accordingly, the process can be operated according to the given requirements. If it is necessary to produce more butenes, the first reactor is operated separately. If the demand for propene increases, the second reactor can be included accordingly.

Besides, the segregated reactors can be used to give the overall system even more degrees of freedom. For example, the feed ratio and volume flow can be adjusted between the reactors via intermediate dosing to further intensify the reaction. It is possible at this point to implement recycling or to provide for a separation of the first product flow, whereby the inlets of the respective reactors experience a further significant increase in productivity. These further approaches increase economic efficiency further.

B Forced Dynamic Operation

In the main part of the thesis, Part III, the potential of the forced dynamic operation was illustrated for the hydrolysis of acetic anhydride to acetic acid as a case study. In the following, first, the potential of other input parameter modulations is shown, then the calculation of stability and optimization parameters is explained and finally, a new function for periodic modulation of the process is discussed.

B.1 Theoretical Evaluation

Analogous to the theoretical considerations of the NFR method for an assumed system parameter set (Table 8.1) and a kinetic model with corresponding parameters (Table 7.3) for the simultaneous modulation of the input concentration and the total flow (Figure 8.4), is shown in Figure B.1 for the simultaneous periodic variation of the input concentration and the input temperature.

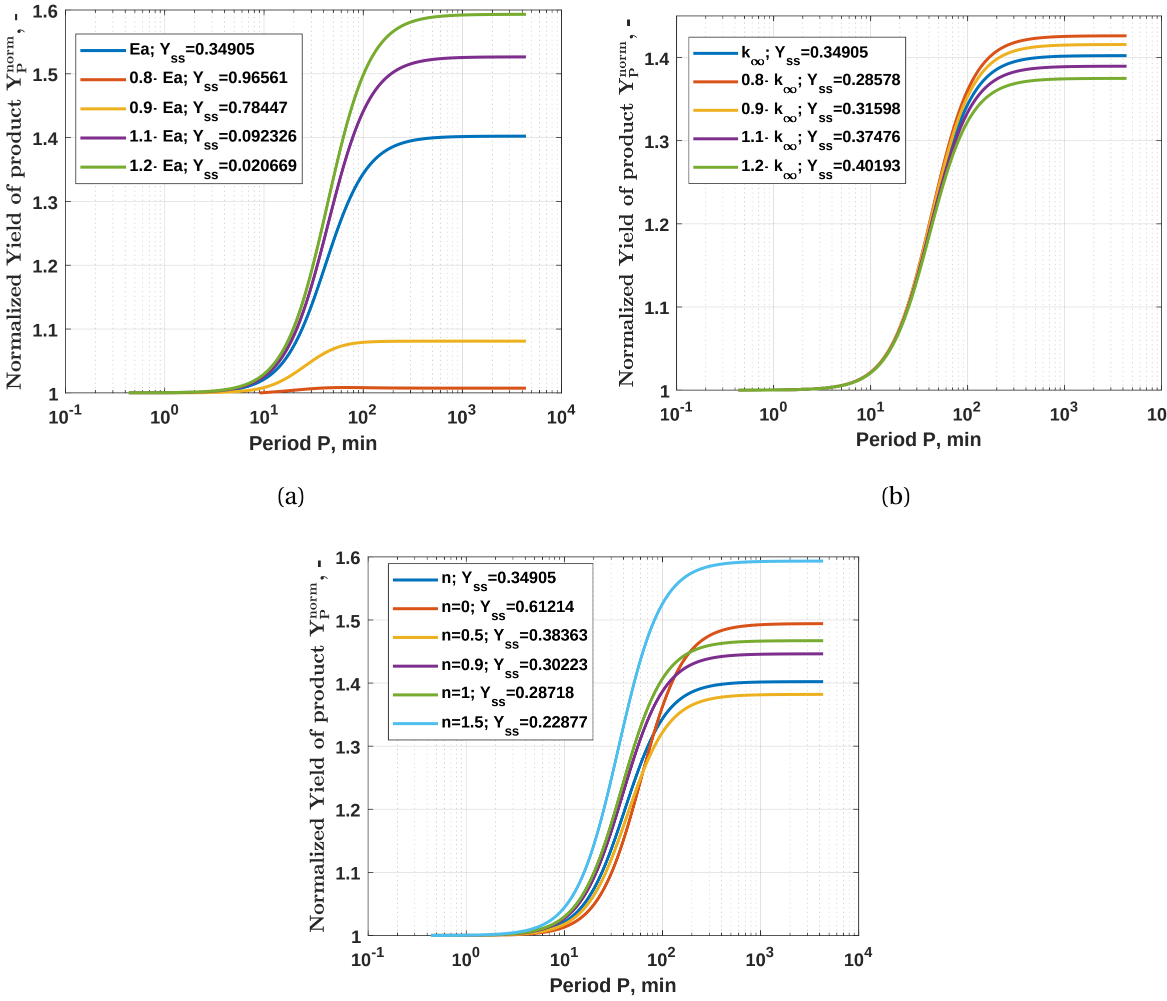

(a)

(b)

(c)

Figure B.1: Influence of the (a) activation energy E_A, (b) the collision factor k_∞ and (c) the reaction order n on the normalized product yield for the simultaneous modulation of inlet concentration and inlet temperature with amplitudes of $A_C = 85$ % and $A_T = 7$ % with individual optimal phase differences.

Here the sensitivity of the change by dynamic operation to the individual kinetic parameters is displayed. Thus the influence of the activation energy E_A (Figure B.1a), the impact factor k_∞ (Figure B.1b) and the reaction order n (Figure B.1c) are plotted.

B.2 Sinusoidal Wave

The introduced three asymmetrical second order FRF are needed to determine with eq. (8.13) the DC component of the molar outlet flow of the product P, $N_{P,DC} = \overline{\dot{N}_P(t)}$, which is then required to quantify the performance of forced periodic operation using for example eq. (8.29).
Since it is efficient to derive the FRF based on non-dimensional balance equation [Nikolić et al., 2016a; Nikolić et al., 2016b], it is convenient to use instead of the frequency f a dimensionless frequency ω defined as:

$$\omega = f \cdot \frac{V_R}{F_{tot}} \tag{B.1}$$

The following three functions are valid for the type of modulation investigated in the conjunction with the process goal specified ([Nikolic Paunic, 2016] with U = 0):

(a) The asymmetrical second order FRF for modulation of the inlet reactant concentration, $c_R^{in}(t)$:
$H_{P,2,CC}(\omega,-\omega) = \frac{(1+\alpha^*)^2}{B_{P,S}} \cdot \frac{\left((n(n-1)\omega^2+n^2(1-2\beta^{*2}\gamma^*)-n(1+\beta^*\gamma^*)^2)\right)}{(\omega^2+1)(\omega^2+B_{P,s}^2)}$

(b) The asymmetrical second order FRF for modulation of the total inlet flow rate, $F_{tot}(t)$:
$H_{P,2,FF}(\omega,-\omega) = \frac{1}{2B_{P,S}} \cdot \frac{((-n^2\alpha^{*2}-n\alpha^*(\alpha^*+2(1+\beta^*\gamma^*))-2\beta^*\gamma^*(1+\beta^*\gamma^*)-2\beta^{*2}\gamma^*))}{(\omega^2+B_{P,s}^2)}$

(c) The asymmetrical second order FRF defining the cross-effect for simultaneous modulation of inlet reactant concentration and total flow rate:
$H_{P,2,CF}(\omega,-\omega) = Re(H_{P,2,CF}(\omega,-\omega)) + j \cdot Im(H_{P,2,CF}(\omega,-\omega))$
with
$Re\big(H_{P,2,CF}(\omega,-\omega)\big) = \frac{(1+\alpha^*)^2}{B_{P,S}} \cdot \frac{\left(n\left((\omega^2+1)(\omega^2+B_{P,s}^2-(\alpha^*+1))-\beta^*\gamma^*(\alpha^*-2\beta^*)\right)\right)}{(\omega^2+1)(\omega^2+B_{P,s}^2)}$
$Re\big(H_{P,2,CF}(\omega,-\omega)\big) = \frac{(1+\alpha^*)^2}{B_{P,S}} \cdot \frac{j\omega n\left(\omega^2+1+\beta^*\gamma^*(\alpha^*-2\beta^*)\right)}{(\omega^2+1)(\omega^2+B_{P,s}^2)}$

The above applied new four dimensionless parameters α^*, β^*, γ^* and $B_{P,s}$ are defined based on the steady-state values of the reactant concentration, $c_{R,SS}$, and the temperature, T_{SS}, as follows:

$$\alpha^* = k_\infty \cdot exp\left(-\frac{E_A}{R \cdot T_{SS}}\right) c_{R,SS}^{n-1} \cdot \frac{V_R}{F_{tot}} \tag{B.2}$$

$$\beta^* = \frac{\Delta_R H \cdot k_\infty \cdot exp\left(-\frac{E_A}{R \cdot T_{SS}}\right) \cdot c_{R,SS}^{n}}{\rho \cdot c_P \cdot T_{SS}} \cdot \frac{V_R}{F_{tot}} \tag{B.3}$$

$$\gamma^* = \frac{E_A}{R \cdot T_{SS}} \tag{B.4}$$

$$B_{P,s} = 1 + n\alpha^* + \beta^*\gamma^* \tag{B.5}$$

It should be mentioned, that α^* corresponds to a characteristic Damköhler number and $B_{P,S}$ is a classical stability parameter, which must by positive to assure a stable steady-state, which is a requirement for the application of the NFR method.
From the real and imaginary parts of $H_{P,2,CF}$ two phase shifts corresponding to performance extrema can be calculated using eq. (8.15) [Nikolić et al., 2016a], with the previously defined summarized parameters a, b and c.
The values corresponding to the reference situation using the parameters given in Tables 8.1 and 8.2 are: $c_{R,SS}^{ref}$ = 0.482 mol/L, T_S^{ref} = 27.8 °C (section 8). Using the reference frequency $\omega^{ref} = 4.167 \cdot 10^{-4}$ Hz the following values result: α^{*ref} = 0.5903, β^{*ref} = -0.0125, γ^{*ref}=13.6126 and $B_{P,S}^{ref}$ = 1.2190, ϕ_{max}^{ref} = 157° and ϕ_{min}^{ref} = -36° = 324°.
For the optimal phase shift $\phi_{opt}^{ref} = \phi_{max}^{ref}$ eq. (8.21) leads to

$N_{P,DC}^{max} = \overline{\dot{N}_P(t)} = 0.025$ mol/min.

With the DC component value, the values reported of $\Delta Y_P = 5.9$ % (eq. (8.30)) and $Y_P^{norm} = 1.17$ (eq. (8.31)) are obtained.

Figure B.2 shows a schematic representation of the entire facility as it was used for the experiments and is shown in Figure 7.2. In contrast to Figure 7.1, the thermostats and the valve for switching the temperature regimes are included here.

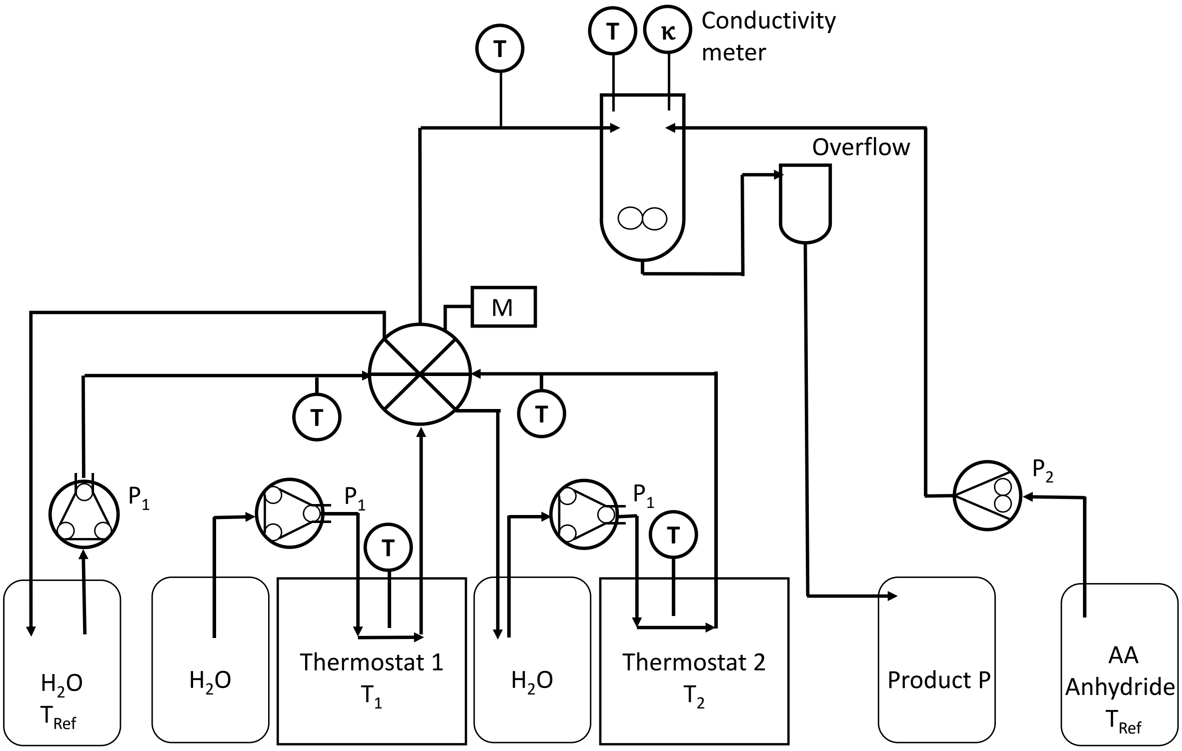
T
T
κ
Conductivity meter
Overflow
M
T
T
P1
P1
T
P1
T
P2
H2O TRef
H2O
Thermostat 1 T1
H2O
Thermostat 2 T2
Product P
AA Anhydride TRef

Figure B.2: Flow sheet of the realized experimental setup for forced dynamic parameter perturbation.

In Figure B.3 the implemented voltages for the separate acetic anhydride and water pumps are shown. These plotted functions confirm the assumption that the input modulations are exactly imposed as coupled harmonic functions for the individual flows.

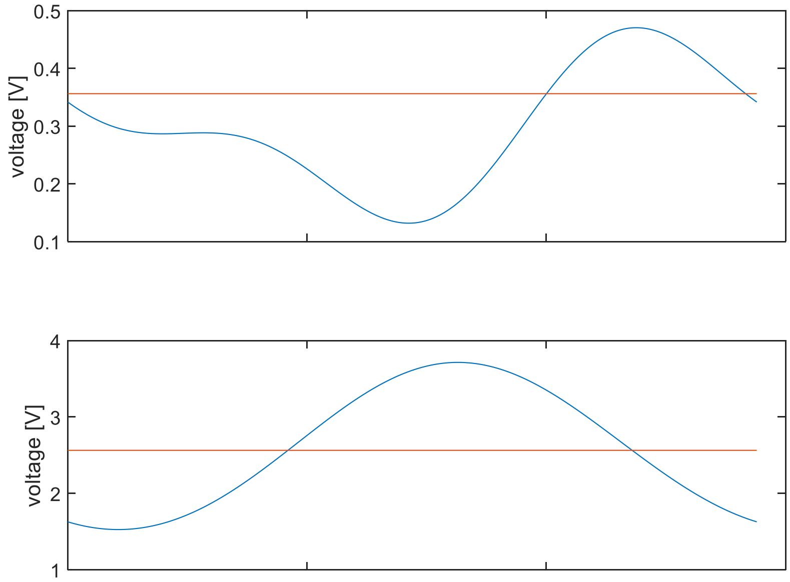

Figure B.3: Implemented voltages for the individual pumps for acetic anhydride (top) and water (bottom) with previously established steady-state (V_R = 298 ml, F_W = 40 ml/min and F_{AA} = 3 ml/min) and subsequent dynamic operation with the following parameter: frequency f = $4.167 \cdot 10^{-4}$ Hz, amplitude of inlet concentration A_C = 85 %, amplitude of total flow A_F = 55 % and phase difference $\phi = 157.33°$).

B.3 Square Wave

In addition to the sinusoidal input modulation, which is intensively displayed in the present thesis, the nonlinear frequency response (NFR) method can validate other functional forms. One extreme is the square-wave function. Here the input signals are switched between on and off in the strongest case.
In the following, first, the derivation of transfer functions for a general input function is shown and afterward, a comparison between sinusoidal and rectangular input functions is explained.

B.3.1 Definition of General Input Function Modulation using NFR

The previously obtained results for the evaluation of nonlinear frequency response analysis of simultaneous modulation of multiple input parameters for sinusoidal input modulation can be extended to a generalized waveform. Therefore, the modulated input is approximated using the Fourier series extension with an infinite number of harmonics [Spiegel, 1974; Petkovska et al., 2018]. When only the first K harmonics are considered, the input modulation can be approximated using the expressions for x (eq. (B.6)) and z (eq. (B.7)).

$$x(t) = \sum_{k=-\infty}^{\infty} \frac{A_{x,k}}{2} e^{jk\omega t} \approx \sum_{k=-K}^{K} \frac{A_{x,k}}{2} e^{jk\omega t} \tag{B.6}$$

$$z(t) \approx \sum_{k=-K}^{K} \frac{A_{z,k}}{2} e^{jk(\omega t+\phi)} \tag{B.7}$$

The k-th harmonics is thereby defined by the forcing amplitudes of each input modulation $A_{x,k}$ and

$A_{z,k}$, the phase shift ϕ and the forcing frequency $k\omega$, with the frequency of the basic harmonics ω. The systems output y(t), as shown in Figure 8.2 can be defined as infinite Volterra series. Though, as for the input modulation parameters, it is more practical to apply a finite number of series elements. The general procedure and expression for the output calculation was demonstrated in the previous section and can be found in more detail in [Nikolic Paunic, 2016]. If the second order frequency response function (FRF) of each individual contribution and by the cross term of both inlet parameter modulations is used and further the input is approximated with a finite sum of the first K harmonics, the DC component of the output Y will be given with the following expression eq. (B.8):

$$\begin{aligned} Y_{DC} \approx & \sum_{k_1=-K}^{K} \sum_{k_2=-K}^{K} \frac{A_{x,k_1}}{2} \frac{A_{x,k_2}}{2} G_{2,xx}(k_1\omega, k_2\omega) + \\ & \sum_{k_1=-K}^{K} \sum_{k_2=-K}^{K} \frac{A_{z,k_1}}{2} \frac{A_{z,k_2}}{2} G_{2,zz}(k_1\omega, k_2\omega) + \\ & \sum_{k_1=-K}^{K} \sum_{k_2=-K}^{K} \frac{A_{x,k_1}}{2} \frac{A_{z,k_2}}{2} G_{2,xz}(k_1\omega, k_2\omega) e^{jk_2\phi} \end{aligned} \tag{B.8}$$

where k_1 and k_2 must add up to a value of zero.

When applying this for a square wave function, the equations eqs. (B.9) and (B.10) are obtained. Only odd harmonics are used for the representation of the rectangular function and that the even value functions are considered zero [Nikolić and Petkovska, 2016]. Here, the equation will be given in the complex form.

$$x(t) \approx \frac{4S_x}{\pi} \sum_{k=-K}^{K} \frac{A_{x,k}}{2} e^{jk\omega t} \tag{B.9}$$

$$z(t) \approx \frac{4S_z}{\pi} \sum_{k=-K}^{K} \frac{A_{z,k}}{2} e^{jk(\omega t + \phi)} \tag{B.10}$$

With S_x and S_z being the designated nominal amplitudes. In an equivalent form, the equations can be given in the harmonic form (eqs. (B.11) and (B.12)).

$$x(t) \approx \frac{4S_x}{\pi} \sum_{k=-K}^{K} \frac{1}{k} sin(k\omega t) \tag{B.11}$$

$$z(t) \approx \frac{4S_z}{\pi} \sum_{k=-K}^{K} \frac{1}{k} sin(\omega t + \phi) \tag{B.12}$$

When approximating the square wave function with the first harmonic, the system's output is represented by the second-order asymmetrical function of the DC component (eq. (B.13)).

$$\begin{aligned} Y_{DC} \approx & \sum_{k=1,3,\ldots}^{K} 2\left(\frac{A_{x,k}}{2}\right)^2 G_{2,xx}(k\omega, -k\omega) + \\ & \sum_{k=1,3,\ldots}^{K} 2\left(\frac{A_{z,k}}{2}\right)^2 G_{2,zz}(k\omega, -k\omega) + \\ & \sum_{k=1,3,\ldots}^{K} \frac{A_{x,k}}{2} \frac{A_{z,k}}{2} G_{2,xz}(k\phi, k\omega) \ . \end{aligned} \tag{B.13}$$

For the case of square wave modulation, the main contributor to the outcome of the system is the cross term of the G_2 functions. Its influence is dependent on the k-th harmonic of the frequency ω and the phase difference ϕ. A mathematical expression is the following:

$$G_{2,xz}(k\phi, k\omega) = cos(k\phi)Re(G_{2,xz}(k\omega, -k\omega)) + sin(k\phi)Im(G_{2,xz}(k\omega, -k\omega)) \; . \tag{B.14}$$

As it was mentioned before and shown later in the present work (section 8.4.3), the optimal phase difference is the essential value, determining if a periodic operation is beneficial or detrimental. In eq. (B.15) the formula is given for the square wave modulation, which is similar to the one for sinusoidal modulation (eq. (8.15)).

$$\phi_{opt,x} = arctan\left(\frac{\sum\limits_{k=1,3,...}^{K} Im(G_{2,xz}(k\omega, -k\omega))}{\sum\limits_{k=1,3,...}^{K} Re(G_{2,xz}(k\omega, -k\omega))}\right) \tag{B.15}$$

B.3.2 Experimental Implementation

It was possible to show that multiple input parameters could be varied simultaneously with a harmonic function in a sinusoidal form. For better industrial realization, it is of interest to implement waveforms that are of different shape and maybe even easier to implement. In [Nikolić and Petkovska, 2016] Nikolic presented the derived NFR functions for a general waveform.

From the variety of possible input modulations, the square wave function is an interesting and easy to control possibility. The first numerical simulations indicated that this type of input function is capable of resulting in greater improvements compared to the sinusoidal harmonic. This enhancement is based on the higher nonlinearity of the square wave. It is possible to approximate the square wave with harmonics of n-th order eq. (B.16).

$$x(t) = \frac{4}{\pi} \sum_{k=1}^{\infty} \frac{sin(2\pi(2k-1)ft)}{2k-1} \tag{B.16}$$

The outcome of this *Fourier expansion* is illustrated in Figure B.4. It is apparent that for higher terms of k, the obtained harmonic function is oscillating around the higher and lower level of the square wave function. The difference is further minimized until an almost perfect Dirac-like change is observed.

Such higher nonlinearities are beneficial for the output change, predicted by the method of nonlinear frequency response. Below, the derivation of the function for the square wave modulation will be summarized and afterward, the simultaneous modulation of multiple input parameters will be experimentally validated.

Comparison Sinusoidal and square wave

First, it remains to be assessed to what extent the use of a different input parameter variation has a positive effect on the chemical process. For this purpose, Figure B.5 illustrates the yield of the product obtained by the simultaneous modulation of several input parameters for a sinusoidal and rectangular periodic variation over the period duration. These are evaluated in comparison to stationary operation. The set steady-state operating parameters, as well as the kinetic data, are analogous to the previous calculation and are shown in Table 8.1.

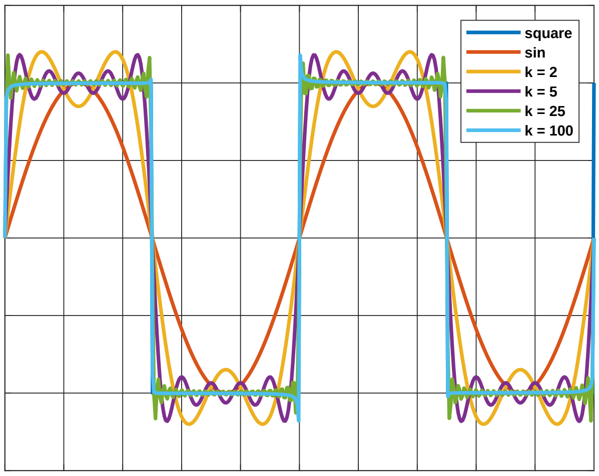

Figure B.4: Graphical display of fourier expansion of different values k.

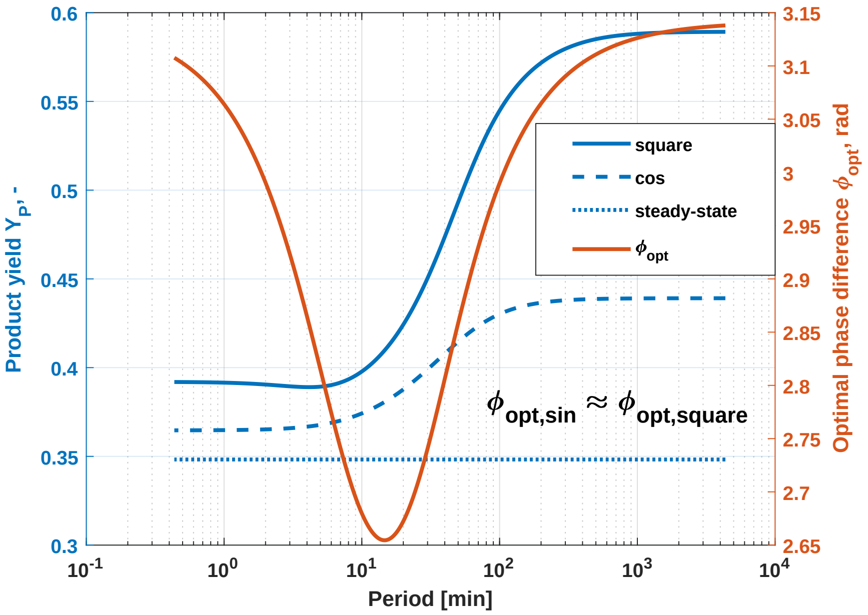

Figure B.5: Predicted yield of product (blue) and optimal phase difference (orange) as function of period, comparing sinusoidal and square wave input modulation for the hydrolysis of acetic anhydride.

The graph (Figure B.5) shows the potential of the rectangular function. The dynamically excited system lies above stationary operation over the entire range of the period duration. The form of the function follows that of the sinusoidal variation. However, the results for the rectangle function over the entire range are above the values of the sinusoidal function. Here it must be mentioned that the calculated average yields are always determined with an optimal phase shift. The value of this phase shift is the same for both input function types.

In the high-frequency range, correspondingly low period durations, 36.5 % yield can theoretically be achieved by sinusoidal forcing functions and 39 % for a rectangle function. By a period duration of 10 min, the curve starts to rise significantly, which extends to the 100-200 min period duration and flattens out or runs against a value.

In contrast to stationary operation with 34.8 %, 43.9 % can be achieved with the sinusoidal function and 58.9 % with the rectangular function. Accordingly, the rectangle function is more promising, especially for very long periods. It must be mentioned that in this case, depending on the residence time in the reactor, different stationary points are set depending on the level of the function.

According to these calculated results, experiments with sinusoidal and rectangular functions were carried out under the same amplitudes of the individual input parameter variations (A_C and A_F), period duration of 40min and phase shift (ϕ_{opt}) between the input parameters.

Compared to the sinusoidal modulations, the measured values of the product do not follow a perfect rectangular function. This mismatch results from the fact that, on the one hand, the individual input flows do not follow ideal functions (see Figure B.6), since only the input parameters have to be rectangular. On the other hand, ideal mixing does not occur within the system and it takes corresponding time to change between the operating states. For a sinusoidal course, the changes are significantly smaller at any time, so that the output flow can also describe a harmonic oscillation.

It becomes apparent (Figure B.7) that for a rectangular function the minimum is lower and the maximum of the molar product stream is significantly higher than in the case of a sinusoidal variation. In the case of an input concentration of 0.74 mol/l, a period of 40 min, an input concentration amplitude A_C of 85 % and a volume flow amplitude A_F of 55 %, and a phase shift of 157.33°, improvements of 5.95 % are predicted for a sine function and 12.47 % for a rectangular function. These values are based on the difference between the time-averaged yield and the steady-state operating point. Experimentally, however, 4.1 % and 11.91 % improvement could be achieved, with predictions of 5.95 and 12.11%. Thus the deviations are around minor and it can be stated that the predictions of the NFR agree well with the experimental results.

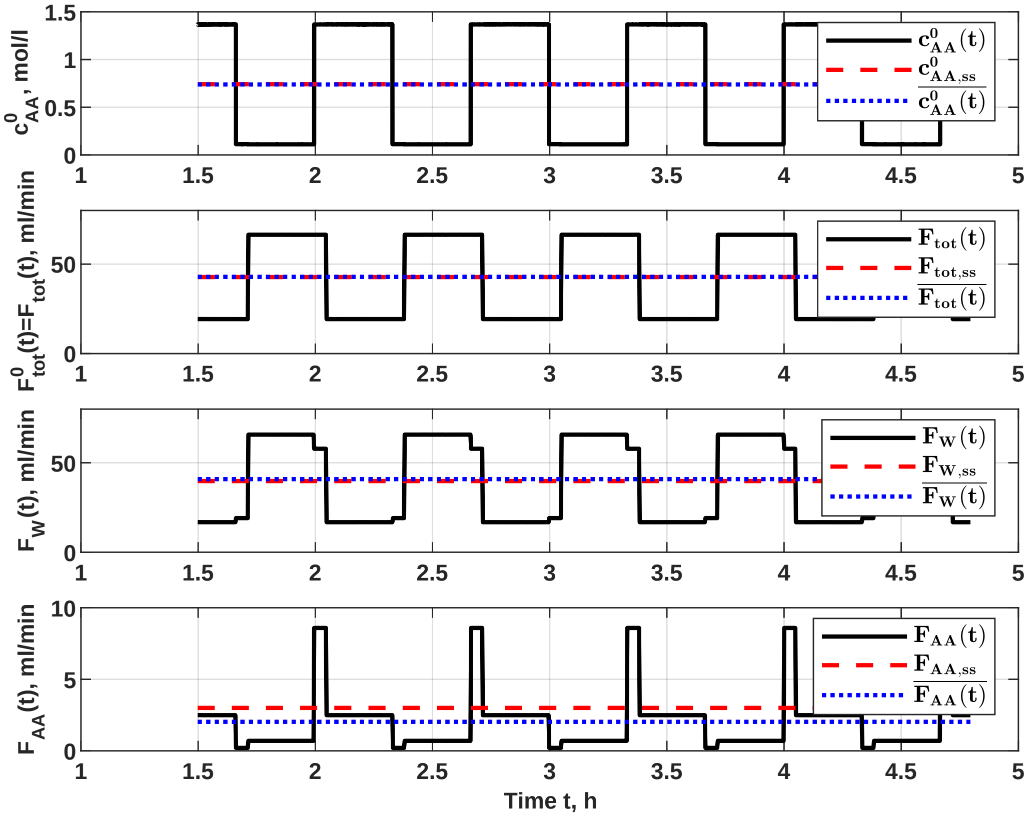

Figure B.6: Input signals for simultaneous modulation of inlet concentration $A_C = 85$ % and total flow rate $A_F = 55$ % for a period of 40 min and with optimal phase difference applied for square wave input function, with inlet concentration of anhydride (top), total volumetric flow rate (second), water flow rate (third) and acetic anhydride flow rate (bottom) with a square wave function.

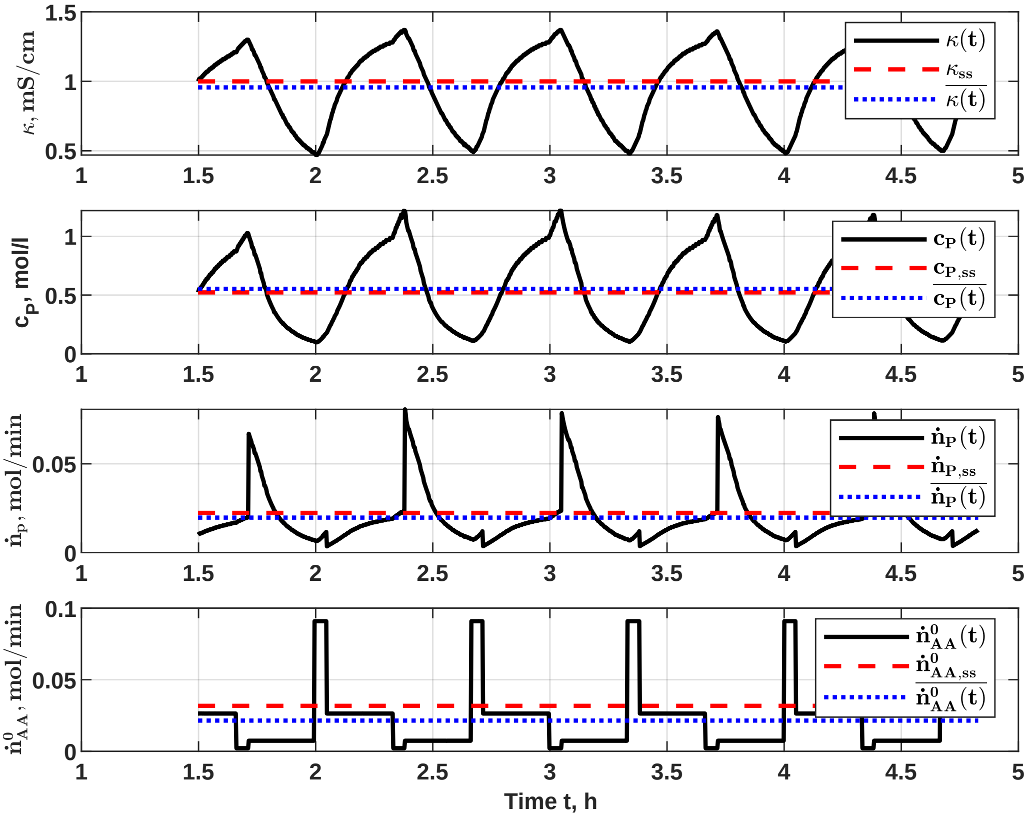

Figure B.7: Output signals for simultaneous modulation of inlet concentration A_C = 85 %, total flow rate A_F = 55 % and a period of 40 min with an optimal phase difference, presenting (a) conductivity at the outlet (top), product concentration at the outlet (second), molar product flow (third) and inlet molar product flow (bottom)

Implemented voltage functions for the simultaneous modulation of the inlet concentration and the total flow rate in a square waveform, with an optimal phase difference ϕ_{opt} between the two input parameters.

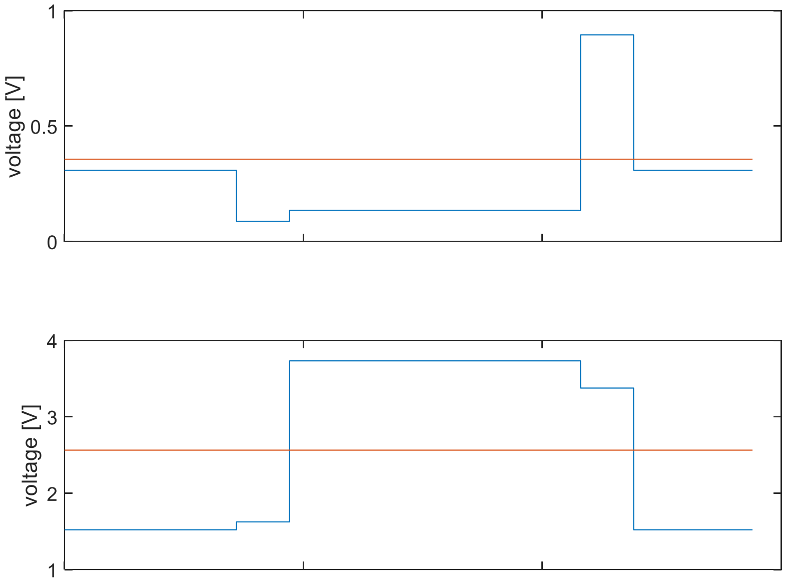

Figure B.8: Implemented voltages for the individual pumps for acetic anhydride (top) and water (bottom) with previously established steady-state (V_R = 298 ml, F_W = 40 ml/min and F_{AA} = 3 ml/min) and subsequent dynamic operation with the following parameter for square wave input functions: frequency f = $4.167 \cdot 10^{-4}$ Hz, amplitude of inlet concentration A_C = 85%, amplitude of total flow A_F = 55 % and phase difference ϕ = 157.33°).